

# 國立交通大學

材料科學與工程研究所

博 士 論 文

含共軛吡啶質子受體懸掛基氫鍵側鏈高分子之超分子  
組裝於有機光電材料之應用



**Supramolecular Assembly of H-Bonded Side-Chain  
Polymers Containing Conjugated Pyridyl H-Acceptor  
Pendants for Organic Electro-Optical Materials  
Applications**

研 究 生：梁宗琦  
指 導 教 授：林宏洲 博士

中華民國九十八年七月

含共軛吡啶質子受體懸掛基氫鍵側鏈高分子之超分子

組裝於有機光電材料之應用

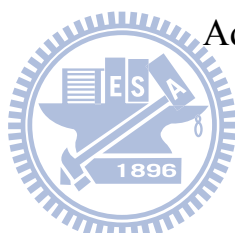
**Supramolecular Assembly of H-Bonded Side-Chain  
Polymers Containing Conjugated Pyridyl H-Acceptor  
Pendants for Organic Electro-Optical Materials  
Applications**

研究生：梁宗琦

Student: Tzung-Chi Liang

指導教授：林宏洲

Advisor: Prof. Hong-Cheu Lin



國立交通大學

材料科學與工程學系

博士論文

A Thesis

Submitted to Department of Materials Science and Engineering

College of Engineering

National Chiao Tung University

In Partial Fulfillment of the Requirement

For the Degree of Doctor of Philosophy of Science

In Materials Science and Engineering

July 2009

Hsinchu, Taiwan

中華民國九十八年七月

**Supramolecular Assembly of H-Bonded Side-Chain  
Polymers Containing Conjugated Pyridyl H-Acceptor  
Pendants for Organic Electro-Optical Materials  
Applications**

Student: Tzung-Chi Liang

Advisor: Prof. Hong-Cheu Lin

Department of Materials Science and Engineering National Chiao Tung  
University



First, two H-bonded acceptor polymers and were successfully prepared by polymerization of fluorescent pyridyl monomers, which were synthesized via Sonogashira coupling and Wittig-Horner reactions. Supramolecular side-chain and cross-linking polymers (i.e., H-bonded polymer complexes) were obtained by complexation of light-emitting H-acceptor polymers with various proton donor (H-donor) acids. Mesogenic and photoluminescent (PL) properties of light-emitting H-acceptor polymers can be adjusted not only by the central structures of the conjugated pyridyl cores but also by their surrounding non-fluorescent H-donor acids. Redder shifts of PL emissions in H-bonded polymer complexes occurred when the light-emitting H-acceptor polymers were complexed with H-donors having smaller pKa values.

Second, a series of PL and liquid crystalline (LC) self-H-bonded side-chain copolymers consisting of pyridyl H-acceptors and isomeric acid H-donors (i.e., *para*-, *meta*-, and *ortho*-benzoic acids) were synthesized. Supramolecular H-bonded complexes were also obtained by mixing the photoluminescent H-acceptor homopolymer with isomeric H-donor homopolymers. The formation of H-bonds was confirmed by FTIR, DSC, and XRD measurements. Moreover, PL and LC properties of the H-bonded copolymers and complexes were affected not only by the H-bonding effect of the supramolecular structures but also by the acid-substituted positions of isomeric H-donors. In combination with different functionalized gold nanoparticles (which bear acid or acid-free surfactants), the emission intensities of nanocomposites containing self-H-bonded copolymer (bearing both H-acceptor and H-donor moieties) and non-self-H-bonded copolymer (bearing acid-protected moieties), respectively, were quenched to different extents by varying the concentration of gold nanoparticles. The copolymeric H-acceptors and surface-modified gold nanoparticles demonstrated diverse morphological and PL quenching effects on the supramolecular architectures of nanocomposites, which result from competition between the H-donors from the acid pendants on copolymers and the acid surfactants on gold nanoparticles.

Third, this approach is exploring hydrogen-bonded (H-bonded) supramolecular assembled behavior via both TEM and fluorescence quenching studies through organic solvent dissolving and evaporating processes. Different lateral methyl- and methoxy-substituted groups with pyridyl terminus of fluorescent side-chain polymers, it performed that the H-bonded interactions affect the fluorescence quenching effectively upon the addition of surface-modified gold nanoparticles bearing acid and acid-free surfactants in the fluorescence titrations experiments. We demonstrated that homopolymer **PBOT1** has the highest  $K_{sv}$  constant in the compared fluorescent

side-chain polymers. In addition, we established the exponential equation to predict Stern-Volmer constant in various pyridyl units of polymers from the experimental information. TEM studies displayed that interesting H-bonded supramolecular behavior of addition into the carboxylic acid units of surface-modified gold nanoparticles. It is clearly observed that homogeneously gold nanoparticles distributions are on the fluorescent side-chain polymers. Thus, the TEM morphologies of H-bonded architectures demonstrate the versatility of the self-assembled processes in supramolecular nanocomposites of H-acceptor polymers and surface-modified gold nanoparticles.

Finally, novel supramolecular side-chain polymers were constructed by complexation of H-acceptor polymers, i.e., side-chain conjugated polymers containing pyridyl pendants, with low-band-gap H-donor dyes (bearing terminal cyanoacrylic acids) in a proper molar ratio. H-bonded polymer complexes exhibited broad absorption peaks in the range of 440-462 nm with optical band-gaps of 2.11-2.25 eV. The PSC device containing H-bonded polymer complex blended with PCBM (1:1 w/w) gave the best preliminary result with an overall power conversion efficiency (PCE) of 0.50%, a short-circuit current of 3.17 mA/cm<sup>2</sup>, an open-circuit voltage of 0.47 V, and a fill factor of 34%.

# 含共軛吡啶質子受體懸掛基氫鍵側鏈高分子之超分子 組裝於有機光電材料之應用

學生：梁宗琦

指導教授：林宏洲 博士

國立交通大學材料科學與工程研究所



本論文研究方向為探討一系列包含共軛吡啶質子受體氫鍵側鏈高分子之合成，利用超分子組裝的特性，在三大方向在有機光電材料為研究主軸。

第一個部份，成功的聚合出以 Sonogashira coupling 和 Wittig-Horner 反應合成出的兩種發光吡啶單體，進而將發光高分子與不同的質子予體錯合形成超分子側鏈與交聯高分子錯合物，而此氫鍵高分子錯合物之液晶及發光性質可以被吡啶共軛段及不同質子予體所調整。然而，含有較小 pKa 值的質子予體可以讓氫鍵高分子錯合物得到紅位移的發光。

第二個部份，成功的將吡啶單體與苯酸同分異構物（即，*para*-、*meta*-、和 *ortho*-）共聚出液晶及發光氫鍵高分子。藉由 FTIR、DSC、XRD 鑑定其氫鍵的形成。此外，此氫鍵高分子與其錯合物之液晶及發光性質不但與氫鍵效應有關，也被共聚不同位置的苯酸同分異構物所影響。接著，結合不同改質的奈米金球（酸或無酸改質），隨著加入的奈米金球濃度變化，自身氫鍵（含有吡啶與酸）與無自身氫鍵高分子（含有吡啶與酸保護）的奈米複合材料，其 PL 發光強度將有不

同程度的驟息。進一步，利用 TEM 觀察自身氫鍵與無自身氫鍵高分子混合改質奈米金球，而其微觀現象和 PL 驟息程度相互呼應，解釋了自身氫鍵高分子的酸與改質金球的酸相互競爭所造成。

第三個部份，描述兩種不同吡啶基比例系列的發光高分子超分子奈米複合材料，即，側面甲基高分子和側面甲氧基高分子，進而與質子予體的奈米粒子發展出可區分的聚集現象在 TEM 影像裡。質子受體高分子不但顯示了高程度聚集，而且可以使質子予體的奈米粒子均勻分散。並且，酸表面改質的奈米金球與側面甲氧基的高分子之間的氫鍵作用力，比起無酸表面改質的奈米金球更有效的影響了發光驟息的現象。此外，與側面甲基高分子比起來，側面甲氧基高分子更容易的捕捉酸表面改質的奈米金球在超分子組裝的奈米複合材料裡。吡啶基質子受體高分子與質子予體的奈米粒子的氫鍵作用力可以解釋相似的發光驟息效應。我們以實驗數據建立了在不同的吡啶基高分子的指數方程式，進而可以預測 Stern-Volmer 常數。發展了多種奈米複合材料包含兩種發光高分子(甲氧基和甲基高分子)與表面改質的奈米金球(酸和無酸改質)，進而展示出差異性的聚集現象在 TEM 影像。未來我們可以基於奈米金球發光驟息的回復性，在化學感測與生醫感測研究領域作進一步的發展。

最後一個部份，氫鍵側鏈高分子與染料型質子予體結合（含末端羧酸基）。氫鍵高分子錯合物得到了從 440 至 462 nm 寬廣的吸收能帶，且其光學能隙大約在 2.11-2.25 eV 之間。結果發現，在 AM 1.5G、100 mW/cm<sup>2</sup> 的模擬太陽光下，將合成出之氫鍵高分子錯合物與 PCBM ([6,6]-phenyl C<sub>61</sub>-butyric acid methyl ester)混合為主動層材料，成功地以 1:1 w/w 的混合比例得到一具有短路電流 3.17 mA/cm<sup>2</sup>、開路電壓 0.47 V、填充因子 34%及最高之光電轉換效率 0.50%之有機太陽能電池。

## ACKNOWLEDGEMENTS

本論文首先感謝林宏洲老師這些年來對我的照顧及鼓勵，老師對於研究上的辛苦用心及待人處世的教導，使我一路成長，如今順利完成博士學業，老師指導的恩惠，學生將永記於心。感謝韋光華老師、黃華宗老師、林建村老師、賴榮豐老師、韓建中老師於百忙之中審核論文並給予寶貴的建議及指正。在研究的過程中，也非常感謝朱治偉老師在實驗元件上大力的支持，使的本論文能更趨完善。

博士班近五年的時光使我獲益良多，很幸運也很快樂地在這實驗室度過這些日子，在此特別感謝實驗室的學長們在實驗上的教導與幫助，並感謝實驗室的眾多的同學及學弟妹在實驗上的協助，使我的實驗得以順利完成，還有陳智實驗室、呂志鵬實驗室以及許許多多材料所的學長、同學、學弟妹們在這些日子的陪伴，使我的交大生活更增添的許多歡樂。

最後要特別由衷地感謝一直栽培我的父母親、姐姐、弟弟，謝謝你們一路上的支持與鼓勵，讓我能在無後顧之憂下求學並完成博士學位。



## Table of Contents

Abstract.....	I
Acknowledgements.....	VII
Table of Contents.....	VIII
Table Lists.....	XII
Figure Lists.....	XIII
<b>Chapter 1 Introduction.....</b>	<b>1</b>
1.1 Introduction of Supramolecular Polymers.....	1
1.1.1 Hydrogen Bonding Enforced by Liquid Crystallinity .....	3
1.2 Chemical Sensors Based on Amplifying Fluorescent Conjugated Polymers ..	7
1.3 Assembly of Nanoparticles Based on Supramolecular Chemistry .....	11
1.3.1 Miscellaneous Recognition and Sensors.....	13
1.4 Supramolecular in Organic Devices.....	18
<b>Chapter 2 Study of Supramolecular Side-Chain and Cross-Linking Polymers by Complexation of Various H-Donor Acids with H-Acceptor Copolymers Containing Pendent Carbazole and Fluorescent Pyridyl Units.....</b>	<b>22</b>
2.1 Introduction.....	23
2.2 Experimental.....	30
2.2.1 Materials .....	30
2.2.2 Preparation of Supramolecular Complexes .....	38
2.2.3 Measurements and Characterization.....	39
2.3 Results and Discussion .....	40
2.3.1 Synthesis and Characterization of Polymers.....	41
2.3.2 FT-IR Spectroscopy of H-Bonded Polymer Complexes .....	42
2.3.3 Thermal Behavior .....	44
2.3.4 X-ray Diffraction Analysis .....	54

2.3.5 Optical Properties.....	59
2.4 Conclusions.....	66
<b>Chapter 3 Supramolecular Assembly of H-Bonded Copolymers/Complexes/Nanocomposites and Fluorescence Quenching Effects of Surface-Modified Gold Nanoparticles on Fluorescent Copolymers Containing Pyridyl H-Acceptors and Acid H-Donors .....</b>	<b>68</b>
3.1 Introduction.....	69
3.2 Experimental Section.....	74
3.2.1 Materials .....	74
3.2.2 Preparation of H-Bonded Complexes ( <b>PBT1/P7-P9</b> ) .....	78
3.2.3 Preparation of Nanocomposites Consisting of Gold Nanoparticles and Polymers .....	78
3.2.4 Characterizations.....	79
3.3 Results and Discussion .....	81
3.3.1 Synthesis and Characterization.....	81
3.3.2 FT-IR Spectroscopic Studies.....	82
3.3.3 Phase Characterization.....	85
3.3.4 Optical Properties.....	90
3.3.5 Fluorescence Quenching Effects of Copolymers by Surface-Modified Gold Nanoparticles .....	94
3.3.6 TEM Analyses.....	100
3.4 Conclusions.....	103
<b>Chapter 4 Supramolecular Fluorescence Quenching Effects of H-Donor Surface-Modified Gold Nanoparticles on Fluorescent H-Acceptor Polymers/Copolymers Containing Lateral Methyl- and Methoxy-Substituted Groups.....</b>	<b>105</b>
4.1 Introduction.....	106

4.2 Experimental Section .....	110
4.2.1 Materials .....	110
4.2.2 Synthesis of Surface-Functionalized Gold Nanoparticles <b>AuSC10</b> and <b>AuSCOOH</b> .....	110
4.2.3 Preparation of Nanocomposites Consisting of Gold Nanoparticles and Polymers .....	112
4.2.4 Measurements and Characterization .....	113
4.3 Results and Discussion .....	113
4.3.1 FT-IR Spectroscopic Studies .....	113
4.3.2 Fluorescence Quenching Effects of Copolymers by Surface-Modified Gold Nanoparticles .....	115
4.3.3 TEM Analyses .....	125
4.4 Conclusions .....	128
<b>Chapter 5 Supramolecular Assembly of H-Bonded Side-Chain Polymers Containing Conjugated Pyridyl H-Acceptor Pendants and Various Low-Band-Gap H-Donor Dyes Bearing Cyanoacrylic Acid Groups for Organic Solar Cell Applications .....</b>	<b>130</b>
5.1 Introduction .....	131
5.2 Experimental .....	137
5.2.1 Materials .....	137
5.2.2 Preparation of Supramolecular Polymer Complexes .....	137
5.2.3 Measurements and Characterization .....	138
5.2.4 Device Fabrication and Characterization of Polymer Solar Cells (PSCs) .....	140
5.3 Results and Discussion .....	141
5.3.1 FT-IR Spectroscopy of H-Bonded Polymer Complexes .....	141

5.3.2 Phase Behavior.....	144
5.3.3 Optical Properties.....	150
5.3.4 Electrochemical Properties .....	155
5.3.5 Photovoltaic Cell Properties .....	160
5.4 Conclusions.....	168
<b>Chapter 6 Conclusion .....</b>	<b>170</b>
References.....	176

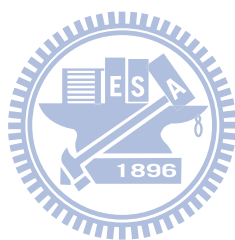


## Table Lists

<b>Table 2.1</b> Molecular Weights and Thermal Properties of H-Acceptor Polymers .....	51
<b>Table 2.2</b> Thermal Properties of H-Bonded Polymer Complexes <sup>a,b</sup> .....	52
<b>Table 2.3</b> The <i>d</i> -spacing and Tilt Angle Values of the Sc Phase in H-Bonded Polymer Complexes.....	57
<b>Table 2.4</b> Absorption and Photoluminescence Spectral Data of H-Acceptor Polymers .....	61
<b>Table 2.5</b> Photophysical Properties of H-Acceptor Polymers and H-Bonded Polymer Complexes in Solid Films.....	65
<b>Table 3.1</b> Characterization of Copolymers <b>P1-P6</b> and H-Donor Homopolymers <b>P7-P9</b> .....	77
<b>Table 3.2</b> Thermal Properties of Polymers and H-Bonded Homopolymer Complexes .....	88
<b>Table 3.3</b> Absorption and PL Emission Spectral Data of Polymers and H-Bonded Homopolymer Complexes in THF Solutions and Solid Films .....	92
<b>Table 3.4</b> Stern-Volmer Constants ( <i>K<sub>sv</sub></i> ) of Copolymers <b>P1</b> and <b>P4</b> Titrated with Different Nanoparticle Quenchers ( <b>AuSCOOH</b> and <b>AuSC10</b> ) in THF Solutions .....	98
<b>Table 4.1</b> Stern-Volmer Constant ( <i>K<sub>sv</sub></i> ) for Polymers <b>PBT1-PBOT3</b> Titrated with Different Nanoparticle Quenchers ( <b>AuSCOOH</b> and <b>AuSC10</b> ) in THF Solutions ...	121
<b>Table 5.1</b> Thermal Properties of H-Acceptor Polymers ( <b>P1-P2</b> ), H-Donor Dyes ( <b>S1-S4</b> ), Acid-Protected Dye <b>S1P</b> , H-Bonded Polymer Complexes ( <b>P1/S1-P1/S4</b> and <b>P2/S1-P2/S4</b> ), and Physical Blend <b>P1/S1P</b> .....	148
<b>Table 5.2</b> Absorption and Photoluminescence Spectral Data of H-Acceptor Polymers ( <b>P1-P2</b> ), H-Donor Dyes ( <b>S1-S4</b> ), Acid-Protected Dye <b>S1P</b> , H-Bonded Polymer Complexes ( <b>P1/S1-P1/S4</b> and <b>P2/S1-P2/S4</b> ), and Physical Blend <b>P1/S1P</b> .....	152
<b>Table 5.3</b> Electrochemical Potentials and Energy Levels of H-Acceptor Polymers ( <b>P1-P2</b> ), H-Donor Dyes ( <b>S1-S4</b> ), and H-Bonded Polymer Complexes ( <b>P1/S1-P1/S4</b> and <b>P2/S1-P2/S4</b> ).....	158
<b>Table 5.4</b> Photovoltaic Properties of PSC Devices Containing an Active Layer of H-Bonded Polymer Complexes:PCBM = 1:1 (w/w) with a Device Configuration of ITO/PEDOT:PSS/H-Bonded Polymer Complexes:PCBM/Ca/Al <sup>a</sup> .....	165
<b>Table 5.5</b> Photovoltaic Properties of PSC Devices Containing an Active Layer of Dyes <b>S1-S4</b> :PCBM = 1:1 (w/w) with a Device Configuration of ITO/PEDOT:PSS/	

Dyes <b>S1-S4</b> :PCBM/Ca/Al <sup>a</sup> .....	165
<b>Table 5.6</b> Photovoltaic Properties of PSC Devices Containing an Active Layer of Mixture:PCBM = 1:1 (w/w) with a Device Configuration of ITO/PEDOT:PSS/ Mixture:PCBM/Ca/Al <sup>a</sup> .....	166
<b>Table 5.7</b> Photovoltaic Parameters for Bulk-Heterojunction PSC Devices Containing Different Weight Ratios of Blended H-Bonded Polymer Complex <b>P1/S3</b> :PCBM <sup>a</sup> ..	166

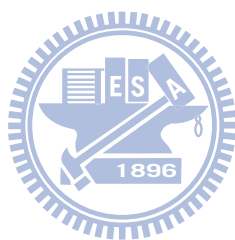


## Figure Lists

- Figure 1.1** Molecular structures consisting of non-covalent bonds: such as metal bonds, ionic forces, and H-bonds.....3
- Figure 1.2** Liquid crystalline supramolecular polymers developed by Lehn, based on triple hydrogen bonds: from chiral, tartaric acid based monomers **c** and from rigid monomers **d**. .....6
- Figure 1.3** Demonstration of amplified quenching in a CP. The determination of the Stern-Volmer quenching reveals the constant for binding of paraquat to a single cyclophane receptor (top). In the polymer the larger (amplified) quenching constant reflects the fact that the quencher can be bound to any of the repeating units visited by the exciton (bottom). .....10
- Figure 1.4** (a) Scheme 1, a chemosensor is composed of two functional elements, a receptor and a reporter group, which need not be separate in identity, (b) this account describes an approach to enhancing the sensitivity of chemosensors in effect by “wiring chemosensory molecules in series” (Scheme 2), (c) for the sake of clarity, some representative conducting polymers are shown in Scheme 3. .... 11
- Figure 1.5** Programmed pseudorotaxane assembly at the surface of AuNPs by heterosupramolecular chemistry. ....13
- Figure 1.6** Self-assembly based on selective control of non-covalent interactions provides a powerful tool for the creation of structured systems at a molecular level. This paper present a polymer-mediated “bricks and mortar” strategy for the ordering of nanoparticles into structured assemblies. .... 14
- Figure 1.7** This paper has a system where recognition element-functionalized diblock copolymers are used to self-assemble complementary nanoparticles. The size of the aggregate both in solution and in thin films is controlled through block length. .... 15
- Figure 1.8** Amine-functionalized polymers have been used to simultaneously assemble carboxylic acid functionalized gold and silica nanoparticles into extended aggregates, and nanoparticle segregation within the aggregate regulated through order of component addition. .... 15
- Figure 1.9** (A) Fluorescence resonance energy transfer (FRET) within a CdSe/ZnS QD/Texas-Red-functionalized duplex DNA. (B) FRET process in the DNA 3/2 duplex structure. (C) FRET process in the DNA duplex structure consisting of the 1-functionalized Au NP and **2**. .... 17

<b>Figure 1.10</b> Schematic presentation of reversion process from oxidized to reduced glutathione based on the modulation in photoluminescent quenching efficiency between chromophore and AuNPs. (Bottom) Chemical structure of GSH and GSSG. ....	17
<b>Figure 1.11</b> Superstructure of self-assembly of [60]fullerene derivative <b>1</b> with perylene bisimide <b>5</b> by H-bonding.....	20
<b>Figure 1.12</b> The incorporation of a ruthenium complex into the donor-acceptor conjugated polymers has the potential to facilitate the charge carrier generation.....	20
<b>Figure 1.13</b> Pyrrolidinofullerenes bearing chelating pyridyl groups (PyFs) on vacuum-evaporated films of zinc phthalocyanine (ZnPc) in donor-acceptor bilayer heterojunctions formed by deposition of solution-processed. It is shown that coordination complexes are formed at the interface between these donor and acceptor components; such association facilitates photoinduced charge separation and results in improved performance of the photovoltaic devices.....	21
<b>Figure 2.1</b> Schematic illustration of singly/doubly H-bonded processes for H-bonded side-chain/cross-linking polymers.....	27
<b>Figure 2.2</b> Mono-acid (singly H-bonded) and bis-acid (doubly H-bonded) donors used in supramolecular side-chain/cross-linking polymers, respectively.....	27
<b>Figure 2.3</b> Infrared spectra for <b>PBOT2 (18)</b> , <b>THDA (22)</b> , and H-bonded polymer complex <b>PBOT2/THDA (18/22)</b> at room temperature. ....	43
<b>Figure 2.4</b> DSC heating curves (second scans) of H-acceptor polymers <b>14-19</b> . ....	51
<b>Figure 2.5</b> Phase diagrams of mesophases in (a) H-bonded polymer complexes of <b>PBT</b> and (b) H-bonded polymer complexes of <b>PBOT</b> upon heating.....	53
<b>Figure 2.6</b> Liquid crystalline textures of H-bonded polymer complexes observed by POM (a) the Sc phase in <b>PBT1/ONA (14/21)</b> at 160 °C (cooling) (b) the Sc phase in <b>PBT2/ONA (15/21)</b> at 110 °C (cooling) (c) the nematic phase in <b>PBT2/THDA (15/22)</b> at 180 °C (cooling) (d) the Sc phase in <b>PBOT1/THDA (17/22)</b> at 160 °C (cooling).....	54
<b>Figure 2.7</b> X-ray diffraction patterns of H-bonded polymer complexes (a) the Sc phase in <b>PBOT1/OBA (17/20)</b> at 115 °C, <b>PBOT1/ONA (17/21)</b> at 120 °C, and <b>PBOT1/THDA (17/22)</b> at 160 °C; (b) the nematic phase in <b>PBT2/THDA (15/22)</b> and <b>PBOT2/THDA (18/22)</b> at 130 °C. ....	58
<b>Figure 2.8</b> X-ray diffraction patterns for H-bonded polymer complex <b>PBT1/ONA (14/21)</b> upon cooling from the isotropic phase (180 °C) to solid (50 °C). ....	59



<b>Figure 2.9</b> (a) Absorption spectra and (b) PL spectra (excited at the maximum absorption wavelengths) in THF solutions (c) normalized PL spectra (excited at the maximum absorption wavelengths) of H-acceptor polymers <b>14-19</b> in solid films.....	62
<b>Figure 2.10</b> Normalized PL spectra (excited at the maximum absorption wavelengths) of (a) H-acceptor polymer <b>PBT2 (15)</b> and its H-bonded polymer complexes <b>PBT2/OBA (15/20)</b> , <b>PBT2/ONA (15/21)</b> , and <b>PBT2/THDA (15/22)</b> in solid films; (b) H-acceptor polymer <b>PBOT2 (18)</b> and its H-bonded polymer complexes <b>PBOT2/OBA (18/20)</b> , <b>PBOT2/ONA (18/21)</b> , and <b>PBOT2/THDA (18/22)</b> in solid films. ....	66
<b>Figure 3.1</b> Schematic illustration of acid-functionalized gold nanoparticles ( <b>AuSCOOH</b> ) blended with self-H-bonded copolymer <b>P1</b> and non-self-H-bonded copolymer <b>P4</b> .....	73
<b>Figure 3.2</b> Infrared spectra of (a) H-acceptor homopolymer <b>PBT1</b> , H-donor homopolymer <b>P7</b> , and H-bonded homopolymer complexes <b>PBT1/P7</b> ; (b) copolymers <b>P1</b> and <b>P4</b> in solid films.....	84
<b>Figure 3.3</b> (a) X-ray diffraction (XRD) patterns of copolymer <b>P1</b> and H-bonded complex <b>PBT1/P7</b> in the Sc phase at 130°C. (b) XRD intensity against angle profiles obtained in the nematic phase of copolymer <b>P2</b> at 70°C.....	89
<b>Figure 3.4</b> (a) PL spectra of copolymers <b>P1-P6</b> in THF solutions (b) normalized PL spectra of copolymers <b>P1-P6</b> and H-bonded homopolymer complexes <b>PBT1/P7</b> , <b>PBT1/P8</b> , and <b>PBT1/P9</b> in solid films.....	93
<b>Figure 3.5</b> Fluorescence quenching spectra of copolymers <b>P1</b> and <b>P4</b> titrated by surface-functionalized nanoparticles ( <b>AuSCOOH</b> and <b>AuSC10</b> ) in THF solutions: (a) <b>P1</b> and (b) <b>P4</b> by varying the concentration of acid-donor-modified gold nanoparticles ( <b>AuSCOOH</b> ); (c) <b>P1</b> and (d) <b>P4</b> by varying the concentration of non-acid-modified gold nanoparticles ( <b>AuSC10</b> ). ....	99
<b>Figure 3.6</b> Corresponding Stern-Volmer plots of copolymers <b>P1</b> and <b>P4</b> for increasing concentrations of acid-modified gold nanoparticles ( <b>AuSCOOH</b> ) and non-acid-modified gold nanoparticles ( <b>AuSC10</b> ) in THF solutions. ....	99
<b>Figure 3.7</b> TEM images of acid-functionalized gold nanoparticles ( <b>AuSCOOH</b> ) blended with (a) self-H-bonded copolymer <b>P1</b> , (b) acid-protected copolymer <b>P4</b> , and (c) alkyl-functionalized gold nanoparticles ( <b>AuSC10</b> ) blended with self-H-bonded copolymer <b>P1</b> .....	102
<b>Figure 4.1</b> Schematic illustration of two series of different lateral methyl- and	

methoxy-substituted groups of H-bonded polymers blended with <b>AuSCOOH</b> . .....	110
<b>Figure 4.2</b> Molecular structures of different lateral methyl- and methoxy-substituted groups of fluorescent side-chain polymers <b>PBT1-PBT3</b> and <b>PBOT1-PBOT3</b> . .....	112
<b>Figure 4.3</b> Infrared spectra for <b>AuSCOOH</b> , <b>PBOT1</b> , and H-bonded nanocomposite <b>PBOT1/AuSCOOH</b> at room temperature.....	115
<b>Figure 4.4</b> Fluorescence quenching spectra of polymers in THF solutions (a) <b>PBOT1</b> and (b) <b>PBT1</b> by varying the concentration of acid-donor-modified gold nanoparticles <b>AuSCOOH</b> (c) <b>PBOT1</b> and (d) <b>PBT1</b> by varying the concentration of non-acid-modified gold nanoparticles <b>AuSC10</b> . .....	122
<b>Figure 4.5</b> Corresponding Stern-Volmer plots of polymers <b>PBT1</b> (■), <b>PBT2</b> (●), <b>PBT3</b> (▲), <b>PBOT1</b> (▼), <b>PBOT2</b> (◆), and <b>PBOT3</b> (★) by increasing the concentration of acid-modified gold nanoparticles <b>AuSCOOH</b> and polymers <b>PBT1</b> (□), <b>PBT2</b> (○), <b>PBT3</b> (△), <b>PBOT1</b> (▽), <b>PBOT2</b> (◇), and <b>PBOT3</b> (☆) by increasing the concentration of non-acid-modified gold nanoparticles <b>AuSC10</b> in THF solutions, where polymers <b>PBT1-PBOT1</b> by increasing the concentration of non-acid-modified gold nanoparticles <b>AuSC10</b> are replotted from inset of Figure..	123
<b>Figure 4.6</b> Schematic curves showing the dependence of Stern-Volmer constant ( $K_{sv}$ ) on pyridyl units' X mol% of polymers, which follow the experimental equation of $K_{sv} = A[1-\exp(-BX)]$ , where A and B are constants for the exponential curve fittings. ..	124
<b>Figure 4.7</b> UV-visible spectra of polymers (a) <b>PBOT1</b> titrated by varying the concentration of acid-donor-modified gold nanoparticles ( <b>AuSCOOH</b> ) and (b) <b>PBT1</b> by varying the concentration of non-acid-modified gold nanoparticles ( <b>AuSC10</b> ) in THF solutions.....	125
<b>Figure 4.8</b> TEM images of (a) acid-modified gold nanoparticles <b>AuSCOOH</b> and blended with polymers (b) <b>PBOT1</b> , (c) <b>PBT1</b> , and (d) alkyl-functionalized gold nanoparticles ( <b>AuSC10</b> ) blended with polymer <b>PBT1</b> . .....	128
<b>Figure 5.1</b> Schematic illustration of complexation processes for H-bonded side-chain polymers.....	136
<b>Figure 5.2</b> H-acceptor polymers ( <b>P1</b> and <b>P2</b> ) and H-donor dyes ( <b>S1-S4</b> ) used in the H-bonded polymer complexes ( <b>P1/S1-P1/S4</b> and <b>P2/S1-P2/S4</b> ).....	136
<b>Figure 5.3</b> Acid-protected dye <b>S1P</b> without carboxylic end functionality.....	137
<b>Figure 5.4</b> FTIR spectra of (a) H-acceptor polymer <b>P2</b> , H-donor dye <b>S1</b> , and H-bonded polymer complex <b>P2/S1</b> , and (b) H-acceptor polymer <b>P1</b> , H-donor dye <b>S1</b> ,	

acid-protected dye <b>S1P</b> , H-bonded polymer complex <b>P1/S1</b> , and physical blend <b>P1/S1P</b> .....	143
<b>Figure 5.5</b> (a) Optical texture of the nematic phase in H-bonded polymer complex <b>P2/S4</b> observed by POM at 130 °C (cooling) and (b) XRD intensity against angle profiles obtained from H-bonded polymer complexes <b>P1/S1</b> and <b>P2/S4</b> at 130 °C (in the nematic phase).....	149
<b>Figure 5.6</b> UV-visible absorption spectra of H-acceptor polymers <b>P1-P2</b> and H-donor dyes <b>S1-S4</b> (a) in THF solutions and (b) in solid films. ....	153
<b>Figure 5.7</b> UV-visible absorption spectra of (a) H-bonded polymer complexes <b>P1/S1-P1/S4</b> and (b) H-bonded polymer complexes <b>P2/S1-P2/S4</b> in solid films.....	154
<b>Figure 5.8</b> Cyclic voltammograms of H-bonded polymer complexes (a) <b>P1/S1-P1/S4</b> and (b) <b>P2/S1-P2/S4</b> . ....	159
<b>Figure 5.9</b> Energy band diagram with HOMO/LUMO levels of H-bonded polymer complexes <b>P1/S1-P1/S4</b> (as electron donors) and PCBM (as an electron acceptor) in relation to the work functions of ITO, PEDOT:PSS, and Al (HOMO value of PCBM was obtained from Reference 112). ....	160
<b>Figure 5.10</b> <i>I</i> - <i>V</i> curves (under simulated AM 1.5 solar irradiation) dependencies of PSC devices with an active layer of blended (a) H-bonded polymer complexes <b>P1/S1-P1/S4:PCBM</b> (1:1 w/w) and (b) H-bonded polymer complexes <b>P2/S1-P2/S4:PCBM</b> (1:1 w/w).....	167
<b>Figure 5.11</b> <i>I</i> - <i>V</i> curves of PSC devices containing an active layer of H-bonded polymer complex <b>P1/S3:PCBM</b> (w/w) with different weight ratios under simulated AM 1.5 solar irradiation.....	168

# Chapter 1

## Introduction

### 1.1 Introduction of Supramolecular Polymers

With the introduction of supramolecular polymers, which are polymers based on monomeric units held together with directional and reversible secondary interactions, the playground for polymer scientists has broadened and is not restricted to macromolecular species, in which the repetition of monomeric units is mainly governed by covalent bonding. The importance of supramolecular interactions within polymer science is beyond discussion and dates back to the first synthesis of synthetic polymers; the materials properties of, e.g., nylons, are mainly the result of cooperative hydrogen bonding. More recently, many exciting examples of programmed structure formation of polymeric architectures based on the combination of a variety of secondary supramolecular interactions have been disclosed.

When the covalent bonds that hold together the monomeric units in a macromolecule are replaced by highly directional noncovalent interactions (Figure 1.1), supramolecular polymers are obtained. In recent years, a large number of concepts have been disclosed that make use of these noncovalent interactions. Although most of the structures disclosed keep their polymeric properties in solution,

it was only after the careful design of multiple-hydrogen-bonded supramolecular polymers that systems were obtained that show true polymer materials properties, both in solution and in the solid state. Polymers based on this concept hold promise as a unique class of novel materials because they combine many of the attractive features of conventional polymers with properties that result from the reversibility of the bonds between monomeric units. Architectural and dynamic parameters that determine polymer properties, such as degree of polymerization, lifetime of the chain, and its conformation, are a function of the strength of the noncovalent interaction, which can reversibly be adjusted. This results in materials that are able to respond to external stimuli in a way that is not possible for traditional macromolecules. These aspects of supramolecular polymers have led to a recent surge in attention for this promising class of compounds<sup>1-3</sup> and have stimulated us to bring together materials science and supramolecular chemistry.<sup>4</sup> On the other hand, it is obvious that a large number of important properties of polymers require the covalent and irreversible bonding of the repeating units in the main chain. For applications in which all of these properties are important, supramolecular polymers are not the perfect choice. However, the opportunity to combine macromolecules and concepts derived from supramolecular polymers also has an enormous potential to alter the properties of polymers in a controlled way.

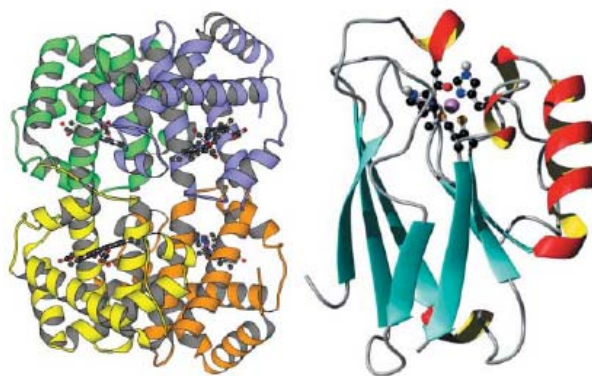


**Figure 1.1** Molecular structures consisting of non-covalent bonds: such as metal bonds, ionic forces, and H-bonds.

### 1.1.1 Hydrogen Bonding Enforced by Liquid Crystallinity

The first hydrogen-bonded supramolecular polymers all showed liquid crystallinity, although the separate components making up these polymers displayed a narrow liquid crystalline regime or no liquid crystallinity at all. The liquid crystalline phase in the supramolecular polymer is stabilized by the increased aspect ratio of aggregates compared to the constituent molecules. There is a strong cooperativity between association and the induction of the liquid crystalline phase, because anisotropy in the liquid crystal strongly enhances the degree of polymerization of the hydrogen-bonded molecules.<sup>5</sup> Liquid crystalline supramolecular polymers are unique in the respect that they combine the potential to exhibit the electrooptical properties associated with lowmolar-mass liquid crystals with the benefit of the good mechanical properties of conventional polymers.<sup>6</sup> Odijk,<sup>7,8</sup> van der Schoot,<sup>9</sup> and Ciferri<sup>10</sup> developed a theoretical basis for the relation between chain growth and orientation in

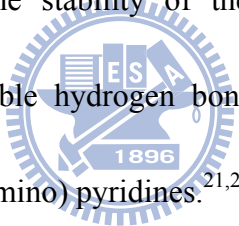
supramolecular liquid crystals.

The group of Lehn is recognized to be the first to develop a supramolecular main-chain polymer. By triple hydrogen bonding between difunctional diaminopyridines **b** and difunctional uracil **c** derivatives (Figure 1.2) supramolecular polymer chains were formed **c**.<sup>11,12</sup> The 1:1 mixture of **a** and **b** exhibits liquid crystallinity over a broad temperature window, whereas, in contrast, the pure compounds are solids which melt in an isotropic liquid without displaying a liquid crystalline phase. Because of the chirality of the tartaric acid spacer used, the fibers observed by electron microscopy showed biased helicity.<sup>13</sup> Lehn and co-workers expanded the scope of supramolecular polymers by the development of rigid rod polymers (**d**, Figure 1.2).<sup>14,15</sup> In these polymers, a rigid 9,10-dialkoxyanthracene core connects the hydrogenbonded groups via an imide group. Because of the increased molecular rigidity, the system is not thermotropic liquid crystalline, but a lyotropic liquid crystalline phase is observed in apolar solvents, that is birefringent and highly viscous.

A number of supramolecular liquid crystalline polymers based on a single hydrogen bond have been reported. Incorporation of single hydrogen-bonding units is synthetically more straightforward than those with triple hydrogen bonds, and, particularly, the single hydrogen bond between a pyridyl unit and carboxylic acids has

been utilized frequently in supramolecular liquid crystalline polymers (LCP's).<sup>16-20</sup>

The complexation between a pyridyl unit and a carboxylic acid is stronger than carboxylic acid dimerization; a  $K_a$  value of approximately  $500 \text{ M}^{-1}$  was estimated for the pyridyl/carboxylic acid complex.<sup>17</sup> Kato and Fréchet have described a variety of self-assembled side-chain liquid crystalline polymers (SLCPs), with various backbones.<sup>18,19</sup> Polyacrylates and polysiloxanes functionalized with pendant benzoic acids display stable mesophases upon selfassembly with stilbazoles. The reverse principle has been employed for the formation of supramolecular liquid crystalline polyurethanes.<sup>20</sup> Furthermore, the stability of the induced mesophase has been enlarged by employing the double hydrogen bond between benzoic acids in the polymer main-chain and 2-(acylamino) pyridines.<sup>21,22</sup>





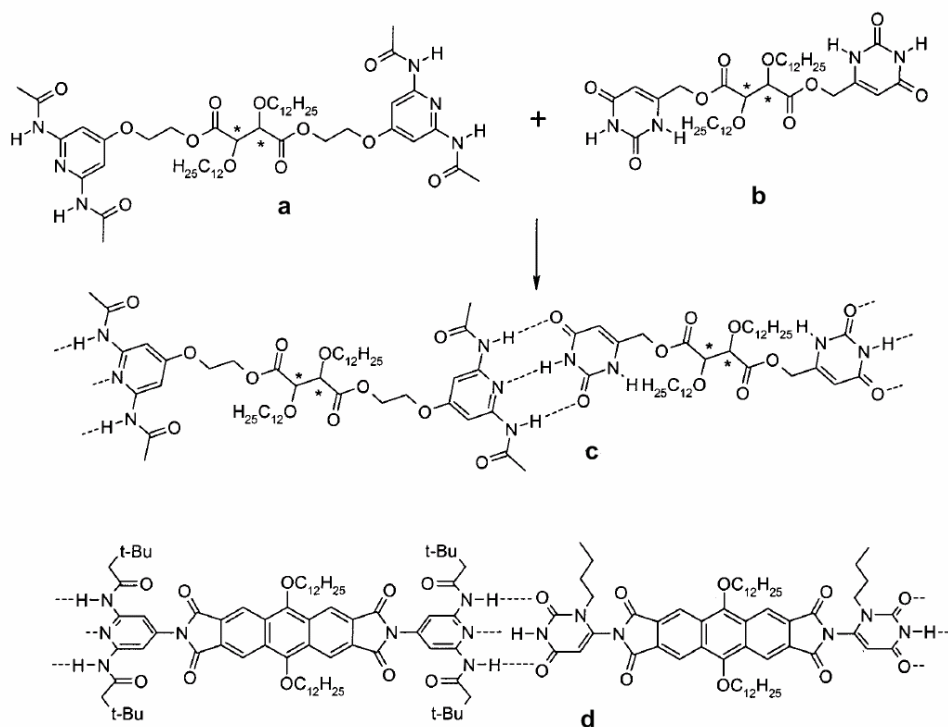


**Figure 1.2** Liquid crystalline supramolecular polymers developed by Lehn, based on triple hydrogen bonds: from chiral, tartaric acid based monomers **c** and from rigid monomers **d**.

Utilization of the single hydrogen bond between pyridine and benzoic acids in SLCP's has been a source of inspiration for other groups in the development of main-chain supramolecular polymers based on diacids and dipyridines.<sup>23-26</sup> Supramolecular rodcoil polymers have been developed by assembly of 4,4'-bipyridines and telechelic polypropylene oxide with benzoic acid end-groups, which show highly ordered liquid crystalline phases.<sup>27</sup> The use of tartaric acid derivatives in combination with bipyridine units resulted in the formation of hydrogen-bonded, chiral main-chain LCP's, as has been shown by circular dichroism measurements, optical microscopy, and X-ray data.<sup>28,29</sup>

## 1.2 Chemical Sensors Based on Amplifying Fluorescent Conjugated Polymers

The field of chemical sensing is becoming ever more dependent upon novel materials. Polymers, crystals, glasses, particles, and nanostructures have made a profound impact and have endowed modern sensory systems with superior performance. Electronic polymers have emerged as one of the most important classes of transduction materials; they readily transform a chemical signal into an easily measured electrical or optical event. The dominant attribute that has driven interest in fluorescent conjugated polymers (CPs) sensory materials is their ability to produce signal gain in response to interactions with analytes. This has led to them being referred to as amplifying fluorescent polymers (AFPs), while some researchers have referred to this gain in terms of superquenching. In analogy to microelectronic devices, the increased sensitivity (amplification) is derived from the ability of a conjugated polymer to serve as a highly efficient transport medium. However, unlike a silicon circuit, which transports electrons or holes, AFPs transport electronic excited states. The geometric relaxation of molecular structure around an excited state gives it a finite size. As a result, it is typical to refer to these excited states as quasiparticles called excitons. Excitons in AFPs are highly mobile and can diffuse throughout an isolated polymer chain or within an AFP solid by mechanisms that involve both

through space dipolar couplings and strong mixing of electronic states.

Although more recently Swager and co-workers used exciton mobility within conjugated polymers to develop other mechanisms for amplified fluorescent detection, this study serves as a general introduction to the prototypical mechanism of chemical sensing by amplified fluorescence quenching with conjugated polymers.<sup>30</sup> Amplification in a poly(phenylene ethynylene) (PPE) possessing well-defined cyclophane receptors integrated directly into the polymer backbone, effectively connecting the receptors in series. Cyclophane receptors were chosen because they form complexes with paraquat, a powerful electron acceptor and well-known electron-transfer quenching agent. To determine the ability of exciton transport to amplify binding events, a model compound containing a single receptor with the same local environment was synthesized. The large binding constant of the receptors resulted in paraquat quenching processes that were static in nature. In other words, the quencher is bound to the receptor and, once generated, the excited state is immediately and quantitatively quenched. Quenching due to diffusion of the quencher to an excited state was insignificant in this case. The quenching processes in AFPs can be analyzed by Stern-Volmer relationships (eqs 1 and 2),

$$F_0/F = (1 + K_{SV}[Q]) \quad (1)$$

$$\tau_0/\tau = (1 + k_q\tau_0[Q]) \quad (2)$$

where  $F$  is the fluorescence intensity as a function of quencher concentration  $[Q]$ ,  $\tau_0$  is the lifetime without added quencher, and  $\tau$  is the lifetime at  $[Q]$ . The slope of the plots gives the Stern-Volmer quenching constant ( $K_{SV}$ ) or the diffusional quenching constant ( $k_q$ ).

A linear relationship of  $[Q]$  with  $F_0/F$  implies a purely static (bound to the polymer) or dynamic (diffusion limited) quenching. Moderate to large binding constants give rise to Stern-Volmer quenching constants ( $K_{SV}$ ) that exceed the rate achievable at the diffusion limit, and hence, static quenching can be inferred. Another method to determine if quenching in an AFP is static or dynamic is to determine the dependence of the lifetime on the quencher concentration (eq 2).

The apparent binding constant of the receptor-containing AFP measured by the Stern-Volmer method is the individual repeating unit binding constant multiplied by the amplification factor. Comparison of the apparent binding constant ( $K_{SV}$ ) of receptor PPEs revealed a linear increase with molecular weight up to a critical molecular weight of  $\sim 1.3 \times 10^2$  phenylene ethynylene repeating units (Figure 1.3).<sup>31</sup> Higher chain lengths did not increase the apparent binding constant. These results reveal that the exciton was not able to visit the entire length of the higher molecular weight polymers because of its limited mobility and its finite lifetime (there is always competitive relaxation to the ground state). The amplification is due to exciton

mobility and should be properly separated from the binding constant. However, this analysis is seldom performed because of the need for nontrivial synthesis and other complexities inherent to polymer aggregates and thin films (*Vide infra*). This method also can be used to determine the exciton diffusion length of a CP in solution (Figure 1.4).<sup>32</sup>

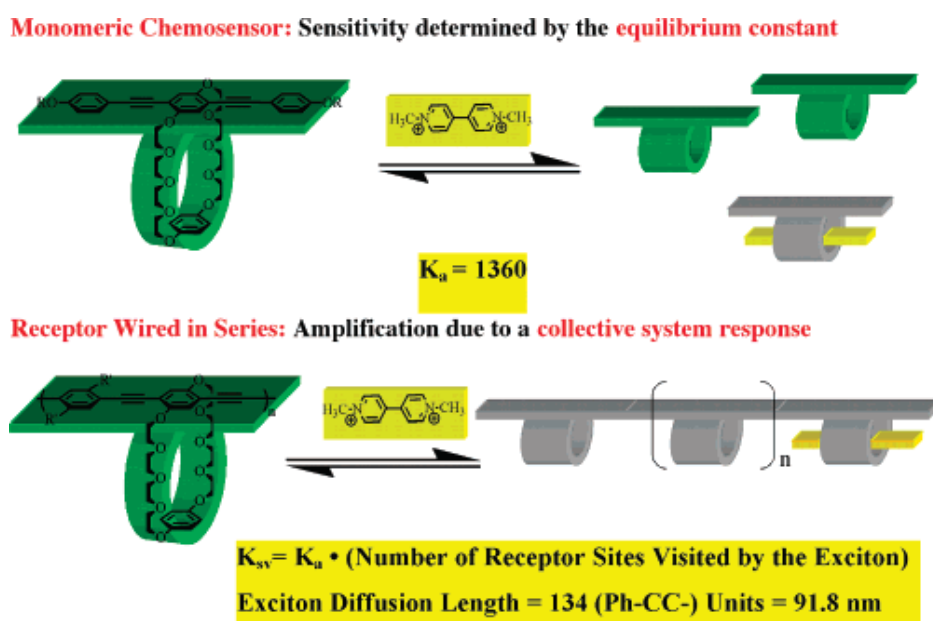


**Figure 1.3** Demonstration of amplified quenching in a CP. The determination of the Stern-Volmer quenching reveals the constant for binding of paraquat to a single cyclophane receptor (top). In the polymer the larger (amplified) quenching constant reflects the fact that the quencher can be bound to any of the repeating units visited by the exciton (bottom).

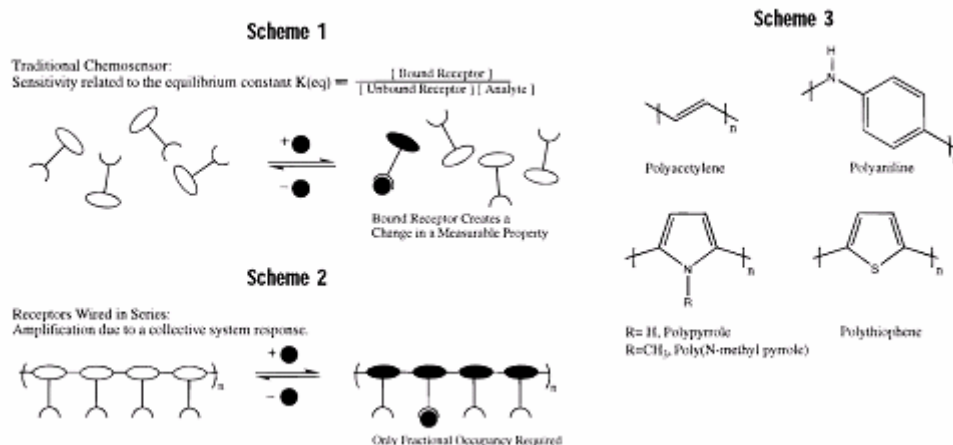


**Figure 1.4** (a) Scheme 1, a chemosensor is composed of two functional elements, a receptor and a reporter group, which need not be separate in identity, (b) this account describes an approach to enhancing the sensitivity of chemosensors in effect by “wiring chemosensory molecules in series” (Scheme 2), (c) for the sake of clarity, some representative conducting polymers are shown in Scheme 3.

### 1.3 Assembly of Nanoparticles Based on Supramolecular Chemistry

Acid-base chemistry has been involved in molecular recognition and has been studied using various techniques.<sup>33-35</sup> For instance, the structures formed by adsorption of carboxyalkylphosphonic acids on metal oxides were compared to those formed with  $\omega$ -mercaptocarboxylic acids and gold nanoparticles (AuNPs) cores using  $^1\text{H}$  fast magic angle spinning (MAS), heteronuclear correlation (HETCOR), and  $^1\text{H}$  doublequantum (DQ) MAS solid-state NMR.<sup>36</sup> Infrared reflection spectroscopic data were used to characterize the interfacial structures derived from the interfacial reactivity at the interconnecting linkages of core-shell nanoparticle networks and pH-tunable networks consisting of head-to-head hydrogen-bonded carboxylic acid terminals.<sup>37,38</sup> Nanoparticle arrays obtained by mixing anionic bilayer membranes and

cationic, quaternary ammonium-stabilized AuNPs were immobilized densely into the hydrophilic interlayers of dispersed lamellar structures to form a quasi-1D structure.<sup>39</sup> A pseudorotaxane assembly was achieved at the surface of AuNPs, pointing to similarities with the binding of a drug molecule by the receptor sites on the surface of a cell (Figure 1.5).<sup>40</sup> Evidence for film formation was also found in the case of AuNPs terminated by carboxylic acid groups.<sup>41-43</sup>

For amide-functionalized AuNPs, IR and <sup>1</sup>H NMR studies revealed that intramolecular H-bonding was highly dependent on the distance of the amide from the core.<sup>44</sup> Polyhedral oligomeric silsesquioxanes functionalized by diaminopyridines self-assembled with complementary thymines into spherical aggregates.<sup>45</sup> IR spectroscopy and cyanide-mediated decomposition of the gold cores of amide-stabilized AuNPs showed a strong correlation between the strength of the intramolecular H-bonding and the rate of decomposition.<sup>46</sup> Interaction of nitroxyl radicals with AuNPs, monitored by paramagnetic probes, resulted in loss of the EPR signal, due to exchange interaction of the unpaired electron with conduction band electrons of the AuNPs. Catalytic oxidation of a probe was also found when dioxygen was present.<sup>47</sup>

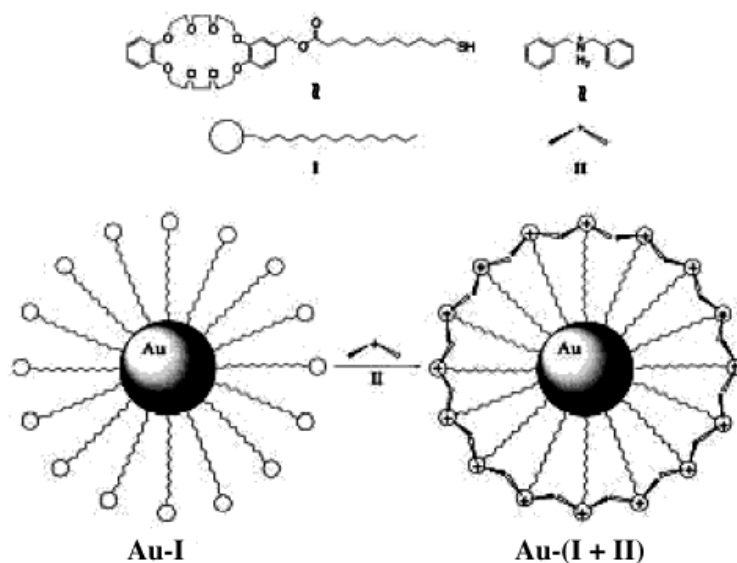


**Figure 1.5** Programmed pseudorotaxane assembly at the surface of AuNPs by heterosupramolecular chemistry.

### 1.3.1 Miscellaneous Recognition and Sensors

The controlled assembly of nanoparticles in solution based on supramolecular chemistry, i.e., noncovalent bonding,<sup>48</sup> is a general strategy leading to well-organized AuNP materials. Thus, approaches have been reported using hydrogen-bonding,<sup>48b</sup>  $\pi$ - $\pi$ ,<sup>48c</sup> host-guest,<sup>48d</sup> van der Waals,<sup>48e</sup> electrostatic,<sup>48f</sup> charge-transfer,<sup>48g</sup> and antigen-antibody<sup>48h</sup> interactions.

Amide-functionalized AuNPs were also used as optical sensors for anions.<sup>49</sup> AuNPs functionalized with 15-crown-5 recognize  $K^+$  in water,<sup>50a</sup> and  $Li^+$ <sup>50b</sup> and heavy metal ions<sup>51,52</sup> were recognized using AuNP-based sensors. Rotello and co-workers reported the synthesis and self-assembly of gold nanoparticles with inherent optical properties (Figure 1.6). The recognition properties based on H-bonding were used to



assemble AuNPs into micelles using polymers (Figure 1.7).<sup>53</sup> Furthermore, amine-functionalized polymers have been used to simultaneously assemble carboxylic acid functionalized gold and silica nanoparticles into extended aggregates, and nanoparticle segregation within the aggregate regulated through order of component addition (Figure 1.8).<sup>54</sup>

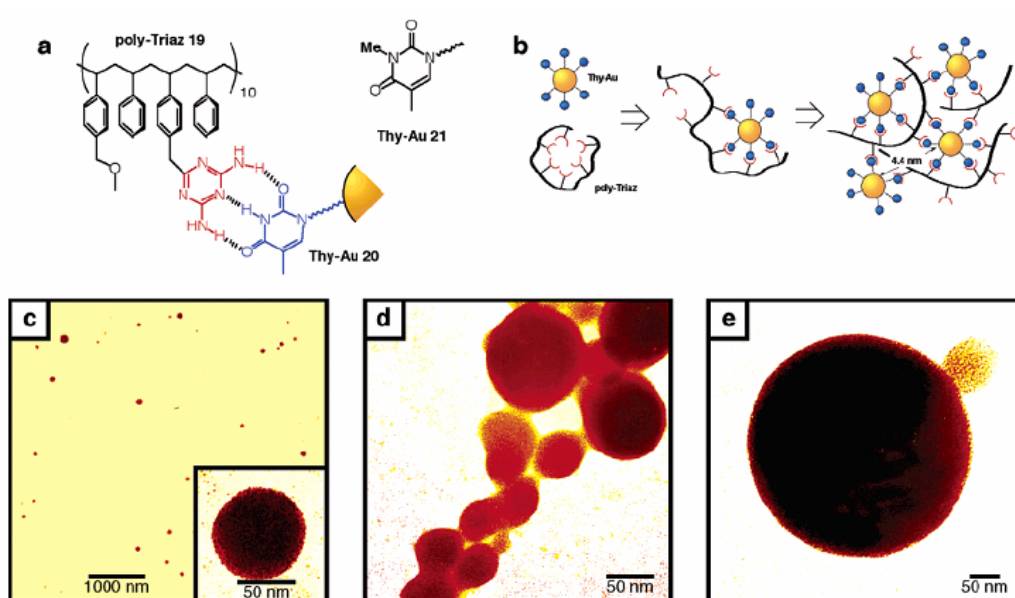


**Figure 1.6** Self-assembly based on selective control of non-covalent interactions provides a powerful tool for the creation of structured systems at a molecular level. This paper present a polymer-mediated “bricks and mortar” strategy for the ordering of nanoparticles into structured assemblies.

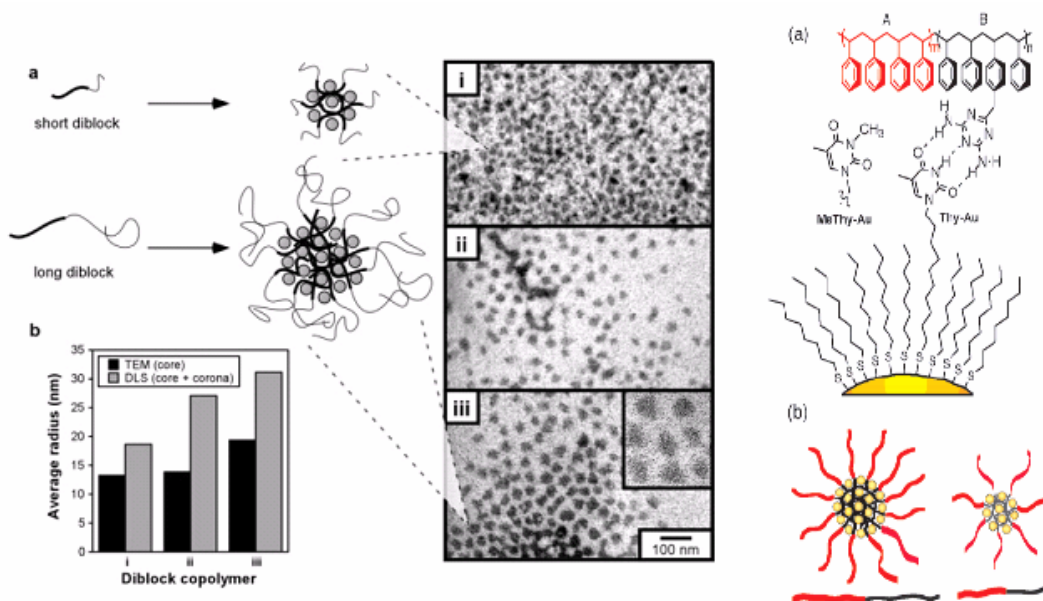


**Figure 1.7** This paper has a system where recognition element-functionalized diblock copolymers are used to self-assemble complementary nanoparticles. The size of the aggregate both in solution and in thin films is controlled through block length.

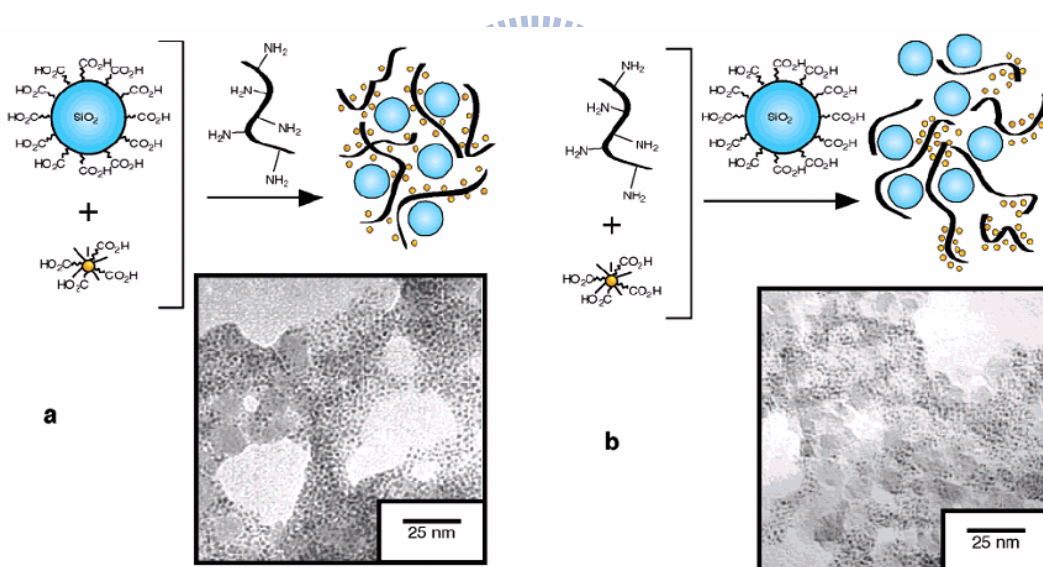


**Figure 1.8** Amine-functionalized polymers have been used to simultaneously assemble carboxylic acid functionalized gold and silica nanoparticles into extended aggregates, and nanoparticle segregation within the aggregate regulated through order of component addition.

AuNPs have also been used for vapor sensing.<sup>55a,b</sup> The sensitivity of the plasmon band with the core environment is obviously a source of sensing, and the optical

response (Surface Plasmon Band) has been modeled.<sup>56</sup> Electrochemical genosensors for the detection of the Factor V Leiden mutation from polymerase chain reaction amplicons using the oxidation signal of AuNPs at +1.20 V were described.<sup>55c</sup> DNA-AuNP assemblies have also been used as colorimetric lead biosensors.<sup>55d</sup> *N*-Methylimidazole-functionalized AuNPs were reported to recognize bis- and tris-Zn porphyrins.<sup>55e</sup> Conjugates of AuNPs-oligonucleotides are of great current interest because of the potential use of the programmability of DNA base-pairing to organize nanocrystals in space and the multiple ways of providing a signature for the detection of precise DNA sequences (Figure 1.9).<sup>57</sup> Furthermore, in the presence of other metal ions, such as  $\text{Cu}^{2+}$ ,  $\text{Co}^{2+}$ ,  $\text{Fe}^{3+}$ ,  $\text{Ni}^{2+}$ ,  $\text{Zn}^{2+}$ ,  $\text{Pb}^{2+}$  and  $\text{Ag}^+$ , the gold nanoparticles of the quenched nanocomposites (containing fluorophores) can be replaced with the metal ions to different extents due to the stronger re-coordination or re-complexation of the metal ions with fluorophores, and therefore recover the fluorescence of the chromophores to behave as chemosensors. In addition, the gold nanoparticles of the quenched nanocomposites can also be reacted with the reduced glutathione in the presence of glutathione reductase enzyme, and then recover the fluorescence of the chromophores to behave as biosensors (Figure 1.10).<sup>58</sup> The sensor applications of this work can be further developed to detect the metal ions and biomolecules based on the modulation of fluorescence quenching and recovery.

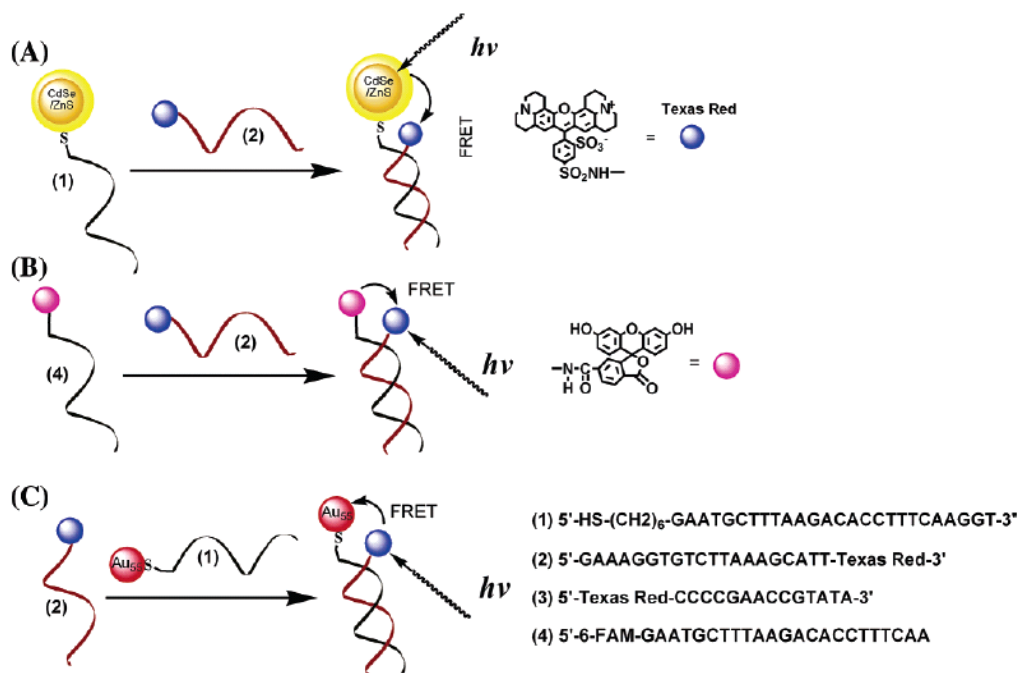


**Figure 1.9** (A) Fluorescence resonance energy transfer (FRET) within a CdSe/ZnS QD/Texas-Red-functionalized duplex DNA. (B) FRET process in the DNA 3/2 duplex structure. (C) FRET process in the DNA duplex structure consisting of the 1-functionalized Au NP and 2.

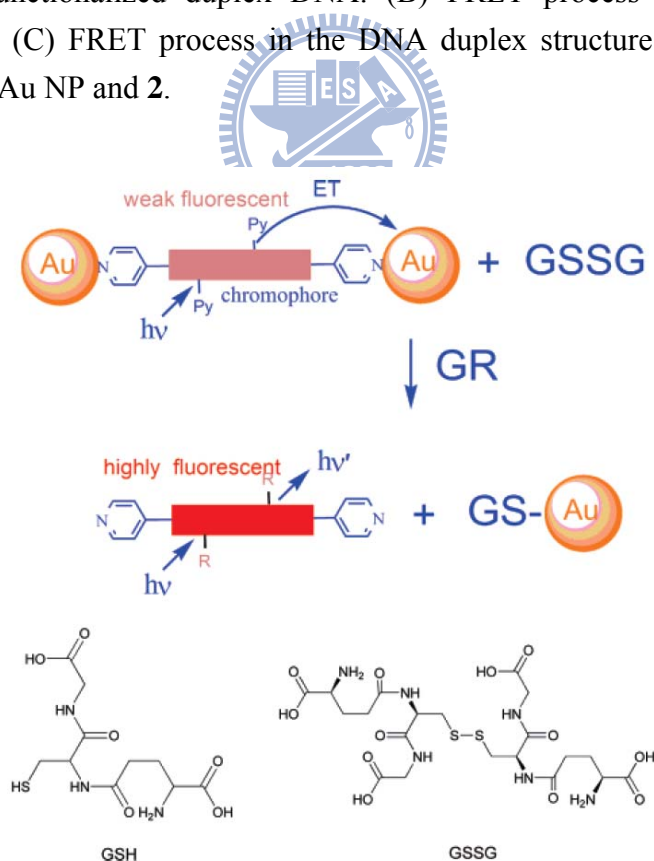


**Figure 1.10** Schematic presentation of reversion process from oxidized to reduced glutathione based on the modulation in photoluminescent quenching efficiency between chromophore and AuNPs. (Bottom) Chemical structure of GSH and GSSG.

## 1.4 Supramolecular in Organic Devices

One of the major challenges in the field of electronics based on organic molecules is the design of functional, multicomponent architectures possessing long-range ordering. Having an electron-donating as well as an electron-accepting chromophore is a prerequisite to obtain organic photovoltaics. It has also been demonstrated that incorporation of energy- or electron-accepting chromophores into  $\pi$ -conjugated polymer backbones can rigorously alter the electrooptical properties of the resulting copolymers. The copolymers can be characterized by either almost exclusive emission from the incorporated acceptor moiety or efficient charge transfer. Recently, an end was put to a long discussion about undesired green emission in polyfluorenes, which appeared to arise from efficient energy transfer to small amounts of oxidized monomer,<sup>59</sup> indicating the necessity for high-purity polymers.

The viability of this functional approach has been shown by the successful tuning of electroluminescence in a light-emitting diode (LED) consisting of PPV with dangling porphyrins.<sup>60</sup> Also, a photovoltaic device based on a blend of PPV and polyfluorene with dangling perylene proved to yield high external quantum efficiencies in both the perylene and the polyfluorene absorption regions, due to energy transfer from the polyfluorene to the perylene with near unit efficiency.<sup>61</sup> Moreover, connecting the electrooptical properties in organic devices have been

established through the supramolecular interactions, e.g. H-bonds, in organic, dendritic, and polymeric H-bonded complex systems. This was illustrated by a recent report on a triple hydrogen-bonded triad consisting of a central perylene that was connected to two C<sub>60</sub> chromophores (Figure 1.11).<sup>62</sup> Novel monomer and PPV-donor and PPV-acceptor bearing a terminal terpyridine chelating unit were reported (Figure 1.12).<sup>63</sup> Three new photoactive supramolecular dyads have been prepared by complexing the ruthenium with the PPV-terpyridine ligands. Studies on the incorporation of such ligands and supramolecular building blocks into polymers were performed through photophysical properties. An efficient energy transfer process from the conjugated polymer block to the metal complex was shown. Moreover, the preparation of several different fullerene-based materials bearing chelating pyridyl groups (PyFs, Figure 1.13)<sup>64</sup> was reported, with a comparative investigation of their interactions with ZnPc in solid thin films and evaluation of the performance of these materials in bilayer organic solar cells. To achieve efficient photocurrent generation in a wide spectral region, they merged bulk heterojunction MDMO-PPV/PCBM cells and bilayer ZnPc/PyF cells in a multicomponent device structure. The combination of bilayer fullerene/ZnPc and bulk heterojunction fullerene/polymer photovoltaic devices can be considered a promising approach to achieve a wide spectral response in organic solar cells while retaining the good charge-transfer and transport properties

of established materials.

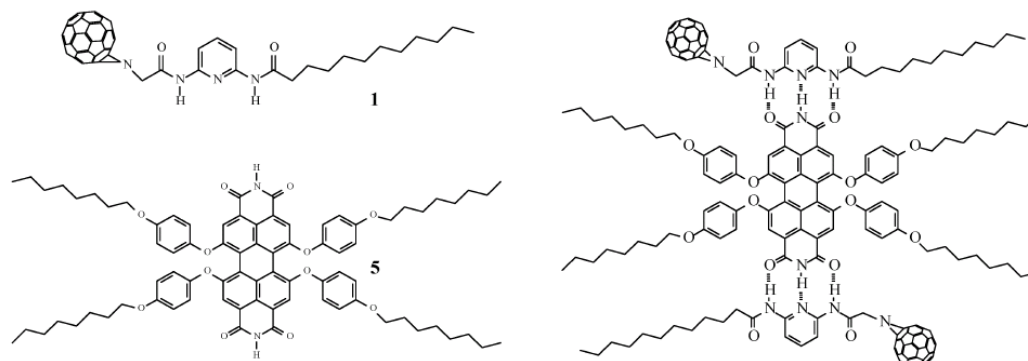


**Figure 1.11** Superstructure of self-assembly of [60]fullerene derivative **1** with perylene bisimide **5** by H-bonding.

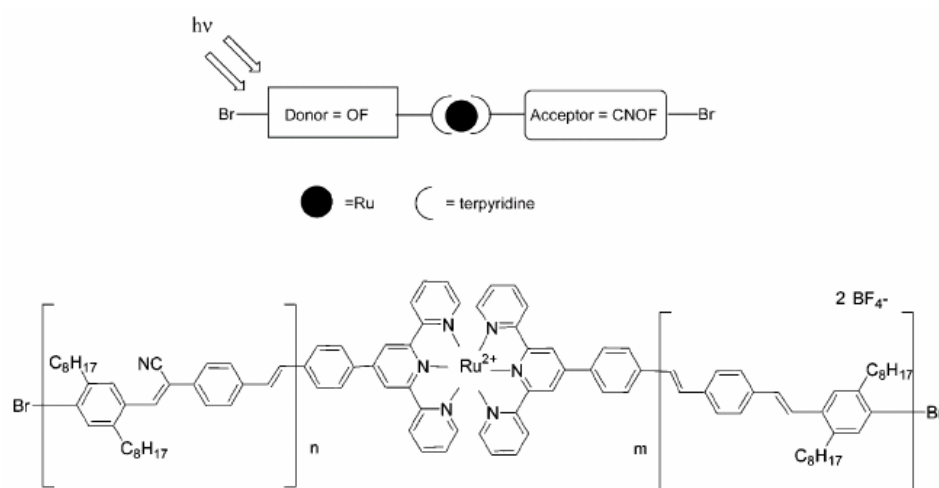


**Figure 1.12** The incorporation of a ruthenium complex into the donor-acceptor conjugated polymers has the potential to facilitate the charge carrier generation.

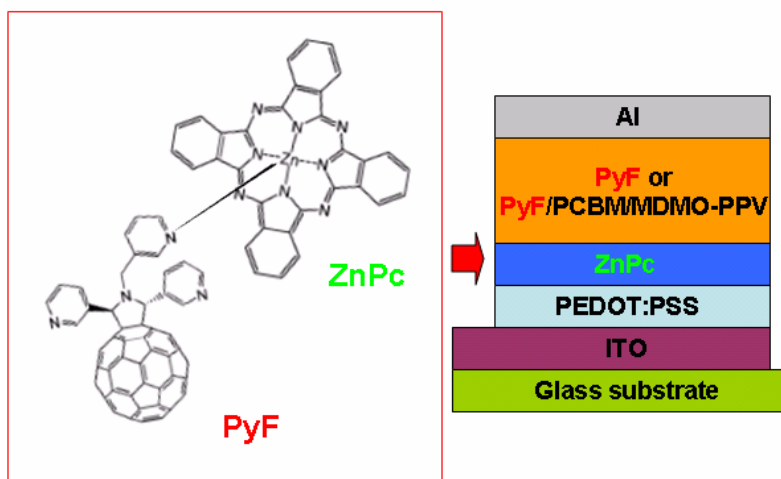


**Figure 1.13** Pyrrolidinofullerenes bearing chelating pyridyl groups (PyFs) on vacuum-evaporated films of zinc phthalocyanine (ZnPc) in donor-acceptor bilayer heterojunctions formed by deposition of solution-processed. It is shown that coordination complexes are formed at the interface between these donor and acceptor components; such association facilitates photoinduced charge separation and results in improved performance of the photovoltaic devices.





## Chapter 2

# Study of Supramolecular Side-Chain and Cross-Linking Polymers by Complexation of Various H-Donor Acids with H-Acceptor Copolymers Containing Pendent Carbazole and Fluorescent Pyridyl Units

*Two H-bonded acceptor (H-acceptor) homopolymers 14 and 17 were successfully prepared by polymerization of fluorescent pyridyl monomers PBT and PBOT (12 and 13), which were synthesized via Sonogashira coupling and Wittig-Horner reactions. In order to increase the glass transition temperatures as well as reduce the  $\pi$ - $\pi$  stacking of the photoluminescent (PL) H-acceptor copolymers and their H-bonded polymer complexes, fluorescent monomers 12 and 13 were copolymerized with N-vinylcarbazole monomer CAZ (23) to produce H-acceptor copolymers 15-16 and 18-19. Supramolecular side-chain and cross-linking polymers (i.e., H-bonded polymer complexes) obtained by complexation of light-emitting H-acceptor polymers 14-19 with various proton donor (H-donor) acids 20-22 were further characterized by DSC, POM, FTIR, XRD, and PL measurements. The mesomorphic properties can be tuned from the nematic phase in H-acceptor*

*homopolymers (14 and 17) to the tilted smectic C phase in their H-bonded polymer complexes (14/20-21 and 17/20-22) by the introduction of H-donor acids (20-22). Moreover, the PL properties of light-emitting H-acceptor polymers can be adjusted not only by the central structures of the conjugated pyridyl cores but also by their surrounding non-fluorescent H-donor acids. In general, redder shifts of PL emissions in H-bonded polymer complexes occurred when the light-emitting H-acceptor polymers were complexed with H-donors having smaller pKa values.*

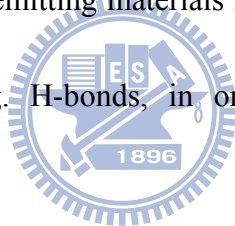
## **2.1 Introduction**

Supramolecular chemistry is a new and exciting branch of chemistry encompassing systems held together by non-covalent bonds, and such complexes have considerable application potentials in the rapidly developing fields of molecular electronics and optoelectronics.<sup>48a,65,66</sup> More recently, the concept of supramolecular chemistry has been applied to the design of liquid crystalline (LC) polymers in the expectation that molecular interactions may be amplified into macroscopically observable phenomena of self-assembled phases, i.e., liquid crystallinity.<sup>67</sup> Supramolecular liquid crystals are molecular complexes generated from complexation of molecular species through non-covalent interactions, e.g., hydrogen bonding. Kato and Fréchet first exploited two different and independent components to generate

liquid crystals through intermolecular hetero-hydrogen-bonding interaction, and this concept in turn resulted in numerous findings of such supramolecular liquid crystals.<sup>18,19</sup> The mesogenic properties can be easily modified by miscellaneous proton donors and acceptors, and new liquid crystalline properties, which are different from those of their original moieties, can be easily obtained by the introduction of supramolecular structures. Many kinds of H-bonds and building elements have been explored in the H-bonded structures to stabilize liquid crystalline phases.<sup>68</sup> Therefore, side-chain liquid crystalline polymers consisting of polymer backbones, flexible spacers, and mesogenic pendants have great potentials in various utilizations as novel technological materials, such as optical switching elements, optical storage devices, and information displays. Among these approaches, intermolecular H-bonding is simply acquired by complexation of H-bonded donor (H-donor) carboxylic (or benzoic) acid groups with H-bonded acceptor (H-acceptor) pyridyl moieties. Several series of H-bonded polymer complexes and side-chain liquid crystalline polymers through intermolecular H-bonding (interaction between benzoic acid and pyridine) have been reported lately.<sup>69,70</sup>

The advantages of using organic materials to manufacture electroluminescent (EL) devices are their excellent film-forming properties, processing feasibilities of flexible devices, highly efficient EL properties, and low costs of fabrication.<sup>71</sup> As we

know, poly(*N*-vinylcarbazole) (PVK) has attracted attention due to its applications related to polymer light-emitting diodes (PLEDs) in which the hole transporting layer is formed by PVK or it can be blended with other light-emitting materials. Such PLED devices have shown remarkably high luminescence efficiencies and relatively facile color tunabilities.<sup>72-74</sup> In contrast to PVK, Romero et al.<sup>75</sup> observed an increase in the external quantum efficiency of PLED devices based on the copolymerization of carbazole units with short thiophene segments, so carbazole units were also used to copolymerize with fluorescent pyridyl moieties in our study. Moreover, tuning emission colors in organic light-emitting materials have been established through the supramolecular interactions, e.g. H-bonds, in organic, dendritic, and polymeric H-bonded complex systems.<sup>76-78</sup>



In this report, fluorescent pyridyl H-acceptors as pendent groups were incorporated into the side-chain polymeric structures rather than as small molecules in our previous studies.<sup>76-78</sup> The purpose of the present study for side-chain conjugated pyridyl polymers is to explore the self-assembled utilization of singly and doubly H-bonded structures (as shown in the schematic illustration of Figure 2.1) in preparing for supramolecular side-chain and cross-linking polymers, respectively. As shown in Schemes 2.1 and 2.2, fluorescent H-acceptor monomers **PBT** and **PBOT** (**12** and **13**) and their corresponding H-acceptor homopolymers (**14** and **17**)

containing three-conjugated aromatic rings (including two lateral substituted methyl and methoxy groups with one pyridyl terminus) were prepared, and both pyridyl H-acceptor monomers **12** and **13** were further reacted with different molar ratios of carbazole monomer **CAZ (23)** to produce copolymers **15-16** and **18-19**, respectively. Thus, the glass transition temperatures of the H-acceptor polymers can be controlled by the contents of pendent carbazole monomer **CAZ (23)** in H-acceptor polymers (**14-16** and **17-19**). In addition to the syntheses of such fluorescent H-acceptor monomers and polymers, two series of different H-acceptor polymers **PBT1-PBT3 (14-16)** and **PBOT1-PBOT3 (17-19)** were complexed with asymmetric mono-functional H-donors **OBA (20)** and **ONA (21)** as well as symmetric bi-functional H-donor **THDA (22)**, respectively (as shown in Figure 2.2). By incorporating of H-acceptor polymers to H-donor acids with different pKa values, the light-emitting properties of the supramolecular polymer complexes can be easily adjusted. Singly/doubly H-bonded processes of side-chain/cross-linking H-bonded polymers were confirmed and investigated by means of their liquid crystalline properties, X-ray diffraction (XRD) patterns, and photoluminescent (PL) properties.

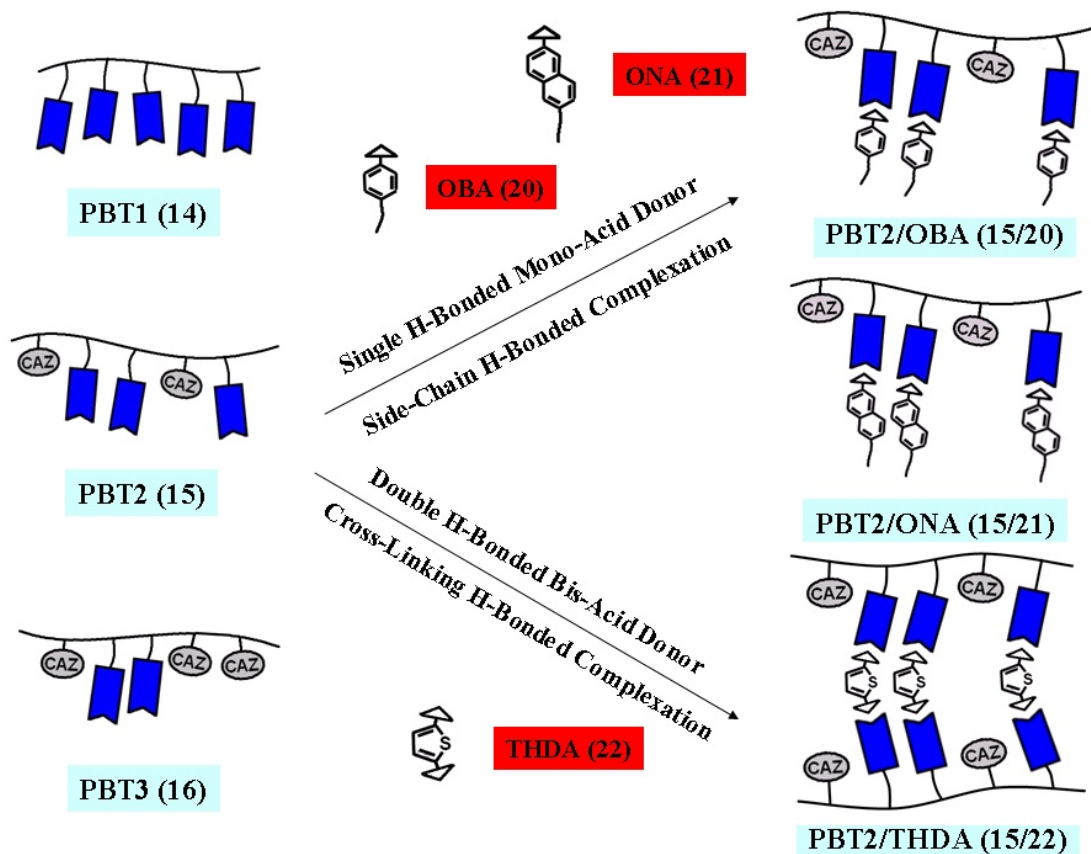


**Figure 2.1** Schematic illustration of singly/doubly H-bonded processes for H-bonded side-chain/cross-linking polymers.

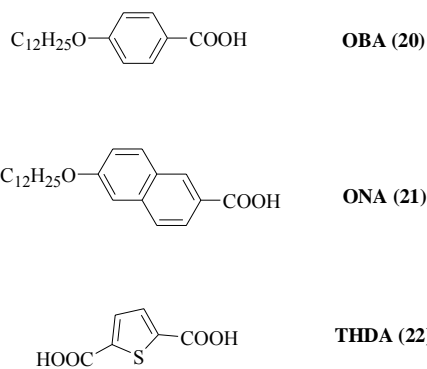
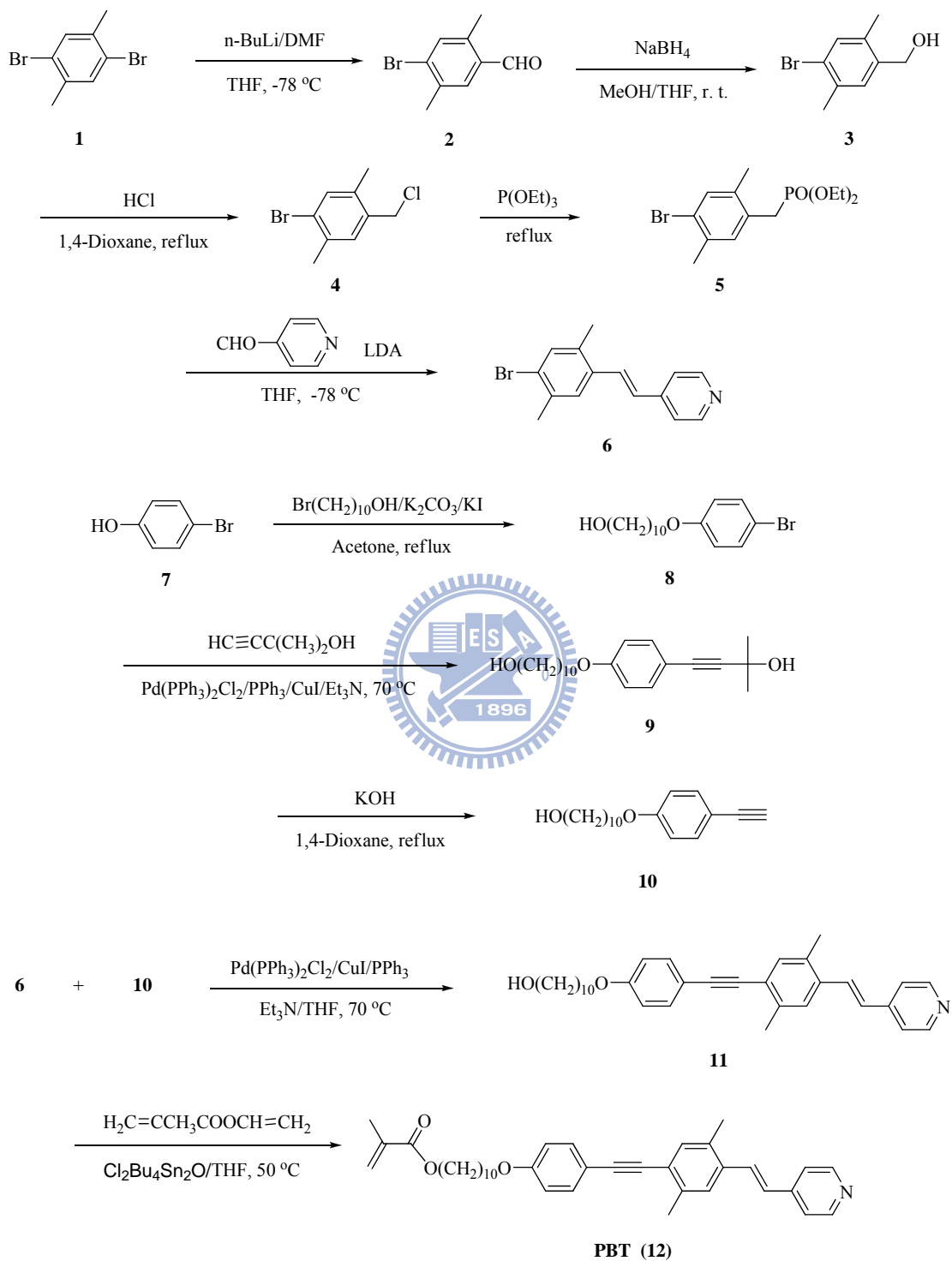
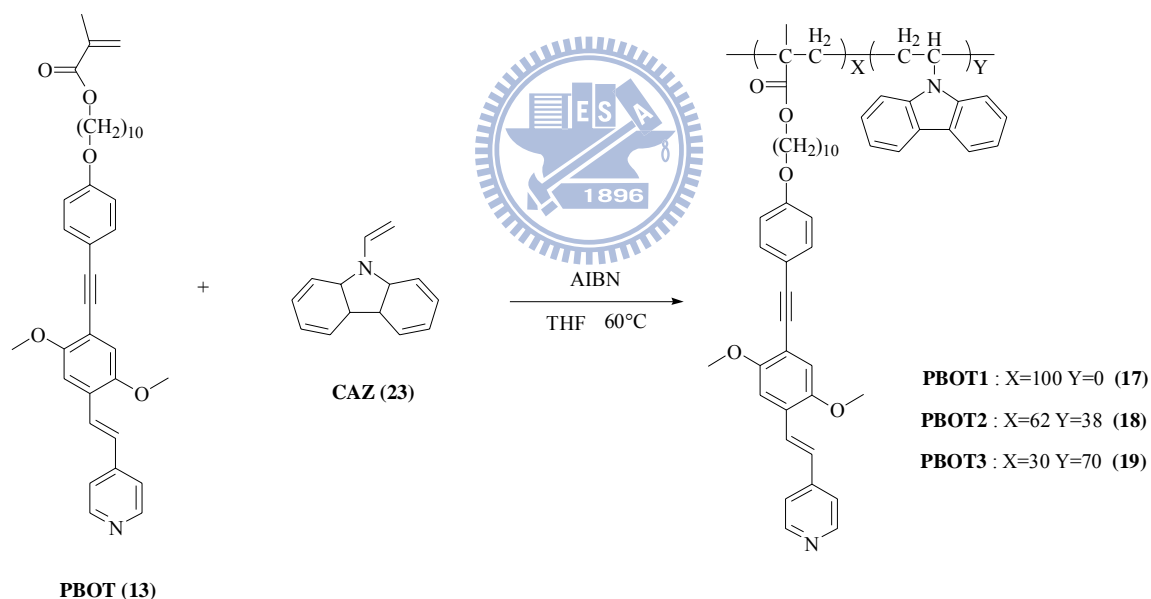
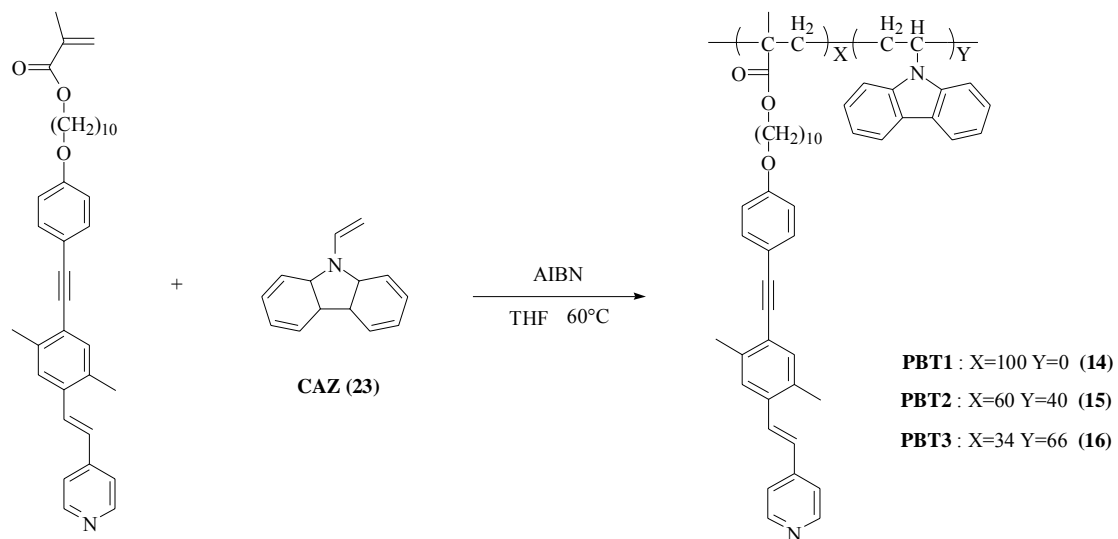


**Figure 2.2** Mono-acid (singly H-bonded) and bis-acid (doubly H-bonded) donors used in supramolecular side-chain/cross-linking polymers, respectively.

### Scheme 2.1 Synthetic Routes of Monomer PBT (12).



## Scheme 2.2 Synthetic Routes of H-Acceptor Polymers.





## 2.2 Experimental

### 2.2.1 Materials

*N*-vinylcarbazole **CAZ (23)** was purchased from Aldrich Chemical Co. and used without further purification. Azobisisobutyronitrile (AIBN) was purchased from Kanto Chemical Co. and recrystallized from ethanol at 40 °C followed by drying in a vacuum oven. Proton donors **OBA (20)** and **ONA (21)** were identified as the required materials by <sup>1</sup>H and <sup>13</sup>C NMR spectroscopy and elementary analyses, which were reported in our previous results,<sup>78</sup> and proton donors thiophene-2,5-dicarboxylic acid **THDA (22)** was purchased from Aldrich Chemical Co. Chemicals and solvents were reagent grades and purchased from Aldrich, Acros, TCI, and Lancaster Chemical Co. Dichloromethane and THF were distilled to keep anhydrous before use. The other chemicals were used without further purification.

#### Syntheses of H-Acceptor Monomers **PBT (12)** and **PBOT (13)**

The synthetic route of monomer **PBT (12)** is shown in Scheme 2.1, and its synthetic procedures are described as follows:

**4-Bromo-2,5-dimethylbenzaldehyde (2)**. 2,5-Dibromo-*p*-xylene **1** (6.9 g, 26.3 mmol) was dissolved in 60 mL of dry THF purged with nitrogen. A solution of *n*-BuLi (13.7 mL, 34.2 mmol, 2.5 M in hexane) was added dropwise to a rapidly stirred THF at -78 °C. The rate of addition was adjusted to keep the temperature

below  $-78\text{ }^{\circ}\text{C}$ . After the solution was stirred to react for 2 h at  $-78\text{ }^{\circ}\text{C}$ , a solution of DMF (4.1 mL, 52.6 mmol) was added dropwise to keep at the same temperature. After 2 h, the reaction was quenched with water and extracted with ethyl acetate. The organic extracts were dried over  $\text{Na}_2\text{SO}_4$  and then evaporated. The crude product was purified and recrystallized from n-hexane to give a white crystal. Yield: 5.0 g (90%).  $^1\text{H-NMR}$  (ppm,  $\text{CDCl}_3$ ):  $\delta$  10.19 (s, 1H), 7.63 (s, 1H), 7.47 (s, 1H), 2.60 (s, 3H), 2.43 (s, 3H).

**4-Bromo-2,5-dimethylbenzyl alcohol (3).** To a stirred solution of compound **2** (5.0 g, 23.7 mmol) in 100 mL of THF/MeOH (1:1),  $\text{NaBH}_4$  (0.9 g, 23.7 mmol) was added very slowly and reacted at room temperature. After 1 h, the solution was cooled to  $0\text{ }^{\circ}\text{C}$  by ice bath, acidified with dilute HCl solution, and extracted with ethyl acetate. The resulting extracts in organic phase were combined and washed with water. Then, the organic extracts were dried over  $\text{Na}_2\text{SO}_4$  and evaporated. The crude product was purified and recrystallized from dichloromethane/2-propanol to give a colorless crystal. Yield: 4.1 g (80%).  $^1\text{H-NMR}$  (ppm,  $\text{CDCl}_3$ ):  $\delta$  7.33 (s, 1H), 7.21 (s, 1H), 4.61 (s, 2H), 2.35 (s, 3H), 2.27 (s, 3H).

**1-Bromo-4-chloromethyl-2,5-dimethoxybenzene (4).** A stirred solution of compound **3** (4.1 g, 19 mmol) in 1,4-dioxane (150 mL) was added with concentrated HCl (20 mL, 3N), and then the mixture was refluxed for 10 h. After the reaction was

completed, the crude mixture was added with water. The organic layer was extracted with ethyl acetate, dried over Na<sub>2</sub>SO<sub>4</sub> and evaporated. The crude product was purified by flash column chromatography (silica gel, n-hexane/ethyl acetate 40:1) to give a white solid. Yield: 4.0 g (89%). <sup>1</sup>H-NMR (ppm, CDCl<sub>3</sub>): δ 7.36 (s, 1H), 7.15 (s, 1H), 4.51 (s, 2H), 2.36 (s, 6H).

**(4-Bromo-2,5-dimethylbenzyl)diethylphosphonate (5).** Compound **4** (4.0 g, 17.1 mmol) was mixed with an excess of triethylphosphite (20 mL) and heated to reflux for 12 h under reduced pressure. The excess of triethylphosphite was removed after reaction. The crude product was purified and washed with hot hexane to give a white solid. Yield: 5.1 g (90%). <sup>1</sup>H-NMR (ppm, CDCl<sub>3</sub>): δ 7.28 (s, 1H), 7.07 (s, 1H), 4.08-3.95 (m, 10H), 3.06 (s, 1H), 2.99 (s, 1H), 2.28 (s, 3H), 2.26 (s, 3H).

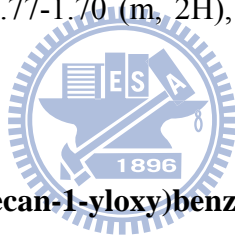
**1-Bromo-2,5-dimethyl-4-[2-(4-pyridyl)ethenyl]benzene (6).** Compound **5** (5.1 g, 15.1 mmol) was dissolved in 60 mL of dry THF purged with nitrogen. A solution of lithium diisopropylamide (22.7 mL, 45.3 mmol, 2.5 M in hexane) was added dropwise to a rapidly stirred solution at -78 °C. The rate of addition was adjusted to maintain the temperature below -78 °C. After the solution was stirred to react for 30 min at -78 °C, a solution of pyridine-4-carboxaldehyde (2 mL, 21.1 mmol) was added dropwise and stirred for 30 min to come back to room temperature. After that, the mixture was stirred to react for 18 h at room temperature. The reaction was quenched

with water and extracted with dichloromethane. Subsequently, the organic layer was dried over  $\text{Na}_2\text{SO}_4$  and evaporated. The crude product was purified by column chromatography (silica gel, dichloromethane/acetone 20:1) to give a yellow solid. Yield: 3.7 g (85%).  $^1\text{H-NMR}$  (ppm,  $\text{CDCl}_3$ ):  $\delta$  8.56 (d,  $J = 4.8$  Hz, 2H), 7.42 (s, 1H), 7.40 (d,  $J = 16.2$  Hz, 1H), 7.36 (s, 1H), 7.35 (d,  $J = 4.8$  Hz, 2H), 6.88 (d,  $J = 16.2$  Hz, 1H), 2.38 (s, 3H), 2.35 (s, 3H).

**10-(4-Bromophenoxy)-decan-1-ol (8).** A mixture of 4-bromophenol **7** (4.9 g, 28.5 mmol), potassium carbonate (8.7 g, 62.7 mmol), 10-bromodecanol (7.4 g, 31.4 mmol), and a few amount of potassium iodide in acetone (200 mL) was heated to reflux and stirred under nitrogen for 48 h. After cooling to room temperature, the solvent was removed under reduced pressure. The residue was taken up in water and extracted with ethyl acetate. Then, the organic layer was dried over  $\text{Na}_2\text{SO}_4$  and evaporated. The crude product was purified by column chromatography (silica gel, n-hexane/ethyl acetate 3:1) to give a white solid. Yield: 8.3 g (88%).  $^1\text{H-NMR}$  (ppm,  $\text{CDCl}_3$ ):  $\delta$  7.33 (d,  $J = 9.0$  Hz, 2H), 6.75 (d,  $J = 9.0$  Hz, 2H), 3.89 (t,  $J = 6.3$  Hz, 2H), 3.62 (t,  $J = 6.6$  Hz, 2H), 1.78-1.69 (m, 2H), 1.59-1.50 (m, 2H), 1.41-1.29 (m, 12H).

**4-[4-(10-Hydroxy-decyloxy)-phenyl]-2-methyl-3-butyn-2-ol (9).** A solution of compound **8** (8.3 g, 25.3 mmol),  $\text{PPh}_3$  (13.1 mg, 0.51 mmol), and  $\text{CuI}$  (73 mg, 0.38 mmol) in dry triethylamine (80 mL) was degassed with nitrogen for 5 min.

2-Methyl-3-butyn-2-ol (3.7 mL, 38 mmol) and Pd(PPh<sub>3</sub>)<sub>2</sub>Cl<sub>2</sub> (180 mg, 0.25 mmol) were added to the solution at room temperature and the mixture was stirred to react at 70 °C for 12 h. The mixture was filtered and the solvent was removed in vacuum. Afterward, the crude mixture was extracted using dichloromethane. The organic solution was washed with water, and then dried over Na<sub>2</sub>SO<sub>4</sub> and evaporated. The crude product was followed by purifying with column chromatography (silica gel, n-hexane/ethyl acetate 2:1) to give a light yellow solid. Yield: 4.7 g (56%). <sup>1</sup>H-NMR (ppm, CDCl<sub>3</sub>): δ 7.31 (d, *J* = 9.0 Hz, 2H), 6.79 (d, *J* = 9.0 Hz, 2H), 3.92 (t, *J* = 6.6 Hz, 2H), 3.62 (t, *J* = 6.6 Hz, 2H), 1.77-1.70 (m, 2H), 1.60 (s, 6H), 1.58-1.50 (m, 2H), 1.42-1.29 (m, 12H).



**4-Ethynyl-1-(10-hydroxydecan-1-yloxy)benzene (10).** A solution of compound **9** (4.7 g, 14.2 mmol) and finely powdered KOH (2.39 g, 42.6 mmol) in 1,4-dioxane (80 mL) was refluxed under nitrogen for 3 h. After cooling to room temperature, the solvent was removed under reduced pressure. The residue was taken up in water and extracted with ethyl acetate, and then acidified with 150 mL of HCl (3 N). The organic solution was washed with water, and then dried over Na<sub>2</sub>SO<sub>4</sub> and evaporated. The crude product was purified by column chromatography (silica gel, n-hexane/ethyl acetate 4:1) to give a light yellow solid. Yield: 3.6 g (92%). <sup>1</sup>H-NMR (ppm, CDCl<sub>3</sub>): δ 7.39 (d, *J* = 9.0 Hz, 2H), 6.80 (d, *J* = 9.0 Hz, 2H), 3.92 (t, *J* = 6.6 Hz, 2H), 3.62 (t, *J* =

6.6 Hz, 2H), 2.97 (s, 1H), 1.80-1.70 (m, 2H), 1.57-1.50 (m, 2H), 1.42-1.29 (m, 12H).

**10-{4-[2,5-Dimethyl-4-(2-pyridin-4-yl-vinyl)-phenylethynyl]-phenoxy}-decan-1-ol (11).** A mixture of compound **6** (3.7 g, 12.7 mmol), PPh<sub>3</sub> (170 mg, 0.64 mmol), and CuI (120 mg, 0.64 mmol) in dry triethylamine (80 mL) was degassed with nitrogen for 5 min. Compound **10** (3.6 mL, 13.3 mmol) and Pd(PPh<sub>3</sub>)<sub>2</sub>Cl<sub>2</sub> (90 mg, 0.13 mmol) were added to the solution at room temperature, and afterward the reaction mixture was stirred to react at 70 °C for 12 h. The mixture was filtered and the solvent was removed in vacuum. Next, the crude mixture was extracted using dichloromethane. The organic solution was washed with water, and then dried over Na<sub>2</sub>SO<sub>4</sub> and evaporated. The crude product was purified by column chromatography (silica gel, dichloromethane) to give a light yellow solid. Yield: 4.4 g (72%). <sup>1</sup>H-NMR (ppm, CDCl<sub>3</sub>): δ 8.61 (d, *J* = 6.0 Hz, 2H), 7.56 (d, *J* = 15.9 Hz, 1H), 7.51 (s, 1H), 7.49 (d, *J* = 8.7 Hz, 2H), 7.44 (d, *J* = 6.0 Hz, 2H), 7.36 (s, 1H), 6.98 (d, *J* = 15.9 Hz, 1H), 6.90 (d, *J* = 8.7 Hz, 2H), 4.00 (t, *J* = 6.6 Hz, 2H), 3.68 (t, *J* = 6.6 Hz, 2H), 2.53 (s, 3H), 2.44 (s, 3H), 1.82 (m, 2H), 1.60 (m, 2H), 1.49-1.16 (m, 12H).

**2-Methyl-acrylic acid**

**10-{4-[2,5-dimethyl-4-(2-pyridin-4-yl-vinyl)-phenylethynyl]-phenoxy}-decyl ester PBT (12).** Compound **11** (1.0 g, 2.1 mmol), vinyl methacrylate (1.24 ml, 0.01 mmol), 1,3-dichloro-1,1,3,3-tetrabutyl-distannoxane (92 mg, 0.83 mmol),

2,6-di-tert-butyl-4-methyl phenol (27 mg, 1.3 mmol), and 2 ml of THF were added to a round-bottom flask. The solution was stirred at 50 °C for 48 h. Finally, the crude product of monomer **PBT (12)** was purified by column chromatography (aluminium oxide, n-hexane/dichloromethane 4:1) to give a light yellow solid. Yield: 0.54 g (47%).  
<sup>1</sup>H-NMR (ppm, CDCl<sub>3</sub>): δ 8.57 (d, *J* = 5.4 Hz, 2H), 7.51 (d, *J* = 16.2 Hz, 1H), 7.46 (s, 1H), 7.44 (d, *J* = 8.7 Hz, 2H), 7.39 (d, *J* = 5.4 Hz, 2H), 7.31 (s, 1H), 6.93 (d, *J* = 16.2 Hz, 1H), 6.85 (d, *J* = 8.7 Hz, 2H), 6.08 (s, 1H), 5.53 (s, 1H), 4.12 (t, *J* = 6.9 Hz, 2H), 3.96 (t, *J* = 6.9 Hz, 2H), 2.49 (s, 3H), 2.39 (s, 3H), 1.93 (s, 3H), 1.77 (m, 2H), 1.65 (m, 2H), 1.49-1.20 (m, 12H). <sup>13</sup>C NMR (ppm, CDCl<sub>3</sub>): δ 159.30, 149.92, 145.09, 137.62, 134.60, 133.63, 133.60, 132.96, 130.52, 127.20, 126.47, 125.20, 123.72, 121.00, 115.30, 114.59, 94.65, 87.04, 77.52, 77.10, 76.67, 68.09, 64.84, 29.49, 29.46, 29.37, 29.25, 29.21, 28.62, 26.03, 25.99, 20.39, 19.20, 18.37. MS (EI): *m/z* [M<sup>+</sup>] 549.3, calcd *m/z* [M<sup>+</sup>] 549.32. Anal. Calcd. for C<sub>37</sub>H<sub>43</sub>NO<sub>3</sub>: C 80.84, H 7.88, N 2.55. Found: C 80.56, H 7.95, N 2.77.

**1-[[4-(10-Methacryloyloxy-decyloxy)-phenyl]-ethynyl]-2,5-dimethoxy-4-[2-(4-pyridyl)ethenyl]benzene PBOT (13).** The synthetic procedures of monomer **PBOT (13)** were described in our previous report.<sup>79</sup> <sup>1</sup>H NMR (ppm, CDCl<sub>3</sub>): δ 8.57 (d, *J* = 4.5 Hz, 2H), 7.66 (d, *J* = 16.5 Hz, 1H), 7.50 (d, *J* = 9.0 Hz, 2H), 7.39 (d, *J* = 4.5 Hz, 2H), 7.11 (s, 1H), 7.04 (d, *J* = 16.5 Hz, 1H), 7.04 (s, 1H), 6.87 (d, *J* = 9.0 Hz, 2H),

6.10 (s, 1H), 5.55 (s, 1H), 4.14 (t,  $J = 6.6$  Hz, 2H), 3.97 (t,  $J = 6.6$  Hz, 2H), 3.96 (s, 3H), 3.89 (s, 3H), 3.62 (t,  $J = 6.6$  Hz, 2H), 1.95 (s, 3H), 1.81–1.75 (m, 2H), 1.58–1.53 (m, 2H), 1.42–1.30 (m, 12H). HRMS (EI): calcd for  $C_{37}H_{43}NO_5$ , 581.3141; found 581.3146. Anal. Calcd for  $C_{37}H_{43}NO_5$ : C, 76.39; H, 7.45; N, 2.41. Found: C, 76.15; H, 7.37; N, 2.44.

### Syntheses of Polymers

The synthetic routes of polymers are shown in Scheme 2.2.

#### Homopolymers of PBT1 (14) and PBOT1 (17)

Monomers (1.0 g) of **PBT (12)** and **PBOT (13)** were dissolved in THF (5 mL), and then AIBN (3 mol%) was added as an initiator. After 24 h of reaction, the polymerization was terminated and the polymers were precipitated by a large amount of ether. The crude products were redissolved several times in THF and reprecipitated into a large amount of ether to afford 0.56 g of polymers. The yields were 65 ~ 49%.

#### Copolymers PBT2-PBT3 (15-16) and PBOT2-PBOT3 (18-19)

Monomers (total amount 1.2 g) of **PBT (12)/CAZ (23)** or **PBOT (13)/CAZ (23)** with the desired molar ratios were dissolved in THF (6 mL), and then AIBN (3 mol%) was added as an initiator. The reaction mixtures were flushed with nitrogen for 5 min and then heated in a water bath at 60 °C to initiate polymerization. After 24 h of reaction, the polymerization was terminated and the copolymers were precipitated by



a large amount of ether. The products were redissolved several times in THF and reprecipitated in ether.

**PBT1 (14).** Yield: 49%.  $^1\text{H}$  NMR (ppm, *d*-dioxane):  $\delta$  0.89-1.75 (b, 18H), 1.93 (s, 3H), 2.33 (s, 3H), 2.46 (s, 3H), 3.84-4.03 (b, 4H), 6.78-7.61 (m, 10H), 8.51 (s, 2H).

**PBT2 (15).** Yield: 55%.  $^1\text{H}$  NMR (ppm, *d*-dioxane):  $\delta$  0.88-1.85 (b, 19H), 1.95 (s, 3H), 2.34 (s, 3H), 2.48 (s, 3H), 3.80-4.03 (b, 4H), 6.81-8.20 (m, 18H), 8.51 (s, 2H).

**PBT3 (16).** Yield: 50%.  $^1\text{H}$  NMR (ppm, *d*-dioxane):  $\delta$  0.92-1.88 (b, 19H), 1.96 (s, 3H), 2.36 (s, 3H), 2.49 (s, 3H), 3.80-4.05 (b, 4H), 6.82-8.22 (m, 18H), 8.53 (s, 2H).

**PBOT1 (17).** Yield: 58%.  $^1\text{H}$  NMR (ppm, *d*-dioxane):  $\delta$  0.88-1.78 (b, 18H), 2.08 (s, 3H), 3.79-4.02 (m, 10H), 6.79-7.78 (m, 10H), 8.50 (s, 2H).

**PBOT2 (18).** Yield: 62%.  $^1\text{H}$  NMR (ppm, *d*-dioxane):  $\delta$  0.90-1.83 (b, 19H), 2.10 (s, 3H), 3.80-4.05 (m, 10H), 6.78-8.19 (m, 18H), 8.50 (s, 2H).

**PBOT3 (19).** Yield: 65%.  $^1\text{H}$  NMR (ppm, *d*-dioxane):  $\delta$  0.87-1.85 (b, 19H), 2.16 (s, 3H), 3.83-4.10 (m, 10H), 6.65-8.21 (m, 18H), 8.51 (s, 2H).

### 2.2.2 Preparation of Supramolecular Complexes

In all cases, all proton donors (as shown in Figure 2.2) and acceptor polymers were dissolved in THF to make a clear solution. After that, most of the solvents were evaporated under ambient conditions, which were followed by drying in a vacuum oven at 60 °C for several hours. The complexation of H-donor acids and H-acceptor

polymers through hydrogen bonding occurred during the solvent evaporation. The complexes of all H-acceptor polymers with H-donor acids **OBA (20)** and **ONA (21)** had the equal molar amount of pyridyl H-acceptor and carboxylic acid H-donor groups (in 1:1 molar ratio) to form singly H-bonded supramolecules (H-bonded side-chain polymers), and with **THDA (22)** had the double amounts of pyridyl H-acceptor groups to those of carboxylic acid H-donor groups (in 2:1 molar ratio) to form doubly H-bonded supramolecules (H-bonded cross-linking polymers).

### 2.2.3 Measurements and Characterization

<sup>1</sup>H NMR spectra were recorded on a Varian unity 300 MHz spectrometer using CDCl<sub>3</sub> and *d*-dioxane as solvents. Elemental analyses were performed on a HERAEUS CHN-OS RAPID elemental analyzer. Fourier transform infrared (FT-IR) spectra were performed a Nicolet 360 FT-IR spectrometer. The textures of mesophases were characterized by a polarizing optical microscope (POM, model: Leica DMLP) equipped with a hot stage. Temperatures and enthalpies of phase transitions were determined by differential scanning calorimetry (DSC, model: Perkin Elmer Pyris 7) at a heating and cooling rate of 10 °C/min under nitrogen. Transition temperatures (°C) and enthalpies (in parentheses, kJ/mol) were determined by DSC second scans. Thermogravimetric analyses (TGA) were conducted on a Du Pont Thermal Analyst 2100 system with a TGA 2950 thermogravimetric analyzer at a

heating rate of 20 °C/min under nitrogen. Gel permeation chromatography (GPC) analyses were conducted with a Water 1515 separations module using polystyrene as a standard and THF as an eluant. UV-visible absorption spectra were recorded in dilute THF solutions ( $10^{-6}$  M) on a HP G1103A spectrophotometer, and photoluminescence (PL) spectra were obtained on a Hitachi F-4500 spectrophotometer. Thin films of UV-vis and PL measurements were spin-coated on quartz substrates from THF solutions with a concentration of 1 wt%. The PL quantum yields ( $\Phi_{\text{PL}}$ ) of polymers were measured with 9,10-diphenylanthracene as a reference (in cyclohexane,  $\Phi_{\text{PL}} = 0.9$ ).<sup>80</sup> Synchrotron powder X-ray diffraction (XRD) measurements were performed at beamline BL17A of the National Synchrotron Radiation Research Center (NSRRC) in Taiwan, where the X-ray wavelength used was 1.32633 Å. X-ray diffraction XRD data were collected using imaging plates (IP, of an area =  $20 \times 40 \text{ cm}^2$  and a pixel resolution of 100) curved with a radius equivalent to the sample-to-image plate distance of 280 mm, and the diffraction signals were accumulated for 3 min. The powder samples were packed into a capillary tube and heated by a heat gun, where the temperature controller was programmable by a PC with a PID feed back system. The scattering angle theta values were calibrated by a mixture of silver behenate and silicon.

### 2.3 Results and Discussion

### 2.3.1 Synthesis and Characterization of Polymers

As shown in Scheme 2.1, monomer **PBT (12)** was successfully synthesized via Sonogashira coupling and Wittig-Horner reactions to obtain three-conjugated aromatic rings. In order to synthesize the designed methacrylate monomer containing end-capping pyridine, it is crucial to avoid H-bonding of the pyridine moiety, and thus no acidic reactants can be used. Therefore, vinyl methacrylate (instead of methacryloyl chloride) was finally used as a reactant according to the literature<sup>81</sup> to get a high yield of methacrylate **PBT (12)**, where 1,3-dichloro-1,1,3,3-tetrabutyl-distannoxane was required as a catalyst to proceed this reaction and the polymerization of **PBT** was avoided by using an inhibitor 2,6-di-tert-butyl-4-methyl phenol. Two analogous series side-chain polymers composed of monomers **PBT (12)** and **PBOT (13)** with different lateral methyl and methoxy groups in central cores were synthesized. Finally, methacrylate monomers **PBT (12)** and **PBOT (13)** were in conjunction with *N*-vinylcarbazole **CAZ (23)** during the conventional synthesis of random free radical copolymerization, where the contents of **CAZ** units in the copolymers were determined by <sup>1</sup>H NMR. All of these polymers were dissolved in high polar organic solvents (such as THF and DMF) to form good transparent films on glass substrates. The average molecular weights obtained from GPC are illustrated in Table 2.1. The number-average molecular

weights ( $M_n$ ) of polymers are between 8800 and 15000 g/mol with polydispersity indexes (PDI) between 1.47 and 2.93.

### 2.3.2 FT-IR Spectroscopy of H-Bonded Polymer Complexes

All H-bonded polymer complexes consisting of appropriate (fully H-bonded) molar ratios of H-acceptor polymers (**14-19**) and H-donors (**20-22**) were prepared by slow evaporation of THF solutions and followed by drying in vacuo. The formation of hydrogen bonding in supramolecular side-chain and cross-linking polymers containing donors **OBA (20)**, **ONA (21)**, and **THDA (22)** was confirmed by FT-IR spectroscopy. As shown in Figure 2.3, IR spectra of **PBOT2 (18)**, **THDA (22)**, and H-bonded polymer complex **PBOT2/THDA (18/22)** are compared to analyze the hydrogen bonds in the supramolecular cross-linking structure of **PBOT2/THDA (18/22)**. In contrast to the O-H band of pure **THDA (22)** (H-bonded cross-linker) at 2652 and 2552  $\text{cm}^{-1}$ , the weaker O-H band observed at 2535 and 1926  $\text{cm}^{-1}$  in H-bonded polymer complex **PBOT2/THDA (18/22)** is indicative of stronger hydrogen bonding between the pyridyl group of **PBOT2 (18)** and the carboxylic acid of **THDA (22)** in the H-bonded polymer complex. On the other hand, a C=O stretching vibration appeared at 1719  $\text{cm}^{-1}$  in H-bonded polymer complex **PBOT2/THDA (18/22)**, which shows that the carbonyl group was in a less associated state than that in pure **THDA (22)** (H-bonded cross-linker) with a weaker C=O

stretching vibration appeared at  $1670\text{ cm}^{-1}$ . Both results suggest that hydrogen bonds were formed between H-acceptor **PBOT2 (18)** and H-donor **THDA (22)** in the solid state of H-bonded polymer complex **PBOT2/THDA (18/22)**. Some other supramolecular polymers also have the similar consequences of H-bonding formation as the H-bonded polymer complex demonstrated here.<sup>17</sup>

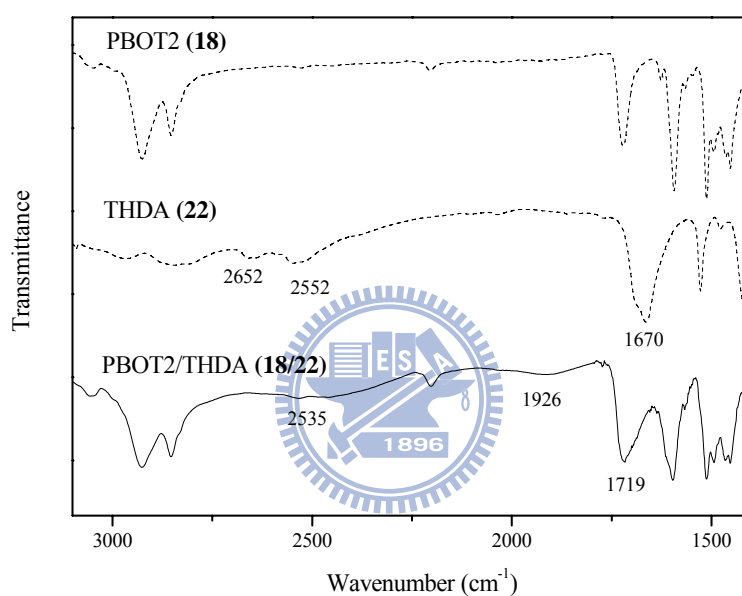


**Figure 2.3** Infrared spectra for **PBOT2 (18)**, **THDA (22)**, and H-bonded polymer complex **PBOT2/THDA (18/22)** at room temperature.

### 2.3.3 Thermal Behavior

The phase transition temperatures and corresponding enthalpy changes of all polymers and H-bonded polymer complexes were characterized by DSC and POM, where the mesomorphic properties (the nematic and Sc phases) were affected by the type of H-donor acids and H-acceptor pyridyl polymers (containing lateral methyl- and methoxy-substituted groups). The thermal stabilities of the polymers evaluated by thermogravimetric analysis (TGA) under nitrogen are summarized in Table 2.1. TGA analyses indicate that the degradation temperatures ( $T_d$ ) with 5% of weight loss under nitrogen are between 335 and 389 °C. The results of TGA show that the  $T_d$  values of the polymers are gradually decreased by increasing the molar ratio of the **CAZ** units in both series of polymers **PBT1-PBT3 (14-16)** and **PBOT1-PBOT3 (17-19)**. In addition, lateral methyl-substituted polymers **PBT1-PBT3 (14-16)** have higher  $T_d$  values than analogous lateral methoxy-substituted polymers **PBOT1-PBOT3 (17-19)**, respectively. The glass transition temperatures ( $T_g$ ) of the polymers determined by differential scanning calorimetry (DSC) under nitrogen are also listed in Table 2.1. The glass transition temperatures of all polymers are between 51 and 130 °C, whereas their isotropization temperatures were not observed up to 250 °C. As shown in Figure 2.4, the  $T_g$  values of the polymers are gradually enhanced by increasing the molar ratio of the **CAZ** units, i.e., **PBT3 (16) > PBT2 (15) > PBT1 (14)** and **PBOT3 (19) >**

**PBOT2 (18) > PBOT1 (17)**. This obviously indicates that the presence of the bulky and rigid **CAZ** moieties in the copolymers will enhance the steric hindrance of the pendants and suppresses the free volume of the copolymers effectively. Generally, the lateral methoxy-substituted polymers show higher glassy transition temperatures ( $T_g$ ) than the corresponding methyl-substituted polymers, which might be because the higher polarity of the lateral methoxy groups in the H-acceptor pyridyl pendants may stabilize the frozen smectic layered structure by the succeeding mesogenic arrangement. As for the phase behavior of polymers **PBT1-PBT3 (14-16)** and **PBOT1-PBOT3 (17-19)** shown in Table 2.1, it suggests that the incorporation of **CAZ** units in copolymers **(14-19)** is detrimental to the formation of the nematic phase, so copolymers **PBT3 (16)** and **PBOT3 (19)** with the highest concentration of **CAZ** units (c.a. 70% molar ratio) do not possess any mesophase in both series. This phenomenon could be explained by that the **CAZ** units with nonmesogenic property may dilute and hinder the molecular packing of the liquid crystalline arrangements.

All H-bonded polymer complexes consisting of appropriate (fully H-bonded) molar ratios of H-acceptors (polymers) and H-donors were prepared by slow evaporation of THF solutions and followed by drying in vacuo. The thermal properties of all H-bonded polymer complexes are illustrated in Figure 2.5 and Table 2.2. Similar to polymers **PBT1-PBT3 (14-16)** and **PBOT1-PBOT3 (17-19)**, the



phase transition temperatures of these H-bonded polymer complexes have the same tendency. In order to investigate the effects of H-donors to form various supramolecular structures, three different H-donors, i.e., two asymmetric mono-functional H-donors **OBA (20)** and **ONA (21)** along with one symmetric bi-functional H-donor **THDA (22)**, were utilized in the H-bonded side-chain/cross-linking polymers. These H-donors consist of three different rigid cores, such as phenylene, naphthalene, and thiophene groups, where **THDA (22)** containing a thiophene unit serves as a double H-donor (kinked H-bonded cross-linker). Some H-bonded polymer complexes in Figure 2.5 and Table 2.2 exhibit melting temperatures ( $T_m$ ) but without  $T_g$ , indicating their crystalline nature. In contrast to the nematic phase of pure H-acceptor polymers **PBT1-PBT2 (14-15)** and **PBOT1-PBOT2 (17-18)**, the smectic phase is introduced in their corresponding H-bonded polymer complexes due to the extended H-bonded mesogens by the combined rigid cores of H-donors. However, the nematic phase is recovered in the H-bonded cross-linking polymers composed of double H-donor **THDA (22)** and H-acceptor copolymers with a medium concentration of **CAZ** units, i.e., **PBT2/THDA (15/22)** and **PBOT2/THDA (18/22)**, where the rod-rod interactions of H-bonded mesogens are reduced due to the dilution effect from the copolymerization of **CAZ** units in H-acceptor copolymers **PBT2 (15)** and **PBOT2 (18)**. In addition, due

to the non-mesomorphic property of H-acceptor polymers **PBT3 (16)** and **PBOT3 (19)**, no mesomorphism is observed in all H-bonded polymer complexes containing H-acceptor copolymers **PBT3 (16)** and **PBOT3 (19)** with the highest concentration of **CAZ** units.

Comparing the phase transition temperatures of the H-bonded polymer counterparts containing different H-donors **OBA (20)**, **ONA (21)**, and **THDA (22)**, it demonstrates that longer and more rigid H-bonded structures will have higher isotropization temperatures ( $T_i$ ), i.e., H-bonded polymer complexes containing **THDA (22)** > those containing **ONA (21)** > those containing **OBA (20)**. For example, the  $T_i$  values of analogous H-bonded polymer complexes are in the order of **PBT1/THDA (14/22)** > **PBT1/ONA (14/21)** > **PBT1/OBA (14/20)**, i.e., 200.8 °C, 174.2 °C, and 149.1 °C, respectively. Moreover, comparing analogous H-bonded polymer complexes consisting of the same H-acceptor polymers, the highest isotropization temperatures ( $T_i$ ) and the broadest mesomorphic ranges were observed in the supramolecular cross-linking polymers containing double H-donor **THDA (22)**. For instance, the H-bonded polymer networks **PBT1/THDA (14/22)** and **PBOT1/THDA (17/22)**, where double H-donor **THDA (22)** acts as H-bonded cross-linkers (acceptor:donor = 2:1), have the highest  $T_i$  values and the broadest smectic phase ranges in the analogues of H-bonded polymer complexes, respectively. In general, the

phase transition temperatures of H-bonded side-chain/cross-linking polymers will be enhanced while the H-bonded central cores are longer and more rigid.

Interestingly, by increasing the molar ratios of **CAZ** units in the H-bonded polymer networks, the smectic phase disappears but the nematic phase forms in **PBT2/THDA (15/22)** and **PBOT2/THDA (18/22)**, which is attributed to the **CAZ** segments in H-bonded polymer complexes **PBT2/THDA (15/22)** and **PBOT2/THDA (18/22)** (containing **PBT2 (15)** and **PBOT2 (18)** with a medium concentration of **CAZ** segments, c.a. 40% molar ratio) eliminate the layered arrangement of the H-bonded smectogens. However, in contrast to the nematic phase in supramolecular cross-linking polymers **PBT2/THDA (15/22)** and **PBOT2/THDA (18/22)**, supramolecular side-chain polymers **PBT2/OBA-PBT2/ONA (15/20-15/21)** and **PBTO2/OBA-PBOT2/ONA (18/20-18/21)** containing **PBT2 (15)** and **PBOT2 (18)** maintain the smectic phase, which are originated from the stronger  $\pi$ - $\pi$  interactions of linear rods in the more linear H-bonded side-chain structures with pendent H-donors **OBA (20)** and **ONA (21)** rather than the weaker rod-rod interactions in the more kinked cross-linking structures with double H-donor **THDA (22)**. Furthermore, the mesophases even disappear in all H-bonded polymer complexes containing H-acceptor polymers **PBT3 (16)** and **PBOT3 (19)** due to the most concentrated **CAZ** segments in copolymers **PBT3 (16)** and **PBOT3 (19)** (with the highest concentration

of **CAZ** segments, c.a. 70% molar ratio), which destroy the mesomorphic arrangements completely. Besides, compared with **PBT2/OBA (15/20)** and **PBT2/ONA (15/21)**, analogous supramolecular side-chain polymers **PBT1/OBA (14/20)** and **PBT1/ONA (14/21)** containing H-acceptor homopolymer **PBT1** (without **CAZ** units) have higher  $T_i$  values (i.e., 149.1 and 174.2 °C higher than 129 and 143.9 °C, respectively) and broader smectic phase ranges (i.e., 76.4 and 71.8 °C broader than 21.7 and 46.1 °C, respectively). Similar trends of reduction in  $T_i$  values occur for supramolecular cross-linking polymers as increasing **CAZ** contents in the H-acceptor polymers. Hence, it is demonstrated that the mesogenic ranges and  $T_i$  values of these H-bonded polymer complexes are apparently reduced with increasing **CAZ** contents in the H-acceptor polymers.



In terms of lateral substitutions, the lateral methoxy groups in the H-bonded polymer complexes containing H-acceptor homopolymer **PBT1** are larger than the lateral methyl groups in the H-bonded polymer complexes containing H-acceptor homopolymer **PBOT1** to hinder the molecular packing, and thus to cause the reduction of the mesogenic phase and  $T_i$  values prominently. For instance, in contrast to **PBT1/OBA (14/20)** and **PBT1/ONA (14/21)** containing H-acceptor homopolymer **PBT1** (with lateral methyl groups), analogous H-bonded polymer complexes **PBTO1/OBA (17/20)** and **PBOT1/ONA (17/21)** containing H-acceptor

homopolymer **PBOT1** (with lateral methoxy groups) have lower  $T_i$  values (i.e., 127.7 and 138.0 °C lower than 149.1 and 174.2 °C, respectively) and narrower smectic phase ranges (i.e., 17.0 and 23.9 °C narrower than 76.4 and 71.8 °C, respectively). Thus, the steric effect plays an important role on the mesogenic and thermal properties, where the larger lateral substitution may be detrimental to the molecular packing as well as the mesomorphic ranges and  $T_i$  values. Above all, by utilization of H-acceptor polymers (mainly possess the nematic phase), various mesomorphic properties as shown in Figure 2.6 can be introduced to the H-bonded polymer complexes, including H-bonded side-chain/cross-linking polymers complexed with asymmetric mono-functional and symmetric bi-functional H-donors. The smectic and nematic phases in the H-bonded polymer complexes were not only identified by POM but also could further be confirmed by X-ray diffraction (XRD) measurements.

**Table 2.1 Molecular Weights and Thermal Properties of H-Acceptor Polymers**

H-acceptor polymer	composition (% CAZ) <sup>a</sup>	M <sub>n</sub> <sup>b</sup>	M <sub>w</sub> <sup>b</sup>	PDI <sup>b</sup>	T <sub>d</sub> <sup>c</sup> (°C)	phase transitions <sup>d</sup> (°C)
<b>PBT1 (14)</b>	0	8800	20400	2.31	389	G 51 N <sup>e</sup>
<b>PBT2 (15)</b>	40	12200	32100	2.63	373	G 63 N <sup>e</sup>
<b>PBT3 (16)</b>	66	9200	13600	1.47	359	G 130 K <sup>e</sup>
<b>PBOT1 (17)</b>	0	10100	20100	1.99	362	G 61 N <sup>e</sup>
<b>PBOT2 (18)</b>	38	9700	19100	1.96	341	G 70 N <sup>e</sup>
<b>PBOT3 (19)</b>	70	15000	44000	2.93	335	G 103 K <sup>e</sup>

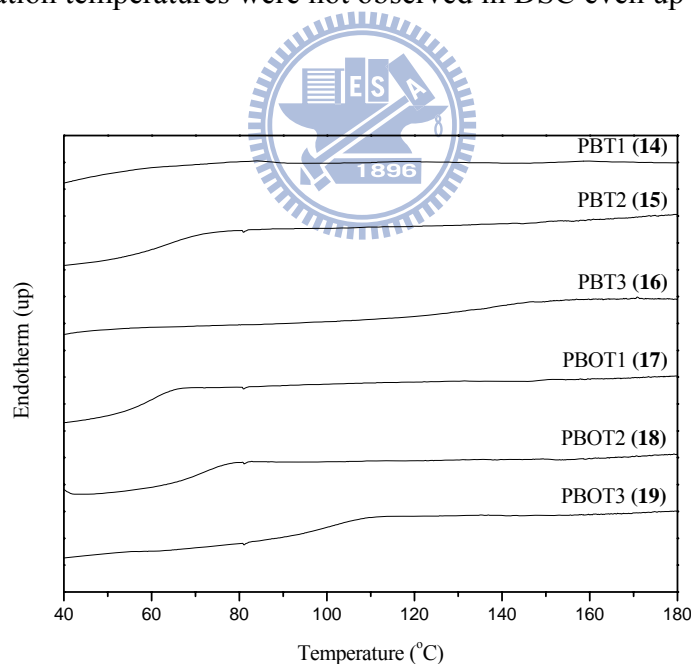
<sup>a</sup> The content of CAZ groups in copolymers (mol%) were determined by NMR.

<sup>b</sup> Molecular weight determined was by GPC in THF, based on polystyrene standards.

<sup>c</sup> Temperature (°C) at 5% weight loss was measured by TGA at a heating rate of 20 °C/min under nitrogen.

<sup>d</sup> Glass transition temperature (°C) was determined by DSC at a heating rate of 10 °C/min. G = glassy state; K = crystalline; N = nematic.

<sup>e</sup> The isotropization temperatures were not observed in DSC even up to 250 °C.

**Figure 2.4** DSC heating curves (second scans) of H-acceptor polymers **14-19**.

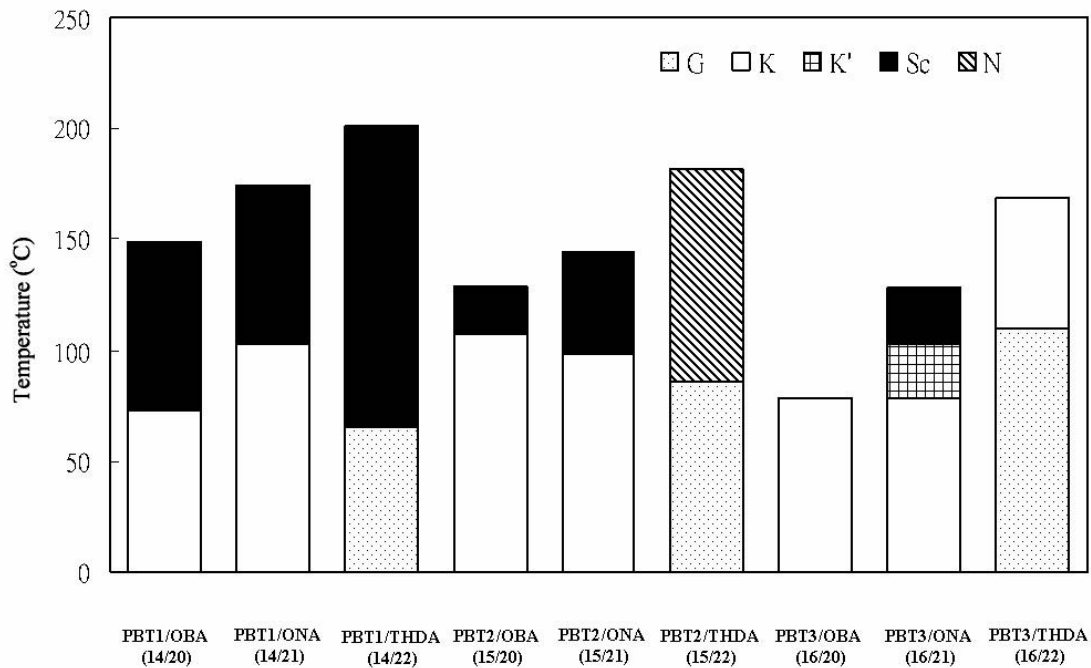
**Table 2.2 Thermal Properties of H-Bonded Polymer Complexes<sup>a,b</sup>**

H-bonded polymer complex	heating	cooling
<b>PBT1/OBA (14/20)</b>	K 72.7 (2.0) Sc 149.1 (3.3) I	I 145.5 (-3.1) Sc 67 <sup>c</sup> K
<b>PBT1/ONA (14/21)</b>	K 102.4 (3.96) Sc 174.2 (7.79) I	I 171.5 (-8.06) Sc 91 <sup>c</sup> K
<b>PBT1/THDA (14/22)</b>	G 65.4 Sc 200.8 (6.21) I	I 174.9 (-5.83) K
<b>PBT2/OBA (15/20)</b>	K 107.3 (1.71) Sc 129 <sup>c</sup> I	I 124 <sup>c</sup> Sc 105.7 (-1.53) K
<b>PBT2/ONA (15/21)</b>	K 97.8 (1.21) Sc 143.9 (1.54) I	I 141.4 (-1.68) Sc 91 <sup>c</sup> K
<b>PBT2/THDA (15/22)</b>	G 85.8 N 181.6 (7.1) I	I 180 <sup>c</sup> N 82.1 (-6.85) G
<b>PBT3/OBA (16/20)</b>	K 78.1(3.6) I	I 72 <sup>c</sup> K
<b>PBT3/ONA (16/21)</b>	K 78.1 (1.55) K' 102.9 (2.3) I	I 96 <sup>c</sup> K
<b>PBT3/THDA (16/22)</b>	G 109.3 K 168.6 (2.3) I	I 159 <sup>c</sup> K 106.6 G
<b>PBOT1/OBA (17/20)</b>	K 74.2 (0.7) K' 110.7 (3.24) Sc 127.7 (0.07) I	I 120.3 (-0.06) Sc 108.3 (-3.13) K
<b>PBOT1/ONA (17/21)</b>	G 58.8 K 114.1 (1.85) Sc 138.0 (2.83) I	I 133.1 (-2.51) Sc 106.3 (-0.91) K' 83.5 (-1.11) K
<b>PBOT1/THDA (17/22)</b>	G 87.1 Sc 211.2 (5.7) I	I 195 <sup>c</sup> Sc 86.3 G
<b>PBOT2/OBA (18/20)</b>	K 75.4 (1.75) Sc 127.3 (0.06) I	I 120.8 (-0.05) Sc 62.1 (-2.06) K
<b>PBOT2/ONA (18/21)</b>	G 66.6 K 105.4 (2.15) Sc 131.2 (3.85) I	I 127 <sup>c</sup> Sc 103.9 (-2.15) K' 79.6 (-1.64) K
<b>PBOT2/THDA (18/22)</b>	G 109.8 N 168.6 (3.4) I	I 157 <sup>c</sup> N 105.8 G
<b>PBOT3/OBA (19/20)</b>	K 77.5 (3.9) I	I 60.2 (-3.2) K
<b>PBOT3/ONA (19/21)</b>	K 79.4 (-1.7)K' 99.5 (2.0) I	I 90 <sup>c</sup> K
<b>PBOT3/THDA (19/22)</b>	G 82.3 K 157 <sup>c</sup> I	I 148 <sup>c</sup> K 78.2 G

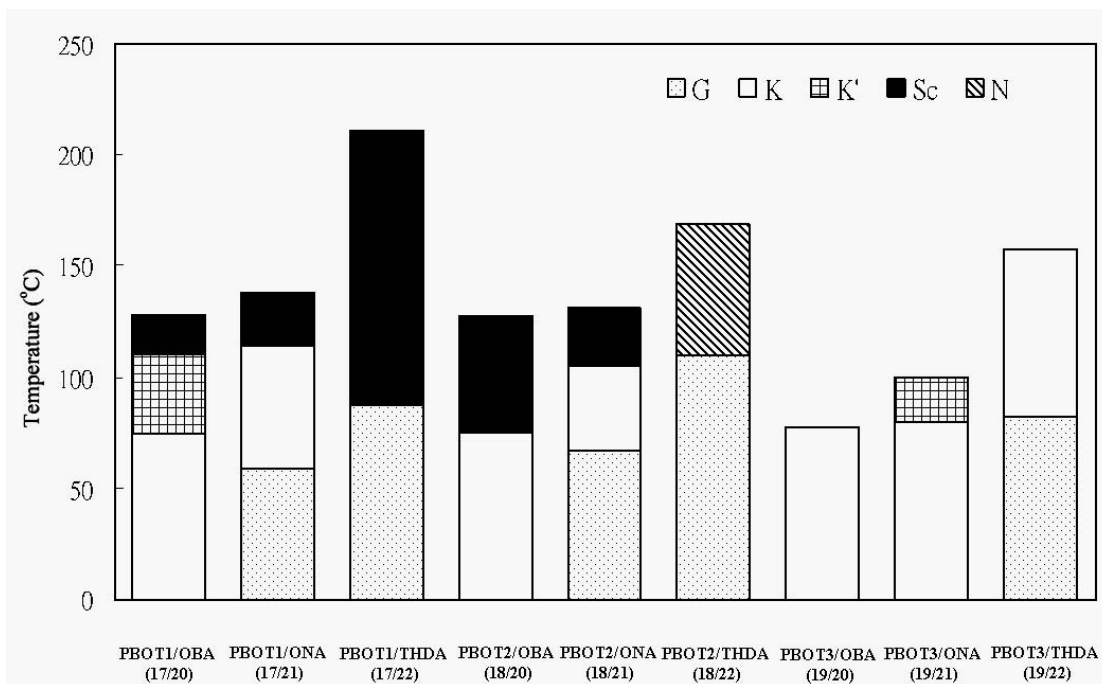
<sup>a</sup> Transition temperatures (°C) and enthalpies (in parentheses, kJ/mol) were determined by DSC (heating and cooling rate of 10 °C/min).

<sup>b</sup> G = glassy state; K = crystalline; Sc = smectic C; N = nematic; I = isotropic.

<sup>c</sup> The phase transition temperatures were obtained from POM.



(a)



(b)

**Figure 2.5** Phase diagrams of mesophases in (a) H-bonded polymer complexes of **PBT** and (b) H-bonded polymer complexes of **PBOT** upon heating.



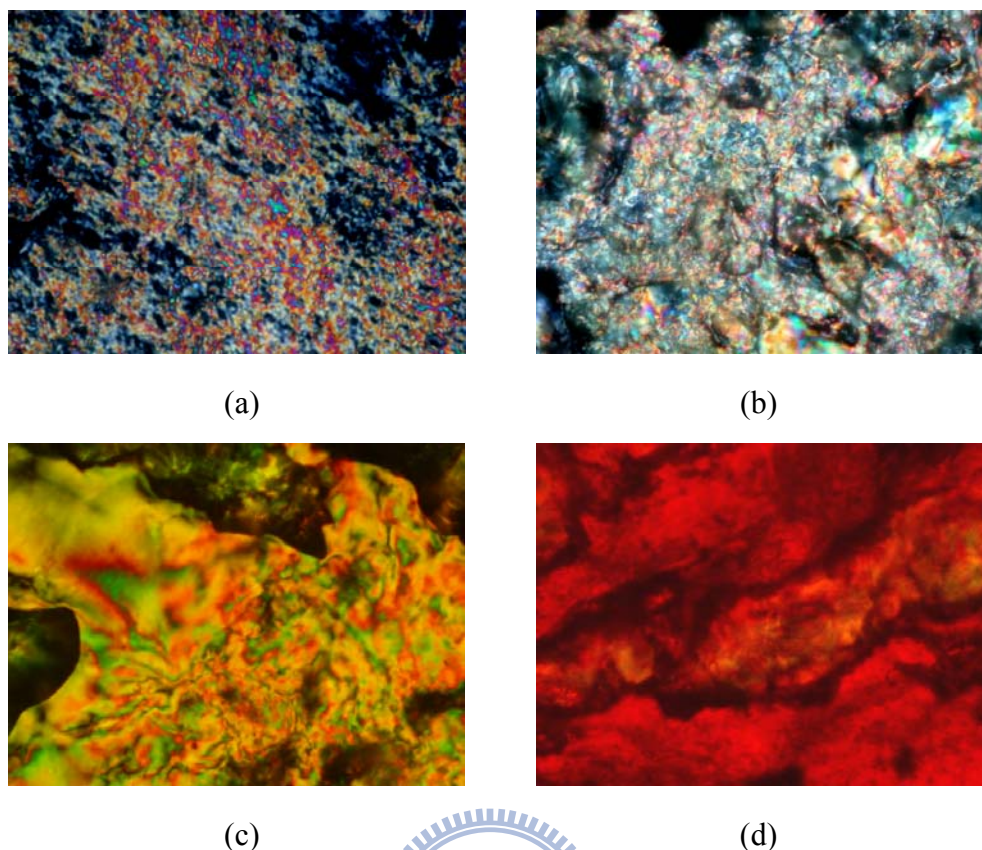


**Figure 2.6** Liquid crystalline textures of H-bonded polymer complexes observed by POM (a) the Sc phase in **PBT1/ONA (14/21)** at 160 °C (cooling) (b) the Sc phase in **PBT2/ONA (15/21)** at 110 °C (cooling) (c) the nematic phase in **PBT2/THDA (15/22)** at 180 °C (cooling) (d) the Sc phase in **PBOT1/THDA (17/22)** at 160 °C (cooling).

### 2.3.4 X-ray Diffraction Analysis

To elucidate the structure of the mesophases, XRD measurements were accomplished at the temperature ranges of mesophases for all H-bonded polymer complexes (see Table 2.3). In order to prove the formation of the supramolecular structures, the smectic layer arrangements can be characterized to evaluate the H-bonded architectures. Based on the theoretical geometries estimated by CS ChemOffice, the molecular lengths of H-bonded polymer complexes **PBT1/OBA**

(14/20), **PBT1/ONA (14/21)**, and **PBT1/THDA (14/22)** are 55.7, 58.1, and 75.4 Å, respectively, which are calculated from the molecular projection lengths of the fully extended molecular lengths along the rigid cores. In addition, the tilt angle calculations by Chemoffice do not consider their Van der Waals radius. Moreover, measurements of the lengths of the molecules are made in a rigid conformation (all-trans) and this is not exactly what occurs in the mesophase. The values presented are only rough estimates. As shown in Table 2.3 and Figure 2.7(a), the XRD patterns of H-bonded polymer complexes **PBOT1/OBA (17/20)**, **PBOT1/ONA (17/21)**, and **PBOT1/THDA (17/22)** indicate that the layer *d*-spacing values at 115, 120, and 160 °C are 49.3, 50.0, and 63.0 Å, respectively. In general, the XRD data demonstrate the *d*-spacing values at different temperatures, from which the individual tilt angles can be estimated. According to these findings in XRD experiments, the tilt angles of are 27.7°, 30.6°, and 33.3°, respectively, as H-acceptor polymer **PBOT1 (17)** was H-bonded to H-donors **OBA (20)**, **ONA (21)**, and **THDA (22)**. These results support that most H-bonded polymer complexes are suitable to be identified as the tilted smectic C phase by XRD measurements, and their tilt angles in Table 2.3 can be calculated from the theoretical molecular model. In contrast to the longer (even though kinked) doubly H-bonded rods of supramolecular cross-linking polymers containing bi-functional H-donor **THDA (22)** (as a H-bonded cross-linker), the

supramolecular side-chain polymers containing mono-functional H-donors **OBA (20)** and **ONA (21)** always have smaller *d*-spacing values due to their shorter singly H-bonded rods. Moreover, compared with **OBA (20)**, H-donor **ONA (21)** possesses a longer rigid naphthyl group, so the *d*-spacing values of the H-bonded polymer complexes containing **ONA (21)** will be a little longer (c.a. 2.4 Å) in contrast to those containing **OBA (20)**. Regarding the H-bonded polymer complexes containing H-acceptor polymers with different contents of **CAZ** units in Table 2.3, it is interesting that all *d*-spacing values of H-bonded polymer complexes bearing H-acceptor homopolymers **PBT1 (14)** and **PBOT1 (17)** (without **CAZ** units) are larger than those bearing H-acceptor copolymers **PBT2 (15)** and **PBOT2 (18)** bearing **CAZ** units, respectively. As described previously, the **CAZ** segments reduce the molecular packing of smectogens, so the smaller *d*-spacing values are induced by that the smectic layers are more disordered and the pendent mesogens are separated (and diluted) by **CAZ** units. Furthermore, the lack of small angle XRD patterns (for smectogens) in the mesophase of H-bonded polymer complexes **PBT2/THDA (15/22)** and **PBOT2/THDA (18/22)** support the existence of the nematic phase (see Figure 2.7(b)). As shown in Figure 2.8, the diffraction patterns of H-bonded polymer complex **PBT1/ONA (14/21)** indicate the diffraction peak is increased upon cooling from the isotropic phase (180 °C) to the crystalline state (50 °C), so the layer *d*-spacing

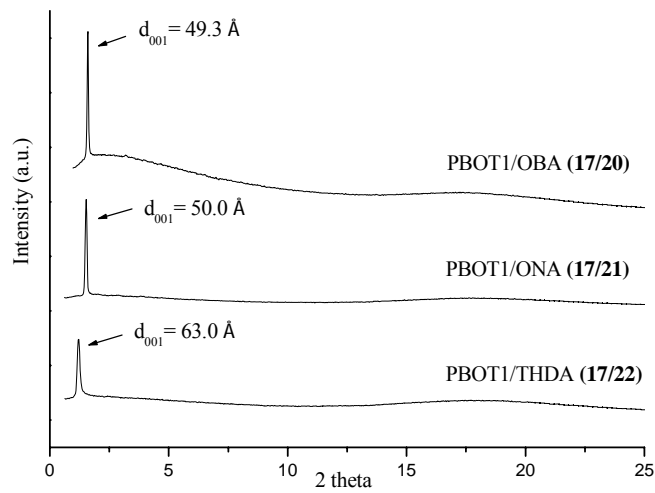
value (in the inset of Figure 2.8) reduces from 50.1 Å (at 160 °C) to 49.7 Å (at 120 °C), which could be due to the increase of tilt angle by decreasing temperature. The disappearance of small-angle diffraction peak at 180 °C indicates the absence of the layered smectic structure in the isotropic phase.

**Table 2.3 The *d*-spacing and Tilt Angle Values of the Sc Phase in H-Bonded Polymer Complexes**

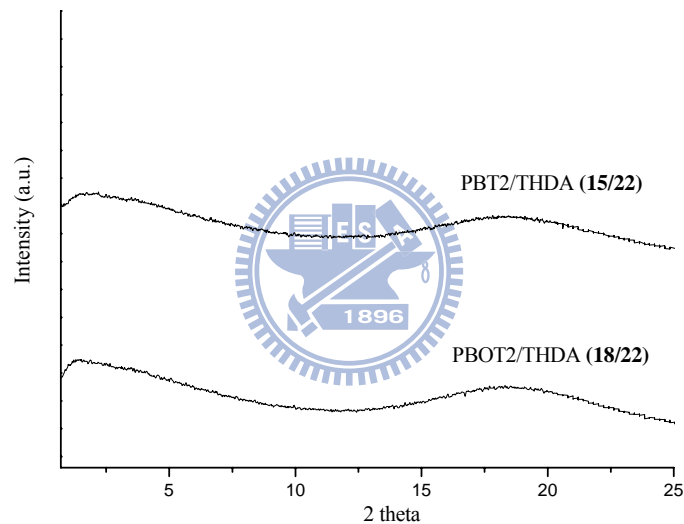
H-bonded polymer complex	phase	measured <i>d</i> spacing (Å) (cooling)	theoretical molecular length (Å) <sup>b</sup>	tilt angle(°)
<b>PBT1/OBA (14/20)</b>	Sc	46.9 (130 °C)	55.7	32.7
<b>PBT1/ONA (14/21)</b>	Sc	50.1 (160 °C)	58.1	30.4
<b>PBT1/THDA (14/22)</b>	Sc	61.8 (165 °C)	75.4	35.0
<b>PBT2/OBA (15/20)</b>	Sc	42.2 (130 °C)	55.7	40.7
<b>PBT2/ONA (15/21)</b>	Sc	50.3 (110 °C)	58.1	30.0
<b>PBT2/THDA (15/22)</b>	N <sup>a</sup>	-	-	-
<b>PBOT1/OBA (17/20)</b>	Sc	49.3 (115 °C)	55.7	27.7
<b>PBOT1/ONA (17/21)</b>	Sc	50.0 (120 °C)	58.1	30.6
<b>PBOT1/THDA (17/22)</b>	Sc	63.0 (160 °C)	75.4	33.3
<b>PBOT2/OBA (18/20)</b>	Sc	43.0 (120 °C)	55.7	39.5
<b>PBOT2/ONA (18/21)</b>	Sc	46.9 (120 °C)	58.1	36.2
<b>PBOT2/THDA (18/22)</b>	N <sup>a</sup>	-	-	-

<sup>a</sup> Nematic phase was observed by POM and confirmed by XRD (no layer *d*-spacing peaks).

<sup>b</sup> The theoretical molecular lengths of H-bonded polymer complexes were estimated by the sum of molecular projection lengths of the H-bonded components along the rigid cores through molecular modeling.



(a)



(b)

**Figure 2.7** X-ray diffraction patterns of H-bonded polymer complexes (a) the Sc phase in **PBOT1/OBA (17/20)** at 115 °C, **PBOT1/ONA (17/21)** at 120 °C, and **PBOT1/THDA (17/22)** at 160 °C; (b) the nematic phase in **PBT2/THDA (15/22)** and **PBOT2/THDA (18/22)** at 130 °C.

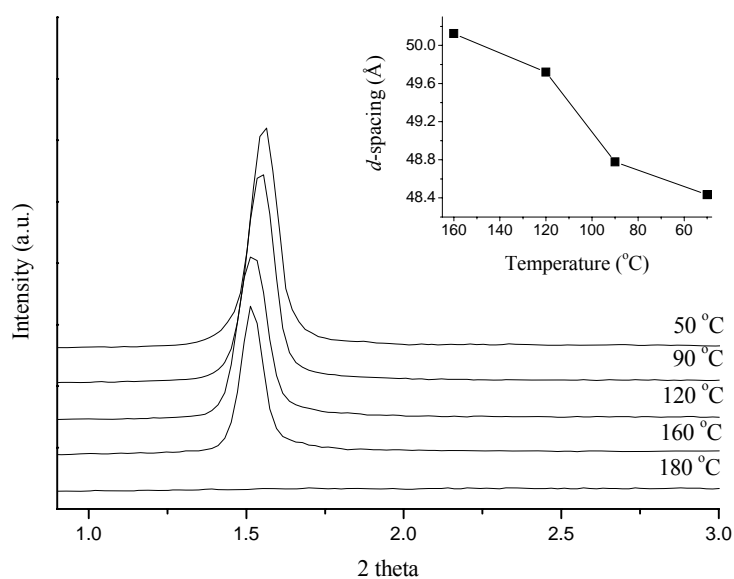


**Figure 2.8** X-ray diffraction patterns for H-bonded polymer complex **PBT1/ONA (14/21)** upon cooling from the isotropic phase (180 °C) to solid (50 °C).

### 2.3.5 Optical Properties

The absorption and PL spectral data of all luminescent H-acceptor polymers **PBT1-PBT3 (14-16)** and **PBOT1-PBOT3 (17-19)** (in both THF solutions and solid films) as well as all H-bonded polymer complexes (in solid films) are summarized in Tables 4-5. The PL quantum yields ( $\Phi_{\text{PL}}$ ) of polymers **PBT1-PBT3 (14-16)** and **PBOT1-PBOT3 (17-19)** in solutions were excited at the maximum absorption peak as listed in Table 2.4. As shown in Figure 2.9(a), the maximum absorption peaks of **PBT** and **PBOT** series are 350 and 384 (322) nm, respectively. The absorption bands of **PBT1-PBT3 (14-16)** in THF solutions at c.a. 294, 330, and 344 nm are originated from the combined absorption bands of **CAZ** pendent groups. The additional absorption bands of polymers **PBOT1-PBOT3 (17-19)** at 320-322 nm are assigned to

the  $n-\pi^*$  transition<sup>82</sup> contributed from the lateral methoxy groups in conjugated chromophores. Similarly, **PBOT1-PBOT3 (17-19)** have the same tendency by increasing the content of **CAZ** units. In Figure 2.9(b), the PL spectra of H-acceptor polymers **PBT1-PBT3 (14-16)** emitted blue light c.a. 431-440 nm in THF solutions. In comparison with luminescent homopolymer **PBT1 (14)**, the slightly blue-shifted PL spectra of copolymers **PBT2** and **PBT3 (15 and 16)** can be explained by the dilution effect of the incorporated **CAZ** units to reduce the aggregation of the pyridyl chromophores, which also can enhance PL quantum yields ( $\Phi_{\text{PL}} = 40\text{-}59\%$ ) by copolymerization with **CAZ** units. Correspondingly, similar blue-shifted PL spectra ( $\lambda_{\text{PL,sol}} = 445\text{-}449$  nm) and enhanced PL quantum yields ( $\Phi_{\text{PL}} = 49\text{-}63\%$ ) were observed in THF solutions of analogous H-acceptor polymers **PBOT2-PBOT3 (18-19** with lateral methoxy groups) due to the dilution effects of **CAZ** units in copolymers. Furthermore, in contrast to polymers **PBT1-PBT3 (14-16)**, polymers **PBOT1-PBOT3 (17-19)** have more red-shifted PL emissions due to the stronger electron donating effect of lateral methoxy groups, which induce smaller energy band gaps in chromophores. In Figure 2.9(c), comparing polymers **PBT1-PBT3 (14-16** with lateral methyl groups) and **PBOT1-PBOT3 (17-19** with lateral methoxy groups), the PL spectra in solid films are more red-shifted than those in THF solutions, which indicate that more serious  $\pi-\pi$  stacking and molecular aggregation occur in solid films.

Additionally, due to the larger separation of chromophores by the larger size of lateral methoxy groups in **PBOT1-PBOT3 (17-19)**, they have higher PL quantum yields ( $\Phi_{\text{PL}} = 49\text{-}63\%$ ) than **PBT1-PBT3 (14-16)** with lateral methyl groups ( $\Phi_{\text{PL}} = 40\text{-}59\%$ ), respectively.

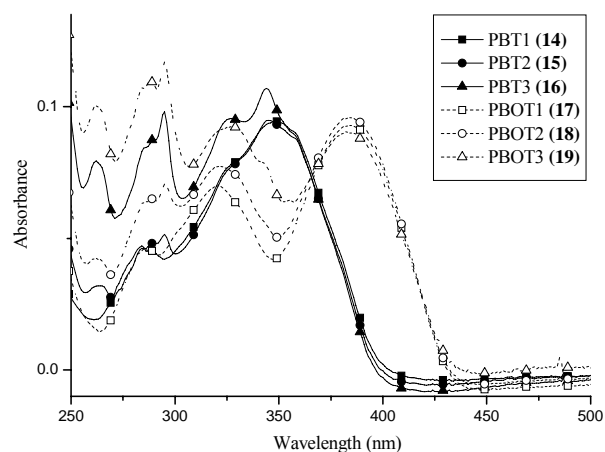
**Table 2.4 Absorption and Photoluminescence Spectral Data of H-Acceptor Polymers**

H-acceptor polymer	$\lambda_{\text{abs,sol}}^a$ (nm)	$\lambda_{\text{PL,sol}}^a$ (nm)	$\lambda_{\text{PL,film}}$ (nm)	$\Phi_{\text{PL,sol}}^b$ (%)
<b>PBT1 (14)</b>	350	440	487	40
<b>PBT2 (15)</b>	345	435	479	51
<b>PBT3 (16)</b>	344	431	471	59
<b>PBOT1 (17)</b>	322 384	449	494	49
<b>PBOT2 (18)</b>	320 384	447	492	56
<b>PBOT3 (19)</b>	320 382	445	485	63

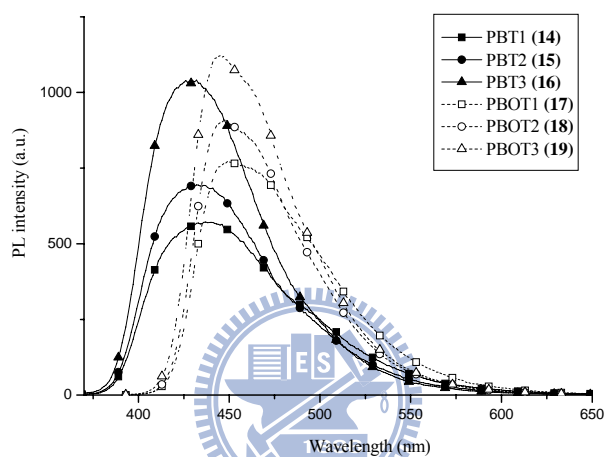
<sup>a</sup> Absorption and PL emission spectra were recorded in dilute THF solutions at room temperature.

<sup>b</sup> PL quantum yield in THF and 9,10-diphenylanthracene is the reference of quantum yield.

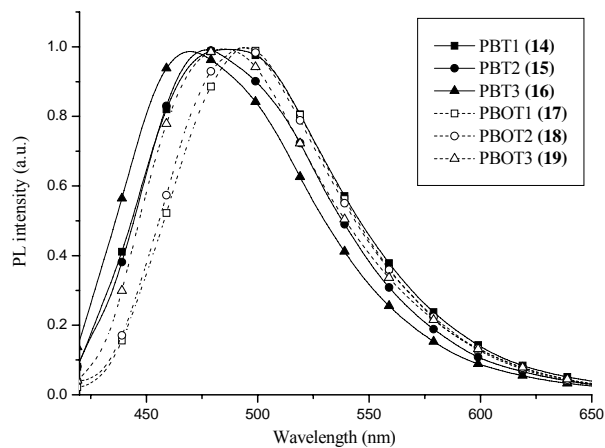




(a)



(b)



(c)

**Figure 2.9** (a) Absorption spectra and (b) PL spectra (excited at the maximum absorption wavelengths) in THF solutions (c) normalized PL spectra (excited at the maximum absorption wavelengths) of H-acceptor polymers **14-19** in solid films.

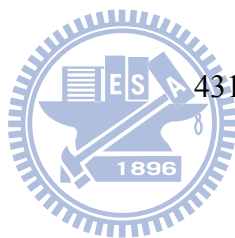
As shown in Table 2.5, the H-donor acids play an important role to induce the PL emission shift of light-emitting H-acceptor polymers in H-bonded polymer complexes because of their different acidities being able to tune the emission colors ( $\lambda_{\max}$ ) by H-bonds. The proton donors in the H-bonded polymer complexes do not have PL properties due to lacking of conjugated structures, so they only offer the solid solvent environments with different pKa values (**OBA (20)**: pKa  $\sim$  4.21; **ONA (21)**: pKa  $\sim$  4.17; **THDA (22)**: pKa  $\sim$  3.49). Thus, different degrees of H-bonding occur in H-bonded polymer complexes for various acids H-bonded with light-emitting H-acceptor polymers, i.e., different electron densities and energy band-gaps of light-emitting H-bonded polymer complexes are induced by the H-bonding of distinct solid H-donors. In Table 2.5, compared with H-acceptor polymers **PBT1-PBT3 (14-16)**, their H-bonded polymer complexes can generate 30-40 nm of red-shifted PL emissions in  $\lambda_{\max}$  as H-bonded to the asymmetric mono-functional H-donors **OBA (20)** and **ONA (21)**, and up to 74-78 nm of red-shifted PL emissions in  $\lambda_{\max}$  as H-bonded to the symmetric bi-functional H-donor **THDA (22)**. The redder-shifted PL emissions are originated from the stronger H-bonded effect of H-donor acids with smaller pKa values and thus to generate stronger H-bonding in corresponding H-bonded polymer complexes. Similarly, the PL emission peaks of the H-bonded polymer complexes containing H-acceptor polymers **PBOT1-PBOT3 (17-19)** are red-shifted about 43-51

nm as complexed with **OBA (20)** and **ONA (21)**, and red-shifted 86-93 nm as complexed with **THDA (22)**. For instance, compared with H-acceptor polymers **PBT2 (15)** and **PBOT2 (18)**, different extents of red-shifted PL emissions occurred in solid films of their H-bonded polymer complexes **PBT2/OBA-PBT2/THDA (15/20-15/22)** and **PBOT2/OBA-PBOT2/THDA (18/20-18/22)** (were excited at the maximum absorption wavelengths) in Figure 2.10. In general, by decreasing pKa values of proton donors, more red-shifted wavelengths of PL emissions of H-bonded polymer complexes were observed. In comparison with H-bonded polymer complexes containing **PBT1-PBT3 (14-16)**, those containing H-acceptor polymers **PBOT1-PBOT3 (17-19)** possess larger red-shifted PL emissions by the formation of H-bonded polymer complexes due to their stronger electron donating effect of lateral methoxy groups. Besides, H-bonded polymer complexes containing H-acceptor polymers with different **CAZ** contents appear to have similar degrees of red-shifted PL emissions in analogous H-bonded polymer complexes. Hence, the pKa values of H-donors are more important than the steric effect of **CAZ** contents in the H-bonded polymer complexes. Consequently, the results demonstrate that more red-shifted PL emissions happen in the H-bonded polymer complexes as H-donors with smaller pKa values are H-bonded to the light-emitting H-acceptor polymers. Therefore, PL emission colors, i.e.,  $\lambda_{\max}$  values, of H-bonded polymer complexes can be tuned not

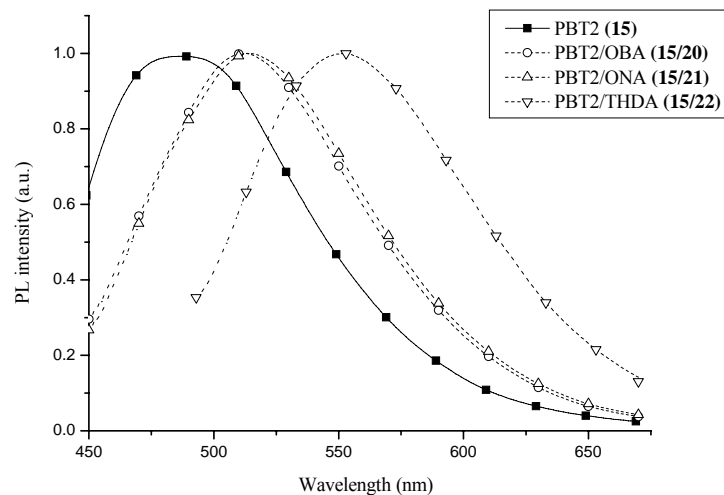
only by adjusting the light-emitting conjugated pyridyl cores but also by changing the non-emitting H-donors with different pKa values.

**Table 2.5 Photophysical Properties of H-Acceptor Polymers and H-Bonded Polymer Complexes in Solid Films**

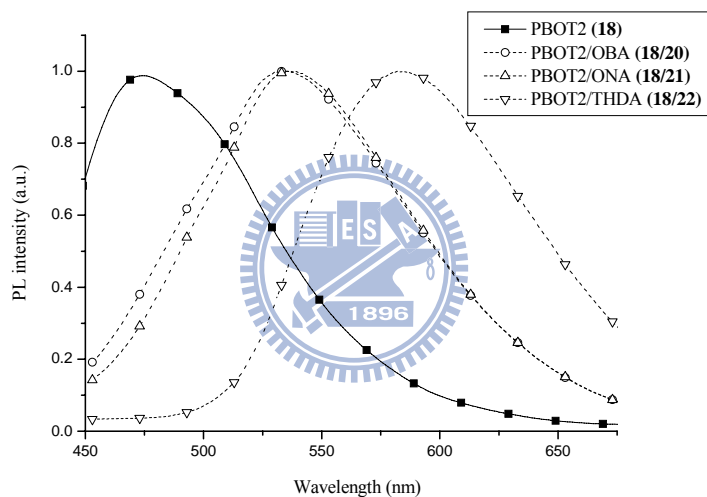
H-acceptor polymer or H-bonded polymer complex	$\lambda_{\text{PL,sol}}$ (nm)	$\lambda_{\text{PL, film}}$ (nm)	$\Delta\lambda_{\text{PL, film}}^a$ (nm)
<b>PBT1 (14)</b>	440	487	-
<b>PBT1/OBA (14/20)</b>		517	30
<b>PBT1/ONA (14/21)</b>		521	34
<b>PBT1/THDA (14/22)</b>		565	78
<b>PBT2 (15)</b>	435	479	-
<b>PBT2/OBA (15/20)</b>		512	33
<b>PBT2/ONA (15/21)</b>		514	35
<b>PBT2/THDA (15/22)</b>		553	74
<b>PBT3 (16)</b>	431	471	-
<b>PBT3/OBA (16/20)</b>		505	34
<b>PBT3/ONA (16/21)</b>		511	40
<b>PBT3/THDA (16/22)</b>		546	75
<b>PBOT1 (17)</b>	449	494	-
<b>PBOT1/OBA (17/20)</b>		543	49
<b>PBOT1/ONA (17/21)</b>		542	48
<b>PBOT1/THDA (17/22)</b>		587	93
<b>PBOT2 (18)</b>	447	492	-
<b>PBOT2/OBA (18/20)</b>		535	43
<b>PBOT2/ONA (18/21)</b>		537	45
<b>PBOT2/THDA (18/22)</b>		582	90
<b>PBOT3 (19)</b>	445	485	-
<b>PBOT3/OBA (19/20)</b>		536	51
<b>PBOT3/ONA (19/21)</b>		534	49
<b>PBOT3/THDA (19/22)</b>		571	86



<sup>a</sup> The difference of PL emissions between the H-acceptor polymer and its H-bonded polymer complex.



(a)



(b)

**Figure 2.10** Normalized PL spectra (excited at the maximum absorption wavelengths) of (a) H-acceptor polymer **PBT2 (15)** and its H-bonded polymer complexes **PBT2/OBA (15/20)**, **PBT2/ONA (15/21)**, and **PBT2/THDA (15/22)** in solid films; (b) H-acceptor polymer **PBOT2 (18)** and its H-bonded polymer complexes **PBOT2/OBA (18/20)**, **PBOT2/ONA (18/21)**, and **PBOT2/THDA (18/22)** in solid films.

## 2.4 Conclusions

In conclusion, H-donors (asymmetric mono-functional H-donors and symmetric bi-functional H-donor) and H-acceptor polymers were utilized to control the

mesomorphic and photoluminescent properties effectively by the concept of supramolecular architecture. The H-acceptor copolymers were composed of different molar ratios of pendent N-vinylcarbazole units and light-emitting H-acceptor groups randomly to increase the glass transition temperatures and to reduce the  $\pi$ - $\pi$  stacking of the conjugated H-acceptor chromophores in the copolymers as well as in their H-bonded polymer complexes. The supramolecular architectures of H-bonded side-chain/cross-linking polymers were also confirmed by FTIR and XRD measurements. They have distinct mesomorphism and phase transition temperatures related to their supramolecular structures with different nonlinearities and rigidities. The mesomorphic properties were changed from the nematic phase to the smectic C phase by the introduction of H-bonds to the supramolecular polymers, and then shifted to the nematic and non-mesogenic phases by various H-donor acids and H-acceptor copolymers with corresponding supramolecular side-chain/cross-linking structures. In addition, the emission color of light-emitting H-acceptor polymers can be tuned by their surrounding non-emitting H-donors. Redder shifts in PL emissions were observed in the H-bonded supramolecules with H-donors having smaller pKa values.

## Chapter 3

# Supramolecular Assembly of H-Bonded Copolymers/Complexes/Nanocomposites and Fluorescence Quenching Effects of Surface-Modified Gold Nanoparticles on Fluorescent Copolymers Containing Pyridyl H-Acceptors and Acid H-Donors

*A series of photoluminescent (PL) and liquid crystalline (LC) self-H-bonded side-chain copolymers (P1-P3) consisting of pyridyl H-acceptors and isomeric acid H-donors (i.e., para-, meta-, and ortho-benzoic acids) were synthesized. Supramolecular H-bonded complexes were also obtained by mixing the photoluminescent H-acceptor homopolymer PBT1 (containing pyridyl pendants) with isomeric H-donor homopolymers P7-P9. The formation of H-bonds was confirmed by FTIR, DSC, and XRD measurements. Moreover, PL and LC properties of the H-bonded copolymers and complexes were affected not only by the H-bonding effect of the supramolecular structures but also by the acid-substituted positions of isomeric H-donors. In combination with different functionalized gold nanoparticles (which bear acid or acid-free surfactants), the emission intensities of nanocomposites containing self-H-bonded copolymer P1 (bearing both H-acceptor and H-donor*

*moieties) and non-self-H-bonded copolymer P4 (bearing acid-protected moieties), respectively, were quenched to different extents by varying the concentration of gold nanoparticles. The copolymeric H-acceptors and surface-modified gold nanoparticles demonstrated diverse morphological and PL quenching effects on the supramolecular architectures of nanocomposites, which result from competition between the H-donors from the acid pendants on copolymers and the acid surfactants on gold nanoparticles.*

### **3.1 Introduction**

Self-assembled phenomena through molecular recognition between complementary constituents have been explored in various areas, such as biomaterials, liquid crystalline (LC) materials, and materials for electro-optical applications.<sup>65c,b,67c,83</sup> Not only innovative LC properties of novel supramolecules consisting of two different components can be generated through intermolecular hetero-hydrogen-bonding interaction, but also directed self-assembly of nano-scaled building blocks using non-covalent interactions (e.g. hydrogen bonding, acid/base proton transfer, and electrostatic forces) has been amplified into macroscopically observable phenomena.<sup>50b,84</sup> More recently, there is considerable interest in the research of conjugated polymers as highly sensitive chemosensors due to their potential applications in chemistry and biology,<sup>32,85</sup> which are based on the different



fluorescence quenching capabilities caused by the varying degrees of supramolecular interactions with particular chemical or biological systems.<sup>30b,86</sup> Poly(*p*-phenylene)s, poly(*p*-phenylene ethynylene)s, poly(*p*-phenylene vinylene)s, polythiophenes, and polyfluorenes with receptor groups, such as crown ethers, pyridine derivatives, and ionic groups, in the side-chains or main-chains have been successfully used for sensing ions and biological species.<sup>87</sup> Design and synthesis of fluorescent side-chain conjugated polymers with supramolecular assembly, which are able to exhibit either chromogenic and/or fluorogenic responses due to non-covalent interactions, have particularly gained considerable attentions recently.<sup>58b,88</sup>

Self-assembly of nanoparticles into nanocomposites provides a direct pathway for incorporating the particles' unique physical properties into the functional materials.<sup>33</sup> Due to the stability and biocompatibility of gold, gold nanoparticles protected by mixed monolayer provide highly attractive models for biological and fluorescent conjugated polymers.<sup>89</sup> Many high performance fluorescence assay methods have been developed by taking advantage of this superquenching ability of gold nanoparticles for optically sensing biologically important ions and molecules. Gold nanoparticles can be functionalized so as to become soluble in water as well as in organic solvents with readily variable monolayer structures. Rotello and co-workers reported the synthesis and self-assembly of gold nanoparticles with

inherent optical properties in the literature.<sup>45,48b,53,54</sup> Murray and co-workers have investigated the quenching of fluorophores that are attached to monolayer-protected gold nanoparticles, and also the electron transfer from excited fluorophores to gold nanoparticles.<sup>90</sup> Direct binding between a fluorophore and a metal surface often results in the quenching of the fluorophore's excited states. In this scenario, both energy transfer and electron transfer processes are considered to be major deactivation pathways for excited fluorophores on a metal surface.<sup>91</sup> Furthermore, in the presence of other metal ions, such as  $\text{Cu}^{2+}$ ,  $\text{Co}^{2+}$ ,  $\text{Fe}^{3+}$ ,  $\text{Ni}^{2+}$ ,  $\text{Zn}^{2+}$ ,  $\text{Pb}^{2+}$  and  $\text{Ag}^+$ , the gold nanoparticles of the quenched nanocomposites (containing fluorophores) can be replaced with the metal ions to different extents due to the stronger re-coordination or re-complexation of the metal ions with fluorophores, and therefore recover the fluorescence of the fluorophores to behave as chemosensors.<sup>58a,b</sup> In addition, the gold nanoparticles of the quenched nanocomposites can also be reacted with the reduced glutathione in the presence of glutathione reductase enzyme, and then recover the fluorescence of the fluorophores to behave as biosensors.<sup>58c</sup> The sensor applications of this work can be further developed to detect the metal ions and biomolecules based on the modulation of fluorescence quenching and recovery.

Previously, several series of H-bonded fluorescent complexes/dendrimers and side-chain supramolecular polymers consisting of pyridyl fluorophores (small

molecular H-acceptors) and various non-luminescent acid H-donors (including small molecules, dendrimers, and side-chain polymers) have been generated through intermolecular H-bonded interactions.<sup>70c,76,77,78</sup> The purpose of this study was to explore photoluminescent (PL) self-H-bonded copolymers (**P1-P3**), consisting of *para*-, *meta*-, and *ortho*-benzoic acids (**M1-M3**) and fluorescent pyridyl (**PBT**) units (with an expected molar ratio of 1:1), for their potential applications as proton donors (H-donors) and acceptors (H-acceptors), respectively. In order to evaluate the proton donating (H-donor) capabilities of the benzoic acid moieties, acid-protected monomers **M4-M6** (containing *para*-, *meta*-, and *ortho*-benzoic acid methyl ester units) and its successive acid-protected (non-self-H-bonded) copolymers **P4-P6** were synthesized.



Subsequently, it is more interesting to develop a two-stage self-assembly process in which the recognition (or sensing) of different surface-functionalized gold nanoparticles (with acid and acid-free surfactants) is preceded by the light-emitting copolymers, i.e., self-H-bonded copolymer **P1** (bearing both H-acceptor and H-donor moieties) and non-self-H-bonded copolymer **P4** (bearing acid-protected moieties), correspondingly. Hence, side-chain conjugated copolymers bearing fluorescent pyridyl H-acceptor pendants not only behave as highly selective chemosensors for carboxylic acid H-donors, but also exhibit

distinct fluorescent quenching effects upon the addition of surface-functionalized gold nanoparticles (i.e., **AuSCOOH** and **AuSC10**, which contain acid and acid-free surfactants, respectively). To our knowledge, this approach (as shown in the schematic illustration of Figure 3.1) is the first exploration of the supramolecular assembly of nanocomposites via fluorescence quenching and TEM morphological analyses. The competition between H-donors from the acid surfactants on the gold nanoparticles and the acid pendent groups on the copolymers to form H-bonds with the pyridyl pendants (as H-acceptors) of the copolymers will be surveyed.

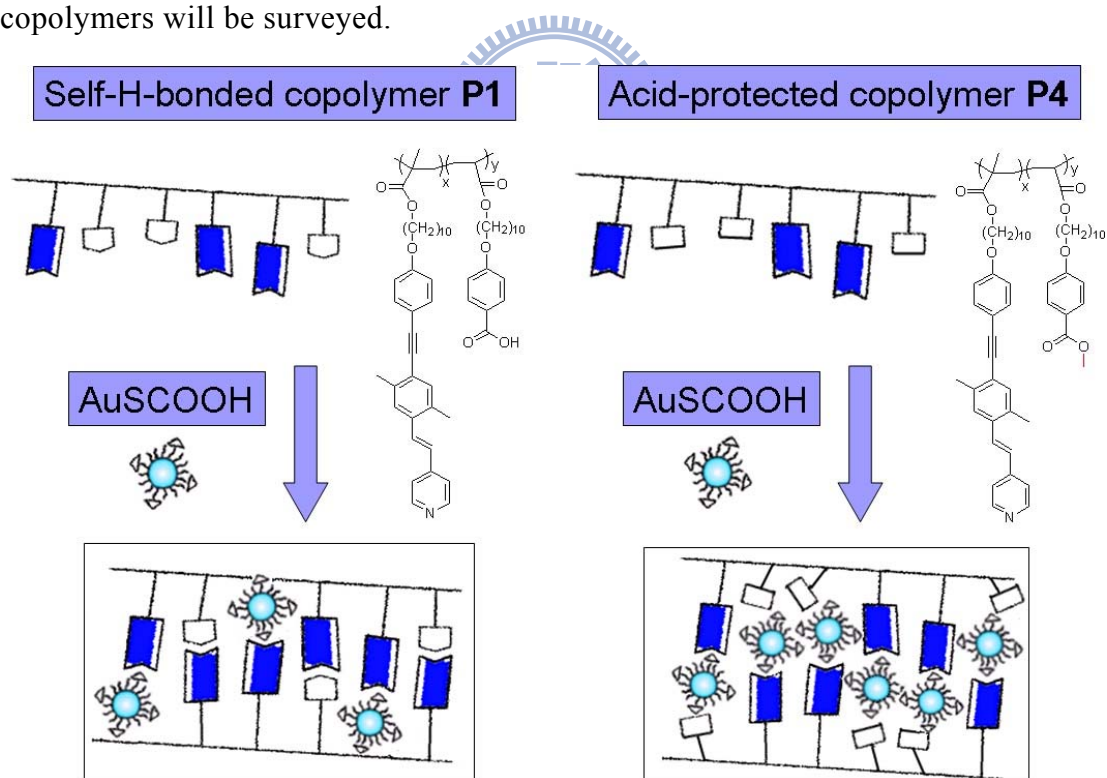


**Figure 3.1** Schematic illustration of acid-functionalized gold nanoparticles (**AuSCOOH**) blended with self-H-bonded copolymer **P1** and non-self-H-bonded copolymer **P4**.

## 3.2 Experimental Section

### 3.2.1 Materials

Chemicals and solvents were reagent grades and purchased from Aldrich, ACROS, TCI, TEDIA, and Lancaster Chemical Co. Dichloromethane and THF were distilled to keep anhydrous before use. The other chemicals were used without further purification.

#### General Synthetic Procedures for Monomers (M1-M6)

The synthetic route of the H-acceptor monomer **PBT** is described in Chapter 2<sup>92</sup> and isomeric H-donor monomers **M1-M3** (i.e., *para*-, *meta*-, and *ortho*-benzoic acids) were prepared according to the procedure reported by Portugall et al.<sup>93</sup> Monomers **M4-M6**, with methyl-ester protecting groups, were also successfully synthesized by the same synthetic method as the H-donor monomers **M1-M3**. The chemical structures for all products were confirmed by <sup>1</sup>H NMR spectroscopy and elemental analyses.

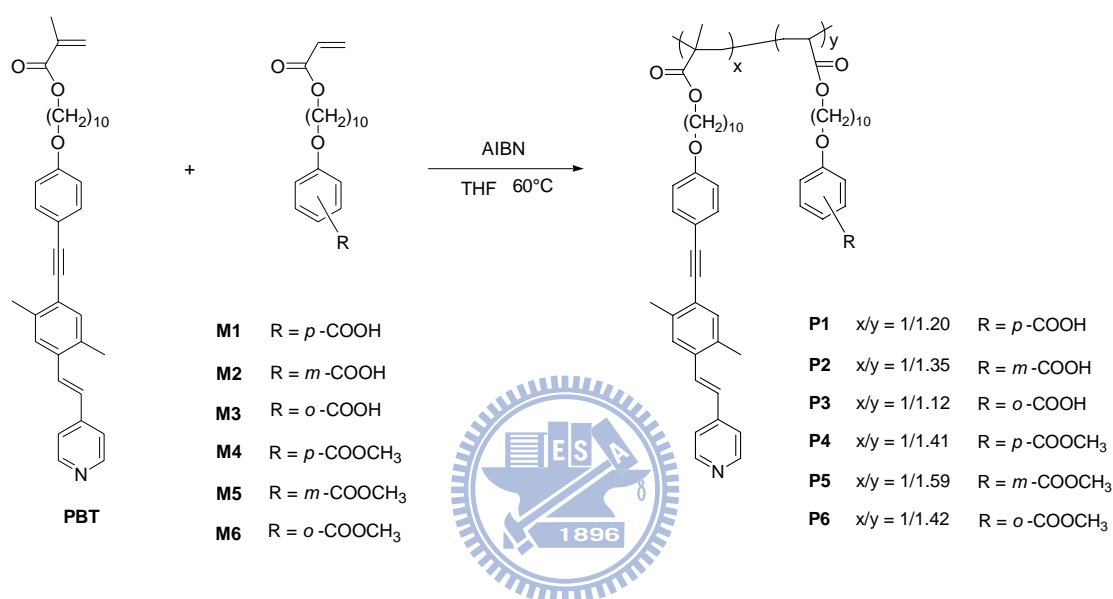
#### General Synthetic Procedures for Copolymers (P1-P6)

According to Scheme 3.1, copolymers **P1-P6** were synthesized from monomers **M1-M6** (H-donor monomers **M1-M3** and acid-donor-protected monomers **M4-M6**) and the H-acceptor monomer **PBT**. Equal ratios of **PBT** (50%) and monomers **M1-M6** (50%), total amounts ~ 1.2 g, were dissolved in THF (6 mL) with AIBN (3

mol%) added as the initiator. The reaction mixture was flushed with nitrogen for 5 min, and then heated in a water bath at 60°C to initiate polymerization. After 24 h, the reaction was terminated and the polymer was precipitated in a large amount of ether. The resulting copolymers **P1-P6** were re-dissolved several times in THF and re-precipitated in ether/hexane (1:1). The yields of copolymers **P1-P6** were in the range of 45 ~ 67%. The molecular weights and polydispersity index (PDI) values, relative to polystyrene standards, of copolymers **P1-P6** are presented in Table 3.1. The output copolymer compositions of copolymers **P1-P6**, i.e., the molar ratios of monomer **PBT** to (H-donor or acid-protected) monomers **M1-M6**, which were estimated by NMR experiments, are also listed in Table 3.1. In the <sup>1</sup>H NMR spectra of copolymers **P1-P6**, the disappearance of proton peaks in the region of vinyl units (chemical shifts at 5.4-6.1 ppm of methacrylate and acrylate groups) indicated that no monomers were present. The copolymer compositions in copolymers **P1-P6** were estimated by comparing the relative integration areas of the peak at 8.5 ppm, which belong to the two protons of  $\alpha$ -pyridyl groups in **PBT**. The overlapped peaks from 6.7 to 7.9 ppm are assigned to the other aromatic proton regions in **PBT** groups as well as benzoic groups in **M1-M6**, respectively. The copolymer compositions ( $x/y = 1/y$ ) were calculated by the following equation:  $x/y = 1/y = 1/[(\text{total integration areas of aromatic protons in copolymer} - \text{total integration areas of aromatic protons in$

$\text{PBT}/(\text{total integration areas of aromatic protons in M1-M6}) = 1/[(\text{total integration areas of aromatic protons in copolymer} - 12)/4]$ . This is based on the assumption that the total integration area of the pyridyl protons nearest the heterocyclic N atom in each copolymer is equal to 2, i.e., 2 protons.

### Scheme 3.1 Synthetic Routes for Copolymers P1-P6.



### Scheme 3.2 Synthetic Routes for H-Acceptor Homopolymer PBT1 and H-Donor Homopolymers P7-P9.

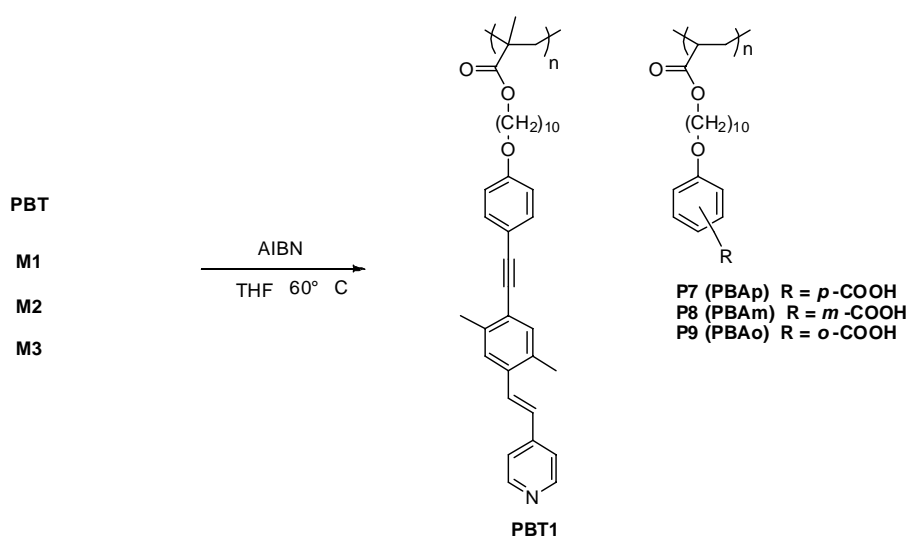


**Table 3.1 Characterization of Copolymers P1-P6 and H-Donor Homopolymers P7-P9**

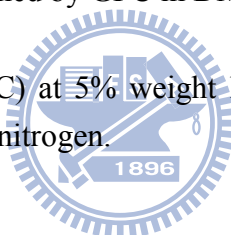
polymer	molar ratio of <b>PBT</b> in feed <sup>a</sup>	molar ratio of <b>PBT</b> in output copolymer <sup>b</sup>	M <sub>n</sub> <sup>c</sup>	M <sub>w</sub> <sup>c</sup>	PDI <sup>c</sup>	T <sub>d</sub> <sup>d</sup> (°C)
<b>PBT1</b>	1	1	8800	20300	2.3	389
<b>P1</b>	0.5	0.45 (1/1.20)	5300	8100	1.5	389
<b>P2</b>	0.5	0.43 (1/1.35)	6200	10800	1.7	374
<b>P3</b>	0.5	0.47 (1/1.12)	6800	9600	1.4	284
<b>P4</b>	0.5	0.40 (1/1.49)	7100	13000	1.8	344
<b>P5</b>	0.5	0.39 (1/1.59)	5600	14900	2.6	345
<b>P6</b>	0.5	0.41 (1/1.42)	5800	12600	2.1	315
<b>P7</b>	-	-	6000	11700	1.9	357
<b>P8</b>	-	-	7100	12200	1.7	346
<b>P9</b>	-	-	6300	10300	1.6	294

<sup>a</sup> Molar ratio of monomer **PBT** in the feed before copolymerization.

<sup>b</sup> Molar ratio of monomer **PBT** in the output copolymers determined by NMR.

<sup>c</sup> Molecular weights were determined by GPC in DMF, based on polystyrene standards.

<sup>d</sup> Decomposition temperatures (°C) at 5% weight loss were measured by TGA at a heating rate of 20°C/min under nitrogen.



### Homopolymers **PBT1** and **P7-P9**

By following Scheme 3.2, the H-acceptor monomer **PBT**, or H-donor monomer **M1-M3**, (1 g) was dissolved in THF (5 mL) with AIBN (3 mol%) added as the initiator. The reaction mixture was flushed with nitrogen for 5 min and then heated in a water bath at 60°C to initiate polymerization. After 24 h, the reaction was terminated and the polymer was precipitated into a large amount of ether. The homopolymers **PBT1** and **P7-P9** were re-dissolved in THF and re-precipitated in hexane several times. The yields were in the range of 49 ~ 85%. The molecular weights and polydispersity index (PDI) values of homopolymers **PBT1** and **P7-P9**



(i.e., H-donor homopolymers **PBAp**, **PBAm**, and **PBAo**) are presented in Table 3.1.

### 3.2.2 Preparation of H-Bonded Complexes (PBT1/P7-P9)

All H-bonded complexes were fabricated from equal molar ratios of H-acceptor homopolymer **PBT1** and H-donor homopolymers **P7-P9** (**PBAp**, **PBAm**, and **PBAo**).

The complexes were dissolved in THF to make a clear solution, and then subsequently dried for several hours in a vacuum oven at 60°C. During solvent evaporation, the complexation through hydrogen bonding occurred between the H-donor and H-acceptor homopolymers. H-bonded complexes **PBT1/P7**, **PBT1/P8**, and **PBT1/P9**, which possess equal molar amounts of both pyridyl (H-acceptor) and carboxylic acid (H-donor) groups (1:1 molar ratio), were produced.

### 3.2.3 Preparation of Nanocomposites Consisting of Gold Nanoparticles and Polymers

The surface-functionalized gold nanoparticles. **AuSCOOH** and **AuSC10**, which contain acid and acid-free surfactants were synthesized, respectively. Nanocomposites were prepared by mixing solutions (0.5 mg/ml) of surface-functionalized gold nanoparticles **AuSCOOH** and **AuSC10** in THF. This was then mixed with solutions of copolymers **P1** and **P4** in DMF (2 mg/ml). The gold nanoparticles began to assemble into nanocomposites within 2 min. The mixed solutions became visibly turbid, indicating that an aggregation process had occurred. After 24 h, the solid

precipitates were collected and washed extensively with hexane. The nanocomposites were then dried overnight before being subjected to Transmission Electron Microscopy (TEM) measurements.

### 3.2.4 Characterizations

<sup>1</sup>H NMR spectra were recorded on a Varian unity 300M Hz spectrometer using CDCl<sub>3</sub>, DMSO-d<sub>6</sub>, d-dioxane, and d-THF as solvents. Elemental analyses were performed on a HERAEUS CHN-OS RAPID elemental analyzer. Fourier transform infrared (FT-IR) spectra were performed on a Nicolet 360 FT-IR spectrometer. The textures of mesophases were characterized by a Leica DMLP polarizing optical microscope (POM) equipped with a hot stage (Linkam LTS350). Temperatures and enthalpies of phase transitions were determined by differential scanning calorimetry (DSC, model: Perkin Elmer Pyris 7) under N<sub>2</sub>, at a heating and cooling rate of 10°C/min. Thermogravimetric analyses (TGA) were conducted on a Du Pont Thermal Analyst 2100 system with a TGA 2950 thermogravimetric analyzer under N<sub>2</sub>, at a heating rate of 20°C/min. Molecular weights and molecular weight distributions were determined through gel permeation chromatography (GPC) using a Waters 510 HPLC, equipped with a 410 differential refractometer, a refractive index (RI) detector, and three Ultrastyrigel columns (100, 500, and 103) connected in series in order to increase different pore sizes, with DMF as eluent at

a flow rate of 0.6 mL/min. The molecular weight calibration curve was obtained using polystyrene standards. UV-visible absorption spectra in dilute THF solutions ( $10^{-6}$  M) were recorded on a HP G1103A spectrophotometer, and photoluminescence (PL) spectra in dilute THF solutions ( $10^{-6}$  M) were obtained on a Hitachi F-4500 spectrophotometer. Thin films of UV-vis and PL measurements were spin-coated (3000 rpm) on quartz substrates from THF solutions with a concentration of 1 wt%. The fluorescence quantum yields ( $\Phi_{\text{PL}}$ ) of the chromophores and H-bonded complexes were determined relative to a standard film of 9,10-diphenylanthracene dispersed in PMMA ( $\Phi = 0.83$ ).<sup>94</sup> Synchrotron powder X-ray diffraction (XRD) measurements were performed at beamline BL17A1 of the National Synchrotron Radiation Research Center (NSRRC), Taiwan, where the X-ray wavelength was 1.32633 Å. The XRD data were collected using imaging plates (IP, of an area =  $20 \times 40$  cm<sup>2</sup> and a pixel resolution of 100) curved with a radius equivalent to the sample-to-image plate distance of 280 mm, and the diffraction signals were accumulated for 3 min. The powder samples were packed into a capillary tube and heated by a heat gun, where the temperature controller was programmable by a PC with a PID feed back system. The scattering angle theta was calibrated by a mixture of silver behenate and silicon. Transmission Electron Microscopy (TEM) analyses were performed using

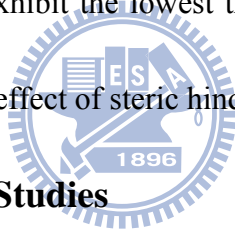
a JEOL 2011 electron microscope with an acceleration voltage of 200 keV. The samples were prepared from THF solutions with a concentration of 1 wt%, and the aggregates were precipitated on TEM sample grids (200 Cu mesh/carbon films).

### 3.3 Results and Discussion

#### 3.3.1 Synthesis and Characterization

Proton acceptor monomer **PBT** containing three-conjugated aromatic rings was successfully synthesized via Sonogashira coupling and Wittig-Horner reactions, whose synthetic route was reported in Chapter 2.<sup>92</sup> Two series of H-donor monomers **M1-M3** and acid-protected monomers **M4-M6** were synthesized. The molecular structures of monomers **M1-M6** were confirmed by <sup>1</sup>H NMR and elemental analyses. According to the synthetic routes shown in Scheme 3.1, copolymers **P1-P6** were synthesized from the H-acceptor monomer **PBT** along with monomers **M1-M6** (H-donor **M1-M3** and acid-protected **M4-M6**), with approximately 1:1 molar ratio, via the conventional synthesis of random free radical copolymerization. The random free radical polymerization of H-donor homopolymers **P7-P9** (**PBAp-PBAo**) and H-acceptor homopolymer **PBT1**, depicted in Scheme 3.2, were proceeded by the same condition in Scheme 3.1. The H-bonding effects on these two series of analogous copolymers, i.e., self-H-bonded copolymers **P1-P3** and non-self-H-bonded copolymers **P4-P6** (containing H-donor monomers **M1-M3** and acid-protected

monomers **M4-M6**, respectively), were evaluated for their thermal, mesogenic, and optical properties. The average molecular weights measured by gel permeation chromatography (GPC), relative to polystyrene standards, are displayed in Table 3.1. The number average molecular weights ( $M_n$ ) of all polymers are between 5300 and 7100 g/mol, and the polydispersity index (PDI) values are between 1.4 and 2.6. Their thermal stability was measured under nitrogen by thermogravimetric analyses (TGA), and these results are also summarized in Table 3.1. The thermal decomposition temperatures ( $T_d$ ) of 5% weight loss are between 284 and 389 °C, where the  $T_d$  values of polymers **P3** and **P9** exhibit the lowest thermal stability (284 and 294 °C, respectively) due to the isomeric effect of steric hindrance in *ortho*-acid.

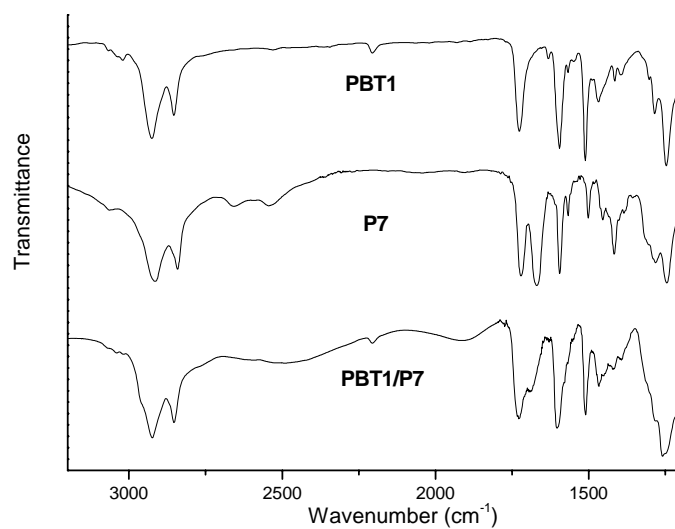


### 3.3.2 FT-IR Spectroscopic Studies

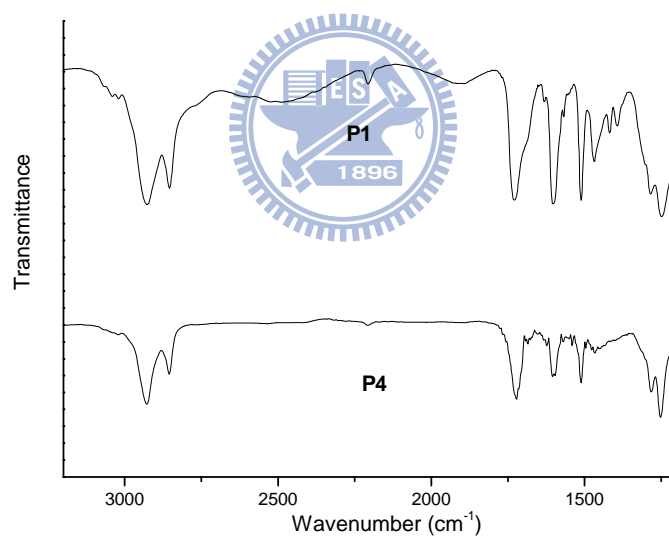
H-bonding effects in mesogenic copolymers **P1-P6** along with H-bonded complexes **PBT1/P7-P9** (H-acceptor homopolymer **PBT1** blended with H-donor homopolymers **P7-P9** in equal molar ratios) were confirmed by FT-IR spectroscopy. The IR spectra of the H-acceptor homopolymer **PBT1**, H-donor homopolymer **P7**, and their H-bonded complexes **PBT1/P7**, shown in Figure 3.2(a), are compared to analyze the formation of H-bonds. In contrast to the O-H band of pure H-donor homopolymer **P7 (PBAp)** at 2658 and 2543  $\text{cm}^{-1}$ , the weaker O-H bands observed at 2528-2491 and 1931-1912  $\text{cm}^{-1}$  in H-bonded complexes **PBT1/P7**, **PBT1/P8**, and

**PBT1/P9** are indicative of stronger H-bonds formed between pyridyl groups of the H-acceptor homopolymer **PBT1** and acid groups of H-donor homopolymers **P7-P9** in their H-bonded complexes **PBT1/P7-P9**. On the other hand, a C=O stretching vibration appeared at 1730-1727  $\text{cm}^{-1}$  in H-bonded complexes **PBT1/P7-P9** (a shoulder appeared at 1690  $\text{cm}^{-1}$  for H-bonded complex **PBT1/P7**). This shows that the carbonyl group is in a more associated state than that it is in the pure H-donor homopolymer **P7**, which contains a weaker C=O stretching vibration appeared at 1720 and 1669  $\text{cm}^{-1}$ . All results suggest that H-bonds were generated in the solid state of H-bonded complexes **PBT1/P7**, **PBT1/P8**, and **PBT1/P9**. As seen in Figure 3.2(b), self-H-bonded copolymers **P1-P3** reveal similar IR spectral profiles to those (Figure 3.2(a)) of H-bonded complexes **PBT1/P7-P9**, respectively. This suggests that analogous H-bonded structures formed in the self-H-bonded copolymers **P1-P3** and in the H-bonded complexes **PBT1/P7-P9**.<sup>17</sup> However, in comparison with self-H-bonded copolymers **P1**, acid-protected copolymer **P4** in Figure 3.2(b) shows a weaker C=O stretching vibration appeared at 1720  $\text{cm}^{-1}$  for lack of H-bonding interaction. The C=O stretching peak is sharper because there is less resonance for C=O stretching in the non-self-H-bonded copolymer **P4**, and so do acid-protected copolymers **P5-P6** for lack of H-bonds. Meanwhile, a shifted peak at 1600  $\text{cm}^{-1}$  from a disturbance of the 1590  $\text{cm}^{-1}$  ring mode was observed in Figure 3.2(a), which indicated a change in the

strength of the acid-pyridine interactions.



(a)



(b)

**Figure 3.2** Infrared spectra of (a) H-acceptor homopolymer **PBT1**, H-donor homopolymer **P7**, and H-bonded homopolymer complexes **PBT1/P7**; (b) copolymers **P1** and **P4** in solid films.

### 3.3.3 Phase Characterization

The thermal properties, including glass transition temperatures ( $T_g$ ) and isotropization temperatures ( $T_i$ ) with corresponding enthalpies, of these copolymers and H-bonded complexes, determined by DSC and POM, are shown in Table 3.2. The glass transition temperatures of copolymers **P1-P6** and H-bonded complexes **PBT1/P7**, **PBT1/P8**, and **PBT1/P9** (H-acceptor homopolymer **PBT1** blended with H-donor homopolymers **P7-P9** in equal molar ratios) are ca. 22 ~ 57 °C. Moreover, all self-H-bonded copolymers **P1-P3** containing H-donors have higher  $T_g$  and  $T_i$  values than their corresponding non-self-H-bonded copolymers **P4-P6**, which do not contain H-donors. This is because the self-H-bonded cross-linking polymer structures, in copolymers **P1-P3**, have a longer rigid core than the non-H-bonded side-chain polymer structures in acid-protected copolymers **P4-P6**. Both  $T_g$  and  $T_i$  values of H-bonded complexes **PBT1/P7**, **PBT1/P8**, and **PBT1/P9** have a similar tendency (i.e., **PBT1/P7** > **PBT1/P8** > **PBT1/P9**) as those of self-H-bonded copolymers **P1-P3** (*para*-acid-substituted copolymer **P1** > *meta*-acid-substituted copolymer **P2** > *ortho*-acid-substituted copolymer **P3**). Overall, the *para*-substituted copolymer **P1** and the H-bonded complex **PBT1/P7** exhibit the highest  $T_g$  and  $T_i$  values because they have the most linear H-bonded (cross-linking) structures.

Because of the linear H-bonded structures of self-H-bonded copolymer **P1** and



H-bonded complex **PBT1/P7** (containing *para*-acid-substituted homopolymer **P7**), the smectic phase was only generated in the *para*-acid-substituted copolymer **P1** with a mesomorphic range of 92 °C and in the H-bonded complex **PBT1/P7** with a mesomorphic range of 114 °C. The H-bonded complex **PBT1/P7** had a wider mesophase range than self-H-bonded copolymer **P1**, because the H-bonded complex (**PBT1/P7**) contains highly ordered H-bonded mesogens (from homopolymer blends) in the smectic arrangement. Due to the same reason of highly ordered H-bonds in H-bonded complexes, the nematic phases observed in nonlinear H-bonded structures (with non-*para*-acid-substituted H-donors) of H-bonded complexes **PBT1/P8** and **PBT1/P9** were wider than those of self-H-bonded copolymers **P2-P3**. This result suggests that the steric factor related to the isomeric acid-substituted positions in H-donors is decisive for the formation of the mesomorphism in all H-bonded structures. In addition, the acid-protected copolymers **P4-P6** (which lack H-bonds) possess the nematic phase adopted from the H-acceptor **PBT** moieties (with the nematic phase between 42°C and 71°C), which is similar to observations with the homopolymer **PBT1**. However, non-self-H-bonded copolymers **P4-P6** have lower phase transition temperatures (including the isotropization temperature  $T_i$ ) than homopolymer **PBT1** due to the dilution effect of the acid-protected monomer moieties (**M4-M6**) in copolymers **P4-P6**.

To further elucidate the mesomorphic behavior in Table 3.2, POM and XRD measurements were performed at the mesophasic ranges of all copolymers and H-bonded complexes. The mesophases of copolymer **P1** and H-bonded complex **PBT1/P7** were characterized by POM. To confirm the formation of supramolecular structures, the smectic layer arrangements for copolymer **P1** and H-bonded complex **PBT1/P7** were characterized by *d*-spacing values of XRD measurements. The theoretical value of the fully-extended molecular length of copolymer **P1** is 57.8 Å, estimated using CS ChemOffice. The *d*-spacing values of copolymer **P1** and the H-bonded complex **PBT1/P7** at 130°C are 50.3 and 52.4 Å, respectively (Figure 3.3(a)). These XRD measurements support the hypothesis that the copolymer **P1** and H-bonded complex **PBT1/P7** are suitable to be identified as the tilted smectic C phase with tilt angles of 29.6° and 25.0°, respectively. On the other hand, the absence of d-layer spacing peaks, for copolymers **P2-P6** and H-bonded complexes **PBT1/P8** and **PBT1/P9**, indicates that these species possess the nematic phase. For instance, Figure 3.3(b) shows the XRD intensity against angle profiles obtained in the nematic phase of copolymer **P2** at 70 °C.

**Table 3.2 Thermal Properties of Polymers and H-Bonded Homopolymer Complexes**

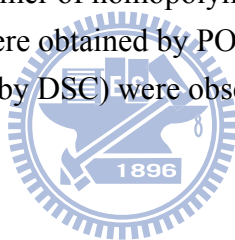
polymer/complex	Phase transitions, °C <sup>a</sup>
<b>PBT1</b> <sup>b</sup>	glass 51 N 145 <sup>c</sup> I
<b>P1</b>	glass 57 Sc 149 (3.7) I
<b>P2</b>	glass 52 N 80 <sup>c</sup> I
<b>P3</b>	glass 42 N 69 <sup>c</sup> I
<b>P4</b>	glass 22 N 58 <sup>c</sup> I
<b>P5</b>	glass 22 N 47 <sup>c</sup> I
<b>P6</b>	glass 24 N 45 <sup>c</sup> I
<b>PBT1/P7</b> <sup>d</sup>	glass 53 Sc 167 (4.3) I
<b>PBT1/P8</b> <sup>d</sup>	glass 30 N 94 (1.8) I
<b>PBT1/P9</b> <sup>d</sup>	glass 24 N 80 <sup>c</sup> I

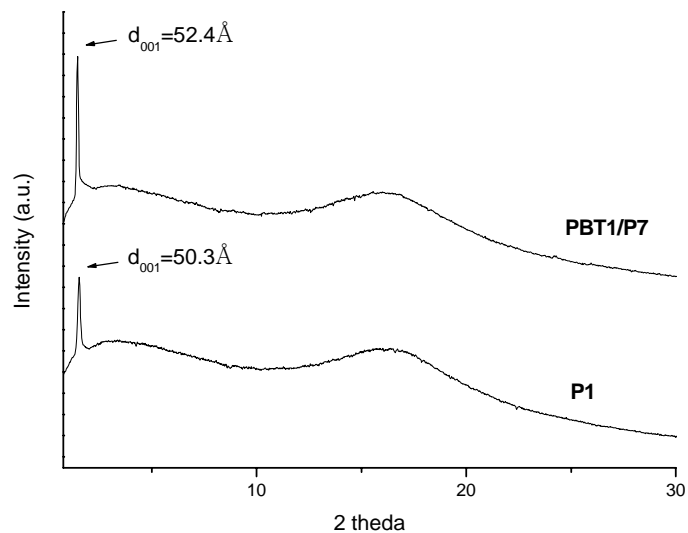
<sup>a</sup> Phase transition temperatures (°C) and enthalpies (in parentheses, kJ/mol) were determined by DSC at a heating rate of 10 °C/min.

<sup>b</sup> Phase transitions of **PBT** (monomer of homopolymer **PBT1**): K 42° N 71° I.

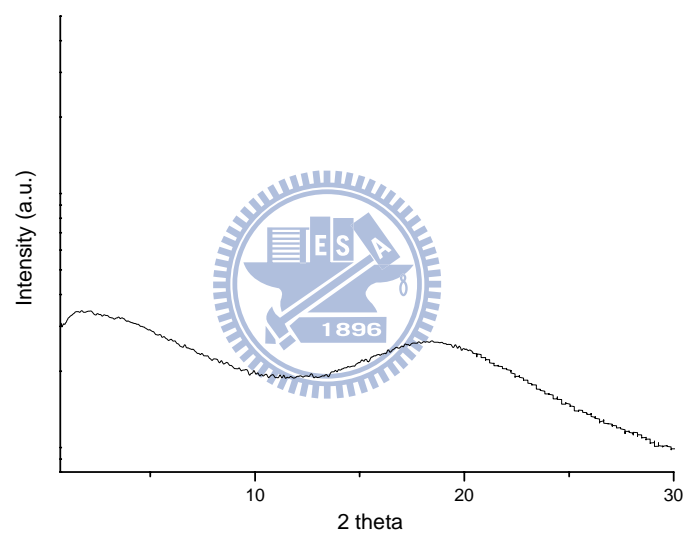
<sup>c</sup> Phase transition temperatures were obtained by POM and confirmed by XRD.

<sup>d</sup> No detectable *T<sub>g</sub>* temperatures (by DSC) were observed in homopolymers **P7-P9**.





(a)



(b)

**Figure 3.3** (a) X-ray diffraction (XRD) patterns of copolymer **P1** and H-bonded complex **PBT1/P7** in the Sc phase at 130°C. (b) XRD intensity against angle profiles obtained in the nematic phase of copolymer **P2** at 70°C.

### 3.3.4 Optical Properties

The absorption and PL spectral data of all copolymers **P1-P6** (in both THF solutions and solid films) and H-bonded complexes **PBT1/P7**, **PBT1/P8**, and **PBT1/P9** (in solid films) are summarized in Table 3.3 and Figure 3.4. As shown in Table 3.3, the maximum absorption peaks of copolymers **P1-P6**, near 350 nm (in THF solutions), are mainly attributed to the **PBT** units. In Table 3.3 and Figure 3.4, PL emissions at 444-447 nm (in THF solutions) and at 515-529 nm (in solids for self-H-bonded copolymers **P1-P3**) are all red-shifted in contrast to PL emissions of acid-protected copolymers **P4-P6** (without H-bonds) at 429-431 nm (in THF solutions) and at 466-472 nm (in solids), respectively. Therefore, compared with PL emissions of non-self-H-bonded copolymers **P4-P6**, the H-bonding effects on PL emission wavelengths ( $\lambda_{\text{max}}$ ) of self-H-bonded copolymers **P1-P3** are further enhanced in solids (red-shifted 43-63 nm) than in solutions (red-shifted 15-16 nm). However, due to the PL quenching effect by the aggregation of longer self-H-bonded chromophores in copolymers **P1-P3**, the acid-protected copolymers **P4-P6** (without H-bonds) exhibit higher PL quantum yields (in both solutions and solid films) than the self-H-bonded copolymers **P1-P3**. For all copolymers (**P1-P6**), it is apparent that more  $\pi$ - $\pi$  stacking and molecular aggregation occur in solid films than in solutions. The aggregation phenomena are even more pronounced for **P1-P3** in solid films due to the

self-H-bonded structures.

On the basis of our findings, non-luminescent acids are important for inducing various wavelength shifts in PL emissions of luminescent H-acceptors by tuning the pKa values of H-donors in self-H-bonded copolymers and homopolymer complexes.

The H-donor moieties with different pKa values, i.e., *para*-H-donor (**M1**): pKa ~ 4.36; > *meta*-H-donor (**M2**): pKa ~ 4.19; > *ortho*-H-donor (**M3**): pKa ~ 4.15,<sup>95</sup> offer a solid solvent environment in the H-bonded copolymers and complexes. Therefore, the PL emission wavelengths of H-bonded complexes in solid films are related to the pKa values as follows: **PBT1/P7** < **PBT1/P8** < **PBT1/P9**. Additionally, in contrast to self-H-bonded copolymers **P2-P3**, the *para*-substituted acid has the smallest acidity, and therefore the weakest H-donor effect which induces the smallest red-shifted PL emission in the solid film of copolymer **P1**. However, both acidic and steric effects of isomeric H-donors play important roles on the PL properties of H-bonded structures.

The molecular  $\pi$ - $\pi$  stacking in the H-bonded bending structures consisting of *meta*- and *ortho*-substituted H-donors were suppressed owing to the steric hindrance of *meta*- and *ortho*-substitution. Thus, the PL emission wavelengths of copolymers **P2** and **P3** in solid films have the following order: *meta*-**P2** (529 nm) > *ortho*-**P3** (523 nm), which is in the reverse order of acidity. In general, the results demonstrate that similar red-shifted PL emissions occur when isomeric H-donors are complexed to

form supramolecular structures in both self-H-bonded copolymers (**P1-P3**) and H-bonded homopolymer complexes (**PBT1/P7-P9**). Moreover, the acidities and steric structures of the isomeric H-donors do affect the molecular packing and PL emission wavelengths of the H-bonded supramolecular architectures. Therefore, the  $\lambda_{\max}$  values, which correspond to the emission colors, of the photoluminescence in the supramolecular systems can be tuned not only by adjusting the emitting cores but also by changing the isomeric structures of the H-donors.

**Table 3.3 Absorption and PL Emission Spectral Data of Polymers and H-Bonded Homopolymer Complexes in THF Solutions and Solid Films**

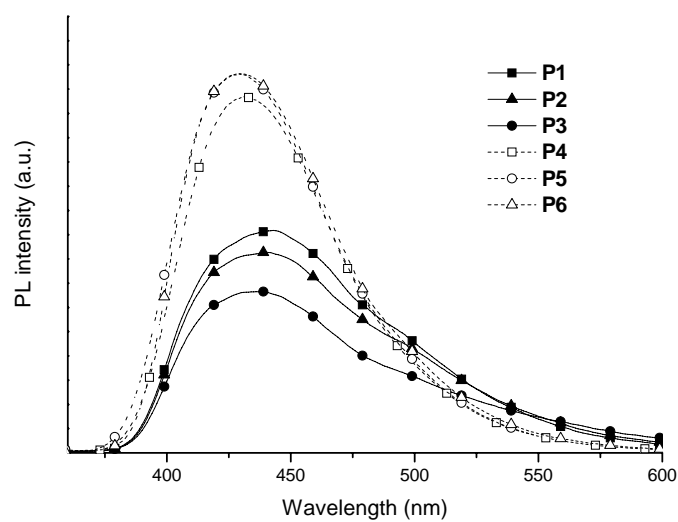
polymer/ complex	absorption		PL emission		$\Phi$ (%) (sol) <sup>c</sup>	$\Phi$ (%) (film) <sup>d</sup>
	$\lambda_{\max}$ (nm) solution <sup>a</sup>	film	$\lambda_{\max}$ (nm) <sup>b</sup> solution <sup>a</sup>	film		
<b>PBT1</b>	350	357	440	487	40	20
<b>P1</b>	349	359	447	515	43	17
<b>P2</b>	349	361	445	529	39	14
<b>P3</b>	350	361	444	523	35	16
<b>P4</b>	347	359	431	472	58	22
<b>P5</b>	348	360	429	466	60	23
<b>P6</b>	349	360	429	466	60	26
<b>PBT1/P7</b>	-	358	-	514	-	18
<b>PBT1/P8</b>	-	363	-	522	-	16
<b>PBT1/P9</b>	-	360	-	525	-	15

<sup>a</sup> Absorption and PL emission spectra were recorded in dilute THF solutions at room temperature.

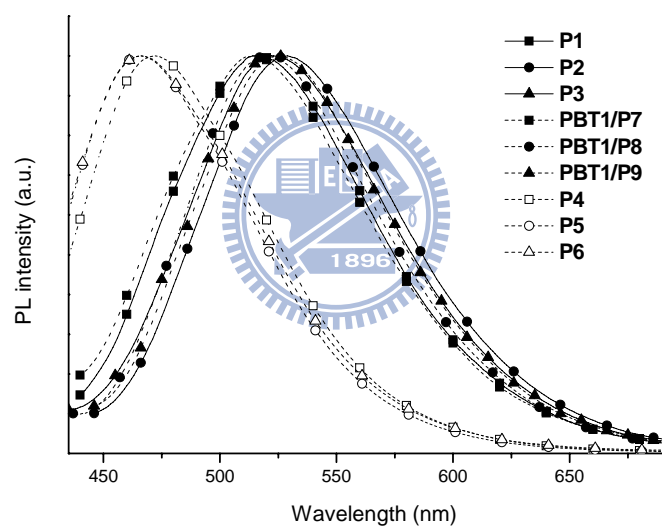
<sup>b</sup> PL emissions were excited at the maximum absorption peaks.

<sup>c</sup> PL quantum yield of 9,10-diphenylanthrance in THF ( $10^{-6}$  M) as the reference quantum yield in solutions.

<sup>d</sup> PL quantum yield of 9,10-diphenylanthrance blended in PMMA as the reference quantum yield in solid film.



(a)



(b)

**Figure 3.4** (a) PL spectra of copolymers **P1-P6** in THF solutions (b) normalized PL spectra of copolymers **P1-P6** and H-bonded homopolymer complexes **PBT1/P7**, **PBT1/P8**, and **PBT1/P9** in solid films.



### 3.3.5 Fluorescence Quenching Effects of Copolymers by Surface-Modified Gold Nanoparticles

In the fluorescence quenching studies, where acid-donor-modified **AuSCOOH** nanoparticles and non-acid-modified **AuSC10** nanoparticles (diameter ca. 5 ~ 6 nm) were doped, the photoluminescence (PL) spectra of copolymers **P1** and **P4** were monitored in the presence of different concentrations of surface-modified gold nanoparticles (Figure 3.5). The fluorescence spectra of pure copolymers **P1** and **P4** exhibit maximum PL emissions at 447 nm and 431 nm with corresponding quantum yields of 43% and 58%, respectively. In Figure 3.5(a) and 3.5(b), copolymers **P1** and **P4** demonstrated dramatic decreases in fluorescence intensities upon the addition of **AuSCOOH** nanoparticles (which contain 21% carboxylic acid surfactants). Upon the addition of **AuSCOOH**, progressive fluorescence quenching effects on copolymer **P1** (blended with **AuSCOOH**) were observed by increasing the concentration of **AuSCOOH**. It is conceivable that the polymer nanocomposite **P1-AuSCOOH** reduced the fluorescence emission intensities by H-bonding complexation of the fluorescent pyridyl units with the acid surfactant on **AuSCOOH**. The H-donor (*para*-benzoic acid) units in self-H-bonded copolymer **P1** were easily H-bonded with the pyridyl H-acceptor groups and competed with the acid H-donor surfactants on **AuSCOOH** nanoparticles. However, as shown in Figure 3.5(b), the titration of

acid-protected copolymer **P4** by **AuSCOOH** nanoparticles displays a similar PL quenching trend as Figure 3.5(a). This suggests that the complexation of acid-protected copolymer **P4** and **AuSCOOH** nanoparticles has a similar H-bonding interaction as that in the nanocomposite **P1-AuSCOOH**. Unlike the self-H-bonded copolymer **P1**, there is no H-donor competition from the acid-protected copolymer **P4** during the H-bonding complexation process in the nanocomposite **P4-AuSCOOH**. Hence, the excitons of acid-protected copolymer **P4** are more easily trapped by the charge-transfer quenchers of **AuSCOOH** than those of the self-H-bonded copolymer **P1**. As a comparison, the solutions of copolymers **P1** and **P4** were titrated with another nanoparticle counterpart, alkyl-functionalized gold nanoparticles (**AuSC10**, which bears acid-free surfactants). Both PL titrations of copolymers **P1** and **P4** by **AuSC10** nanoparticles (Figure 3.5(c) and 3.5(d)) resulted in similar PL reductions after increasing the concentration of **AuSC10** nanoparticles. However, due to less H-bonding interactions of non-acid-modified **AuSC10** nanoparticles (containing acid-free surfactants) with copolymers **P1** and **P4**, **AuSC10** nanoparticles have much weaker PL quenching effects on **P1** and **P4** than acid-modified **AuSCOOH** nanoparticles (Figure 3.5(a) and 3.5(b), respectively). Comparing the insets of Figure 3.5(a)-(d), the fluorescence quenching curves for copolymers **P1** and **P4** titrated by **AuSCOOH** (Figure 3.5(a)-(b)) are totally different from those titrated by **AuSC10**

(Figure 3.5(c)-(d)). The lower quenching effects observed for PL titrations of **AuSC10** nanoparticles on copolymers **P1** and **P4** are owed to the absence of H-bonding interactions between copolymers (**P1** and **P4**) and the acid-free surfactants on **AuSC10** nanoparticles.

The PL quenching behavior follows the Stern-Volmer relation  $I_0/I = 1 + K_{SV}[Q]$ ,<sup>96</sup> where  $I_0$  and  $I$  are the emission intensities of the fluorescent copolymers (**P1** and **P4**) in the absence and presence of the quencher Q (surface-modified gold nanoparticles), respectively,  $K_{SV}$  is the Stern-Volmer quenching constant, and  $[Q]$  is the concentration of the quencher. Figure 3.6 demonstrates Stern-Volmer plots of copolymers **P1** and **P4** for various concentrations of acid-modified **AuSCOOH** nanoparticles and non-acid-modified **AuSC10** nanoparticles, which are replotted from the insets of Figure 3.5(a)-(d). The quenching constants ( $K_{sv}$ ) of copolymers **P1** and **P4** titrated with different nanoparticle quenchers (**AuSCOOH** and **AuSC10**) in THF solutions are obtained from the slope of Figure 3.6 and listed in Table 3.4. In comparison with the fluorescence quenching effects of **AuSCOOH** nanoparticles on copolymers **P1** and **P4**, the quenching constant ( $K_{sv} = 1.20 \times 10^5 \text{ M}^{-1}$ ) of **P1** is smaller than that ( $K_{sv} = 1.41 \times 10^5 \text{ M}^{-1}$ ) of **P4**. This can be explained by that the partial self-quenching effect of H-bonds in copolymer **P1** (with a lower quantum yield than non-self-H-boded copolymer **P4**) is induced by the higher aggregation of

luminescent H-acceptor moieties in **P1** H-bonded to its own H-donor moieties. Similar to the previous results of copolymers **P1** and **P4** titrated with **AuSCOOH**, as copolymers titrated with **AuSC10** nanoparticles, the quenching constant ( $K_{sv} = 1.32 \times 10^4 \text{ M}^{-1}$ ) of **P1** is slightly smaller than that ( $K_{sv} = 1.57 \times 10^4 \text{ M}^{-1}$ ) of **P4**. Due to reduced supramolecular interactions between **AuSC10** and copolymers **P1** and **P4** in the nanocomposites, both  $K_{sv}$  constants of copolymers **P1** and **P4** ( $1.32$  and  $1.57 \times 10^4 \text{ M}^{-1}$  without H-bonds) blended with non-acid-modified gold nanoparticles (**AuSC10**) are much smaller than those ( $1.20$  and  $1.41 \times 10^5 \text{ M}^{-1}$  with H-bonds) H-bonded with acid-donor-modified gold nanoparticles (**AuSCOOH**). Hence, the H-bonding interactions play an important role in our study of the fluorescence quenching effect. Moreover, it will be more interesting to develop a multicomponent self-assembly process involving fluorescence quenching of pyridyl H-acceptors specifically by both acid H-donors from copolymer **P1** and acid-donor-modified gold nanoparticles (**AuSCOOH**). In general, the significant supramolecular interactions between various surface-modified gold nanoparticles and fluorescent polymers can be distinguished by the distinct fluorescence quenching behavior with specific quenching constants ( $K_{sv}$ ). In order to confirm the fluorescence quenching effects on copolymers **P1** and **P4** by **AuSCOOH**, UV-visible absorption analyses of copolymer nanocomposites, containing **AuSCOOH**, were carried out. We would expect the

UV-visible absorption spectra to change if the aggregation of fluorescent polymers is induced by the addition of **AuSCOOH**. In the UV-visible absorption spectra, the absorption peaks of copolymers **P1** and **P4** (350 and 520 nm in THF solutions) titrated by **AuSCOOH** do not red shift with increasing Au nanoparticle concentrations (from 0 to 121  $\mu\text{M}$ ). These were the same processing conditions used for the quenching titrations of fluorescent polymers **P1** and **P4** by Au nanoparticles. The reasonably low concentrations (smaller than 121  $\mu\text{M}$ ) of **AuSCOOH** were maintained to avoid the aggregation of fluorescent copolymers and **AuSCOOH** nanoparticles. Therefore, the aggregation effects on fluorescence quenching can be ignored. The major source of fluorescence quenching is then attributed to energy transfer between fluorescent copolymers (**P1** and **P4**) and Au nanoparticles (**AuSCOOH**).

**Table 3.4 Stern-Volmer Constants ( $K_{sv}$ ) of Copolymers **P1** and **P4** Titrated with Different Nanoparticle Quenchers (**AuSCOOH** and **AuSC10**) in THF Solutions**

	$K_{sv} (M^{-1})^a$	
	<b>P1</b>	<b>P4</b>
<b>AuSCOOH</b>	$1.20 \times 10^5$	$1.41 \times 10^5$
<b>AuSC10</b>	$1.32 \times 10^4$	$1.57 \times 10^4$

<sup>a</sup> The quenching behavior follows the Stern-Volmer relation  $I_0/I = 1 + K_{SV}[Q]$ , where  $I_0$  and  $I$  are the emission intensities of the fluorescent copolymer (**P1** or **P4**) in the absence and presence of the quencher Q (surface-functionalized gold nanoparticles), correspondingly,  $K_{SV}$  is the Stern-Volmer quenching constant, and  $[Q]$  is the concentration of the quencher.

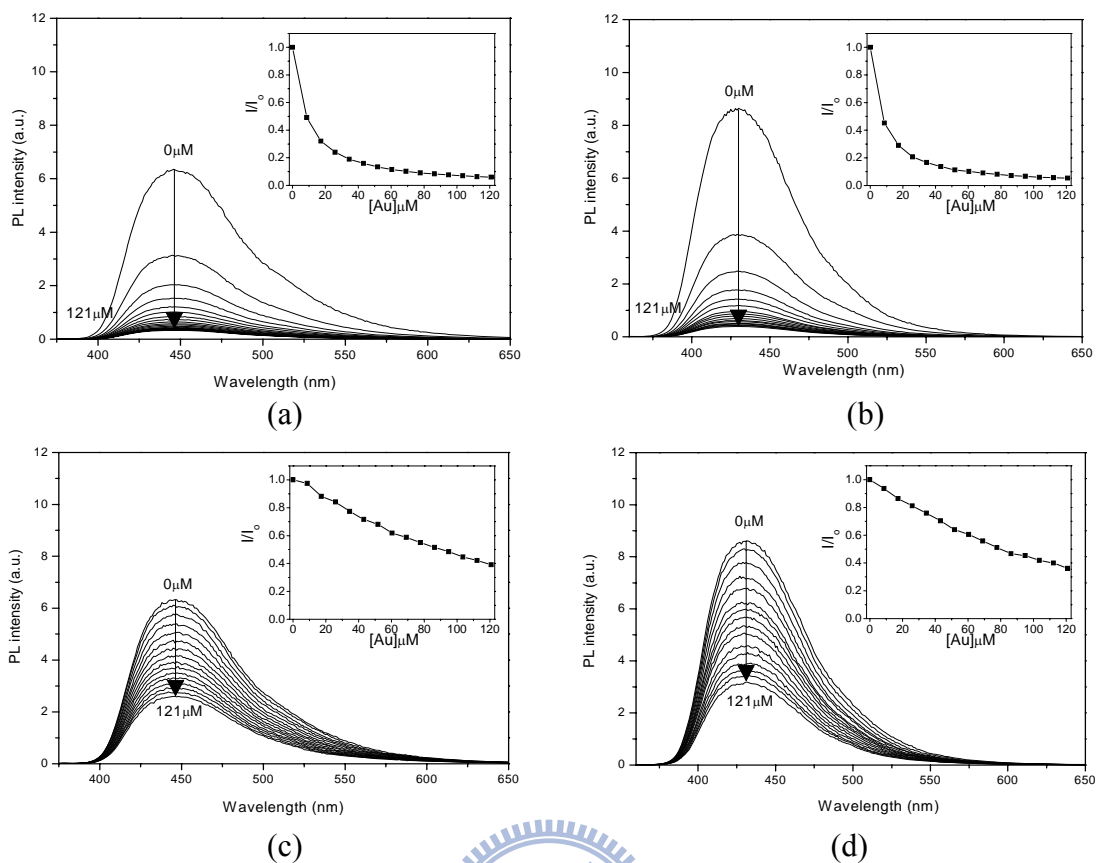


**Figure 3.5** Fluorescence quenching spectra of copolymers **P1** and **P4** titrated by surface-functionalized nanoparticles (**AuSCOOH** and **AuSC10**) in THF solutions: (a) **P1** and (b) **P4** by varying the concentration of acid-donor-modified gold nanoparticles (**AuSCOOH**); (c) **P1** and (d) **P4** by varying the concentration of non-acid-modified gold nanoparticles (**AuSC10**).

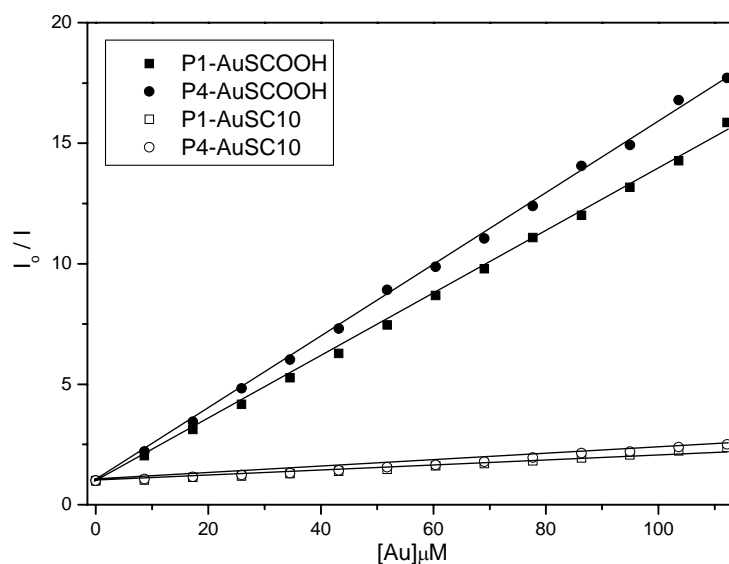


**Figure 3.6** Corresponding Stern-Volmer plots of copolymers **P1** and **P4** for increasing concentrations of acid-modified gold nanoparticles (**AuSCOOH**) and non-acid-modified gold nanoparticles (**AuSC10**) in THF solutions.

### 3.3.6 TEM Analyses

To further confirm the modulation of fluorescence quenching effects on copolymers **P1** and **P4** by acid-donor-modified gold nanoparticles (**AuSCOOH**), transmission electron microscopy (TEM) analysis was carried out on copolymer nanocomposites containing **AuSCOOH** nanoparticles. This provides a further insight into the morphology of the nanoparticle aggregation. Solutions of copolymer nanocomposites, consisting of **P1** and **P4** (2 mg/mL) blended with **AuSCOOH** (0.5 mg/mL) in THF solvent, were drop-cast onto TEM grids. The morphologies of the copolymer nanocomposites into structural ensembles were controlled by the supramolecular self-assembly. Both carboxylic acid units in surface-functionalized gold nanoparticles (**AuSCOOH**) and copolymer **P1** of nanocomposite **P1-AuSCOOH** will compete with each other to form H-bonds with the pyridyl groups in copolymer **P1**. The addition of acid-modified gold nanoparticles (**AuSCOOH**) to copolymers **P1** and **P4** created two distinct aggregate structures. In Figure 3.7(a), **AuSCOOH** nanoparticles (incompletely H-bonded to **P1**) were only partially dispersed in copolymer **P1**. This was due to the self-H-bonded copolymeric structures of the pendent pyridyl H-acceptors self-assembled with its own pendent H-donors in **P1**. Therefore, the layered self-H-bonded copolymeric structures of **P1** were clearly visible in this TEM micrograph. On the other hand, as **AuSCOOH**

nanoparticles were blended with the non-self-H-bonded copolymer **P4**, more carboxylic acid surfactants from **AuSCOOH** nanoparticles were directly H-bonded with the pyridyl H-acceptor groups of the acid-protected copolymer **P4**. **AuSCOOH** nanoparticles were well distributed among copolymer **P4**, as shown in Figure 3.7(b). The self-assembled phenomena of H-bonding between H-donors (from both copolymers and nanoparticles) and polymeric H-acceptors are dependent on all existing carboxylic acid groups (H-donors) available for the supramolecular architectures. Hence, **AuSCOOH** nanoparticles are more homogeneously dispersed in the acid-protected copolymer **P4** and less uniformly dispersed in self-H-bonded copolymer **P1**. Besides, a similar aggregation trend of **AuSCOOH** nanoparticles was observed in the TEM images of nanocomposites containing various isomeric copolymers (self-H-bonded copolymers **P2-P3** and non-self-H-bonded copolymers **P5-P6**). In order to distinguish the contribution from acid and acid-free surfactants on surface-modified nanoparticles (**AuSCOOH** and **AuSC10**, respectively), the self-H-bonded copolymer **P1** was blended with non-acid-modified **AuSC10** nanoparticles (without H-bonds between copolymer **P1** and **AuSC10** nanoparticles). Thus, it is clearly observed in Figure 3.7(c) that non-acid-modified nanoparticles (**AuSC10**) aggregate more extensively. This suggests that no H-bonding interactions occurred between **AuSC10** nanoparticles and copolymer **P1**. Overall, the TEM



morphologies of H-bonded architectures demonstrate the versatility of the self-assembly processes in supramolecular nanocomposites of H-acceptor polymers and H-donor nanoparticles.

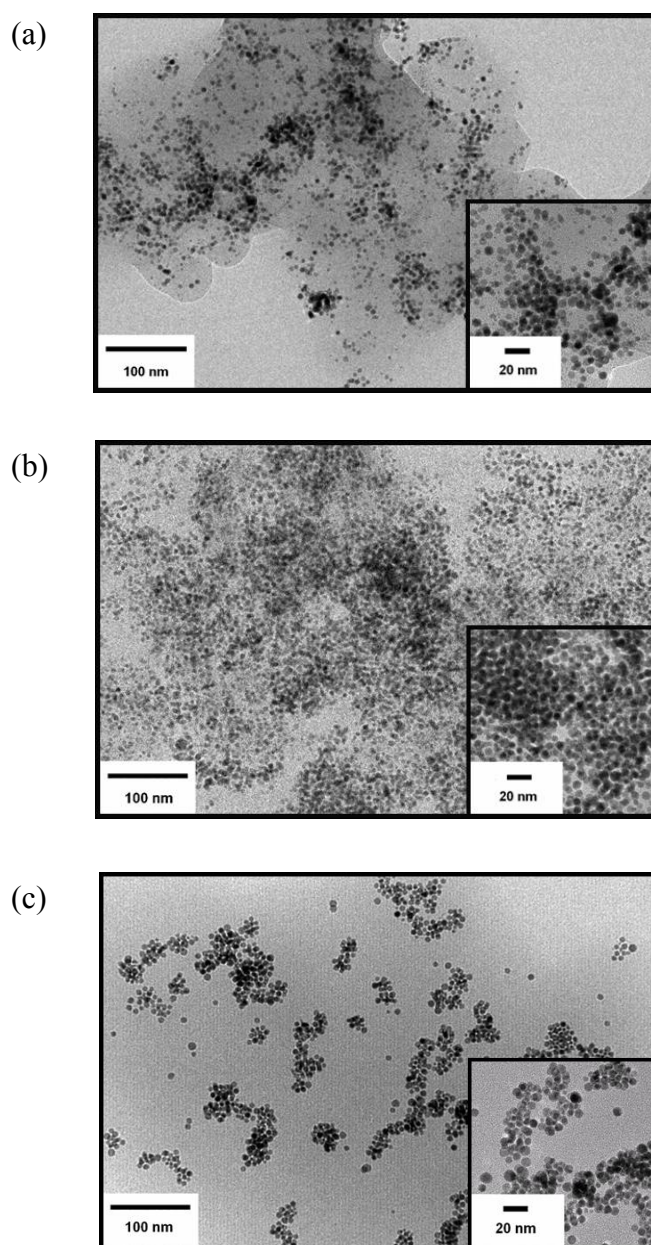


**Figure 3.7** TEM images of acid-functionalized gold nanoparticles (**AuSCOOH**) blended with (a) self-H-bonded copolymer **P1**, (b) acid-protected copolymer **P4**, and (c) alkyl-functionalized gold nanoparticles (**AuSC10**) blended with self-H-bonded copolymer **P1**.

### 3.4 Conclusions

In conclusion, the mesomorphic and photoluminescent properties of H-bonded copolymers and homopolymer complexes are affected by the isomeric H-donors with different acid-substituted (*para*-, *meta*-, and *ortho*-) positions. These H-bonded complexes can generate supramolecular architectures either by self-H-bonded copolymers or by  $\pi$ -conjugated H-acceptor homopolymers blended with H-donor homopolymers. The supramolecular structures have the nematic and smectic C phases that are related to their bent and linear H-bonded structures, respectively. The photoluminescent properties of self-H-bonded copolymers, as well as the H-bonded homopolymer complexes, can be tuned by the isomeric H-donor moieties, and red-shifted PL emissions are expected in the H-bonded structures. Supramolecular architectures that contain H-bonds in self-H-bonded copolymers **P1-P3** and H-bonded homopolymer complexes **PBT1/P7-P9** are further confirmed by FT-IR spectroscopy and XRD measurements. Furthermore, the H-bonding interactions between acid-modified gold nanoparticles (**AuSCOOH**) and acid-protected copolymer **P4** affect the fluorescence quenching more effectively, when compared with fluorescence titrations of acid-free-modified gold nanoparticles (**AuSC10**). Moreover, in contrast to the self-H-bonded copolymer **P1**, the acid-protected copolymer **P4** more readily captures acid-modified gold nanoparticles (**AuSCOOH**) in the supramolecular

assembly of nanocomposites. The H-bonding interactions between the pyridyl H-acceptor (from the copolymers) and the acid H-donor units (from both nanoparticles and copolymers) can explain the similarities in fluorescence quenching effects on both copolymers **P1** and **P4**. Various nanocomposites containing two kinds of fluorescent copolymer counterparts (self-H-bonded copolymer **P1** and acid-protected copolymer **P4**) and surface-modified nanoparticles (acid-modified **AuSCOOH** and acid-free-modified **AuSC10**) were developed to display distinct aggregation phenomena in TEM images. The pyridyl H-acceptor units of copolymer **P1** would not only bind with its own *para*-benzoic acid groups but also with the other proton donor surfactants from **AuSCOOH** nanoparticles. Overall, this study is the first to explore the supramolecular assembly behavior of nanocomposites between fluorescent copolymers and surface-functionalized gold nanoparticles via both PL quenching phenomena and TEM morphologies. Based on the fluorescence quenching and recovery of gold nanocomposites, further chemosensor and biosensor applications of this study can be developed in the near future.

## Chapter 4

# Supramolecular Fluorescence Quenching Effects of H-Donor Surface-Modified Gold Nanoparticles on Fluorescent H-Acceptor Polymers/Copolymers Containing Lateral Methyl- and Methoxy-Substituted Groups

*This approach is exploring hydrogen-bonded (H-bonded) supramolecular assembled behavior via both TEM and fluorescence quenching studies through organic solvent dissolving and evaporating processes. Different lateral methyl- and methoxy-substituted groups with pyridyl terminus of fluorescent side-chain polymers **PBT1-PBOT3**, it performed that the H-bonded interactions affect the fluorescence quenching effectively upon the addition of surface-modified gold nanoparticles bearing acid and acid-free surfactants in the fluorescence titrations experiments. We demonstrated that homopolymer **PBOT1** has the highest  $K_{sv}$  constant in the compared fluorescent side-chain polymers. In addition, we established the exponential equation to predict Stern-Volmer constant in various pyridyl units of polymers from the experimental information. TEM studies displayed that interesting H-bonded supramolecular behavior of addition into the carboxylic acid units of*

*surface-modified gold nanoparticles. It is clearly observed that homogeneously gold nanoparticles distributions are on the fluorescent side-chain polymers. Thus, the TEM morphologies of H-bonded architectures demonstrate the versatility of the self-assembled processes in supramolecular nanocomposites of H-acceptor polymers and surface-modified gold nanoparticles.*

## **4.1 Introduction**

Supramolecular chemistry is a new and exciting branch of chemistry encompassing systems held together by non-covalent bonds, and such complexes have extensive potentials in the rapidly developing fields.<sup>97</sup> More lately, directed self-assembled processes of nano-scaled building blocks using non-covalent interactions (e.g., hydrogen bonding, acid/base proton transfer, and electrostatic forces) have been amplified into macroscopically observable phenomena.<sup>45,54,98</sup> In recent years, there is considerable interest in the fluorescence of conjugated polymers due to their possible applications as highly sensitive chemosensors or biosensors,<sup>32,85</sup> which are based on the different fluorescence quenching capabilities caused by the varying degrees of supramolecular interactions with particular chemical or biological species.<sup>86,99</sup> Poly(*p*-phenylene)s, poly(*p*-phenylene ethynylene)s, poly(*p*-phenylene vinylene)s, polythiophenes, and polyfluorenes with supramolecular receptor groups,

e.g., crown ethers, pyridine derivatives, and ionic groups, in the side-chains or main-chains of the polymers have been successfully used for sensing ions and biological moieties.<sup>87</sup> Design and syntheses of fluorescent side-chain conjugated polymers with supramolecular assembly, which are able to exhibit either chromogenic and/or fluorogenic responses due to non-covalent interactions, have particularly gained broad attentions recently.<sup>88,100</sup>

For fluorescence superquenching by gold nanoparticles, self-assembly of nanoparticles into nanocomposites provides a direct pathway for incorporating the particles' unique physical properties into the functional materials.<sup>33,101</sup> Due to the stability and biocompatibility of gold, gold nanoparticles protected by mixed monolayer provide highly attractive models for biological and fluorescent conjugated polymers.<sup>102</sup> Many high performance methods of fluorescence assays have been developed by taking advantage of this superquenching ability of gold nanoparticles for optically sensing important biological ions and molecules. Gold nanoparticles can be functionalized in order to become soluble in water as well as in organic solvents with readily variable monolayer structures. Rotello and co-workers reported the syntheses and self-assembly of gold nanoparticles with inherent optical properties in the literature.<sup>45,54</sup> Starting with thiol-passivated gold nanoparticles, they used thermal ripening and the Murray place exchange reaction to create nanoparticles featuring

highly monodisperse cores surface-modified with carboxylic acid-functionalized monolayers. Murray and co-workers have investigated the quenching of fluorophores that are attached to monolayer-protected gold nanoparticles, and also the electron transfer from excited fluorophores to gold nanoparticles.<sup>90</sup> Direct binding between a fluorophore and a metal surface often results in the quenching of the fluorophore's excited states.<sup>91</sup> In this scenario, both energy transfer and electron transfer processes are considered to be major deactivation pathways for excited fluorophores on a metal surface. Furthermore, in the presence of other metal ions, such as  $\text{Cu}^{2+}$ ,  $\text{Co}^{2+}$ ,  $\text{Fe}^{3+}$ ,  $\text{Ni}^{2+}$ ,  $\text{Zn}^{2+}$ ,  $\text{Pb}^{2+}$  and  $\text{Ag}^+$ , the gold nanoparticles of the quenched nanocomposites (containing fluorophores) can be replaced with the metal ions to different extents due to the stronger re-coordination or re-complexation of the metal ions with fluorophores, and therefore recover the fluorescence of the chromophores to behave as chemosensors.<sup>58a,b</sup> In addition, the gold nanoparticles of the quenched nanocomposites can also be reacted with the reduced glutathione in the presence of glutathione reductase enzyme, and then recover the fluorescence of the chromophores to behave as biosensors.<sup>58c</sup> The sensor applications of this work can be further developed to detect the metal ions and biomolecules based on the modulation of fluorescence quenching and recovery.

Subsequently, it is more interesting to develop a two-stage self-assembly process

in which the recognition (or sensing) of different surface-functionalized gold nanoparticles (with acid and acid-free surfactants) is proceeded by the light-emitting polymers. Hence, side-chain conjugated polymers bearing fluorescent pyridyl H-acceptor pendants not only behave as highly selective chemosensors for carboxylic acid H-donors, but also exhibit distinct fluorescent quenching effects upon the addition of surface-functionalized gold nanoparticles (i.e., **AuSCOOH** and **AuSC10**, which contain acid and acid-free surfactants, respectively). To our knowledge, this approach is the interesting research of exploring H-bonded supramolecular assembly of nanocomposites via fluorescence quenching and TEM morphological analyses, where the hydrogen bonds were generated from the carboxylic acid units (as proton donors) of the surface-functionalized gold nanoparticles and the pyridyl groups (as proton acceptors) of lateral methyl-substituted groups polymers **PBT1-PBT3** and methoxy-substituted groups polymers **PBTO1-PBOT3** in the Figure 4.1 via organic dissolving and evaporating processes.



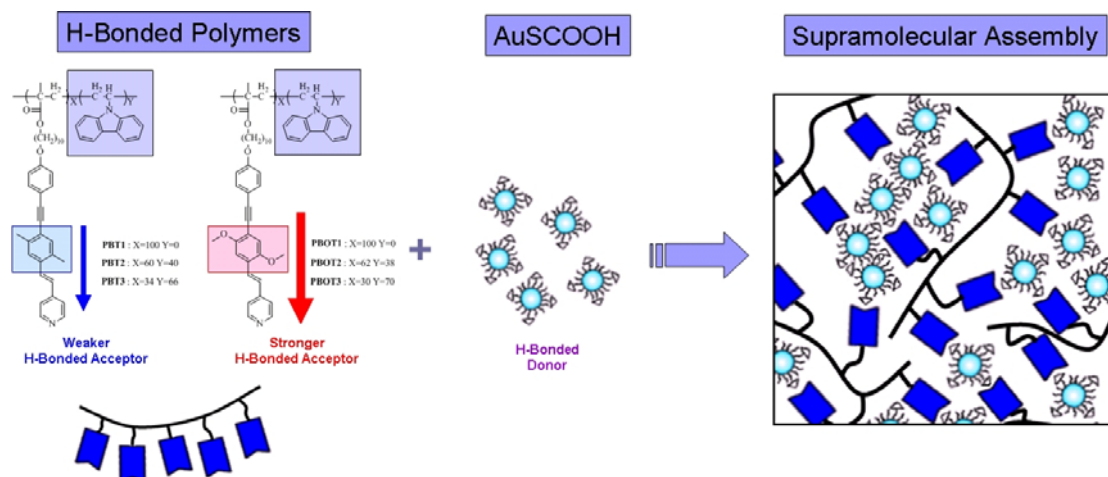


**Figure 4.1** Schematic illustration of two series of different lateral methyl- and methoxy-substituted groups of H-bonded polymers blended with **AuSCOOH**.

## 4.2 Experimental Section

### 4.2.1 Materials

Chemicals and solvents were reagent grades and purchased from Aldrich, ACROS, TCI, and Lancaster Chemical Co. Dichloromethane and THF were distilled to keep anhydrous before use. The other chemicals were used without further purification. The synthetic routes of proton acceptor polymers **PBT** and **PBOT** (as shown in Figure 4.2) were reported in Chapter 2.<sup>92</sup> The chemical structures for all products were confirmed by <sup>1</sup>H NMR spectroscopy and elemental analyses.

### 4.2.2 Synthesis of Surface-Functionalized Gold Nanoparticles

#### **AuSC10 and AuSCOOH**

The surface-functionalized gold nanoparticles (**AuSC10** bearing acid-free surfactants) used in this study were prepared through standard Brust-Schiffrin methodology.<sup>103</sup> Hydrogen tetrachloroaurate aqueous solution (30 mL, 30 mmol) was

mixed with tetraoctylammonium bromide (TOAB) in toluene solution (80 mL, 50 mmol). The two-phase mixture was vigorously stirred until all tetrachloroaurate was transferred into the organic layer, and then dodecanethiol (20  $\mu$ L) was added to the organic phase. A freshly prepared aqueous solution of sodium borohydride (25 mL, 0.4 mol) was slowly added with vigorous stirring. After further stirring for 3 h, the organic phase was separated, and the standard Brust reaction mixture was evaporated without removing TOAB and dried completely under reduced pressure. The black solid obtained was heat-treated at 165°C at a heating rate of 2°C/min and held at this temperature for 30 min.<sup>104</sup> The thermally 'ripened' product was dissolved in toluene and washed with methanol to remove excess thiol ligands and TOAB, then **AuSC10** nanoparticles with alkyl surfactants were obtained. In the subsequent Murray place exchange reaction,<sup>105</sup> **AuSC10** nanoparticles (60 mg) were combined with the proper amount of 11-mercaptoundecanoic acid in dichloromethane (3 mg of **AuSC10**/mL) and reacted for 48 h. After the exchange reaction was completed, the reaction mixture was concentrated using a rotary evaporator. After washing these products with a large amount of ethanol and acetone, no further purifications were conducted on these samples. Then, the acid-functionalized gold nanoparticles (**AuSCOOH**) with a diameter ca. 5 ~ 6 nm were obtained, and the monolayer compositions of **AuSCOOH** nanoparticles with both acid and alkyl surfactants were characterized by <sup>1</sup>H NMR

featured 79% decanethiol and 21% carboxylic acid thiol functionalities.<sup>106</sup> In our studies of nanocomposites, both THF-soluble gold nanoparticles, i.e., alkyl-functionalized gold nanoparticles (**AuSC10** bearing acid-free surfactants) and acid-functionalized gold nanoparticles (**AuSCOOH** bearing acid surfactants), were used.

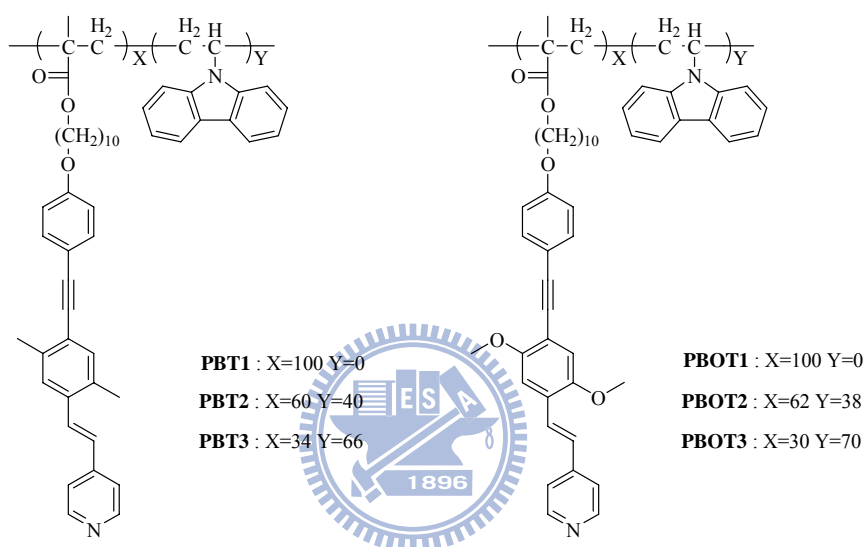


**Figure 4.2** Molecular structures of different lateral methyl- and methoxy-substituted groups of fluorescent side-chain polymers **PBT1-PBT3** and **PBOT1-PBOT3**.

### 4.2.3 Preparation of Nanocomposites Consisting of Gold Nanoparticles and Polymers

The surface-functionalized gold nanoparticles, **AuSCOOH** and **AuSC10**, which contain acid and acid-free surfactants, respectively. Nanocomposites were prepared by mixing solutions (0.5 mg/ml) of surface-functionalized gold nanoparticles **AuSCOOH** and **AuSC10** in THF. This was then mixed with solutions of two series of H-acceptor polymers **PBT1-PBT3** and **PBOT1-PBOT3** in THF (2 mg/ml). The

gold nanoparticles began to assemble into nanocomposites within 2 min. The mixed solutions became visibly turbid, indicating that an aggregation process had occurred. After 24 h, the solid precipitates were collected and washed extensively with hexane. The nanocomposites were then dried overnight before being subjected to Transmission Electron Microscopy (TEM) measurements.

#### **4.2.4 Measurements and Characterization**

<sup>1</sup>H NMR spectra were recorded on a Varian unity 300M Hz spectrometer using CDCl<sub>3</sub> and DMSO-d<sub>6</sub> as solvents. UV-visible absorption spectra were recorded in dilute THF solutions (10<sup>-6</sup> M) on a HP G1103A spectrophotometer, and photoluminescence (PL) spectra were obtained on a Hitachi F-4500 spectrophotometer. Fourier transform infrared (FT-IR) spectra were performed on a Nicolet 360 FT-IR spectrometer. Transmission Electron Microscopy (TEM) analyses were performed using a JEOL 2011 electron microscope with an acceleration voltage of 200 keV. The samples were prepared from THF solutions with a concentration of 1 wt%, and the aggregates were precipitated on TEM sample grids (200 Cu mesh/carbon films).

### **4.3 Results and Discussion**

#### **4.3.1 FT-IR Spectroscopic Studies**

The formation of hydrogen bonding in two series supramolecular side-chain

polymers **PBT1-PBT3** and **PBOT1-PBOT3** containing acid-modified gold nanoparticles **AuSCOOH** was confirmed by FT-IR spectroscopy. As shown in Figure 4.3, IR spectra of **PBOT1**, **AuSCOOH**, and H-bonded nanocomposite **PBOT1/AuSCOOH** are compared to analyze the hydrogen bonds. In contrast to acid-modified gold nanoparticles **AuSCOOH**, the weaker O-H band observed at 2525 and 1920  $\text{cm}^{-1}$  in H-bonded nanocomposite **PBOT1/AuSCOOH** is indicative of hydrogen bonding between the pyridyl group of **PBOT1** and acid-modified gold nanoparticles **AuSCOOH** in the H-bonded nanocomposite. On the other hand, a C=O stretching vibration appeared at 1695  $\text{cm}^{-1}$  in H-bonded nanocomposite **PBOT1/AuSCOOH**, which shows that the carbonyl group was in a less associated state than that in acid-modified gold nanoparticles **AuSCOOH** with a weaker C=O stretching vibration appeared at 1660  $\text{cm}^{-1}$ . Both results suggest that hydrogen bonds were formed between H-acceptor **PBOT1** and H-donor **AuSCOOH** in the solid state H-bonded nanocomposite **PBOT1/AuSCOOH**. Some other supramolecular polymers also have the similar consequences of H-bonding formation as the H-bonded polymer complex demonstrated here.<sup>17</sup>

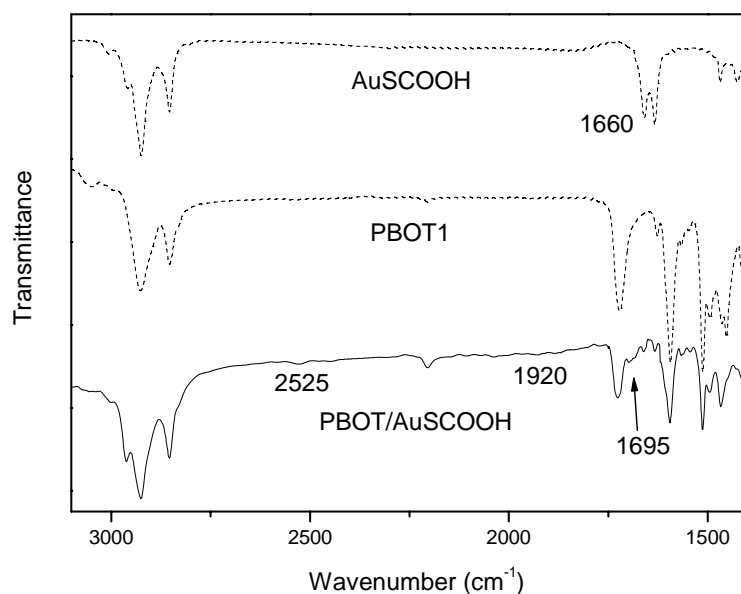


**Figure 4.3** Infrared spectra for **AuSCOOH**, **PBOT1**, and H-bonded nanocomposite **PBOT1/AuSCOOH** at room temperature.

### 4.3.2 Fluorescence Quenching Effects of Copolymers by Surface-Modified Gold Nanoparticles

In the fluorescence quenching studies, where acid-donor-modified **AuSCOOH** nanoparticles and non-acid-modified **AuSC10** nanoparticles (diameter ca. 5 ~ 6 nm) were doped, the photoluminescence (PL) spectra of two polymers **PBOT1** and **PBT1** were monitored in the presence of different concentrations of surface-modified gold nanoparticles (Figure 4.4). In Chapter 2, the fluorescence spectra of polymer **PBT1** emitted blue light at 440 nm in THF solutions. In comparison with luminescent polymer **PBT1**, polymer **PBOT1** was more red-shifted PL emissions at 440 nm due to the stronger electron donating effect of lateral methoxyl groups, which induce smaller

energy band gaps in chromophores. In Figure 4.4(a) and 4.4(b), H-acceptor polymers **PBOT1** and **PBT1** demonstrated dramatic decreases in fluorescence intensities upon the addition of **AuSCOOH** nanoparticles (which contain 21% carboxylic acid surfactants). Upon the addition of **AuSCOOH**, progressive fluorescence quenching effects on polymers **PBOT1** and **PBT1** (blended with **AuSCOOH**) were observed by increasing the concentration of **AuSCOOH**. It is conceivable that the polymer nanocomposites **PBOT1-PBT1/AuSCOOH** reduced the fluorescence emission intensities by H-bonding complexation of the fluorescent pyridyl units with the acid surfactant on **AuSCOOH**. In Figure 4.4(a), the polymer **PBOT1** was easily H-bonded with the acid H-donor surfactants on **AuSCOOH** nanoparticles due to the stronger electron donating effect of lateral methoxyl groups, which induce higher affinity on **AuSCOOH**. However, as shown in Figure 4.4(b), the titration of methyl-substituted polymer **PBT1** by **AuSCOOH** nanoparticles displays a similar PL quenching trend as Figure 4.4(a). This suggests that the complexation of methyl-substituted polymer **PBT1** and **AuSCOOH** nanoparticles has a similar H-bonding interaction as that in the nanocomposite **PBOT1-AuSCOOH**. Unlike the methoxyl-substituted polymer **PBOT1**, weaker electron donating effect of lateral methyl groups from the methyl-substituted polymer **PBT1** during the H-bonding complexation process in the nanocomposite **PBT1-AuSCOOH**. Hence, the excitons of methoxyl-substituted

polymer **PBOT1** are more easily trapped by the charge-transfer quenchers of **AuSCOOH** than those of the methyl-substituted polymer **PBT1**. As a comparison, the solutions of polymers **PBOT1** and **PBT1** were titrated with another nanoparticle counterpart, alkyl-functionalized gold nanoparticles (**AuSC10**, which bears acid-free surfactants). PL titrations of polymers **PBOT1** and **PBT1** by **AuSC10** nanoparticles (Figure 4.4(c) and 4.4(d)) resulted in similar PL reductions after increasing the concentration of **AuSC10** nanoparticles. However, due to less H-bonding interactions of non-acid-modified **AuSC10** nanoparticles (containing acid-free surfactants) with polymers **PBOT1** and **PBT1**, **AuSC10** nanoparticles have much weaker PL quenching effects on **PBOT1** and **PBT1** than acid-modified **AuSCOOH** nanoparticles (Figure 4.4(a) and 4.4(b), respectively). Comparing the insets of Figure 4.4(a)-(d), the fluorescence quenching curves for polymers **PBOT1** and **PBT1** titrated by **AuSCOOH** (Figure 4.4(a)-(b)) are totally different from those titrated by **AuSC10** (Figure 4.4(c)-(d)). The lower quenching effects observed for PL titrations of **AuSC10** nanoparticles on polymers **PBOT1** and **PBT1** are owed to the absence of H-bonding interactions between polymers (**PBOT1** and **PBT1**) and the acid-free surfactants on **AuSC10** nanoparticles. In addition, the similar fluorescence quenching curve of **AuSCOOH** nanoparticles were observed in the PL spectra of nanocomposites containing various the content of pyridyl groups in the copolymers



### **PBOT2-PBOT3 and PBT2-PBT3.**

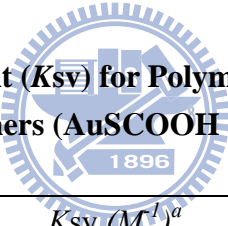
The PL quenching behavior follows the Stern-Volmer relation  $I_0/I = 1 + K_{SV}[Q]$ ,<sup>96</sup> where  $I_0$  and  $I$  are the emission intensities of the fluorescent polymers (**PBOT1-PBT3**) in the absence and presence of the quencher Q (surface-modified gold nanoparticles), respectively,  $K_{SV}$  is the Stern-Volmer quenching constant, and  $[Q]$  is the concentration of the quencher. Figure 4.5 demonstrates Stern-Volmer plots of polymers **PBOT1-PBT3** for various concentrations of acid-modified **AuSCOOH** nanoparticles and non-acid-modified **AuSC10** nanoparticles, which are replotted from the insets of Figure 4.4(a)-(d). The quenching constants ( $K_{sv}$ ) of polymers **PBOT1** and **PBT1** titrated with different nanoparticle quenchers (**AuSCOOH** and **AuSC10**) in THF solutions are obtained from the slope of Figure 4.5 and listed in Table 4.1. In comparison with the fluorescence quenching effects of **AuSCOOH** nanoparticles on polymers **PBOT1** and **PBT1**, the quenching constant ( $K_{sv} = 2.50 \times 10^5 \text{ M}^{-1}$ ) of **PBT1** is smaller than that ( $K_{sv} = 3.31 \times 10^5 \text{ M}^{-1}$ ) of **PBOT1**. This can be explained by that the stronger electron donating effect of lateral methoxyl groups in polymer **PBOT1** which induce higher affinity to complex with **AuSCOOH**. However, different to the previous results of polymers **PBOT1** and **PBT1** titrated with **AuSCOOH**, as polymers titrated with **AuSC10** nanoparticles, the quenching constant ( $K_{sv} = 2.15 \times 10^4 \text{ M}^{-1}$ ) of **PBOT1** is slightly smaller than that ( $K_{sv} = 2.30 \times 10^4 \text{ M}^{-1}$ )

of **PBT1**. It is elucidated that the lateral methoxyl groups in polymer **PBOT1** will connect with **AuSC10** and competed with the pyridyl terminus of polymer **PBOT1**. Due to reduced supramolecular interactions between **AuSC10** and polymers **PBOT1** and **PBT1** in the nanocomposites, both  $K_{sv}$  constants of polymers **PBOT1** and **PBT1** ( $2.15$  and  $2.30 \times 10^4 \text{ M}^{-1}$  without H-bonds) blended with non-acid-modified gold nanoparticles (**AuSC10**) are much smaller than those ( $2.50$  and  $3.31 \times 10^5 \text{ M}^{-1}$  with H-bonds) H-bonded with acid-donor-modified gold nanoparticles (**AuSCOOH**). Hence, the H-bonding interactions play an important role in our study of the fluorescence quenching effect. Moreover, it will be more interesting to develop a multicomponent self-assembly process involving fluorescence quenching of pyridyl H-acceptors from polymers **PBOT1**, **PBT1** and acid-donor-modified gold nanoparticles (**AuSCOOH**). In general, the significant supramolecular interactions between various surface-modified gold nanoparticles and fluorescent polymers can be distinguished by the distinct fluorescence quenching behavior with specific quenching constants ( $K_{sv}$ ). In addition, interestingly, we observe that the decreased of pyridyl unit of polymers, Stern-Volmer constants will be decreased exponentially from the experimental information. We demonstrate to follow the relationship between the Stern-Volmer constant ( $K_{sv}$ ) and the pyridyl units of polymers. Figure 4.6 gives the plot of Stern-Volmer constant vs pyridyl units of polymers, as suggested by the  $K_{sv} =$

$A(1-e^{-BX})$  equation, where A and B are the constants of the experimental equation.  $K_{SV}$  is the Stern-Volmer quenching constant, and X is the percentage of the pyridyl units of polymers. Consequently, it will be easy to predict Stern-Volmer constant in various pyridyl units of polymers from the experimental equation. Due to much smaller  $K_{sv}$  constants of non-acid-modified gold nanoparticles (**AuSC10**) in polymers without supramolecular interactions, both  $K_{sv}$  constants of polymers **PBOT** and **PBT** blended with **AuSC10**, i.e., **AuCS10-PBOT** and **AuCS10-PBT**, are replotted in the inset of Figure 4.6. In order to confirm the fluorescence quenching effects on polymer **PBOT1** by **AuSCOOH**, UV-visible absorption analyses of polymer nanocomposites, containing **AuSCOOH**, were carried out. We would expect the UV-visible absorption spectra to change if the aggregation of fluorescent polymers is induced by the addition of **AuSCOOH**. In the UV-visible absorption spectra (Figure 4.7(a)), the absorption peaks of polymer **PBOT1** (384 and 520 nm in THF solutions) titrated by **AuSCOOH** do not red shift with increasing Au nanoparticle concentrations (from 0 to 121  $\mu\text{M}$ ). These were the same processing conditions used for the quenching titrations of fluorescent polymer **PBOT1** by Au nanoparticles. The reasonably low concentrations (smaller than 121  $\mu\text{M}$ ) of **AuSCOOH** were maintained to avoid the aggregation of fluorescent copolymers and **AuSCOOH** nanoparticles. Therefore, the aggregation effects on fluorescence quenching can be ignored. The major source of fluorescence

quenching is then attributed to energy transfer between fluorescent polymer (**PBOT1**) and Au nanoparticles (**AuSCOOH**). Similarly, as shown in Figure 4.7(b), the absorption peaks of polymer **PBT1** (350 and 520 nm in THF solutions) titrated by **AuSC10** do not red shift with increasing Au nanoparticle concentrations (from 0 to 121  $\mu\text{M}$ ). These were the same processing conditions used for the quenching titrations of fluorescent polymer **PBT1** by non-acid-modified **AuSC10** nanoparticles. Additionally, the similar UV-visible absorption analyses of polymer nanocomposites, containing **AuSCOOH** and **AuSC10**, were observed.

**Table 4.1 Stern-Volmer Constant ( $K_{sv}$ ) for Polymers PBT1-PBOT3 Titrated with Different Nanoparticle Quenchers (**AuSCOOH** and **AuSC10**) in THF Solutions**



	$K_{sv} (M^{-1})^a$					
	<b>PBT1</b>	<b>PBT2</b>	<b>PBT3</b>	<b>PBOT1</b>	<b>PBOT2</b>	<b>PBOT3</b>
<b>AuSCOOH</b>	$2.50 \times 10^5$	$2.17 \times 10^5$	$1.70 \times 10^5$	$3.31 \times 10^5$	$2.67 \times 10^5$	$2.19 \times 10^5$
<b>AuSC10</b>	$2.30 \times 10^4$	$1.96 \times 10^4$	$1.66 \times 10^4$	$2.15 \times 10^4$	$1.82 \times 10^4$	$1.51 \times 10^4$

<sup>a</sup> The quenching behavior follows the Stern-Volmer relation  $I_0/I = 1 + K_{SV}[Q]$ , where  $I_0$  and  $I$  are the emission intensities of the fluorescent polymer (**PBT1-PBOT3**) in the absence and presence of the quencher Q (surface-functionalized gold nanoparticles), respectively,  $K_{SV}$  is the Stern-Volmer quenching constant, and  $[Q]$  is the concentration of the quencher.

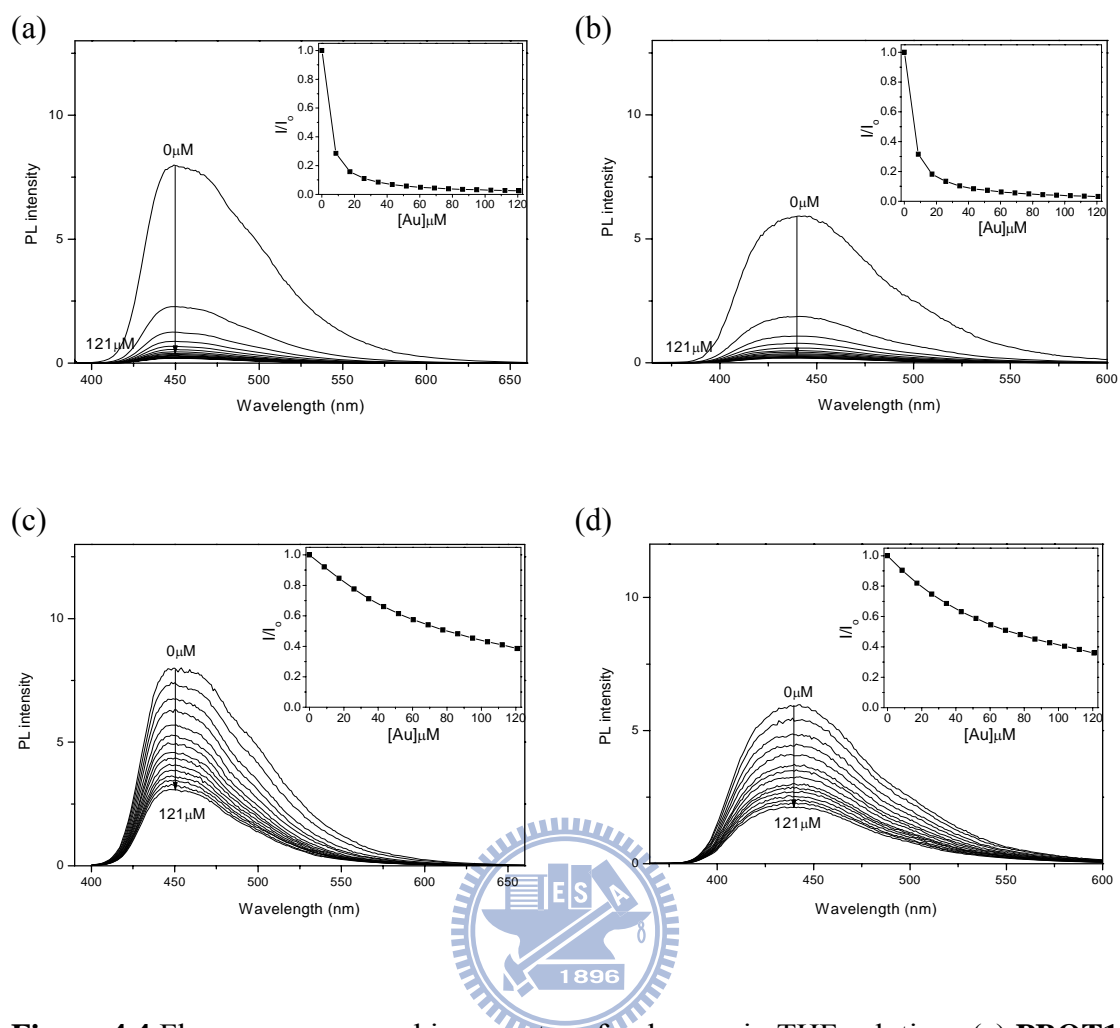


**Figure 4.4** Fluorescence quenching spectra of polymers in THF solutions (a) **PBOT1** and (b) **PBT1** by varying the concentration of acid-donor-modified gold nanoparticles **AuSCOOH** (c) **PBOT1** and (d) **PBT1** by varying the concentration of non-acid-modified gold nanoparticles **AuSC10**.

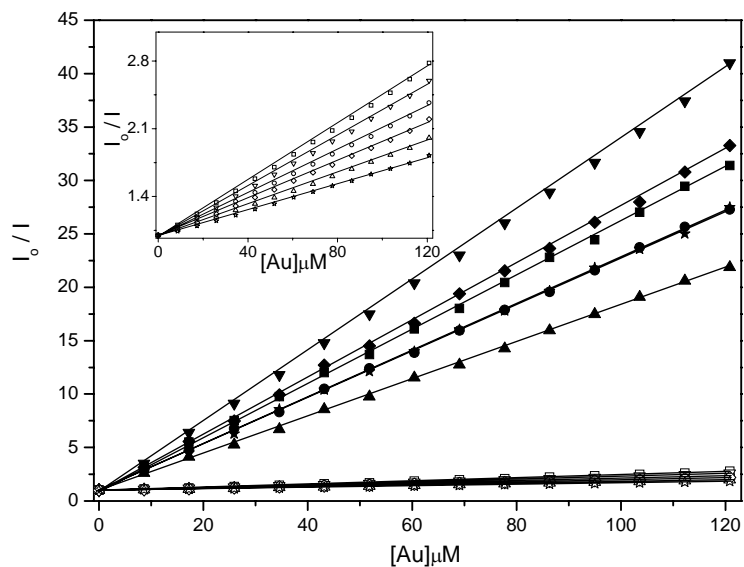


**Figure 4.5** Corresponding Stern-Volmer plots of polymers **PBT1** (■), **PBT2** (●), **PBT3** (▲), **PBOT1** (▼), **PBOT2** (◆), and **PBOT3** (★) by increasing the concentration of acid-modified gold nanoparticles **AuSCOOH** and polymers **PBT1** (□), **PBT2** (○), **PBT3** (△), **PBOT1** (▽), **PBOT2** (◇), and **PBOT3** (☆) by increasing the concentration of non-acid-modified gold nanoparticles **AuSC10** in THF solutions, where polymers **PBT1-PBOT1** by increasing the concentration of non-acid-modified gold nanoparticles **AuSC10** are replotted from inset of Figure.

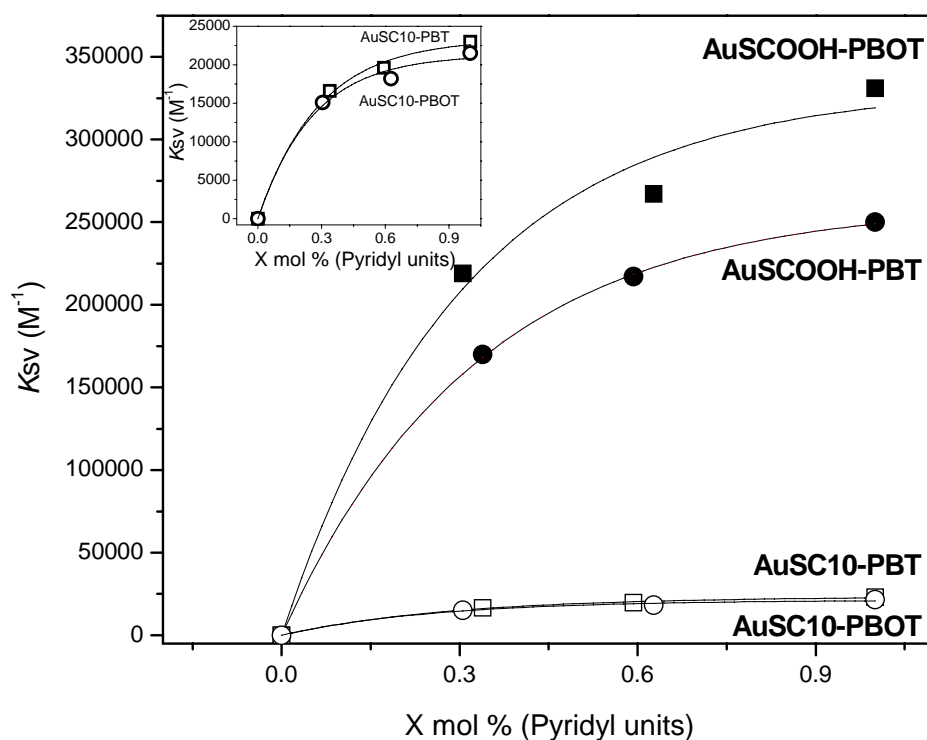
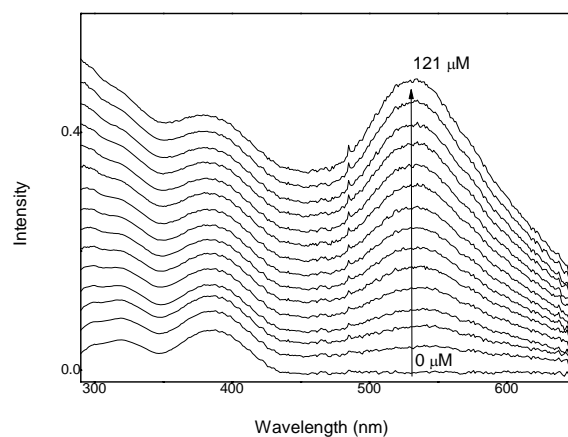
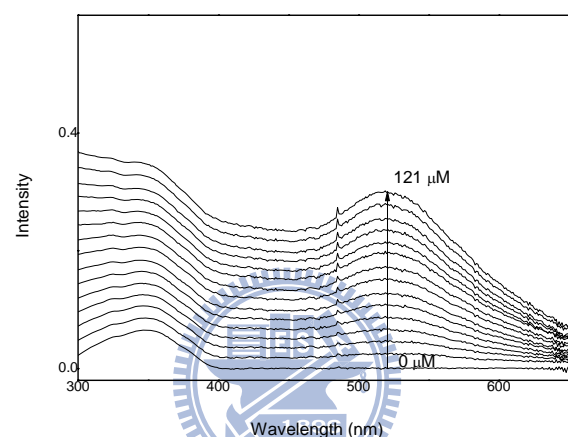


**Figure 4.6** Schematic curves showing the dependence of Stern-Volmer constant ( $K_{sv}$ ) on pyridyl units' X mol% of polymers, which follow the experimental equation of  $K_{sv} = A[1 - \exp(-BX)]$ , where A and B are constants for the exponential curve fittings.



(a)



(b)

**Figure 4.7** UV-visible spectra of polymers (a) **PBOT1** titrated by varying the concentration of acid-donor-modified gold nanoparticles (**AuSCOOH**) and (b) **PBT1** by varying the concentration of non-acid-modified gold nanoparticles (**AuSC10**) in THF solutions.

### 4.3.3 TEM Analyses

To further confirm the modulation of fluorescence quenching effects on two series of polymers **PBTO1** and **PBT1** by acid-donor-modified gold nanoparticles (**AuSCOOH**), transmission electron microscopy (TEM) analysis was carried out on polymer nanocomposites containing **AuSCOOH** nanoparticles. This provides a further insight into the morphology of the nanoparticle aggregation. The



acid-functionalized gold nanoparticles (**AuSCOOH**) with a diameter ca. 5 ~ 6 nm were observed in the Figure 4.8(a). Solutions of polymer nanocomposites, consisting of **PBTO1** and **PBT1** (2 mg/mL) blended with **AuSCOOH** (0.5 mg/mL) in THF solvent, were drop-cast onto TEM grids. The morphologies of the polymer nanocomposites into structural ensembles were controlled by the supramolecular self-assembly. Regarding H-bonded interactions in the polymers, carboxylic acid units in surface-functionalized gold nanoparticles will be connected with pyridyl groups in the polymers to form H-bonds. The addition of acid-donor-modified gold nanoparticles **AuSCOOH** to polymers **PBTO1** and **PBT1** resulted into the formation of extended aggregates. In the case of polymer composites **PBTO1/AuSCOOH** and **PBT1/AuSCOOH**, the morphology of **AuSCOOH** and polymers were strongly dependent on the H-bonded situations of polymers. In Figure 4.8(b) and 4.8(c), the gold nanoparticles **AuSCOOH** were homogeneously dispersed in polymers **PBTO1** and **PBT1** because the H-accepted pyridyl groups in H-bonded structures of polymers in this TEM figure. The self-assembled phenomena of H-bonding between H-donors (from both polymers and nanoparticles) and polymeric H-acceptors are dependent on all existing carboxylic acid groups (H-donors) available for the supramolecular architectures. Hence, **AuSCOOH** nanoparticles are still homogeneously dispersed in the various pyridyl content copolymers. Besides, the similar aggregation trends of

**AuSCOOH** nanoparticles were observed in the TEM images of nanocomposites containing various the content of pyridyl groups in the copolymers **PBOT2-PBOT3** and **PBT2-PBT3**. The gold nanoparticles **AuSCOOH** were only partially dispersed in copolymers **PBOT2-PBOT3** and **PBT2-PBT3** due to the less accepted pyridyl groups in H-bonded structures of copolymers, where the layered **CAZ** structures of copolymers itself were clearly evidenced in this TEM figure. In order to distinguish the contribution from acid and acid-free surfactants on surface-modified nanoparticles (**AuSCOOH** and **AuSC10**, respectively), the polymer **PBT1** was blended with non-acid-modified **AuSC10** nanoparticles (without H-bonds between polymer **PBT1** and **AuSC10** nanoparticles). Thus, it is clearly observed in Figure 4.8(d) that non-acid-modified nanoparticles (**AuSC10**) self-aggregated more extensively. This suggests that no H-bonding interactions occurred between **AuSC10** nanoparticles and polymer **PBT1**. Overall, the TEM morphologies of H-bonded architectures demonstrate the versatility of the self-assembly processes in supramolecular nanocomposites of H-acceptor polymers and H-donor nanoparticles.

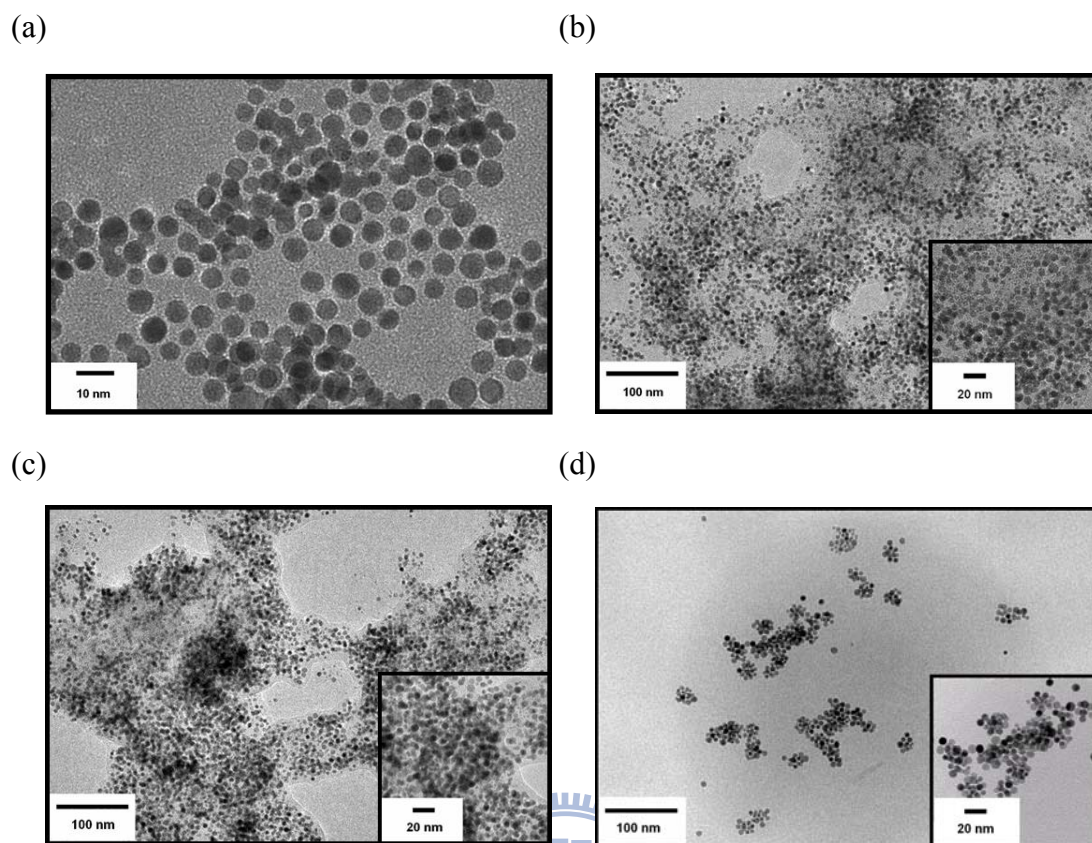


**Figure 4.8** TEM images of (a) acid-modified gold nanoparticles **AuSCOOH** and blended with polymers (b) **PBOT1**, (c) **PBT1**, and (d) alkyl-functionalized gold nanoparticles (**AuSC10**) blended with polymer **PBT1**.

## 4.4 Conclusions

In summary, supramolecular nanocomposites containing two series fluorescent polymers with different pyridyl content, lateral methyl-substituted polymers **PBT1-PBT3** and lateral methoxyl-substituted polymers **PBOT1-PBOT3**, and donor nanoparticles were developed to display distinct aggregation phenomena in TEM images. H-acceptor polymers **PBT1-PBOT3** would not only display highly aggregation but also well dispersion with the proton donor surfactants from nanoparticles **AuSCOOH**. Furthermore, the H-bonding interactions between

acid-modified gold nanoparticles (**AuSCOOH**) and lateral methoxyl-substituted polymer **PBOT1** affect the fluorescence quenching more effectively, when compared with fluorescence titrations of acid-free-modified gold nanoparticles (**AuSC10**). Moreover, in contrast to the lateral methyl-substituted polymer **PBT1**, lateral methoxyl-substituted polymer **PBOT1** more readily captures acid-modified gold nanoparticles (**AuSCOOH**) in the supramolecular assembly of nanocomposites. The H-bonding interactions between the pyridyl H-acceptor (from the polymers) and the acid H-donor units (from both nanoparticles and polymers) can explain the similarities in fluorescence quenching effects on both polymers **PBOT1** and **PBT1**. Moreover, we established the exponential equation to predict Stern-Volmer constant in various pyridyl units of polymers according to these experimental information. Various nanocomposites containing two kinds of fluorescent polymer counterparts (methoxyl-substituted polymer **PBOT1** and methyl-substituted polymer **PBT1**) and surface-modified nanoparticles (acid-modified **AuSCOOH** and acid-free-modified **AuSC10**) were developed to display distinct aggregation phenomena in TEM images. Based on the fluorescence quenching and recovery of gold nanocomposites, further chemosensor and biosensor applications of this study can be developed in the near future.

## Chapter 5

# Supramolecular Assembly of H-Bonded Side-Chain Polymers Containing Conjugated Pyridyl H-Acceptor Pendants and Various Low-Band-Gap H-Donor Dyes Bearing Cyanoacrylic Acid Groups for Organic Solar Cell Applications

*Novel supramolecular side-chain polymers were constructed by complexation of proton acceptor (H-acceptor) polymers, i.e., side-chain conjugated polymers **P1-P2** containing pyridyl pendants, with low-band-gap proton donor (H-donor) dyes **S1-S4** (bearing terminal cyanoacrylic acids) in a proper molar ratio. Besides unique mesomorphic properties confirmed by DSC and XRD results, the H-bonds of supramolecular side-chain structures formed by pyridyl H-acceptors and cyanoacrylic acid H-donors were also confirmed by FTIR measurements. H-donor dyes **S1-S4** in solid films exhibited broad absorption peaks located in the range of 471-490 nm with optical band-gaps of 1.99-2.14 eV. Furthermore, H-bonded polymer complexes **P1/S1-P1/S4** and **P2/S1-P2/S4** exhibited broad absorption peaks in the range of 440-462 nm with optical band-gaps of 2.11-2.25 eV. Under 100 mW/cm<sup>2</sup> of AM 1.5 white-light illumination, the bulk heterojunction polymer solar cell (PSC)*

devices containing an active layer of H-bonded polymer complexes **P1/S1-P1/S4** and **P2/S1-P2/S4** (as electron donors) mixed with [6,6]-phenyl C<sub>61</sub> butyric acid methyl ester (i.e., PCBM, as an electron acceptor) in the weight ratio of 1:1 were investigated. The PSC device containing H-bonded polymer complex **P1/S3** mixed with PCBM (1:1 w/w) gave the best preliminary result with an overall power conversion efficiency (PCE) of 0.50%, a short-circuit current of 3.17 mA/cm<sup>2</sup>, an open-circuit voltage of 0.47 V, and a fill factor of 34%.

## 5.1 Introduction

Self-assembled phenomena through molecular recognition between complementary constituents have been explored in various areas, such as the applications of biomaterials, liquid crystalline (LC) materials, and electro-optical materials.<sup>65,66,68,83,107</sup> Not only innovative LC properties of novel supramolecules consisting of two counterparts can be generated through intermolecular hetero-hydrogen-bonding interactions, but also particular self-assembly of nano-scaled building blocks using non-covalent interactions (e.g. hydrogen bonding, acid/base proton transfer, and electrostatic forces) may be amplified into macroscopically observable phenomena.<sup>50b,84</sup> More recently, direct energy harvesting from sunlight by using photovoltaic cells (PVCs) has increasingly attracted intensified

attention to utilize renewable energy of the nature, especially for the development of organic solar cells.<sup>108</sup> Compared with inorganics (such as Si), organic materials (especially polymers) have the benefits to be easily made into devices with light weight, large area, and flexible panels, so different concepts of solar cell architectures have been developed by organics, including blends of polymers<sup>109-112</sup> and block copolymers<sup>113</sup> with [6,6]-phenyl C<sub>61</sub> butyric acid methyl ester (i.e., PCBM, as an electron acceptor). Among the organic solar cell materials investigated so far, semi-conducting conjugated polymers with electron donor-acceptor architectures are one of the most effective ways to build intramolecular charge transfer (ICT) interaction between the electron donor (D) and electron acceptor (A) segments.<sup>114-116</sup> Conjugated D-A copolymers with strong ICT effects are promising materials for the development of high performance polymer-based PVCs due to the merits of narrow band-gaps,<sup>115</sup> broad absorption bands extending into the near-infrared spectral range, efficient photoinduced charge transfer and separation, pronounced charge photogeneration and collection, and high mobility of ambipolar charge transport.<sup>116</sup> Furthermore, different concepts of solar cell architectures, including the dye blends containing inorganics (PCBM, TiO<sub>2</sub>, and ZnO as electron acceptors) and/or polymers,<sup>117</sup> have been successfully progressed the efficiencies of the bulk heterojunction polymer solar cell (PSC) devices. However, due to the aggregations of

the dyes originated from their strong  $\pi$ - $\pi$  interactions, the power conversion efficiency (PCE) values of PSC devices are limited by the dye contents in the polymer blends. Therefore, the H-bonded interactions of supramolecular polymers in this work can be introduced to reduce the aggregations of the low-band-gap organic dyes (as H-donors) and thus to improve the PCE values for the organic solar cell applications.

It is noticeable that the well-known electron-withdrawing unit would be an aryl-substituted cyano or nitro group, which has been widely utilized in organic solar cell materials, including metal-free dye sensitized solar cell (DSSC) materials.<sup>118</sup> On account of the electron-rich sulfur and nitrogen atoms, especially in heterocyclic structures, polymers and organic molecules<sup>119</sup> containing carbazole, triphenylamine, and thiophene units as the electron-donating moieties have lately attracted considerable interests in the applications of light-emitting diodes,<sup>120</sup> photovoltaic devices,<sup>121</sup> and organic field effect transistors (OFETs).<sup>122</sup> In the past years, various attempts have been made to increase the delocalization of  $\pi$ -electrons by constructing more coplanar conjugated systems to generate low-band-gap dyes. Another approach is to incorporate electron-accepting (A) units (e.g., cyano or nitro groups) with electron-donating (D) units (e.g., carbazole or triphenylamine groups) to produce low-band-gap dyes with resonance structures (i.e.,  $D-A \leftrightarrow D^+A^-$ ).<sup>123</sup> Recently, Lin et al. have introduced some novel conjugated spacers by inserting benzothiadiazole,



benzoselenadiazole, and 1*H*-phenanthro[9,10-*d*]imidazole segments into low-band-gap dyes (bearing D-A structures) for the applications of photovoltaic devices.<sup>124,125</sup>

In order to incorporate low-band-gap organic dyes (as H-donors) into supramolecular polymers for organic solar cell applications, conjugated pyridyl H-acceptors were integrated into the side-chain polymeric structures as the pendent groups rather than as small molecules (acting as luminescent chromophores) in our previous studies.<sup>76,77,92,126</sup> As shown in the schematic illustration of Figure 5.1, supramolecular side-chain polymers (i.e., H-bonded polymer complexes) were constructed by complexation of pyridyl H-acceptor polymers, i.e., side-chain polymers **P1-P2** containing conjugated pyridyl pendants, with low-band-gap H-donor dyes **S1-S4** (bearing terminal cyanoacrylic acids) in a molar ratio of 1:1 for pyridyl and acid units, which would have much more uptaken loads of photovoltaic dyes in the supramolecular polymeric structures (without phase separation) compared with the normal polymer blends. Our detailed investigations will prove that larger aggregations of the acid protected dyes occurred in the polymer blends due to the lack of supramolecular interactions, and a polymer blend of the conjugated H-acceptor polymer **P1** and the acid-protected dye **S1P** (see Figure 5.3) illustrated an obvious reduction in the PCE value in contrast to the supramolecular analogue **P1/S1**.

Different molar ratios of conjugated H-acceptor monomer **PBB** (containing a pyridyl terminus) and hole-transporting monomer **CAZ** (bearing a carbazole unit) were copolymerized through free radical polymerization to obtain H-acceptor polymers (**P1** and **P2**). Both terminal carbazole or triphenylamine groups as electron-donating (D) units were in conjunction with cyanoacrylic acid groups as electron-accepting (A) units to yield low-band-gap H-donor dyes **S1-S4**, which were bridged through various numbers of fluorene, bithiazole, and thiophene units (see Figure 5.2). By incorporating of side-chain conjugated H-acceptor polymers with low-band-gap H-donor dyes, the LC and PVC properties of the supramolecular polymer complexes can be easily adjusted. The present investigation is mainly to explore the supramolecular structures of H-bonded side-chain polymers containing low-band-gap H-donor dyes for the PSC applications. Therefore, the bulk heterojunction PSC devices containing an active layer of H-bonded polymer complexes **P1/S1-P1/S4** and **P2/S1-P2/S4** (as electron donors) mixed with PCBM (as an electron acceptor) were evaluated.

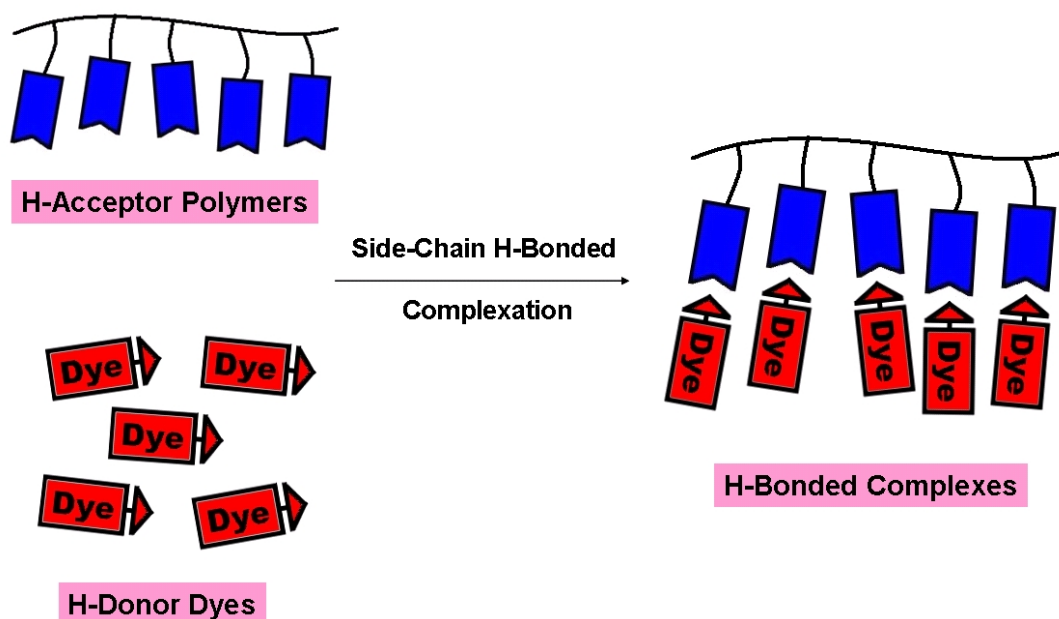


**Figure 5.1** Schematic illustration of complexation processes for H-bonded side-chain polymers.

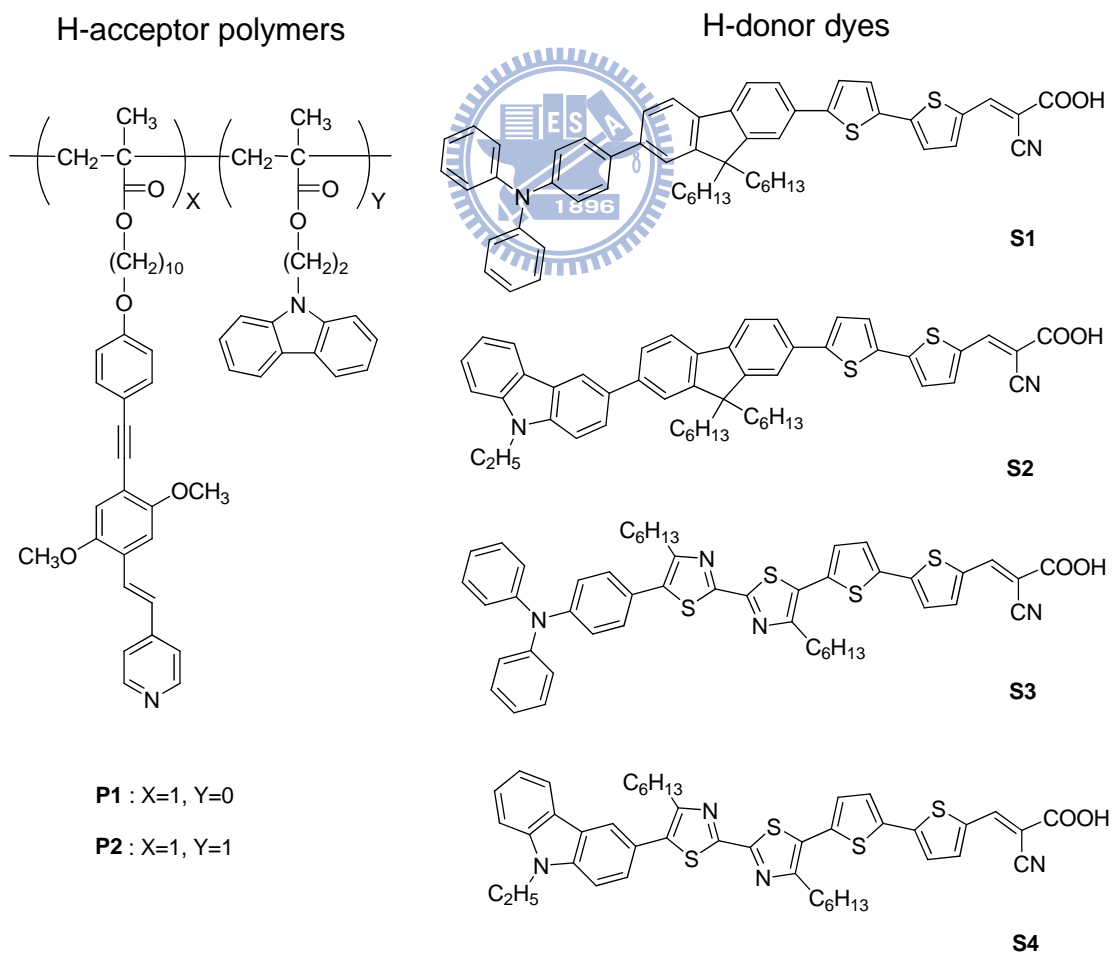


**Figure 5.2** H-acceptor polymers (**P1** and **P2**) and H-donor dyes (**S1-S4**) used in the H-bonded polymer complexes (**P1/S1-P1/S4** and **P2/S1-P2/S4**).

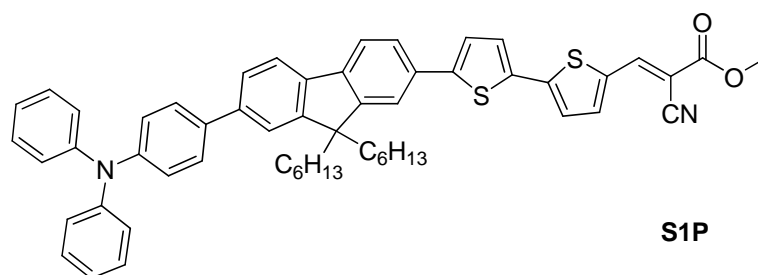


**Figure 5.3** Acid-protected dye **S1P** without carboxylic end functionality.

## 5.2 Experimental

### 5.2.1 Materials

Chemicals and solvents were reagent grades and purchased from Aldrich, ACROS, TCI, and Lancaster Chemical Co. Dichloromethane and THF were distilled to keep anhydrous before use. The other chemicals were used without further purification. The synthetic routes of side-chain conjugated H-acceptor polymers **P1** and **P2** (as shown in Figure 5.2) were reported in our previous publication.<sup>79</sup> H-acceptor polymers (**P1** and **P2**) and H-donor dyes (**S1-S4**) used in the H-bonded polymer complexes (**P1/S1-P1/S4** and **P2/S1-P2/S4**).

### 5.2.2 Preparation of Supramolecular Polymer Complexes

In all cases, all H-donor dyes and H-acceptor polymers (as shown in Figure 5.2) were dissolved in THF to make a clear solution. After then, most of the solvents were evaporated under ambient conditions, which were followed by drying in a vacuum oven at 60 °C for several hours. The complexation of H-donor acids and H-acceptor polymers through hydrogen bonding was proceeded during the solvent evaporation.

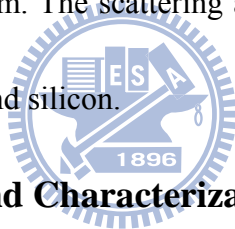
The H-bonded side-chain polymers of all H-acceptor polymers complexed with H-donor dyes **S1-S4** had the equal molar amount of pyridyl H-acceptor and carboxylic acid H-donor groups (in 1:1 molar ratio) to form supramolecular polymer complexes (i.e., H-bonded side-chain polymers).

### 5.2.3 Measurements and Characterization

<sup>1</sup>H NMR spectra were recorded on a Varian unity 300 MHz spectrometer using *d*-DMSO as solvents. Elemental analyses were proceeded on a HERAEUS CHN-OS RAPID elemental analyzer. Fourier transform infrared (FT-IR) spectra were performed on a Nicolet 360 FT-IR spectrometer. The textures of mesophases were characterized by a polarizing optical microscope (POM, model: Leica DMLP) equipped with a hot stage. Temperatures and enthalpies of phase transitions were determined by differential scanning calorimetry (DSC, model: Perkin Elmer Pyris 7) at a heating and cooling rate of 10 °C/min under nitrogen. Thermogravimetric analyses (TGA) were conducted on a Du Pont Thermal Analyst 2100 system with a TGA 2950 thermogravimetric analyzer at a heating rate of 20 °C/min under nitrogen. Gel permeation chromatography (GPC) analyses were executed with a Water 1515 separations module using polystyrene as a standard and THF as an eluant. UV-visible absorption spectra were recorded in dilute THF solutions (10<sup>-6</sup> M) on a HP G1103A spectrophotometer, and photoluminescence (PL) spectra were obtained on a Hitachi

F-4500 spectrophotometer. Thin films of UV-vis and PL measurements were spin-coated on quartz substrates from THF solutions with a concentration of 1 wt%. Cyclic voltammetry (CV) measurements were carried out using a BAS 100 electrochemical analyzer with a standard three-electrode electrochemical cell in a 0.1 M tetrabutylammonium hexafluorophosphate ((TBA)PF<sub>6</sub>) solution (in acetonitrile) at room temperature with a scanning rate of 50 mV/s. During the CV measurements, the solutions were purged with nitrogen for 30s. In each case, a carbon working electrode coated with a thin layer of copolymers, a platinum wire as the counter electrode, and a silver wire as the quasi-reference electrode were used, and Ag/AgCl (3 M KCl) electrode was served as a reference electrode for all potentials quoted herein. The redox couple of ferrocene/ferrocenium ion (Fc/Fc<sup>+</sup>) was used as an external standard. The corresponding highest occupied molecular orbital (HOMO) and lowest unoccupied molecular orbital (LUMO) levels were calculated using  $E_{ox/onset}$  and  $E_{red/onset}$  for experiments in solid films of H-acceptor polymers (**P1** and **P2**), H-donor dyes (**S1-S4**), and H-bonded polymer complexes (**P1/S1-P1/S4** and **P2/S1-P2/S4**), which were performed by drop-casting films with a similar thickness from THF solutions (ca. 5 mg/mL). The LUMO level of PCBM employed was in accordance with the literature datum.<sup>127</sup> The onset potentials were determined from the intersections of two tangents drawn at the rising currents and background currents

of the cyclic voltammetry (CV) measurements. Synchrotron powder X-ray diffraction (XRD) measurements were performed at beamline BL17A of the National Synchrotron Radiation Research Center (NSRRC) in Taiwan, where the X-ray wavelength used was 1.33366 Å. XRD data were collected using imaging plates (IP, of an area =  $20 \times 40 \text{ cm}^2$  and a pixel resolution of 100) curved with a radius equivalent to the sample-to-image plate distance of 280 mm, and the diffraction signals were accumulated for 3 min. The powder samples were packed into a capillary tube and heated by a heat gun, where the temperature controller was programmable by a PC with a PID feed back system. The scattering angle theta values were calibrated by a mixture of silver behenate and silicon.



#### **5.2.4 Device Fabrication and Characterization of Polymer Solar Cells (PSCs)**

The polymer solar cell (PSC) devices in this study were composed of an active layer of blended H-bonded side-chain polymers (**P1/S1-P1/S4** and **P2/S1-P2/S4**) mixed with [6,6]-phenyl C<sub>61</sub> butyric acid methyl ester (i.e., PCBM) in solid films, which was sandwiched between a transparent indium tin oxide (ITO) anode and a metal cathode. Prior to the device fabrication, ITO-coated glass substrates ( $1.5 \times 1.5 \text{ cm}^2$ ) were ultrasonically cleaned in detergent, deionized water, acetone, and isopropyl alcohol. Afterward, the substrates were treated with UV ozone for 15 min, and a layer

of poly(ethylene dioxythiophene): polystyrenesulfonate (PEDOT:PSS, ~30 nm) was subsequently spin-coated onto the substrates. After baking at 130 °C for one hour, the substrates were transferred to a nitrogen-filled glovebox. The PSC devices were fabricated by spin-coating solutions of blended H-bonded polymer complexes:PCBM (with various weight ratios) onto the PEDOT:PSS modified substrates at 600 rpm for 60 s (ca. 200 nm), and placed in a covered glass Petri dish. Initially, the blended solutions were prepared by dissolving both H-bonded polymer complexes (**P1/S1-P1/S4** and **P2/S1-P2/S4**) and PCBM (with a 1:1 weight ratio initially and then with various weight ratios for the optimum H-bonded polymer complex) in chlorobenzene (20 mg/1 mL), followed by continuous stirring for 12 h at 50 °C. In the slow-growth approach, blended H-bonded polymer complexes in solid films were kept in the liquid phase after spin-coating by using the solvent (chlorobenzene) with a high boiling point. Finally, a calcium layer (30 nm) and a subsequent aluminum layer (100 nm) were thermally evaporated through a shadow mask at a pressure below  $6 \times 10^{-6}$  Torr, and the active area of the device was 0.12 cm<sup>2</sup>. All PSC devices were prepared and measured under ambient conditions.

## **5.3 Results and Discussion**

### **5.3.1 FT-IR Spectroscopy of H-Bonded Polymer Complexes**

All H-bonded side-chain polymers consisting of the appropriate molar ratio



(fully H-bonded complexes in a molar ratio of 1:1 for pyridyl and acid units) of H-acceptor polymers (**P1** and **P2**) and H-donor dyes (**S1-S4**) were prepared by slow evaporation of THF solutions and followed by drying in vacuo. The formation of hydrogen bonding in supramolecular side-chain polymers containing H-donor dyes (**S1-S4**) was confirmed by FT-IR spectroscopy. As shown in Figure 5.4(a), IR spectra of H-acceptor polymer **P2**, H-donor dye **S1**, and H-bonded complex **P2/S1** are compared to analyze the hydrogen bonds in the supramolecular structure of H-bonded polymer complex **P2/S1**. In contrast to the O-H band of pure **S1** at 2640 and 2510  $\text{cm}^{-1}$ , the weaker O-H band observed at 2497 and 1902  $\text{cm}^{-1}$  in H-bonded polymer complex **P2/S1** is indicative of stronger hydrogen bonding between the pyridyl group of **P2** and the carboxylic acid of **S1** in the H-bonded complex. On the other hand, a C=O stretching vibration appeared at 1722  $\text{cm}^{-1}$  in H-bonded polymer complex **P2/S1**, which shows that the carbonyl group was in a less associated state than that in pure **S1** with a weaker C=O stretching vibration appeared at 1690  $\text{cm}^{-1}$ . Both results suggest that hydrogen bonds were formed between H-acceptor polymer **P2** and H-donor dye **S1** in the solid state of H-bonded polymer complex **P2/S1**. The other H-bonded polymer complexes also have the similar consequences of H-bonding formation as the H-bonded complex demonstrated here.<sup>17</sup> However, in comparison with H-bonded polymer complex **P1/S1**, physical blend **P1/S1P** (without H-bonds) in Figure 5.4(b)

(see the Supporting Information) shows a weaker C=O stretching vibration appeared at  $1706\text{ cm}^{-1}$  for lack of H-bonding interactions.

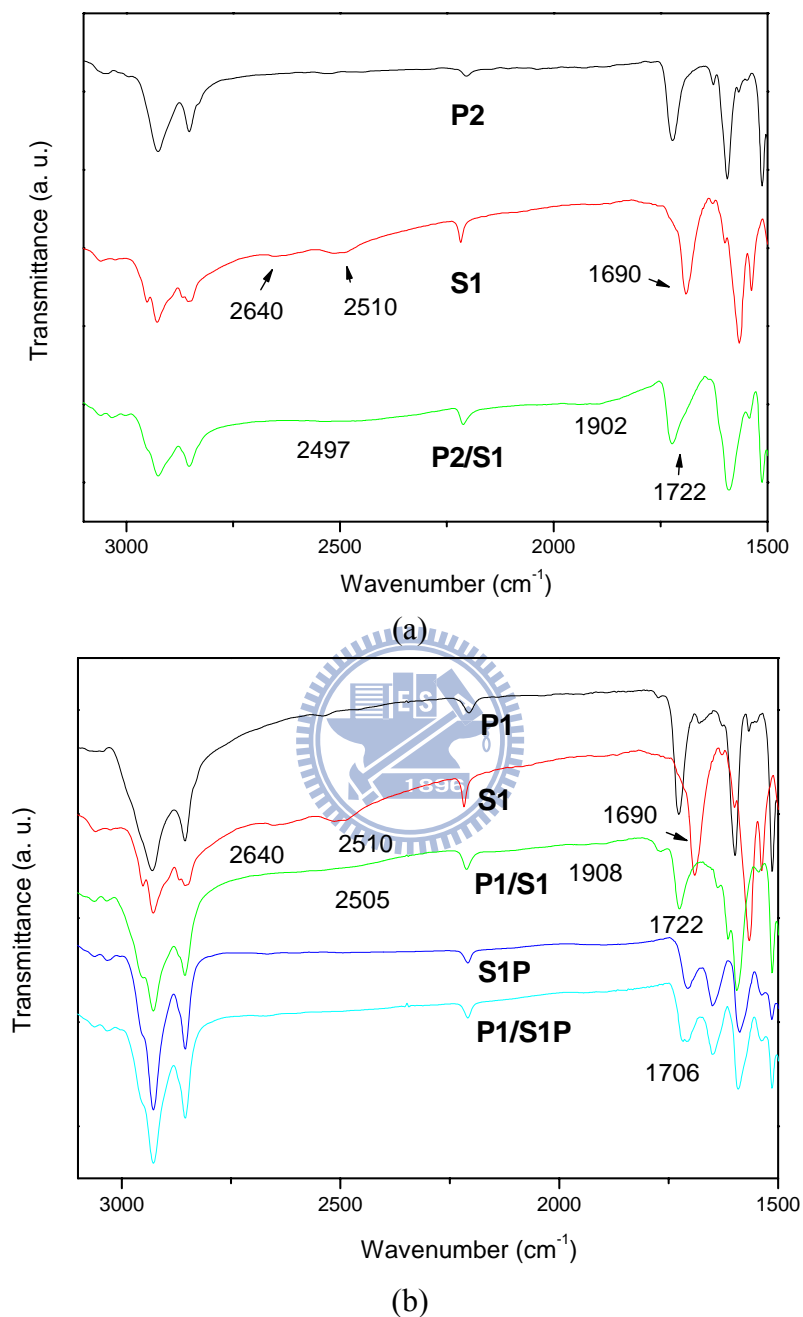


**Figure 5.4** FTIR spectra of (a) H-acceptor polymer **P2**, H-donor dye **S1**, and H-bonded polymer complex **P2/S1**, and (b) H-acceptor polymer **P1**, H-donor dye **S1**, acid-protected dye **S1P**, H-bonded polymer complex **P1/S1**, and physical blend **P1/S1P**.

### 5.3.2 Phase Behavior

The phase transition temperatures of H-acceptor polymers (**P1** and **P2**), H-donor dyes (**S1-S4**), and H-bonded side-chain polymers (i.e., H-bonded polymer complexes **P1/S1-P1/S4** and **P2/S1-P2/S4**) are summarized in Table 5.1, which were determined by DSC (under nitrogen) and POM. The weight-average molecular weights ( $M_w$ ) of H-acceptor polymers **P1** and **P2** (determined by GPC) are 14400 g/mol (PDI = 1.72) and 38100 g/mol (PDI = 3.24), respectively. The glass transition temperatures ( $T_g$ ) of H-acceptor polymers **P1** and **P2** are 63 and 88 °C, respectively.<sup>79</sup> To elucidate the H-bonding effect of H-bonded pendants on the thermal properties of supramolecular side-chain polymers, H-donor dyes **S1-S4** were introduced to be incorporated with H-acceptor side-chain polymers **P1** and **P2**. As shown in Table 5.1, both series of H-bonded complexes containing H-acceptor polymers **P1** and **P2** showed only a single glass transition, which suggests good miscibilities between H-donor dyes (i.e., **S1-S4**) and H-acceptor polymers (i.e., **P1** and **P2**).

Since no melting and crystallization transitions were observed in the DSC measurements, it suggests that these H-bonded complexes possess amorphous characteristics. However, the  $T_g$  values of the H-bonded complexes are notably higher than those of their corresponding H-acceptor polymers **P1** and **P2**. The increases of  $T_g$  values in H-bonded complexes are probably due to the larger  $\pi$ - $\pi$  interactions

originated from the increased rigid-rod lengths of the integrated H-bonded pendants (containing both pyridyl H-acceptor units and H-donor dyes). In contrast to H-acceptor homopolymer **P1** and its H-bonded complexes, H-acceptor copolymer **P2** and its H-bonded complexes possessed higher  $T_g$  values due to the integration of more bulky and rigid **CAZ** components in copolymer **P2**. Comparing the H-bonded complexes containing fluorene-linked dyes (**S1** and **S2**) and bithiazole-linked dyes (**S3** and **S4**), owing to the higher rigidity of bithiazole units in H-donor dyes **S3** and **S4**, the latter H-bonded complexes (**P1-P2/S3** and **P1-P2/S4**) have higher  $T_g$  values than the former H-bonded complexes (**P1-P2/S1** and **P1-P2/S2**), respectively. This obviously indicates that the rigid bithiazole linkers will enhance the aggregation of the pendants in the H-bonded complexes effectively. In contrast to the H-bonded complexes (**P1-P2/S1** and **P1-P2/S3**) containing end-capping triphenylamine dyes (**S1** and **S3**), owing to the higher rigidity and coplanarity of end-capping cabazole units in H-donor dyes (**S2** and **S4**), the analogous H-bonded complexes (**P1-P2/S2** and **P1-P2/S4**) containing end-capping cabazole dyes (**S2** and **S4**) have higher  $T_g$  values.

The isotropization temperatures ( $T_i$ ) have the similar trends as the glass transition temperatures ( $T_g$ ) in H-bonded polymer complexes (**P1/S1-P1/S4** and **P2/S1-P2/S4**). Moreover, comparing analogous H-bonded complexes consisting of the same H-donor dyes, H-bonded complexes containing H-acceptor homopolymer

**P1** possess the higher isotropization temperatures ( $T_i$ ) and the broader mesophasic ranges than those containing H-acceptor copolymer **P2**. In addition, compared with H-bonded polymer complexes **P1/S1** and **P1/S2** bearing fluorene-linked dyes (**S1** and **S2**), H-bonded polymer complexes **P1/S3** and **P1/S4** bearing bithiazole-linked dyes (**S3** and **S4**) have higher  $T_i$  values and broader mesophasic ranges. In general, the isotropization temperatures ( $T_i$ ) and mesophasic ranges of H-bonded side-chain polymers would be enhanced while the H-bonded central cores are longer and more rigid.

As shown in Figure 5.5(a), the mesomorphic behavior of H-bonded polymer complex **P2/S4** (cooling at 130 °C) was confirmed as the nematic phase by the schlieren texture of POM, which was further elucidated by X-ray diffraction (XRD) measurements in Figure 5.5(b) that no sharp d-spacing values, i.e., no layered structures of the smectic phase, were observed in the XRD intensity against angle profiles of H-bonded polymer complexes **P1/S1** and **P2/S4** at 130 °C (in the mesophasic range). According to the POM and XRD measurements, H-acceptor homopolymer **P1** and all H-bonded polymer complexes (**P1/S1-P1/S4** and **P2/S1-P2/S4**) in Table 5.1 were verified to possess the nematic phase, but H-acceptor copolymer **P2** bearing 50% molar ratio of **CAZ** units did not possess any mesophase. Hence, the integration of **CAZ** units in copolymer **P2** is detrimental to the formation

of the mesophase, which can be explained by that the **CAZ** units with non-mesomorphic property may dilute and hinder the molecular packing of the LC arrangements in copolymer **P2**. However, the nematic phase was introduced to the corresponding H-bonded polymer complexes (**P2/S1-P2/S4**) of copolymer **P2** due to the extended H-bonded mesogens by combination of H-acceptor pedants with H-donor dyes. Moreover, the mesophasic ranges and  $T_i$  values of the H-bonded polymer complexes (**P2/S1-P2/S4**) containing copolymer **P2** were apparently reduced by the **CAZ** units of H-acceptor copolymer **P2**, which diluted and interfered the LC arrangements of the H-bonded mesogens in their subsequent H-bonded polymer complexes. However, acid-protected dye **S1P** and physical blend **P1/S1P** (without H-bonds) have lower phase transition temperatures (including the isotropization temperature  $T_i$ ) than H-bonded polymer complex **P1/S1** due to the dilution effect of the acid-protected dye **S1P** moieties in the physical blend **P1/S1P** (see Table 5.1).

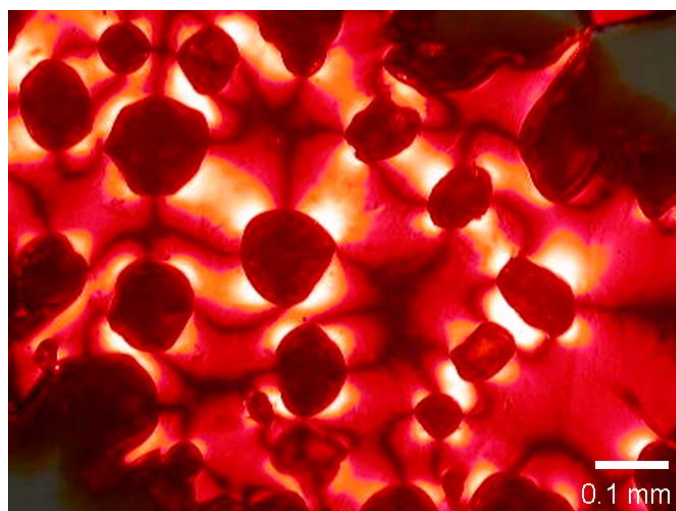
**Table 5.1 Thermal Properties of H-Acceptor Polymers (P1-P2), H-Donor Dyes (S1-S4), Acid-Protected Dye S1P, H-Bonded Polymer Complexes (P1/S1-P1/S4 and P2/S1-P2/S4), and Physical Blend P1/S1P**

Compound	Phase transitions, °C <sup>a,b</sup>
<b>P1</b>	G 63 N 125 <sup>c</sup> I
<b>P2</b>	G 88 K 110 <sup>c</sup> I
<b>S1</b>	K 156 (10.8) I
<b>S2</b>	K 163 (13.4) I
<b>S3</b>	K 173 (25.9) I
<b>S4</b>	K 180 (26.3) I
<b>S1P</b>	K 98 (13.4) I
<b>P1/S1</b>	G 87 N 151 <sup>c</sup> I
<b>P1/S2</b>	G 89 N 155 <sup>c</sup> I
<b>P1/S3</b>	G 96 N 167 <sup>c</sup> I
<b>P1/S4</b>	G 99 N 172 <sup>c</sup> I
<b>P2/S1</b>	G 96 N 141 <sup>c</sup> I
<b>P2/S2</b>	G 98 N 147 <sup>c</sup> I
<b>P2/S3</b>	G 104 N 156 <sup>c</sup> I
<b>P2/S4</b>	G 105 N 162 <sup>c</sup> I
<b>P1/S1P</b>	G 67 K 100 (12.4) I

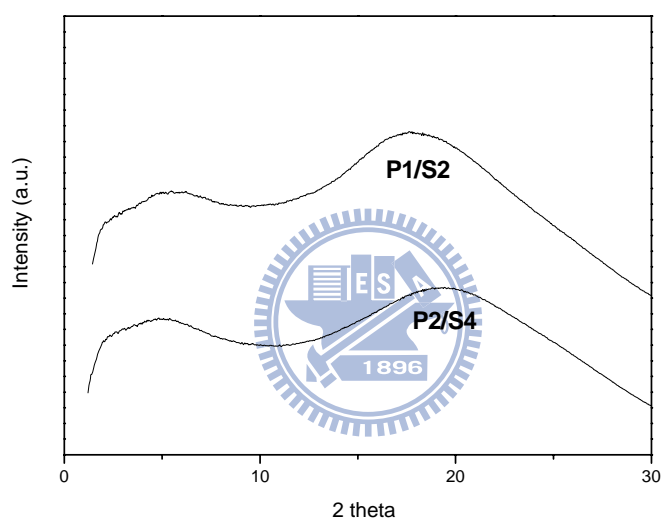
<sup>a</sup> Phase transition temperatures (°C) and enthalpies (in parentheses, kJ/mol) were determined by DSC at a heating rate of 10 °C/min.

<sup>b</sup> G, glassy state; K, crystalline; N, nematic; I, isotropic.

<sup>c</sup> Phase transition temperatures were obtained by POM and confirmed by XRD.



(a)



(b)

**Figure 5.5** (a) Optical texture of the nematic phase in H-bonded polymer complex **P2/S4** observed by POM at 130 °C (cooling) and (b) XRD intensity against angle profiles obtained from H-bonded polymer complexes **P1/S1** and **P2/S4** at 130 °C (in the nematic phase).



### 5.3.3 Optical Properties

The UV-visible absorption spectra of H-acceptor polymers **P1-P2** and H-donor dyes **S1-S4** (in both THF solutions and solid films), and H-bonded polymer complexes **P1/S1-P1/S4** and **P2/S1-P2/S4** (in solid films) are displayed in Figures 5.6 and 5.7, and their photophysical properties are demonstrated in Table 5.2. The absorption energy band-gaps of H-bonded polymer complexes (**P1/S1-P1/S4** and **P2/S1-P2/S4**) could be easily tuned by the introduction of H-donor dyes (**S1-S4**), and their absorption spectra covered broad wavelength ranges for both solutions and solid films. As shown in Figure 5.6, the maximum absorption wavelength ( $\lambda_{\text{abs}}$ ) of H-acceptor polymers **P1-P2** in THF solutions and solid films were 385 and 393 nm, respectively, which were mainly contributed from the **PBB** units. The maximum absorption wavelength ( $\lambda_{\text{abs}}$ ) of H-donor dyes **S1-S4** in THF solutions were in the range of 458-462 nm (in THF solutions) and 471-490 nm (in solid films). Due to the interchain association and  $\pi$ - $\pi$  stacking of these polymers and dyes in solids, the absorption spectra of all H-acceptor polymers and H-donor dyes in solid films were generally larger than those in dilute solutions (i.e., 8 nm red shifts in polymers and 11-30 nm red shifts in dyes). After complexation (in solid films as shown in Figure 5.7), H-bonded polymer complexes **P1/S1-P1/S4** and **P2/S1-P2/S4** displayed blue-shifted absorption peaks (at 440-462 nm) in contrast to H-donor dyes **S1-S4**. The

blue shifted absorption (blue shifted wavelength  $\Delta\lambda_{\text{abs}} = 19\text{-}39$  nm) was due to the dilution effect of H-acceptor polymers as solid solvents for dyes (as solutes) in solid H-bonded polymer complexes. Compared with the H-bonded complexes containing fluorene-linked dyes (**S1** and **S2**), the corresponding H-bonded complexes containing bithiazole-linked dyes (**S3** and **S4**) have longer absorption wavelengths and thus to have lower optical band-gaps, which were originated from the smaller optical band-gaps of bithiazole-linked dyes (**S3** and **S4**) in solid films. Therefore, the H-bonded complexes containing bithiazole-linked dyes (**S3** and **S4**) might have the gifts of lower optical band-gaps for further good performance in photovoltaic properties. However, due to the lack of supramolecular interactions in polymer blend **P1/S1P** and a larger aggregation of the acid-protected dye **S1P**, a red-shifted (33 nm) absorption in the solid film of polymer blend **P1/S1P** than that of H-bonded polymer complex **P1/S1** was observed (see Table 5.2).

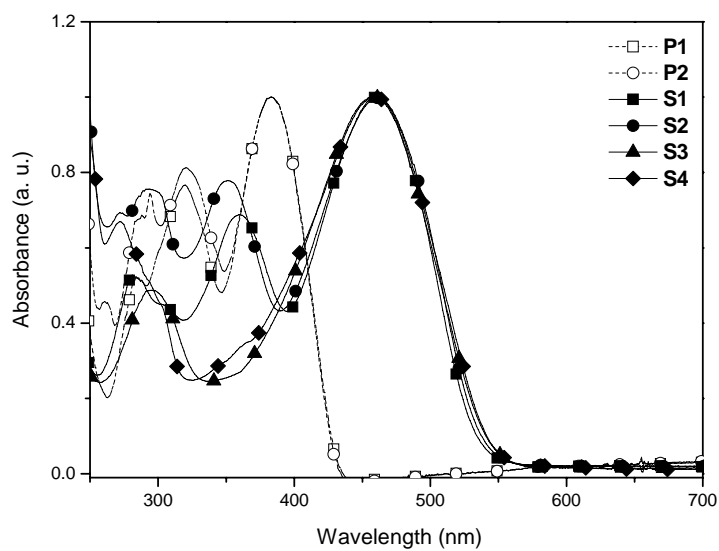
The photoluminescence (PL) spectra of H-acceptor polymers **P1-P2**, H-donor dyes **S1-S4**, and H-bonded polymer complexes **P1/S1-P1/S4** and **P2/S1-P2/S4** (in solid films) are summarized in Table 5.2. Similar to the UV-visible absorption spectra, the PL emission wavelengths of H-bonded polymer complexes **P1/S1-P1/S4** and **P2/S1-P2/S4** (at 611-645) nm were all blue-shifted in contrast to those of H-donor dyes **S1-S4** (at 631-677 nm). The PL emission spectra (in solid films) of the

H-acceptor polymers **P1** and **P2** were dramatically quenched by adding H-donor dyes **S1-S4** in the H-bonded polymer complexes **P1/S1-P1/S4** and **P2/S1-P2/S4**. The corresponding optical quenching properties of these H-bonded complexes in solid films, including the broad optical absorptions and low optical band-gaps, proposed the potential applications in photovoltaic cells.

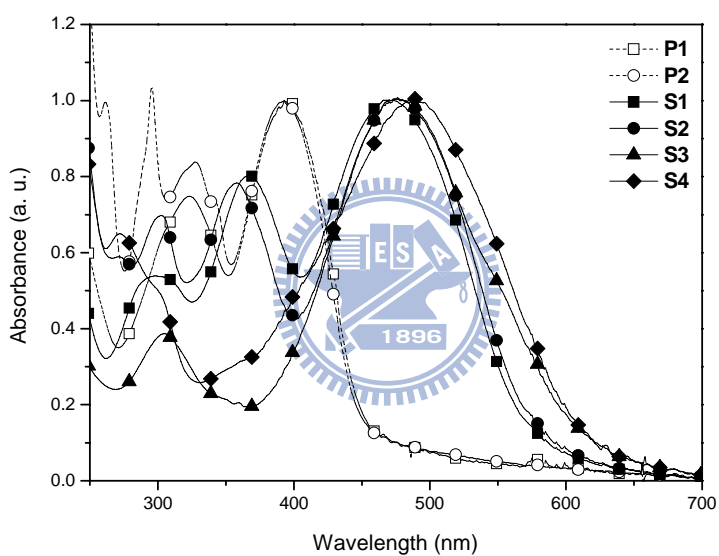
**Table 5.2 Absorption and Photoluminescence Spectral Data of H-Acceptor Polymers (P1-P2), H-Donor Dyes (S1-S4), Acid-Protected Dye S1P, H-Bonded Polymer Complexes (P1/S1-P1/S4 and P2/S1-P2/S4), and Physical Blend P1/S1P**

Compound	$\lambda_{\text{abs,sol}}^a$ (nm)	$\lambda_{\text{abs,fil}}^a$ (nm)	$\lambda_{\text{PL,fil}}^a$ (nm)
<b>P1</b>	385	393	496
<b>P2</b>	385	393	487
<b>S1</b>	460	471	631
<b>S2</b>	462	478	638
<b>S3</b>	458	481	668
<b>S4</b>	460	490	677
<b>S1P</b>	453	471	623
<b>P1/S1</b>	-	440	614
<b>P1/S2</b>	-	445	621
<b>P1/S3</b>	-	462	640
<b>P1/S4</b>	-	451	645
<b>P2/S1</b>	-	440	611
<b>P2/S2</b>	-	448	618
<b>P2/S3</b>	-	457	638
<b>P2/S4</b>	-	452	638
<b>P1/S1P</b>	-	473	623

<sup>a</sup> Absorption and PL emission spectra were recorded in dilute THF solutions.

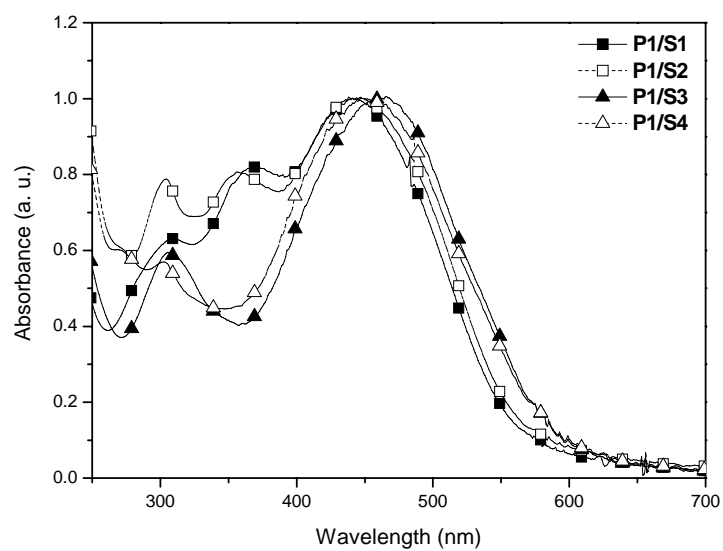


(a)

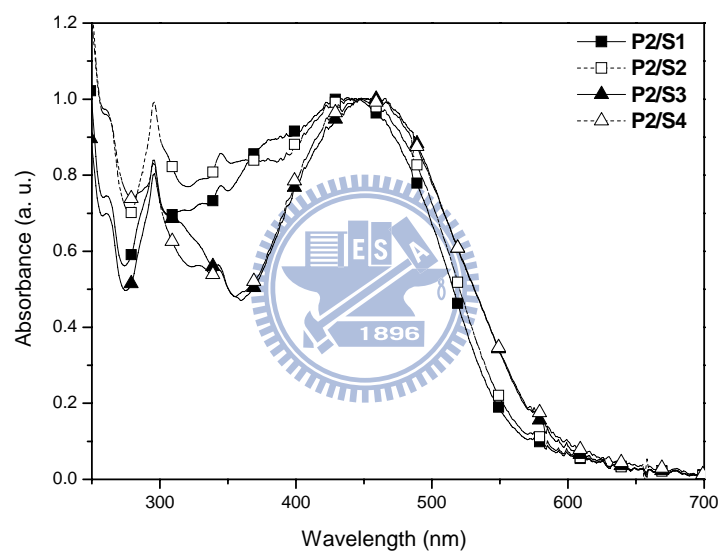


(b)

**Figure 5.6** UV-visible absorption spectra of H-acceptor polymers **P1-P2** and H-donor dyes **S1-S4** (a) in THF solutions and (b) in solid films.



(a)



(b)

**Figure 5.7** UV-visible absorption spectra of (a) H-bonded polymer complexes **P1/S1-P1/S4** and (b) H-bonded polymer complexes **P2/S1-P2/S4** in solid films.

### 5.3.4 Electrochemical Properties

Narrow-band-gap H-bonded side-chain polymers were designed as donor-acceptor type materials by using H-donor dyes containing electron-donating carbazole and triphenylamine moieties and electron-withdrawing cyano moieties. In order to understand the energy band structures of these new narrow-band-gap H-bonded polymer complexes for the PSC device application, the electronic states, i.e., highest occupied molecular orbital (HOMO) and lowest unoccupied molecular orbital (LUMO) levels, of the H-bonded side-chain polymers were investigated by the cyclic voltammetry (CV) measurements. The oxidation and reduction cyclic voltammograms of H-bonded polymer complexes **P1/S1-P1/S4** and **P2/S1-P2/S4** in solid films are displayed in Figure 5.8. H-bonded polymer complexes **P1/S1-P1/S4** and **P2/S1-P2/S4** exhibited quasi-reversible (or reversible) oxidation and reduction peaks as evident from the areas and close proximity of the anodic and cathodic scans. The onset oxidation and reduction potentials (in solid films) of H-acceptor polymers **P1-P2**, H-donor dyes **S1-S4**, and H-bonded polymer complexes **P1/S1-P1/S4** and **P2/S1-P2/S4** are demonstrated Table 5.3. Ag/AgCl was served as a reference electrode, and it was calibrated by ferrocene ( $E_{\text{ferrocene}}^{1/2} = 0.45 \text{ mV vs Ag/AgCl}$ ). The HOMO and LUMO energy levels were estimated by the oxidation and reduction potentials from the reference energy level of ferrocene (4.8 eV below the vacuum

level) according to the following equation:  $E_{\text{HOMO/LUMO}} = [- (E_{\text{onset}} - 0.45) - 4.8]$  eV.

According to the previous estimation, the HOMO and LUMO energy levels as well as the band-gap values directly measured from CV ( $E_{\text{g,cv}}$ ) of all compounds are also summarized in Table 5.3.

As can be seen, all band-gap values of  $E_{\text{g,cv}}$  had the analogous sequences as confirmed by the optical band-gap values observed from UV-vis spectra ( $E_{\text{g,opt}}$ ). By using the H-donor dyes with electron donor-acceptor effects, H-bonded polymer complexes **P1/S1-P1/S4** and **P2/S1-P2/S4** displayed narrower band-gaps (0.68 eV smaller in  $E_{\text{g,opt}}$  and 0.51 eV smaller in  $E_{\text{g,cv}}$ ) compared to H-acceptor polymers **P1-P2** (see Table 5.3). However, due to the dilution results of H-acceptor polymers **P1-P2**, H-bonded polymer complexes **P1/S1-P1/S4** and **P2/S1-P2/S4** presented wider band-gaps in contrast to H-donor dyes **S1-S4**. It is worthwhile to note that the H-bonded complexes containing bithiazole-linked dyes (**S3** and **S4**) have lower optical band-gaps ( $E_{\text{g,cv}}$  and  $E_{\text{g,opt}}$ ) than the corresponding H-bonded complexes containing fluorene-linked dyes (**S1** and **S2**), which was originated from the smaller optical band-gaps of bithiazole-linked dyes (**S3** and **S4**) in solid films. Compared with H-acceptor polymers **P1-P2** and H-donor dyes **S1-S4**, the medium HOMO and LUMO energy levels of H-bonded polymer complexes (**P1/S1-P1/S4** and **P2/S1-P2/S4**) could be adjusted. Therefore, the electrochemical reductions of

H-bonded complexes showed similar LUMO energy levels at ca. (-2.92)-(-3.04) eV, which represented to possess high electron affinities and also make these H-bonded complexes suitable donors for electron injection and transporting to PCBM acceptors (with 0.71-0.83 eV offsets in LUMO levels regarding PCBM with a LUMO level of -3.75 eV as shown in Figure 5.9)<sup>112b</sup> for the polymeric bulk heterojunction solar cell devices. Based on the oxidation potential data, the introduction of electron-withdrawing cyano groups in H-donor dyes to the H-bonded complexes can induce the decreases of HOMO energy levels at ca. (-5.36)-(-5.52) eV, which represented to possess high hole transporting properties and also make these H-bonded complexes suitable donors for hole injection and transporting to PEDOT:PSS layer and then to ITO electrode (with 0.06-0.22 eV offsets in HOMO levels regarding PEDOT:PSS layer with a HOMO level of -5.3 eV as illustrated in Figure 5.9)<sup>112b</sup> for the polymeric bulk heterojunction solar cell devices.<sup>128</sup> Thus, the electrochemical properties of H-bonded complexes could be adjusted by introducing electron-withdrawing cyano groups and electron-donating amine groups of H-donor dyes to the H-bonded complexes, which can reduce the HOMO energy levels and increase the LUMO energy levels of the H-bonded side-chain polymers, and thus to have narrower band-gaps.



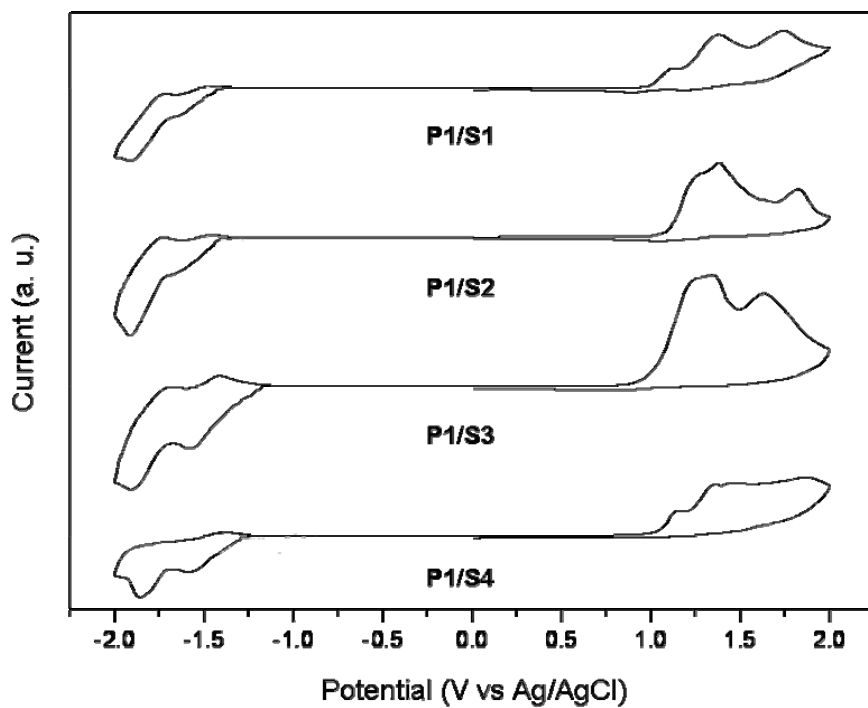
**Table 5.3 Electrochemical Potentials and Energy Levels of H-Acceptor Polymers (P1-P2), H-Donor Dyes (S1-S4), and H-Bonded Polymer Complexes (P1/S1-P1/S4 and P2/S1-P2/S4)**

Compound	$\lambda_{\text{onset,abs}}$ (nm) <sup>a</sup>	$E_{\text{g,opt}}$ (eV) <sup>a</sup>	$E_{\text{ox}}$ (eV) <sup>b</sup>	HOMO (eV) <sup>c</sup>	$E_{\text{re}}$ (eV) <sup>b</sup>	LUMO (eV) <sup>c</sup>	$E_{\text{g,cv}}$ (eV)
<b>P1</b>	445	2.79	1.18	-5.53	-1.67	-2.68	2.85
<b>P2</b>	445	2.79	1.17	-5.52	-1.65	-2.70	2.82
<b>S1</b>	580	2.14	0.96	-5.31	-1.47	-2.88	2.43
<b>S2</b>	587	2.11	1.04	-5.39	-1.40	-2.95	2.44
<b>S3</b>	622	1.99	1.00	-5.35	-1.33	-3.02	2.33
<b>S4</b>	620	2.00	1.03	-5.38	-1.30	-3.05	2.33
<b>P1/S1</b>	552	2.25	1.01	-5.36	-1.43	-2.92	2.44
<b>P1/S2</b>	558	2.22	1.09	-5.44	-1.40	-2.95	2.49
<b>P1/S3</b>	584	2.12	1.01	-5.36	-1.33	-3.02	2.34
<b>P1/S4</b>	586	2.11	1.04	-5.39	-1.32	-3.03	2.36
<b>P2/S1</b>	554	2.24	1.09	-5.44	-1.42	-2.93	2.51
<b>P2/S2</b>	557	2.23	1.17	-5.52	-1.37	-2.98	2.54
<b>P2/S3</b>	581	2.13	1.03	-5.38	-1.31	-3.04	2.34
<b>P2/S4</b>	589	2.11	1.08	-5.43	-1.35	-3.00	2.42

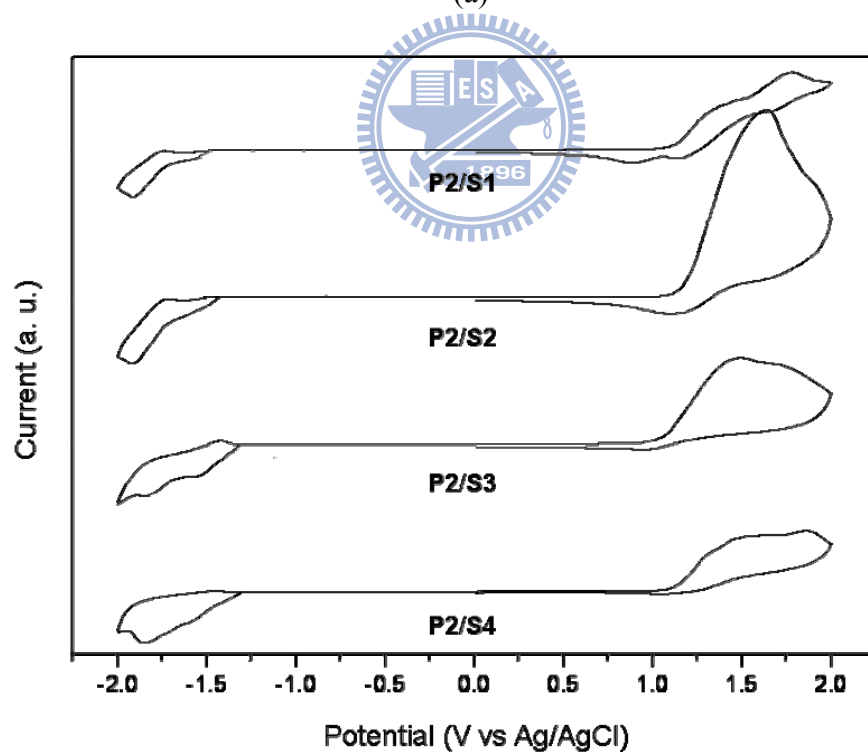
<sup>a</sup> Absorption wavelengths obtained in solid films and optical band-gaps calculated from the equation of  $E_{\text{g,opt}} = 1240/\lambda_{\text{edge}}$ .

<sup>b</sup> Onset oxidation and reduction potentials.

<sup>c</sup>  $E_{\text{HOMO}}/E_{\text{LUMO}} = [-(E_{\text{onset}} - 0.45) - 4.8]$  eV where 0.45 V is the value of ferrocene vs. Ag/Ag<sup>+</sup> and 4.8 eV is the energy level of ferrocene below the vacuum.



(a)



(b)

**Figure 5.8** Cyclic voltammograms of H-bonded polymer complexes (a) **P1/S1-P1/S4** and (b) **P2/S1-P2/S4**.

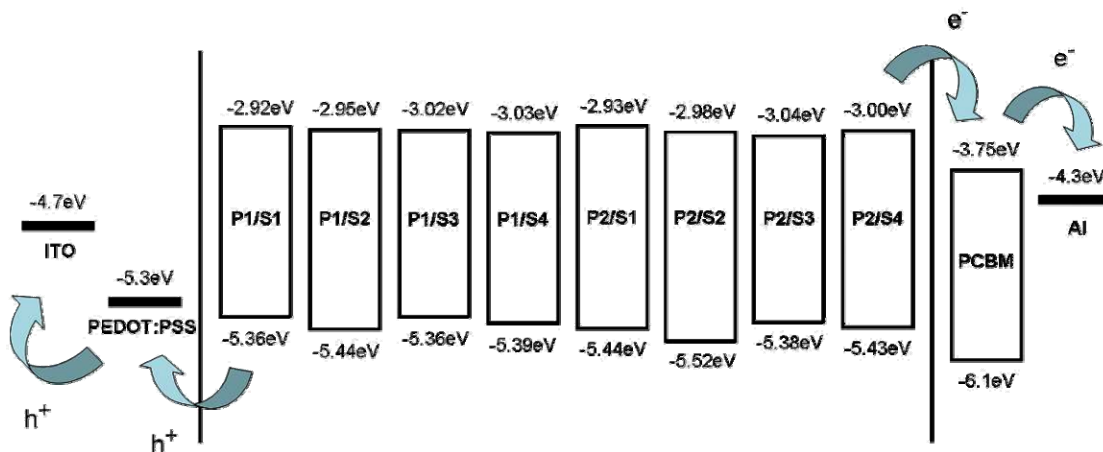


**Figure 5.9** Energy band diagram with HOMO/LUMO levels of H-bonded polymer complexes **P1/S1-P1/S4** (as electron donors) and PCBM (as an electron acceptor) in relation to the work functions of ITO, PEDOT:PSS, and Al (HOMO value of PCBM was obtained from Reference 112).

### 5.3.5 Photovoltaic Cell Properties

The design and syntheses of the H-bonded side-chain polymers **P1/S1-P1/S4** and **P2/S1-P2/S4** is to utilize new narrow band-gap H-donor dyes self-assembled with side-chain conjugated H-acceptor polymers into supramolecular polymeric structures for the PSC applications. To investigate the potential use of H-bonded complexes in PSCs, bulk heterojunction PSC devices with a configuration of ITO/PEDOT:PSS/H-bonded polymer complexes:PCBM (1:1 w/w)/Ca/Al were fabricated from an active layer where H-bonded complexes were blended with a complementary fullerene-based electron acceptor PCBM in a weight ratio of 1:1 (w/w) initially (and later followed with various weight ratios for the optimum H-bonded polymer complex). The PSC devices were measured under AM 1.5 illumination for a

calibrated solar simulator with an intensity of 100 mW/cm<sup>2</sup>. The preliminary photovoltaic properties are summarized in Table 5.4, and the typical *I-V* characteristics of all PSC devices are shown in Figure 5.10. Under the white-light illumination, the short circuit current density ( $I_{sc}$ ), open circuit voltage ( $V_{oc}$ ), fill factor ( $FF$ ), and power conversion efficiency (PCE) values of the PSC devices composed of H-bonded polymer complexes were in the range of 0.42-3.17 mA/cm<sup>2</sup>, 0.38-0.59 V, and 24-34%, 0.06-0.50%, respectively.

The photovoltaic properties of the PSC devices containing H-bonded polymer complexes **P1/S1-P1/S4** and **P2/S1-P2/S4** were dependent on the solubility and film-forming quality of the H-bonded complexes. However, the PCE values of H-bonded complexes **P2/S1-P2/S4** containing H-acceptor copolymer **P2** were apparently smaller than those of **P1/S1-P1/S4**, respectively, because the 1:1 molar ratio of pyridyl and acid units of fully H-bonded **P2/S1-P2/S4** would reduce the content of low-band-gap dyes complexed with H-acceptor copolymer **P2** bearing 50 mol% of pyridyl units. As shown in Table 5.4, both series of H-bonded complexes (**P1/S1-P1/S4** and **P2/S1-P2/S4**) containing electron donors of end-capping triphenylamine dyes (**S1** and **S3**) had better PCE values than those containing end-capping carbazole dyes (**S2** and **S4**), respectively. It might be owing to the larger aggregations of end-capping carbazole dyes (**S2** and **S4**) to reduce the PCE values,

which were confirmed by the redder shifted maximum absorption wavelengths ( $\Delta\lambda_{\text{abs}} = \lambda_{\text{abs,solid}} - \lambda_{\text{abs,solution}}$ ) in solid films of end-capping carbazole dyes ( $\Delta\lambda_{\text{abs}} = 16$  nm for **S2** and  $\Delta\lambda_{\text{abs}} = 30$  nm for **S4**) than those of end-capping triphenylamine dyes ( $\Delta\lambda_{\text{abs}} = 11$  nm for **S1** and  $\Delta\lambda_{\text{abs}} = 23$  nm for **S3**), respectively. Among the PSC devices containing H-bonded polymer complexes, those composed of H-donor dye **S3**, i.e., **P1/S3** and **P2/S3**, had the best photovoltaic performance with enhanced  $I_{\text{sc}}$  values in the corresponding H-bonded complexes **P1/S1-P1/S4** and **P2/S1-P2/S4**, respectively, which might be due to the promoted solubility and better film-forming capability of **S3**. Ideally, the  $I_{\text{sc}}$  values were determined by the product of the photoinduced charge carrier densities and the charge carrier mobilities within the organic semiconductors.<sup>108b</sup> Thus, it can be recognized that the better results of  $I_{\text{sc}}$  and  $FF$  in the PSC device containing **P1/S3** and **P2/S3** were obtained likely due to the well-balanced charge flow and less significant recombination loss<sup>113,129</sup> originated from the highly order structural packing of alkyl side chains. However, the relatively low  $I_{\text{sc}}$  and  $FF$  values in the PSC devices containing **P1/S4** and **P2/S4** were poorly understood at this time, but it might be related to the largest aggregation of **S4** (with the reddest shifted maximum absorption wavelengths in solid,  $\Delta\lambda_{\text{abs}} = 30$  nm) and geminate charge recombination at the interface due to stable charge-transfer states, which limited the values of the photocurrents.<sup>130</sup> Though  $V_{\text{oc}}$  values were related to

the differences between the HOMO energy levels of the polymers and the LUMO energy levels of the acceptors,<sup>131</sup> but it was not noticeably varied among the PSC devices containing H-bonded complexes. In addition, the *I-V* curves and photovoltaic properties of dyes **S1-S4** without complexation with the polymers are illustrated in Table 5.5, which can be compared with the PCE values shown in Table 5.4. In general, the H-bonded polymer complexes containing H-acceptor polymers (**P1** and **P2**) have higher PCE values for the organic solar cells, even though the corresponding dye contents of **S1-S4:PCBM** = 1:1 (w/w) without complexation with polymers in the active layer were almost doubled than those of H-bonded polymer complexes (H-bonded polymer complexes:PCBM = 1:1 w/w). Hence, H-acceptor polymers (**P1** and **P2**) do really improve and facilitate the fabrication of solar cells. In order to demonstrate the contribution of supramolecular structures in H-bonded polymer complexes, one more PSC device containing an active layer of physical blend **P1/S1P** (without H-bonds) has been fabricated to compare their photovoltaic properties with those of H-bonded polymer complex **P1/S1**. Compared with H-bonded polymer complex **P1/S1** (PCE = 0.28%), physical blend **P1/S1P** (without H-bonds) has a smaller PCE value (0.16%) in Table 5.6. The larger aggregations of the acid-protected dye **S1P** occurred in the polymer blend **P1/S1P** due to the lack of H-bonding interactions, which also can be confirmed by the red-shifted (33 nm) absorption of

polymer blend **P1/S1P** in contrast to that of H-bonded polymer complex **P1/S1** in solid films.

Since the best performance of PSC device (with the highest PCE value in Table 5.4) was fabricated by the blend of H-bonded polymer complex **P1/S3**:PCBM (1:1 w/w), the current-voltage characteristics of PSC devices as a function of the weight ratio in H-bonded complex and PCBM were surveyed, and their photovoltaic properties are shown in Figure 5.11 and Table 5.7. The optimum photovoltaic performance with the maximum PCE value of 0.50% ( $I_{sc} = 3.17 \text{ mA/cm}^2$ ,  $V_{oc} = 0.47 \text{ V}$ ,  $FF = 34\%$ ) was obtained in the PSC device having a weight ratio of **P1/S3**:PCBM=1:1. Using lower weight ratios of PCBM in blended H-bonded polymer complex **P1/S3**:PCBM (2:1 w/w) led to the reduction in  $I_{sc}$  values due to the inefficient charge separation and electron transporting properties by the possibly increased aggregation of H-bonded complex **P1/S3**, resulting in the lower PCE results.<sup>132</sup> However, loading larger weight ratios of PCBM in blended H-bonded polymer complex **P1/S3**:PCBM (1:2 and 1:4 w/w) also reduced the  $I_{sc}$  and PCE values, which could be probably attributed to the increased aggregation of PCBM so as to affect the separation of charges. Moreover, an unbalanced charge transporting property would be introduced due to the large PCBM ratio. Hence, both  $I_{sc}$  and PCE values decreased with larger PCBM molar ratios of 1:2 and 1:4 (w/w) because of the

two reasons described here.<sup>133</sup> Overall, the PSC device fabricated by H-bonded polymer complexes **P1/S3:PCBM** (1:1 w/w) reached the highest power conversion efficiency (PCE) of 0.50%, with a short circuit current density ( $I_{sc}$ ) of 3.17 mA/cm<sup>2</sup>, an open circuit voltage ( $V_{oc}$ ) of 0.47 V, and a fill factor ( $FF$ ) of 0.34.

**Table 5.4 Photovoltaic Properties of PSC Devices Containing an Active Layer of H-Bonded Polymer Complexes:PCBM = 1:1 (w/w) with a Device Configuration of ITO/PEDOT:PSS/H-Bonded Polymer Complexes:PCBM/Ca/Al<sup>a</sup>**

Active layer <sup>b</sup> H-Bonded Complexes:PCBM	$V_{oc}$ (V)	$I_{sc}$ (mA/cm <sup>2</sup> )	FF (%)	PCE (%)
<b>P1/S1</b>	0.59	1.67	27	0.28
<b>P1/S2</b>	0.54	1.72	28	0.26
<b>P1/S3</b>	0.47	3.17	34	0.50
<b>P1/S4</b>	0.43	1.70	26	0.19
<b>P2/S1</b>	0.58	0.95	24	0.13
<b>P2/S2</b>	0.53	0.42	27	0.06
<b>P2/S3</b>	0.51	2.29	28	0.32
<b>P2/S4</b>	0.38	0.73	24	0.07

<sup>a</sup> Measured under AM 1.5 irradiation, 100 mW/cm<sup>2</sup>.

<sup>b</sup> H-Bonded Polymer Complexes:PCBM = with the fixed weight ratio of 1:1 (w/w).

**Table 5.5 Photovoltaic Properties of PSC Devices Containing an Active Layer of Dyes S1-S4:PCBM = 1:1 (w/w) with a Device Configuration of ITO/PEDOT:PSS/Dyes S1-S4:PCBM/Ca/Al<sup>a</sup>**

Active layer <sup>b</sup> Dyes S1-S4:PCBM	$V_{oc}$ (V)	$I_{sc}$ (mA/cm <sup>2</sup> )	FF (%)	PCE (%)
<b>S1</b>	0.84	1.18	26	0.25
<b>S2</b>	0.59	1.10	25	0.16
<b>S3</b>	0.54	0.98	25	0.13
<b>S4</b>	0.26	0.73	27	0.05

<sup>a</sup> Measured under AM 1.5 irradiation, 100 mW/cm<sup>2</sup>.

<sup>b</sup> Dyes **S1-S4:PCBM** = with the fixed weight ratio of 1:1 (w/w).



**Table 5.6 Photovoltaic Properties of PSC Devices Containing an Active Layer of Mixture:PCBM = 1:1 (w/w) with a Device Configuration of ITO/PEDOT:PSS/Mixture:PCBM/Ca/Al<sup>a</sup>**

Active layer <sup>b</sup>	$V_{oc}$	$I_{sc}$	FF	PCE
Mixture:PCBM	(V)	(mA/cm <sup>2</sup> )	(%)	(%)
<b>P1/S1</b>	0.59	1.67	27	0.28
<b>P1/S1P</b>	0.52	1.57	20	0.16

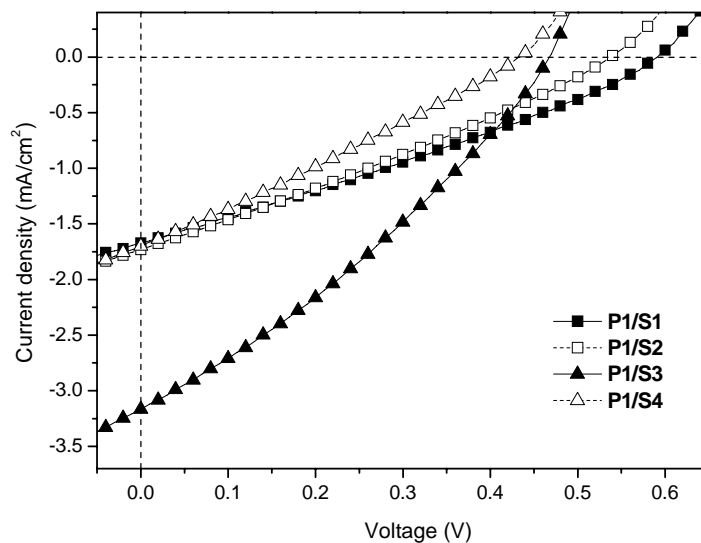
<sup>a</sup> Measured under AM 1.5 irradiation, 100 mW/cm<sup>2</sup>.

<sup>b</sup> **P1/S1** and **P1/S1P**:PCBM = with the fixed weight ratio of 1:1 (w/w).

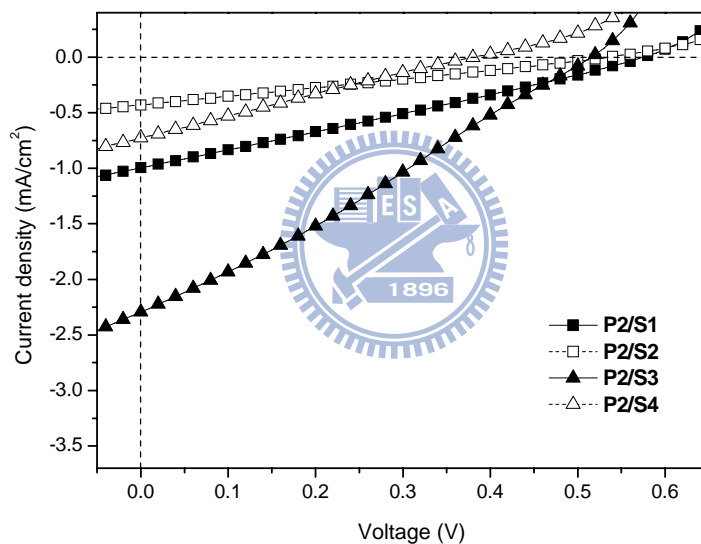
**Table 5.7 Photovoltaic Parameters for Bulk-Heterojunction PSC Devices Containing Different Weight Ratios of Blended H-Bonded Polymer Complex P1/S3:PCBM<sup>a</sup>**

Weight ratios of blended H-Bonded Complex	$V_{oc}$	$I_{sc}$	FF	PCE
P1/S3:PCBM	(V)	(mA/cm <sup>2</sup> )	(%)	(%)
2:1	0.46	2.90	20	0.40
1:1	0.47	3.17	34	0.50
1:2	0.45	2.23	30	0.28
1:4	0.44	1.70	33	0.25

<sup>a</sup> PSC devices with the configuration of ITO/PEDOT:PSS/H-Bonded Polymer Complex **P1/S3**:PCBM/Ca/Al containing an active blended layer composed of various weight ratios of H-Bonded Polymer Complex **P1/S3** and PCBM were measured under AM 1.5 irradiation, 100 mW/cm<sup>2</sup>.



(a)



(b)

**Figure 5.10** *I*-*V* curves (under simulated AM 1.5 solar irradiation) dependencies of PSC devices with an active layer of blended (a) H-bonded polymer complexes **P1/S1-P1/S4:PCBM** (1:1 w/w) and (b) H-bonded polymer complexes **P2/S1-P2/S4:PCBM** (1:1 w/w).

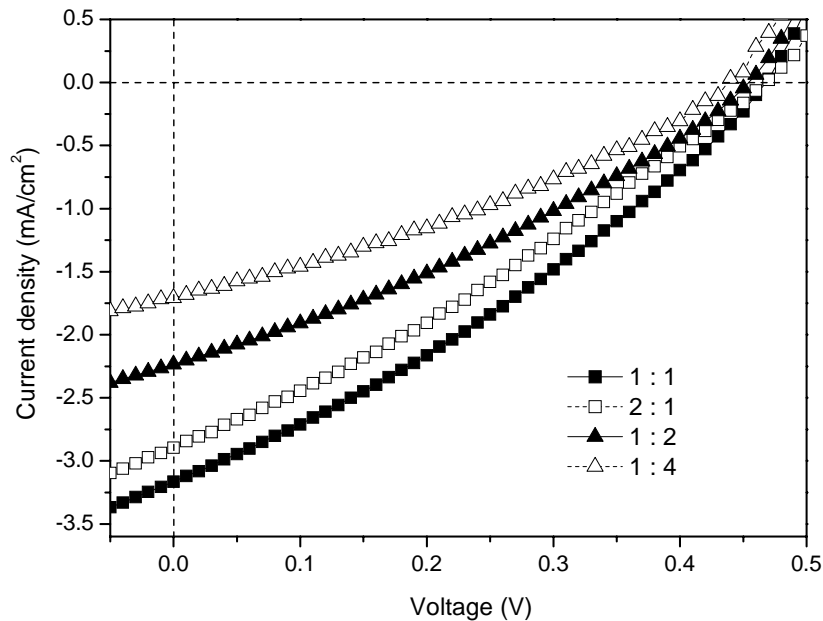


**Figure 5.11** *I-V* curves of PSC devices containing an active layer of H-bonded polymer complex **P1/S3**:PCBM (w/w) with different weight ratios under simulated AM 1.5 solar irradiation.

## 5.4 Conclusions

In conclusion, novel supramolecular side-chain polymers (i.e., H-bonded polymer complexes) were constructed by complexation of pyridyl H-acceptor polymers with low-band-gap H-donor dyes in a molar ratio of 1:1 for pyridyl and acid units, which would have much more uptaken loads of photovoltaic dyes in the supramolecular polymeric structures compared with the normal polymer blends. Due to the lack of supramolecular interactions, the larger aggregations of the acid-protected dyes occurred in the polymer blends, and thus a polymer blend (without H-bonds) containing conjugated H-acceptor polymer **P1** and acid-protected dye **S1P** illustrated an obvious reduction in the PCE value in contrast to the supramolecular analogue **P1/S1**. H-donor dyes (**S1-S4**) and H-acceptor polymers (**P1**

and **P2**) were utilized to control the mesomorphic, photophysical, and photovoltaic properties effectively by the concept of supramolecular architecture. The supramolecular architectures of H-bonded side-chain polymers were also confirmed by FTIR and XRD measurements. The nematic phase was observed by the introduction of various H-donor dyes and H-acceptor polymers with corresponding supramolecular side-chain structures. In addition, compared with H-donor dyes, the optical properties demonstrated that blue-shifted absorptions occurred in these H-bonded complexes as the H-donor dyes were complexed with H-acceptor polymers. Thus, the electrochemical properties of H-bonded complexes were adjusted by introducing electron-withdrawing cyano groups and electron-donating amine groups of H-donor dyes to the H-bonded complexes, which could reduce the HOMO energy levels and increase the LUMO energy levels of the H-bonded side-chain polymers, and thus to have narrower band-gaps than H-acceptor polymers. Due to the reduced content of low-band-gap dyes complexed with H-acceptor copolymer **P2**, the PCE values of H-bonded complexes **P2/S1-P2/S4** containing H-acceptor copolymer **P2** were apparently smaller than those of **P1/S1-P1/S4**, respectively. Preliminary PSC devices based on these H-bonded polymer complex **P1/S3** blended with PCBM acceptors (1:1 w/w) had the power conversion efficiency up to 0.50%, which gave the best performance with the values of  $I_{sc} = 3.17 \text{ mA/cm}^2$ ,  $V_{oc} = 0.47 \text{ V}$ , and  $FF = 34\%$ .

## Chapter 6

### Conclusion

In conclusion, first, H-donors (asymmetric mono-functional H-donors and symmetric bi-functional H-donor) and H-acceptor polymers were utilized to control the mesomorphic and photoluminescent properties effectively by the concept of supramolecular architecture. The H-acceptor copolymers were composed of different molar ratios of pendent N-vinylcarbazole units and light-emitting H-acceptor groups randomly to increase the glass transition temperatures and to reduce the  $\pi$ - $\pi$  stacking of the conjugated H-acceptor chromophores in the copolymers as well as in their H-bonded polymer complexes. The supramolecular architectures of H-bonded side-chain/cross-linking polymers were also confirmed by FTIR and XRD measurements. They have distinct mesomorphism and phase transition temperatures related to their supramolecular structures with different nonlinearities and rigidities. The mesomorphic properties were changed from the nematic phase to the smectic C phase by the introduction of H-bonds to the supramolecular polymers, and then shifted to the nematic and non-mesogenic phases by various H-donor acids and H-acceptor copolymers with corresponding supramolecular side-chain/cross-linking structures. In addition, the emission color of light-emitting H-acceptor polymers can be tuned by their surrounding non-emitting H-donors. Redder shifts in PL emissions

were observed in the H-bonded supramolecules with H-donors having smaller pKa values.

Second, the mesomorphic and photoluminescent properties of H-bonded copolymers and homopolymer complexes are affected by the isomeric H-donors with different acid-substituted (*para*-, *meta*-, and *ortho*-) positions. These H-bonded complexes can generate supramolecular architectures either by self-H-bonded copolymers or by  $\pi$ -conjugated H-acceptor homopolymers blended with H-donor homopolymers. The supramolecular structures have the nematic and smectic C phases that are related to their bent and linear H-bonded structures, respectively. The photoluminescent properties of self-H-bonded copolymers, as well as the H-bonded homopolymer complexes, can be tuned by the isomeric H-donor moieties, and red-shifted PL emissions are expected in the H-bonded structures. Supramolecular architectures that contain H-bonds in self-H-bonded copolymers **P1-P3** and H-bonded homopolymer complexes **PBT1/P7-P9** are further confirmed by FT-IR spectroscopy and XRD measurements. Furthermore, the H-bonding interactions between acid-modified gold nanoparticles (**AuSCOOH**) and acid-protected copolymer **P4** affect the fluorescence quenching more effectively, when compared with fluorescence titrations of acid-free-modified gold nanoparticles (**AuSC10**). Moreover, in contrast to the self-H-bonded copolymer **P1**, the acid-protected copolymer **P4** more readily

captures acid-modified gold nanoparticles (**AuSCOOH**) in the supramolecular assembly of nanocomposites. The H-bonding interactions between the pyridyl H-acceptor (from the copolymers) and the acid H-donor units (from both nanoparticles and copolymers) can explain the similarities in fluorescence quenching effects on both copolymers **P1** and **P4**. Various nanocomposites containing two kinds of fluorescent copolymer counterparts (self-H-bonded copolymer **P1** and acid-protected copolymer **P4**) and surface-modified nanoparticles (acid-modified **AuSCOOH** and acid-free-modified **AuSC10**) were developed to display distinct aggregation phenomena in TEM images. The pyridyl H-acceptor units of copolymer **P1** would not only bind with its own *para*-benzoic acid groups but also with the other proton donor surfactants from **AuSCOOH** nanoparticles. Overall, this study is the first to explore the supramolecular assembly behavior of nanocomposites between fluorescent copolymers and surface-functionalized gold nanoparticles via both PL quenching phenomena and TEM morphologies. Based on the fluorescence quenching and recovery of gold nanocomposites, further chemosensor and biosensor applications of this study can be developed in the near future.

Third, supramolecular nanocomposites containing two series fluorescent polymers with different pyridyl content, lateral methyl-substituted polymers **PBT1-PBT3** and lateral methoxyl-substituted polymers **PBOT1-PBOT3**, and donor

nanoparticles were developed to display distinct aggregation phenomena in TEM images. H-acceptor polymers **PBT1-PBOT3** would not only display highly aggregation but also well dispersion with the proton donor surfactants from nanoparticles **AuSCOOH**. Furthermore, the H-bonding interactions between acid-modified gold nanoparticles (**AuSCOOH**) and lateral methoxyl-substituted polymer **PBOT1** affect the fluorescence quenching more effectively, when compared with fluorescence titrations of acid-free-modified gold nanoparticles (**AuSC10**). Moreover, in contrast to the lateral methyl-substituted polymer **PBT1**, lateral methoxyl-substituted polymer **PBOT1** more readily captures acid-modified gold nanoparticles (**AuSCOOH**) in the supramolecular assembly of nanocomposites. The H-bonding interactions between the pyridyl H-acceptor (from the polymers) and the acid H-donor units (from both nanoparticles and polymers) can explain the similarities in fluorescence quenching effects on both polymers **PBOT1** and **PBT1**. Moreover, we established the exponential equation to predict Stern-Volmer constant in various pyridyl units of polymers according to these experimental information. Various nanocomposites containing two kinds of fluorescent polymer counterparts (methoxyl-substituted polymer **PBOT1** and methyl-substituted polymer **PBT1**) and surface-modified nanoparticles (acid-modified **AuSCOOH** and acid-free-modified **AuSC10**) were developed to display distinct aggregation phenomena in TEM images.



Based on the fluorescence quenching and recovery of gold nanocomposites, further chemosensor and biosensor applications of this study can be developed in the near future.

Finally, novel supramolecular side-chain polymers (i.e., H-bonded polymer complexes) were constructed by complexation of pyridyl H-acceptor polymers with low-band-gap H-donor dyes in a molar ratio of 1:1 for pyridyl and acid units, which would have much more uptaken loads of photovoltaic dyes in the supramolecular polymeric structures compared with the normal polymer blends. Due to the lack of supramolecular interactions, the larger aggregations of the acid-protected dyes occurred in the polymer blends, and thus a polymer blend (without H-bonds) containing conjugated H-acceptor polymer **P1** and acid-protected dye **S1P** illustrated an obvious reduction in the PCE value in contrast to the supramolecular analogue **P1/S1**. H-donor dyes (**S1-S4**) and H-acceptor polymers (**P1** and **P2**) were utilized to control the mesomorphic, photophysical, and photovoltaic properties effectively by the concept of supramolecular architecture. The supramolecular architectures of H-bonded side-chain polymers were also confirmed by FTIR and XRD measurements. The nematic phase was observed by the introduction of various H-donor dyes and H-acceptor polymers with corresponding supramolecular side-chain structures. In addition, compared with H-donor dyes, the optical properties demonstrated that

blue-shifted absorptions occurred in these H-bonded complexes as the H-donor dyes were complexed with H-acceptor polymers. Thus, the electrochemical properties of H-bonded complexes were adjusted by introducing electron-withdrawing cyano groups and electron-donating amine groups of H-donor dyes to the H-bonded complexes, which could reduce the HOMO energy levels and increase the LUMO energy levels of the H-bonded side-chain polymers, and thus to have narrower band-gaps than H-acceptor polymers. Due to the reduced content of low-band-gap dyes complexed with H-acceptor copolymer **P2**, the PCE values of H-bonded complexes **P2/S1-P2/S4** containing H-acceptor copolymer **P2** were apparently smaller than those of **P1/S1-P1/S4**, respectively. Preliminary PSC devices based on these H-bonded polymer complex **P1/S3** blended with PCBM acceptors (1:1 w/w) had the power conversion efficiency up to 0.50%, which gave the best performance with the values of  $I_{sc} = 3.17 \text{ mA/cm}^2$ ,  $V_{oc} = 0.47 \text{ V}$ , and  $FF = 34\%$ .

## References

- (1) *Supramolecular Polymers*; Ciferri, A., Ed.; Marcel Dekker: New York, **2000**.
- (2) Moore, J. S. *Curr. Opin. Colloid Interface Sci.* **1999**, *4*, 108-116.
- (3) Zimmerman, N.; Moore, J. S.; Zimmerman, S. C. *Chem. Ind.* **1998**, 604.
- (4) (a) Brunsveld, L.; Folmer, B. J. B.; Meijer, E. W. *MRS Bull.* **2000**, *25*, 49. (b) Brunsveld, L. Folmer, B. J. B. Meijer, E. W. Sijbesma, R. P. *Chem. Rev.* **2001**, *101*, 4071. (c) Hofmeier, H.; Schubert, U. S. *Chem. Commun.* **2005**, 2423.
- (5) Ciferri, A. *Liq. Cryst.* **1999**, *26*, 489.
- (6) Imrie, C. T. *Trends Polym. Sci.* **1995**, *3*, 22.
- (7) Odijk, T. *J. Phys. (Paris)* **1987**, *48*, 125.
- (8) Odijk, T. *Curr. Opin. Colloid Interface Sci.* **1996**, *1*, 337.
- (9) Van der Schoot, P. *J. Phys. II* **1995**, *5*, 243.
- (10) Ciferri, A. *Macromol. Rapid Commun.* **2002**, *23*, 511.
- (11) Fouquey, C.; Lehn, J.-M.; Levelut, A.-M. *Adv. Mater.* **1990**, *2*, 254.
- (12) Lehn, J.-M. *Makromol. Chem., Macromol. Symp.* **1993**, *69*, 1.
- (13) Gulik-Krczywicki, T.; Fouquey, C.; Lehn, J.-M. *Proc. Natl. Acad. Sci. U.S.A.* **1993**, *90*, 163.
- (14) Kotera, M.; Lehn, J.-M.; Vigneron, J.-P. *J. Chem. Soc. Chem. Commun.* **1994**, 197.

- (15) Kotera, M.; Lehn, J.-M.; Vigneron, J.-P. *Tetrahedron* **1995**, *51*, 1953.
- (16) Aoki, K.-I.; Nakagawa, M.; Ichimura, K. *Chem. Lett.* **1999**, *11*, 1205.
- (17) (a) Lee, J. Y.; Painter, P. C.; Coleman, M. M. *Macromolecules* **1988**, *21*, 954. (b)  
Odinokov, S. E.; Mashkovshky, A. A.; Glazunov, V. P.; Iogansen, A. V.;  
Rassadin, B. V. *Spectrochim. Acta* **1976**, *32A*, 1355.
- (18) Kumar, U.; Kato, T.; Fréchet, J. M. J. *J. Am. Chem. Soc.* **1992**, *114*, 6630.
- (19) Kato, T.; Kihara, H.; Kumar, U.; Uryu, T.; Fréchet, J. M. J. *Angew. Chem., Int.  
Ed.* **1994**, *33*, 1644.
- (20) Ambrozic, G.; Zigon, M. *Macromol. Rapid Commun.* **2000**, *21*, 53.
- (21) Kato, T. *Supramol. Sci.* **1996**, *3*, 53.
- (22) Kato, T.; Nakano, M.; Moteki, T.; Uryu, T.; Ujiie, S. *Macromolecules* **1995**, *28*,  
8875.
- (23) Lee, C.-M.; Jariwala, C. P.; Griffin, A. C. *Polymer* **1994**, *35*, 4550.
- (24) Lee, C.-M.; Griffin, A. C. *Macromol. Symp.* **1997**, *117*, 281.
- (25) Alexander, C.; Jariwala, C. P.; Lee, C. M.; Griffin, A. C. *Macromol. Symp.* **1994**,  
*77*, 283.
- (26) He, C.; Donald, A. M.; Griffin, A. C.; Waigh, T.; Windle, A. H. *J. Polym. Sci.  
Part B: Polym. Phys.* **1998**, *36*, 1617.
- (27) Lee, M.; Cho, B.-K.; Kang, Y.-S.; Zin, W.-C. *Macromolecules* **1999**, *32*, 8531.

- (28) Singh, A.; Lvov, Y.; Qadri, S. B. *Chem. Mater.* **1999**, *11*, 3196.
- (29) He, C.; Lee, C.-M.; Griffin, A. C.; Bouteiller, L.; Lacoudre, N.; Boileau, S.; Fouquey, C.; Lehn, J.-M. *Mol. Cryst. Liq. Cryst. Sci. Technol., Sec. A* **1999**, *332*, 251.
- (30) (a) McQuade, D. T.; Pullen, A. E.; Swager, T. M. *Chem. Rev.* **2000**, *100*, 2537.  
(b) Thomas III, S. W.; Joly, G. D.; Swager, T. M. *Chem. Rev.* **2007**, *107*, 1339.
- (31) (a) Zhou, Q.; Swager, T. M. *J. Am. Chem. Soc.* **1995**, *117*, 7017. (b) Chen, L.; McBranch, D. W.; Wang, H.-L.; Helgeson, R.; Wudl, F.; Whitten, D. G. *Proc. Natl. Acad. Sci. U.S.A.* **1999**, *96*, 12287. (c) Heeger, P. S.; Heeger, A. J. *Proc. Natl. Acad. Sci. U.S.A.* **1999**, *96*, 12219.
- (32) Swager, T. M. *Acc. Chem. Res.* **1998**, *31*, 201.
- (33) (a) Sastry, M.; Rao, M.; Ganesh, K. N. *Acc. Chem. Res.* **2002**, *35*, 847. (b) Daniel, M. C.; Astruc, D. *Chem. Rev.* **2004**, *104*, 293. (c) Burda, C.; Chen, X.; Narayanan, R.; El-Sayed, M. A. *Chem. Rev.* **2005**, *105*, 1025.
- (34) Boal, A. K.; Rotello, V. M. *J. Am. Chem. Soc.* **2002**, *124*, 5019.
- (35) Fullam, S.; Rao, S. N.; Fitzmaurice, D. *J. Phys. Chem. B* **2000**, *104*, 6164.
- (36) Pawsey, S.; McCormick, M.; De Paul, S.; Graf, R.; Lee, Y. S.; Reven, L.; Spiess, H. W. *J. Am. Chem. Soc.* **2003**, *125*, 4174.
- (37) Zheng, W.; Maye, M. M.; Leibowitz, F. L.; Zhong, C.-J. *Analyst* **2000**, *125*, 17.

- (38) Zhang, F. X.; Zheng, W.; Maye, M. M.; Lou, Y.; Li, H.; Zhong, C.-J. *Langmuir* **2000**, *16*, 9639.
- (39) Yonezawa, T.; Onoue, S.-Y.; Kimizuka, N. *Chem. Lett.* **2002**, 528.
- (40) Fitzmaurice, D.; Rao, S. N.; Preece, J. A.; Stoddart, J. F.; Wenger, S.; Zaccheroni, N. *Angew. Chem., Int. Ed.* **1999**, *38*, 1147.
- (41) Hicks, J. F.; Shon, Y. S.; Murray, R. W. *Langmuir* **2002**, *18*, 2288.
- (42) Kumar, A.; Mandale, A. B.; Sastry, M. *Langmuir* **2000**, *16*, 6921.
- (43) Schmid, G.; Bäumle, M.; Beyer, N. *Angew. Chem., Int. Ed.* **2000**, *39*, 181.
- (44) Boal, A. K.; Rotello, V. M. *Langmuir* **2000**, *16*, 9527.
- (45) (a) Carroll, J. B.; Frankamp, B. L.; Rotello, V. M. *Chem. Commun.* **2002**, 1892.  
(b) Shenhar, R.; Rotello, V. M. *Acc. Chem. Res.* **2003**, *36*, 549.
- (46) Paulini, R.; Frankamp, B. L.; Rotello, V. M. *Langmuir* **2002**, *18*, 2368.
- (47) Zhang, Z.; Berg, A.; Levanon, H.; Fessenden, R. W.; Meisel, D. *J. Am. Chem. Soc.* **2003**, *125*, 7959.
- (48) (a) Lehn, J.-M. *Supramolecular Chemistry: Concepts and Perspectives*; VCH: Weinheim, **1995**. (b) Boal, A.; Ilhan, F.; Derouchey, J. E.; Thurn-Albrecht, T.; Russell, T. P.; Rotello, V. M. *Nature* **2000**, *404*, 746. (c) Jin, J.; Iyoda, T.; Cao, C.; Song, Y.; Jiang, L.; Li, T. J.; Zhu, D. B. *Angew. Chem., Int. Ed.* **2001**, *40*, 2135. (d) Liu, J.; Mendoza, S.; Roman, E.; Lynn, M. J.; Xu, R.; Kaifer, A. E. *J.*

- Am. Chem. Soc.* **1999**, *121*, 4304. (e) Patil, V.; Mayya, K. S.; Pradhan, S. D.; Satry, M. *J. Am. Chem. Soc.* **1997**, *119*, 9281. (f) Caruso, F.; Caruso, R. A.; Mohwald, H. *Science* **1998**, *282*, 1111. (g) Naka, K.; Itoh, H.; Chujo, Y. *Langmuir* **2003**, *19*, 5496. (h) Shenton, W.; Davies, S. A.; Mann, S. *Adv. Mater.* **1999**, *11*, 449.
- (49) Watanabe, S.; Sonobe, M.; Arai, M.; Tazume, Y.; Matsuo, T.; Nakamura, T.; Yoshida, K. *Chem. Commun.* **2002**, 2866.
- (50) (a) Lin, S.-Y.; Liu, S.-W.; Lin, C.-M.; Chen, C.-H. *Anal. Chem.* **2002**, *74*, 330.  
(b) Obare, S. O.; Hollowell, R. E.; Murphy, C. J. *Langmuir* **2002**, *18*, 10407.
- (51) *Metal Nanoparticles Synthesis, Characterization and Applications*; Feldheim, D. L., Colby, A. F., Jr., Eds.; Marcel Dekker: New York, **2002**.
- (52) Kim, Y.; Johnson, R. C.; Hupp, J. T. *Nano Lett.* **2001**, *1*, 165.
- (53) (a) Frankamp, B. L.; Uzun, O.; Ilhan, F.; Boal, A. K.; Rotello, V. M. *J. Am. Chem. Soc.* **2002**, *124*, 892. (b) Uzun, O.; Frankamp, B. L.; Sanyal, A.; Rotello, V. M. *Chem. Mater.* **2006**, *18*, 5404.
- (54) (a) Boal, A. K.; Galow, T. H.; Ilhan, F.; Rotello, V. M. *Adv. Funct. Mater.* **2001**, *11*, 461. (b) Cooke, G.; Garety, J. F.; Hewage, S. G.; Rabani, G.; Rotello, V. M.; Woisel, P. *Chem. Commun.* **2006**, 4119. (c) Carroll, J. B.; Frankamp, B. L.; Srivastava, S.; Rotello, V. M. *J. Mater. Chem.* **2004**, *14*, 690.

- (55) (a) Zhang, H.-L.; Evans, S. D.; Henderson, J. R.; Miles, R. E.; Shen, T.-H. *Nanotechnology* **2002**, *13*, 439. (b) Evans, S. D.; Johnson, S. R.; Cheng, Y. L.; Shen, T. *J. Mater. Chem.* **2000**, *10*, 183. (c) Ozsoz, M.; Erdem, A.; Kerman, K.; Ozkan, D.; Tugrul, B.; Topcuoglu, N.; Ekren, H.; Taylan, M. *Anal. Chem.* **2003**, *75*, 2181. (d) Liu, J.; Lu, Y. *J. Am. Chem. Soc.* **2003**, *125*, 6642. (e) Fantuzzi, G.; Pengo, P.; Gomila, R.; Ballester, P.; Hunter, C. A.; Pasquato, L.; Scrimin, P. *Chem. Commun.* **2003**, 1004.
- (56) Xu, H.; Käll, M. *Sens. Actuators B* **2002**, *87*, 244.
- (57) Gill, R.; Willner, I.; Shweky, I.; Banin, U. *J. Phys. Chem. B* **2005**, *109*, 23715.
- (58) (a) He, X.; Liu, H.; Li, Y.; Wang, S.; Li, Y.; Wang, N.; Xiao, J.; Xu, X.; Zhu, D. *Adv. Mater.* **2005**, *17*, 2811. (b) Zhou, X. H.; Yan, J. C.; Pei, J. *Macromolecules* **2004**, *37*, 7078. (c) He, X.; Zhong, Z.; Guo, Y.; Lv, J.; Xu, J.; Zhu, M.; Li, Y.; Liu, H.; Wang, S.; Zhu, Y.; Zhu, D. *Langmuir* **2007**, *23*, 8815.
- (59) Romaner, L.; Pogantsch, A.; Scandiucci de Freitas, P.; Scherf, U.; Gaal, M.; Zojer, E.; List, E. J. W. *Adv. Funct. Mater.* **2003**, *13*, 597.
- (60) Iqbal, R.; Moratti, S. C.; Holmes, A. B.; Yahioğlu, G.; Milgrom, L. R.; Cacialli, F.; Morgado, J.; Friend, R. H. *J. Mater. Sci. Mater. El.* **2000**, *11*, 97.
- (61) Russell, D. M.; Arias, A. C.; Friend, R. H.; Silva, C.; Ego, C.; Grimsdale, A. C.; Müllen, K. *Appl. Phys. Lett.* **2002**, *80*, 2204.



- (62) Liu, Y.; Xiao, S.; Li, H.; Li, Y.; Liu, H.; Lu, F.; Zhuang, J.; Zhu, D. *J. Phys. Chem. B* **2004**, *108*, 6256.
- (63) Duprez, V.; Biancardo, M.; Spanggaard, H.; Krebs, F. C. *Macromolecules* **2005**, *38*, 10436.
- (64) Troshin, P. A.; Koeppe, R.; Peregudov, A. S.; Peregudova, S. M.; Egginger, M.; Lyubovskaya, R. N.; Sariciftci, N. S. *Chem. Mater.* **2007**, *19*, 5363.
- (65) (a) Lehn, J. M. *Science* **2002**, *295*, 2400. (b) Ikkala, O.; ten Brinke, G. *Science* **2002**, *295*, 2407. (c) Stupp, S. I.; Son, S.; Lin, H.-C.; Li, L.-S. *Science* **1993**, *259*, 59. (d) Ajayaghosh, A.; Praveen, V. K. *Acc. Chem. Res.* **2007**, *40*, 644.
- (66) (a) Wessendorf, F.; Gnichwitz, J.-F.; Sarova, G. H.; Hager, K.; Hartnagel, U.; Guldi, D. M.; Hirsch, A. *J. Am. Chem. Soc.* **2007**, *129*, 16057. (b) Nair, K. P.; Breedveld, V.; Weck, M. *Macromolecules* **2008**, *41*, 3429. (c) Sievers, T. K.; Vergin, A.; Möhwald, H.; Kurth, D. G. *Langmuir* **2007**, *23*, 12179. (d) Kim, J.-H.; Rahman, M. S.; Lee, J.-S.; Park, J.-W. *Macromolecules* **2008**, *41*, 3181. (e) Nair, K. P.; Weck, M. *Macromolecules* **2007**, *40*, 211. (f) Nair, K. P.; Pollino, J. M.; Weck, M. *Macromolecules* **2006**, *39*, 931. (g) South, C. R.; Burd, C.; Weck, M. *Acc. Chem. Res.* **2007**, *40*, 63. (h) Broeren, M. A. C.; Linhardt, J. G.; Malda, H.; de Waal, B. F. M.; Versteegen, R. M.; Meijer, J. T.; Löwik, D. W. P. M.; van Hest, J. C. M.; van Genderen, M. H. P.; Meijer, E. W. *J. Polym. Sci. Part A:*

- Polym. Chem.* **2005**, *43*, 6431. (i) Montarnal, D.; Cordier, P.; Soulié-Ziakovic, C.; Tournilhac, F.; Leibler, L. *J. Polym. Sci. Part A: Polym. Chem.* **2008**, *46*, 7925-.
- (j) Vellis, P. D.; Mikroyannidis, J. A.; Lo, C. N.; Hsu C. S. *J. Polym. Sci. Part A: Polym. Chem.* **2008**, *46*, 7702. (k) Cheng, C. C.; Huang, C. F.; Yen, Y. C.; Chang, F. C. *J. Polym. Sci. Part A: Polym. Chem.* **2008**, *46*, 6416. (l) Coluccini, C.; Metrangolo, P.; Parachini, M.; Pasini, D.; Resnati, G.; Righetti, P. *J. Polym. Sci. Part A: Polym. Chem.* **2008**, *46*, 5202. (m) Bosman, A. W.; Sijbesma, R. P. *J. Polym. Sci. Part A: Polym. Chem.* **2008**, *46*, 3877. (n) Aamer, K. A.; Tew, G. N. *J. Polym. Sci. Part A: Polym. Chem.* **2007**, *45*, 1109. (o) Stefopoulos, A. A.; Pefkianakis, E. K.; Papagelis, K.; Andreopoulou, A. K.; Kallitsis, J. K. *J. Polym. Sci. Part A: Polym. Chem.* **2009**, *47*, 2551.
- (67) (a) Kato, T.; Hirota, N.; Fujishima, A.; Fréchet, J. M. J. *J. Polym. Sci. Part A: Polym. Chem.* **1996**, *34*, 57. (b) Kato, T.; Fréchet, J. M. J. Wilson, P. G.; Saito, T.; Uryu, T. Fujishima, A.; Jin, C.; Kaneuchi, F. *Chem. Mater.* **1993**, *5*, 1094. (c) Kato, T.; Mizoshita, N.; Kishimoto, K. *Angew. Chem., Int. Ed.* **2006**, *45*, 38. (d) Kato, T.; Fréchet, J. M. J. *Macromol. Symp.* **1995**, *98*, 311. (e) Kato, T.; Fukumasa, M.; Fréchet, J. M. J. *Chem. Mater.* **1995**, *7*, 368.
- (68) (a) Gimeno, N.; Ros, M. B.; Serrano, J. L.; De la Fuente, M. R. *Chem. Mater.* **2008**, *20*, 1262. (b) Vera, F.; Almuzara, C.; Orera, I.; Barberá, J.; Oriol, L.;

- Serrano, J. L.; Sierra, T. *J. Polym. Sci. Part A: Polym. Chem.* **2008**, *46*, 5528. (c)
- Ma, X. J.; Shen, Y. T.; Deng, K.; Tang, H.; Lei, S. B.; Wang, C.; Yang, Y. L.;  
Feng, X. Z. *J. Mater. Chem.* **2007**, *17*, 4699. (d) Xu, J.; Toh, C. L.; He, C. *J.*  
*Polym. Sci. Part A: Polym. Chem.* **2008**, *46*, 4691. (e) Burke, K. A.; Sivakova,  
S.; McKenzie, B. M.; Mather, P. T. Rowan, S. J. *J. Polym. Sci. Part A: Polym.*  
*Chem.* **2006**, *44*, 5049. (f) Vera, F.; Tejedor, R. M.; Romero, P.; Barberá, J.; Ros,  
M. B.; Serrano, J. L.; Sierra, T. *Angew. Chem., Int. Ed.* **2007**, *46*, 1873. (g)  
Álvarez, L.; Barberá, J.; Puig, L.; Romero, P.; Serrano, J. L.; Sierra, T. *J. Mater.*  
*Chem.* **2006**, *16*, 3768. (h) Barberá, J.; Puig, L.; Romero, P.; Serrano, J. L.;  
Sierra, T. *J. Am. Chem. Soc.* **2006**, *128*, 4487.
- (69) (a) Huang, W.; Han, C. D. *Macromolecules* **2006**, *39*, 4735. (b) Huang, W.; Han,  
C. D. *Macromolecules* **2006**, *39*, 257. (c) Lee, K. M.; Han, C. D. *Polymer* **2003**,  
*44*, 4573. (d) Kim, S. S.; Han, C. D. *Polymer* **1994**, *35*, 93. (e) Xu, J.; Toh, C. L.;  
Liu, X.; Wang, S.; He, C.; Lu, X. *Macromolecules* **2005**, *38*, 1684. (f) Toh, C. L.;  
Xu, J.; Liu, X.; Lu, X.; He, C. *J. Polym. Sci. Part A: Polym. Chem.* **2005**, *43*,  
4731. (g) Cui, L.; Dahmane, S.; Tong, X.; Zhu, L.; Zhao, Y. *Macromolecules*  
**2005**, *38*, 2076. (h) Cui, L.; Zhao, Y. *Chem. Mater.* **2004**, *16*, 2076. (i) Aubertin,  
F.; Zhao, Y. *J. Polym. Sci. Part A: Polym. Chem.* **2004**, *42*, 3445. (j) Bo, Q.;  
Zhao, Y. *J. Polym. Sci. Part A: Polym. Chem.* **2006**, *44*, 1734. (k) Medvedev, A.

- V.; Barmatov, E. B.; Medvedev, A. S.; Shibaev, V. P.; Ivanov, S. A.; Kozlovsky, M.; Stumpe, J. *Macromolecules* **2005**, *38*, 2223. (l) van Zoelen, W.; Alberda van Ekenstein, Z.; Ikkala, O.; ten Brinke, G. *Macromolecules* **2006**, *39*, 6574. (m) Xu, J.; Liu, X.; Lin, T.; Huang, J.; He, C. *Macromolecules* **2005**, *38*, 3554. (n) Hua, F.; Yang, X.; Gong, B.; Ruckenstein, E. *J. Polym. Sci. Part A: Polym. Chem.* **2005**, *43*, 1119.
- (70) (a) Chen, Y. Y.; Tao, Y. T.; Lin, H. C. *Macromolecules* **2006**, *39*, 8559. (b) Chen, Y. Y.; Lin, H. C. *J. Polym. Sci. Part A: Polym. Chem.* **2007**, *45*, 3243. (c) Lin, H. C.; Lin, Y. S.; Lin, Y. S.; Chen, Y. T.; Chao, I.; Li, T. W. *Macromolecules* **1998**, *31*, 7298.
- (71) Burroughes, J. H.; Bradley, D. C.; Brown, A. R.; Marks, R. N.; Mackay, K.; Friend, R. H.; Burn, P. L.; Holmes, A. B. *Nature* **1990**, *347*, 539.
- (72) Yang, Z.; Sokolik, I.; Karasz, F. E. *Macromolecules* **1993**, *26*, 1188.
- (73) Hu, B.; Yang, Z.; Karasz, F. E. *J. Appl. Phys.* **1994**, *76*, 2419.
- (74) Wang, G.; Yuan, C.; Wu, H.; Wei, Y. *J. Appl. Phys.* **1995**, *78*, 2679.
- (75) Romero, D. B.; Schaer, M.; Zuppiroli, L.; Leclerc, M.; Adès, D.; Siove, A. *Synth. Met.* **1996**, *80*, 271.
- (76) Lin, H. C.; Tsai, C. M.; Huang, G. H.; Tao, Y. T. *Macromolecules* **2006**, *39*, 557.
- (77) Wu, C. W.; Lin, H. C. *Macromolecules* **2006**, *39*, 7985.

- (78) Lin, H. C.; Sheu, H. Y.; Chang, C. L.; Tsai, C. *J. Mater. Chem.* **2001**, *11*, 2958.
- (79) Yang, P. J.; Wu, C. W.; Sahu, D.; Lin, H. C. *Macromolecules* **2008**, *41*, 9692.
- (80) Eaton, D. *Pure. Appl. Chem.* **1998**, *60*, 1107.
- (81) Cui, L.; Lattermann, G. *Macromol. Chem. Phys.* **2002**, *203*, 2432.
- (82) Sun, Y. P.; Ma, B.; Bunker, C. E. *J. Phys. Chem. A* **1998**, *102*, 7580.
- (83) (a) Li, X. J.; Wen, R. B.; Zhang, Y.; Zhu, L. R.; Zhang, B. L.; Zhang, H. Q. *J. Mater. Chem.* **2009**, *19*, 236. (b) Kajitani, T.; Kohmoto, S.; Yamamoto, M.; Kishikawa, K. *J. Mater. Chem.* **2004**, *14*, 3449. (c) Pisula, W.; Tomović, Ž.; Wegner, M.; Graf, R.; Pouderoijen, M. J.; Meijer, E. W.; Schenning, A. P. H. J. *J. Mater. Chem.* **2008**, *18*, 2968. (d) Liang, Y. G.; Wang, H. B.; Yuan, S. W.; Lee, Y. G.; Gan, L.; Yu, L. P. *J. Mater. Chem.* **2007**, *17*, 2183. (e) Kato, T.; Matsuoka, T.; Nishii, M.; Kamikawa, Y.; Kanie, K.; Nishimura, T.; Yashima, E.; Ujiiie, S. *Angew. Chem., Int. Ed.* **2004**, *43*, 1969. (f) Mamlouk, H. Heinrich, B. Bourgoigne, C. Donnio, B. Guillon, D. Felder-Flesch, D. *J. Mater. Chem.* **2007**, *17*, 2199.
- (84) Wanunu, M.; Biro, R. P.; Cohen, H.; Vaskevich, A.; Rubinstein, I. *J. Am. Chem. Soc.* **2005**, *127*, 9207.
- (85) (a) Fan, L.-J.; Jones Jr., W. E. *J. Am. Chem. Soc.* **2006**, *128*, 6784. (b) Martínez-Mañez, R.; Sancenón, F. *Chem. Rev.* **2003**, *103*, 4419. (c) Broadwater,

- S. J.; Hickey, M. K.; McQuade, D. T. *J. Am. Chem. Soc.* **2003**, *125*, 11154. (d)
- Fan, L. J.; Jones Jr., W. E. *J. Phys. Chem. B* **2006**, *110*, 7777. (e) Trabolsi, A.; Elhabiri, M.; Urbani, M.; de la Cruz, J. L. D.; Ajamaa, F.; Solladié, N.; Albrecht-Gary, A.-M.; Nierengarten, J. F. *Chem. Commun.* **2005**, 5736.
- (86) (a) Li, H. R.; Valiyaveetil, S. *Macromolecules* **2007**, *40*, 6057. (b) Nurmawati, M. H.; Ajikumar, P. K.; Heng, L. A.; Li, H. R.; Valiyaveetil, S. *Chem. Commun.* **2008**, 4945. (c) Tan, C.; Pinto, M. R.; Schanze, K. S. *Chem. Commun.* **2002**, 446.
- (87) (a) Harrison, B. S.; Ramey, M. B.; Reynolds, J. R.; Schanze, K. S. *J. Am. Chem. Soc.* **2000**, *122*, 8561. (b) Binder, W. H.; Sachsenhofer, R.; Straif, C. J.; Zirbs, R. *J. Mater. Chem.* **2007**, *17*, 2125. (c) Fan, C.; Plaxco, K. W.; Heeger, A. J. *J. Am. Chem. Soc.* **2002**, *124*, 5642. (d) McCullough, R. D.; Ewbank, P. C.; Loewe, R. S. *J. Am. Chem. Soc.* **1997**, *119*, 633. (e) Gaylord, B. S.; Heeger, A. J.; Bazan, G. C. *J. Am. Chem. Soc.* **2003**, *125*, 896. (f) Kim, J.; McQuade, D. T.; McHugh, S. K.; Swager, T. M. *Angew. Chem., Int. Ed.* **2000**, *39*, 3868. (g) Kimura, M.; Horai, T.; Hanabusa, K.; Shirai, H. *Adv. Mater.* **1998**, *10*, 459.
- (88) (a) Thomas, K. G.; Kamat, P. V. *Acc. Chem. Res.* **2003**, *36*, 888. (b) Bayir, A.; Jordan, B. J.; Verma, A.; Pollier, M. A.; Cooke, G.; Rotello, V. M. *Chem. Commun.* **2006**, 4033. (c) Barazzouk, S.; Kamat, P. V.; Hotchandani, S. *J. Phys.*

- Chem. B* **2005**, *109*, 716. (d) Hasobe, T.; Saito, K.; Kamat, P. V.; Troiani, V.; Qiu, H.; Solladié, N.; Kim, K. S.; Park, J. K.; Kim, D.; D'Souza, F.; Fukuzumi, S. *J. Mater. Chem.* **2007**, *17*, 4160. (e) Gadenne, B.; Yildiz, I.; Amelia, M.; Ciesa, F.; Secchi, A.; Arduini, A.; Credi, A.; Raymo, F. M. *J. Mater. Chem.* **2008**, *18*, 2022. (f) Leung, A. C. W.; MacLachlan, M. J. *J. Mater. Chem.* **2007**, *17*, 1923. (g) Tong, H.; Wang, L.; Jing, X.; Wang, F. *Macromolecules* **2003**, *36*, 2584. (h) Wang, D.; Wang, J.; Moses, D.; Bazan, G. C.; Heeger, A. J. *Langmuir* **2001**, *17*, 1262.
- (89) (a) Sih, B. C.; Wolf, M. O. *Chem. Commun.* **2005**, 3375. (b) Corbierre, M. K.; Cameron, N. S.; Sutton, M.; Mochrie, S. G. J.; Lurio, L. B.; Rühm, A.; Lennox, R. B. *J. Am. Chem. Soc.* **2001**, *123*, 10411.
- (90) (a) Huang, T.; Murray, R. W. *Langmuir* **2002**, *18*, 7077. (b) Cheng, P. P. H.; Silvester, D.; Wang, G.; Kalyuzhny, G.; Douglas, A.; Murray, R. W. *J. Phys. Chem. B* **2006**, *110*, 4637.
- (91) Ipe, B. I.; Thomas, K. G.; Barazzouk, S.; Hotchandani, S.; Kamat, P. V. *J. Phys. Chem. B* **2002**, *106*, 18.
- (92) Liang, T. C.; Lin, H. C. *J. Polym. Sci. Part A: Polym. Chem.* **2009**, *47*, 2734.
- (93) Portugall, M.; Ringsdorf, H.; Zentel, R. *Makromol. Chem.* **1982**, *183*, 2311.
- (94) G. G. Guilbault, Ed. *Practical Fluorescence*; Marcel Dekker, Inc.: New York,

**1990.**

- (95) Tehan, B. G.; Lloyd, E. J.; Wong, M. G.; Pitt, W. R.; Montana, J. G.; Manallack, D. T.; Gancia, E. *Quant. Struct.-Act. Relat.* **2002**, *21*, 457.
- (96) Cabarcos, E. L.; Carter, S. A. *Macromolecules* **2005**, *38*, 4409.
- (97) (a) Hendrickson G. R.; Lyon, L. A. *Soft Matter* **2009**, *5*, 29. (b) Vriezema, D. M.; Aragonés, M. C.; Elemans, J. A. A. W.; Cornelissen, J. J. L. M.; Rowan, A. E.; Nolte, R. J. M. *Chem. Rev.* **2005**, *105*, 1445; (c) Hoeben, F. J. M.; Jonkheijm, P.; Meijer, E. W.; Schenning, A. P. H. J. *Chem. Rev.* **2005**, *105*, 1491. (d) Pollino, J. M.; Weck, M. *Chem. Soc. Rev.* **2005**, *34*, 193.
- (98) (a) Mezzenga, R.; Ruokolainen, J.; Canilho, N.; Kasëmi, E.; Schlüter, D. A.; Lee, W. B.; Fredrickson, G. H. *Soft Matter* **2009**, *5*, 92. (b) He, J.; Zhao, Y.; Zhao, Y. *Soft Matter* **2009**, *5*, 308. (c) Moughton, A. O.; Stubenrauch, K.; O'Reilly, R. K. *Soft Matter* **2009**, *5*, 2361. (d) Ott, C.; Hoogenboom, R.; Hoepfener, S.; Wouters, D.; Gohy, J.-F.; Schubert, U. S. *Soft Matter* **2009**, *5*, 84. (e) Wilson, A. J. *Soft Matter* **2007**, *3*, 409. (f) Binder, W. H.; Kluger, C.; Josipovic, M.; Straif, C. J.; Friedbacher, G. *Macromolecules* **2006**, *39*, 8092. (g) Binder, W. H.; Kluger, C.; Straif, C. J.; Friedbacher, G. *Macromolecules* **2005**, *38*, 9405. (h) Binder, W. H.; Gloger, D.; Weinstabl, H.; Allmaier, G.; Pittenauer, E. *Macromolecules* **2007**, *40*, 3097. (g) Ner, Y.; Grote, J. G.; Stuart, J. A.; Sotzing,



- G. A. *Soft Matter* **2008**, *4*, 1448.
- (99) Zhao, X.; Jiang, H.; Schanze, K. S. *Macromolecules* **2008**, *41*, 3422.
- (100)(a) Li, Y.; Wang, T.; Liu, M. *Soft Matter* **2007**, *3*, 1312. (b) Phillips, R. L.; Miranda, O. R.; Mortenson, D. E.; Subramani, C.; Rotello, V. M.; Bunz, U. H. F. *Soft Matter* **2009**, *5*, 607. (c) George, W. N.; Giles, M.; McCulloch, I.; de Mello, J. C.; Steinke, J. H. G. *Soft Matter* **2007**, *3*, 1381.
- (101)(a) Lv, J.; Jiang, L.; Li, C.; Liu, X.; Yuan, M.; Xu, J.; Zhou, W.; Song, Y.; Liu, H.; Li, Y.; Zhu, D. *Langmuir* **2008**, *24*, 8297. (b) Abécassis, B.; Testard, F.; Zemb, T. *Soft Matter* **2009**, *5*, 974.
- (102)(a) Kumar, S.; Pal, S. K.; Kumar, P. S.; Lakshminarayanan, V. *Soft Matter* **2007**, *3*, 896. (b) Fragoso, A.; Sanromà, B.; Ortiz, M.; O'Sullivan, C. K. *Soft Matter* **2009**, *5*, 400.
- (103) Brust, M.; Walker, M.; Bethell, D.; Schiffrin, D. J.; Whyman, R. *J. Chem. Soc., Chem. Commun.* **1994**, 801.
- (104) Teranishi, T.; Hasegawa, S.; Shimizu, T.; Miyake, M. *Adv. Mater.* **2001**, *13*, 1699.
- (105) Ingram, R. S.; Hostetler, M. J.; Murray, R. W. *J. Am. Chem. Soc.* **1997**, *119*, 9175.
- (106)(a) Shaffer, A. W.; Worden, J. G.; Huo, Q. *Langmuir* **2004**, *20*, 8343. (b)

- Worden, J. G.; Dai, Q.; Huo, Q. *Chem. Commun.* **2006**, 1536. (c) Dai, Q.; Worden, J. G.; Trullinger, J.; Huo, Q. *J. Am. Chem. Soc.* **2005**, *127*, 8008.
- (107)(a) Fustin, C. A.; Guillet, P.; Misner, M. J.; Russell, T. P.; Schubert, U. S.; Gohy, J. F. *J. Polym. Sci. Part A: Polym. Chem.* **2008**, *46*, 4719. (b) Guillet, P.; Fustin, C. A.; Lohmeijer, B. G. G.; Schubert, U. S.; Gohy, J. F. *Macromolecules* **2006**, *39*, 5484. (c) Fustin, C. A.; Guillet, P.; Schubert, U. S.; Gohy, J. F. *Adv. Mater.* **2007**, *19*, 1665.
- (108)(a) Winder, N. S.; Saridifti, N. S. *J. Mater. Chem.* **2004**, *14*, 1077. (b) Günes, S.; Neugebauer, H.; Sariciftci, N. S. *Chem. Rev.* **2007**, *107*, 1324. (c) Yang, X.; Loos, J. *Macromolecules* **2007**, *40*, 1353.
- (109)(a) Halls, J. J. M.; Walsh, C. A.; Greenham, N. C.; Marseglia, E. A.; Friend, R. H.; Moratti, S. C.; Holmes, A. B. *Nature* **1995**, *376*, 498. (b) Granstrom, M.; Petritsch, K.; Arias, A. C.; Lux, A.; Andersson, M. R.; Friend, R. H. *Nature* **1998**, *395*, 257. (c) Kietzke, T.; Hörhold, H.-H.; Neher, D. *Chem. Mater.* **2005**, *17*, 6532. (d) Breeze, A. J.; Salomon, A.; Ginley, D. S.; Gregg, B. A.; Tillmann, H.; Hörhold, H.-H. *Appl. Phys. Lett.* **2002**, *81*, 3085. (e) Yu, G.; Gao, J.; Hummelen, J. C. *Science* **1995**, *270*, 1789.
- (110)(a) Shin, R. Y. C.; Kietzke, T.; Sudhakar, S.; Chen, Z. K.; Dodabalapur, A.; Sellinger, A. *Chem. Mater.* **2007**, *19*, 1892. (b) Kietzke, T.; Shin, R. Y. C.; Egbe,

- D. A. M.; Chen, Z. K.; Sellinger, A. *Macromolecules* **2007**, *40*, 4424. (c) Ooi, Z. E.; Tam, T. L.; Shin, R. Y. C.; Chen, Z. K.; Kietzke, T.; Sellinger, A.; Baumgarten, M.; Mullene, K.; deMello, J. C. *J. Mater. Chem.* **2008**, *18*, 4619.
- (111)(a) Brabec, C. J.; Sariciftci, N. S.; Hummelen, J. C. *Adv. Funct. Mater.* **2001**, *11*, 15. (b) Al-Ibrahima, M.; Rotha, H. K.; Zhokhavetsb, U. *Sol. Energy Mater. Sol. Cells* **2005**, *85*, 13.
- (112)Ma, W.; Yang, C.; Gong, X.; Lee, K.; Heeger, A. J. *Adv. Funct. Mater.* **2005**, *15*, 1617.
- (113)Lindner, S. M.; Hüttner, S.; Chiche, A.; Thelakkat, M.; Krausch, G. *Angew. Chem., Int. Ed.* **2006**, *45*, 3364.
- (114)(a) Peet, J.; Kim, J. Y.; Coates, N. E.; Ma, W. L.; Moses, D.; Heeger, A. J.; Bazan, G. C. *Nature Mater.* **2007**, *6*, 497. (b) Mühlbacher, D.; Scharber, M.; Morana, M.; Zhu, Z.; Waller, D.; Gaudiana, R.; Brabec, C. *Adv. Mater.* **2006**, *18*, 2884. (c) Zhu, Z.; Waller, D.; Gaudiana, R.; Morana, M.; Mühlbacher, D.; Scharber, M.; Brabec, C. *Macromolecules* **2007**, *40*, 1981.
- (115)(a) Huo, L.; He, C.; Han, M.; Zhou, E.; Li, Y. F. *J. Polym. Sci. Part A: Polym. Chem.* **2007**, *45*, 3861. (b) Colladet, K.; Fourier, S.; Cleij, T. J.; Lutsen, L.; Gelan, J.; Vanderzande, D. *Macromolecules* **2007**, *40*, 65. (c) Shahid, M.; Ashraf, R. S.; Klemm, E.; Sensfuss, S. *Macromolecules* **2006**, *39*, 7844.

- (116)(a) Zhan, X.; Tan, Z.; Domercq, B.; An, Z.; Zhang, X.; Barlow, S.; Li, Y.; Zhu, D.; Kippelen, B.; Marder, S. R. *J. Am. Chem. Soc.* **2007**, *129*, 7246. (b) Zhu, Y.; Champion, R. D.; Jenekhe, S. A. *Macromolecules* **2006**, *39*, 8712. (c) Champion, R. D.; Cheng, K. F.; Pai, C. L.; Chen, W. C.; Jenekhe, S. A. *Macromol. Rapid Commun.* **2005**, *26*, 1835.
- (117)(a) Gebeyehu, D.; Pfeiffer, M.; Maennig, B.; Drechsel, J.; Werner, A.; Leo, K. *Thin Solid Films* **2004**, *451-452*, 29. (b) Shin, R. Y. C.; Kietzke, T.; Sudhakar, S.; Chen, Z. K.; Dodabalapur, A.; Sellinger, A. *Chem. Mater.* **2007**, *19*, 1892. (c) Kietzke, T.; Shin, R. Y. C.; Egbe, D. A. M.; Chen, Z. K.; Sellinger, A. *Macromolecules* **2007**, *40*, 4424. (d) Ooi, Z. E.; Tam, T. L.; Shin, R. Y. C.; Chen, Z. K.; Kietzke, T.; Sellinger, A.; Baumgarten, M.; Mullene, K.; deMello, J. C. *J. Mater. Chem.* **2008**, *18*, 4619. (e) Mei, J.; Heston, N. C.; Vasilyeva, S. V.; Reynolds, J. R. *Macromolecules* **2009**, *42*, 1482. (f) Fan, B.; Hany, R.; Moser, J. E.; Nüesch, F. *Org. Electron.* **2008**, *9*, 85. (g) Belcher, W. J.; Wagner, K. I.; Dastoor P. C. *Sol. Energy Mater. Sol. Cells* **2007**, *91*, 447. (h) Suresh, P.; Balaraju, P.; Sharma, S. K.; Roy, M. S.; Sharma, G. D. *Sol. Energy Mater. Sol. Cells* **2008**, *92*, 900. (i) Wang, M.; Wang, X. *Sol. Energy Mater. Sol. Cells* **2007**, *91*, 1782. (j) Wang, M.; Wang, X. *Sol. Energy Mater. Sol. Cells* **2008**, *92*, 766. (k) Bouclé, J.; Chyla, S.; Shaffer, M. S. P.; Durrant, J. R.; Bradley, D. D. C.; Nelson,

- J. Adv. Funct. Mater.* **2008**, *18*, 622.
- (118)(a) van Mullekom, H. A. M.; Vekemans, J. A. J. M.; Havinga, E. E.; Meijer, E. *W. Mater. Sci. Eng.* **2001**, *32*, 1. (b) Lim, Y. F.; Shu, Y.; Parkin, S. R.; Anthony, J. E.; Malliaras, G. G. *J. Mater. Chem.* **2009**, *19*, 3049. (c) Roquet, S.; Cravino, A.; Leriche, P.; Alévêque, O.; Frère, P.; Roncali, J. *J. Am. Chem. Soc.* **2006**, *128*, 3459. (d) Yasuda, T.; Imase, T.; Nakamura, Y.; Yamamoto, T. *Macromolecules* **2005**, *38*, 4687. (e) Zhang, Z. G.; Zhang, K. L.; Liu, G.; Zhu, C. X.; Neoh, K. G.; Kang, E. T. *Macromolecules* **2009**, *42*, 3104. (f) Li, K. C.; Hsu, Y. C.; Lin, J. T.; Yang, C. C.; Wei, K. H.; Lin, H. C. *J. Polym. Sci. Part A: Polym. Chem.* **2008**, *46*, 4285. (g) Li, K. C.; Hsu, Y. C.; Lin, J. T.; Yang, C. C.; Wei, K. H.; Lin, H. C. *J. Polym. Sci. Part A: Polym. Chem.* **2009**, *47*, 2073. (h) Li, K. C.; Huang, J. H.; Hsu, Y. C.; Huang, P. J.; Chu, C. W.; Lin, J. T.; Ho, K. C.; Wei, K. H.; Lin, H. C. *Macromolecules* **2009**, *42*, 3681.
- (119)(a) Shen, Z.; Strauss, J.; Daub, J. *Chem. Commun.* **2002**, *5*, 460. (b) Lai, R. Y.; Kong, X.; Jenekhe, S. A.; Bard, A. J. *J. Am. Chem. Soc.* **2003**, *125*, 12631.
- (120)(a) Liu, Y.; Cao, H.; Li, J.; Chen, Z.; Cao, S.; Xiao, L.; Xu, S.; Gong, Q. *J. Polym. Sci. Part A: Polym. Chem.* **2007**, *45*, 4867. (b) Yang, L. Y.; Wang, C.; Li, L. Q.; Janietz, S.; Wedel, A.; Hua, Y. L.; Yin, S. G. *J. Polym. Sci. Part A: Polym. Chem.* **2007**, *45*, 4291.

- (121)(a) Cho, N. S.; Park, J. H.; Lee, S. K.; Lee, J.; Shim, H. K. *Macromolecules* **2006**, *39*, 177. (b) Tang, W.; Kietzke, T.; Vemulamada, P.; Chen, Z. K. *J. Polym. Sci. Part A: Polym. Chem.* **2007**, *45*, 5266.
- (122) Zou, Y.; Wu, W.; Sang, G.; Yang, Y.; Liu, Y.; Li, Y. *Macromolecules* **2007**, *40*, 7231.
- (123)(a) Roncali, J. *Chem. Rev.* **1997**, *97*, 173. (b) Tu, G.; Li, H.; Forster, M.; Heiderhoff, R.; Balk, L. J.; Scherf, U. *Macromolecules* **2006**, *39*, 4327.
- (124)(a) Velusamy, M.; Thomas, K. R. J.; Lin, J. T.; Hsu, Y. C.; Ho, K. C. *Org. Lett.* **2005**, *7*, 1899. (b) Thomas, K. R. J.; Hsu, Y. C.; Lin, J. T.; Lee, K. M.; Ho, K. C.; Lai, C. H.; Cheng, Y. M.; Chou, P. T. *Chem. Mater.* **2008**, *20*, 1830. (c) Tsai, M. S.; Hsu, Y. C.; Lin, J. T.; Chen, H. C.; Hsu, C. P. *J. Phys. Chem. C* **2007**, *111*, 18785. (d) Thomas, K. R. J.; Lin, J. T.; Hsu, Y. C.; Ho, K. C. *Chem. Commun.* **2005**, 4098. (e) Lin, J. T.; Chen, P. C.; Yen, Y. S.; Hsu, Y. C.; Chou, H. H.; Yeh, M. C. P. *Org. Lett.* **2009**, *11*, 97.
- (125)(a) Koumura, N.; Wang, Z. S.; Mori, S.; Miyashita, M.; Suzuki, E.; Hara, K. *J. Am. Chem. Soc.* **2006**, *128*, 14256. (b) Wang, Z. S.; Koumura, N.; Cui, Y.; Takahashi, M.; Sekiguchi, H.; Mori, A.; Kubo, T.; Furube, A.; Hara, K. *Chem. Mater.* **2008**, *20*, 3993. (c) Kim, J. J.; Choi, H.; Lee, J. W.; Kang, M. S.; Song, K.; Kang, S. O.; Ko, J. J. *Mater. Chem.* **2008**, *18*, 5223. (d) Wang, Z. S.; Cui, Y.;

- Dan-oh, Y.; Kasada, C.; Shinpo, A.; Hara, K. *J. Phys. Chem. C* **2007**, *111*, 7224.
- (126) Lin, H. C.; Jiang, M. D.; Wu, S. C.; Jou, L. L.; Chou, K. P.; Huang, C. M.; Wei, K. H. *J. Polym. Sci. Part A: Polym. Chem.* **2009**, in press.
- (127) Chen, C. P.; Chan, S. H.; Chao, T. C.; Ting, C.; Ko, B. T. *J. Am. Chem. Soc.* **2008**, *130*, 12828.
- (128) Roncali, J. *Macromol. Rapid Commun.* **2007**, *28*, 1761.
- (129) Huo, L.; Tan, Z.; Wang, X.; Zhou, Y.; Han, M. F.; Li, Y. F. *J. Polym. Sci. Part A: Polym. Chem.* **2008**, *46*, 4038.
- (130) Morteani, A. C.; Sreearunothai, P.; Herz, L. M.; Friend, R. H.; Silva, C. *Phys. Rev. Lett.* **2004**, *92*, 247402.
- (131)(a) Scharber, M. C.; Mühlbacher, D.; Koppe, M.; Denk, P.; Waldauf, C.; Heeger, A. J.; Brabec, C. J. *Adv. Mater.* **2006**, *18*, 789. (b) Brabec, C. J.; Cravino, A.; Meissner, D.; Sariciftci, N. S.; Fromherz, T.; Rispiens, M. T.; Sanchez, L.; Hummelen, J. C. *Adv. Funct. Mater.* **2001**, *11*, 374.
- (132) Baek, N. S.; Hau, S. K.; Yip, H. L.; Acton, O.; Chen, K. S.; Jen, A. K. Y. *Chem. Mater.* **2008**, *20*, 5734.
- (133) Huang, J. H.; Ho, Z. Y.; Kekuda, D.; Chang, Y.; Chu, C. W.; Ho, K. C. *Nanotechnology* **2009**, *20*, 025202.

## Publication

---

1. T. C. Liang, H. C. Lin\*, “**Study of Supramolecular Side-Chain and Cross-Linking Polymers by Complexation of Various H-Donor Acids with H-Acceptor Copolymers Containing Pendent Carbazole and Fluorescent Pyridyl Units**”, *J. of Polymer Sci. Part A: Polymer Chem.* **2009**, *47*, 2734.
2. T. C. Liang, H. C. Lin\*, “**Supramolecular Assembly of H-Bonded Copolymers/Complexes/Nanocomposites and Fluorescence Quenching Effects of Surface-Modified Gold Nanoparticles on Fluorescent Copolymers Containing Pyridyl H-Acceptors and Acid H-Donors**”, *J. Mater. Chem.* **2009**, *19*, 4753.
3. T. C. Liang, I. H. Chiang, P. J. Yang, D. Kekuda, C. W. Chu, H. C. Lin\*, “**Supramolecular Assembly of H-Bonded Side-Chain Polymers Containing Conjugated Pyridyl H-Acceptor Pendants and Various Low-Band-Gap H-Donor Dyes Bearing Cyanoacrylic Acid Groups for Organic Solar Cell Applications**”, *J. of Polymer Sci. Part A: Polymer Chem.* **2009**, in press.
4. T. C. Liang, H. C. Lin\*, “**Supramolecular Fluorescence Quenching Effects of H-Donor Surface-Modified Gold Nanoparticles on Fluorescent H-Acceptor Polymers/Copolymers Containing Lateral Methyl- and Methoxy-Substituted Groups**”, *Soft Matter* **2009**, submitted.



## 學經歷資料表

姓 名	梁宗琦
性 別	男
出生日期	1980 年 02 月 13 日
婚姻狀況	未婚
E-mail 信箱	devin.mse91g@nctu.edu.tw
聯絡電話	0937629205
通訊地址	300 新竹市大學路 1001 號工程六館 EF707 室
永久地址	830 高雄縣鳳山市龍成里南正二路 211 巷 47 號
學 經 歷	<p>1998 年 9 月- 2002 年 6 月 私立高雄醫學大學化學系 學士</p> <p>2002 年 9 月- 2004 年 7 月 國立交通大學材料科學與 工程學系 碩士</p> <p>2004 年 9 月- 2009 年 7 月 國立交通大學材料科學與 工程學系 博士</p>
專 長	液晶與有機發光高分子材料，奈米金球複合材料，有機太陽能電池材料開發、合成與物性鑑定
學術著作	<ol style="list-style-type: none"> <li>1. <u>T. C. Liang, H. C. Lin*</u>, “<b>Study of Supramolecular Side-Chain and Cross-Linking Polymers by Complexation of Various H-Donor Acids with H-Acceptor Copolymers Containing Pendent Carbazole and Fluorescent Pyridyl Units</b>”, <i>J. of Polymer Sci. Part A: Polymer Chem.</i> <b>2009</b>, <i>47</i>, 2734.</li> <li>2. <u>T. C. Liang, H. C. Lin*</u>, “<b>Supramolecular Assembly of H-Bonded Copolymers/Complexes/Nanocomposites and Fluorescence Quenching Effects of Surface-Modified Gold Nanoparticles on Fluorescent Copolymers Containing Pyridyl H-Acceptors and Acid H-Donors</b>”, <i>J. Mater. Chem.</i> <b>2009</b>, <i>19</i>, 4753.</li> <li>3. <u>T. C. Liang, I. H. Chiang, P. J. Yang, D. Kekuda, C. W. Chu, H. C. Lin*</u>, “<b>Supramolecular Assembly of H-Bonded Side-Chain Polymers Containing Conjugated Pyridyl H-Acceptor Pendants and Various Low-Band-Gap H-Donor Dyes Bearing</b></li> </ol>

	<p><b>Cyanoacrylic Acid Groups for Organic Solar Cell Applications”, <i>J. of Polymer Sci. Part A: Polymer Chem.</i> 2009, in press.</b></p> <p>4. <b><u>T. C. Liang</u>, H. C. Lin*, “Supramolecular Fluorescence Quenching Effects of H-Donor Surface-Modified Gold Nanoparticles on Fluorescent H-Acceptor Polymers/Copolymers Containing Lateral Methyl- and Methoxy-Substituted Groups”, <i>Soft Matter</i> 2009, submitted.</b></p>
--	---

